SMIP17

SMIP17 SEMINAR ON
UTILIZATION OF STRONG-MOTION DATA

Berkeley, California
October 19, 2017

PROCEEDINGS

Sponsored by

California Strong Motion Instrumentation Program
California Geological Survey
California Department of Conservation

Co-Sponsors

California Seismic Safety Commission
California Governor's Office of Emergency Services
Office of Statewide Health Planning and Development
California Department of Transportation

The California Strong Motion Instrumentation Program (CSMIP), a program within the California Geological Survey (CGS) of the California Department of Conservation, records the strong shaking of the ground and structures during earthquakes for analysis and utilization by the engineering and seismology communities, through a statewide network of strong motion instruments (www.conservation.ca.gov/CGS/smip). CSMIP is advised by the Strong Motion Instrumentation Advisory Committee (SMIAC), a committee of the California Seismic Safety Commission. Major program funding is provided by an assessment on construction costs for building permits issued by cities and counties in California, with additional funding from the California Governor's Office of Emergency Services (Cal OES), the Office of Statewide Health Planning and Development (OSHPD) and the California Department of Transportation (Caltrans)

In July 2001, the California Governor's Office of Emergency Services (Cal OES) began funding for the California Integrated Seismic Network (CISN), a newly formed consortium of institutions engaged in statewide earthquake monitoring that grew out of TriNet, funded by FEMA, and including CGS, USGS, Caltech and UC Berkeley. The goals are to record and rapidly communicate ground shaking information in California, and to analyze the data for the improvement of seismic codes and standards (www.cisn.org). CISN produces ShakeMaps of ground shaking, based on shaking recorded by stations in the network, within minutes following an earthquake. The ShakeMap identifies areas of greatest ground shaking for use by OES and other emergency response agencies in the event of a damaging earthquake.

The Center for Engineering Strong Motion Data (CESMD) is operated by the CSMIP in cooperation with the National Strong-Motion Project (NSMP), a part of the Advanced National Seismic System (ANSS) of the U.S. Geological Survey (USGS). The CESMD builds on and incorporates the CISN Engineering Data Center and will continue to serve the California region while expanding to serve other ANSS regions. The Data Center provides strong-motion data rapidly after a significant earthquake in the United States. Users also have direct access to data from previous earthquakes and detailed information about the instrumented structures and sites. The CESMD also provides access to the U.S. and international strong ground motion records through its Virtual Data Center (VDC). The Data Center is co-hosted by CGS and USGS at www.strongmotioncenter.org

DISCLAIMER

SMIP17

SMIP17 SEMINAR ON
UTILIZATION OF STRONG-MOTION DATA

Berkeley, California
October 19, 2017

PROCEEDINGS

Edited by

Moh Huang

Sponsored by

California Strong Motion Instrumentation Program
California Geological Survey
California Department of Conservation

Co-Sponsors

California Seismic Safety Commission
California Governor's Emergency Services
Office of Statewide Health Planning and Development
California Department of Transportation

PREFACE

The California Strong Motion Instrumentation Program (CSMIP) in the California Geological Survey of the California Department of Conservation established a Data Interpretation Project in 1989. Each year CSMIP funds several data interpretation contracts for the analysis and utilization of strong-motion data. The primary objectives of the Data Interpretation Project are to further the understanding of strong ground shaking and the response of structures, and to increase the utilization of strong-motion data in improving post-earthquake response, seismic code provisions and design practices.

As part of the Data Interpretation Project, CSMIP holds annual seminars to transfer recent research findings on strong-motion data to practicing seismic design professionals, earth scientists and post-earthquake response personnel. The purpose of the annual seminar is to provide information that will be useful immediately in seismic design practice and post-earthquake response, and in the longer term, useful in the improvement of seismic design codes and practices. Proceedings and individual papers for each of the previous annual seminars are available at http://www.conservation.ca.gov/cgs/smip/docs/seminar/Pages/default.aspx in PDF format. Due to the State budget restraints, CSMIP did not fund as many projects as in other years and did not hold an annual seminar in 2010 or 2011. The SMIP17 Seminar is the twenty-sixth in this series of annual seminars.

The SMIP17 Seminar is divided into two sessions in the morning and two sessions in the afternoon. There are a total of nine presentations including one invited presentation and eight presentations on the results from CSMIP-funded projects. The sessions in the morning include four presentations. The first session will focus on ground motions. Professor Stewart of UCLA will present small-strain damping for ground response analysis. It will be followed by a presentation by Professor Motamed of University of Nevada Reno on the nonlinear site response at California downhole arrays. The second session will focus on results from building response data: code torsional provisions by Professor Zareian of UC Irvine and building soil-structure interactions by Dr. Ebrahimian of Caltech. During the lunch break, Professor Miranda of Stanford University is invited to present his observations from the M7.1 earthquake occurred in Mexico on September 19, 2017.

The third session in the afternoon will focus on lifeline structures. Professor Taciroglu of UCLA will present spatial variability of bridge foundation input motions. Professor Armstrong will present embankment dam deformations. The last session will include presentations of inelastic response from the ground motions recorded during the 2014 South Napa Earthquake by Dr. Mazzoni of UC Berkeley, and ground motion intensities for record selections by Professor Miranda of Stanford University. Individual papers and the proceedings are available to the SMIP17 participants in an USB flash drive, and will be available at the CSMIP website.

Moh Huang
CSMIP Data Interpretation Project Manager

Appreciation to Members of the Strong Motion Instrumentation Advisory Committee

Main Committee

Farzad Naeim, Chair, Farzad Naeim, Inc.
Norman Abrahamson, Pacific Gas & Electric Company
Bruce Clark, Leighton & Associates
Martin Eskijian, California State Lands Commission (retired)
David Gutierrez, DWR Division of Safety of Dams (retired)
Wilfred Iwan, California Institute of Technology
Mark Mahan, Caltrans
Marshall Lew, Amec Foster Wheeler
Bret Lizundia, Rutherford + Chekene
Chris Tokas, Office of Statewide Health Planning and Development
Robert Anderson (ex-officio), Seismic Safety Commission

Ground Response Subcommittee

Marshall Lew, Chair, Amec Foster Wheeler
Abbas Abghari, Caltrans
Brian Chiou, Caltrans
John Egan, SAGE Engineers
Geoffrey Martin, Univ. of Southern California
Marcia McLaren, Pacific Gas & Electric Company (retired)
Ben Tsai, Pacific Gas & Electric Company (retired)

Buildings Subcommittee

Bret Lizundia, Chair, Rutherford + Chekene
Lucie Fougner, Degenkolb Engineers
Ifa Kashefi, City of Los Angeles
David Leung, City of San Francisco
Eduardo Miranda, Stanford University
Roy Lobo, Office of Statewide Health Planning and Development
Chia-Ming Uang, UC San Diego

Lifelines Subcommittee

Martin Eskijian, Chair, California State Lands Commission (retired)
Craig Davis, Los Angeles Dept. of Water and Power
David Gutierrez, DWR Division of Safety of Dams
Mark Mahan, Caltrans
Faiz Makdisi, SAGE Engineers

Data Utilization Subcommittee

Wilfred Iwan, Chair, California Institute of Technology
Representatives from each Subcommittee

TABLE OF CONTENTS

SMIP17 SEMINAR ON UTILIZATION OF STRONG-MOTION DATA

October 19, 2017

International House at UC Berkeley
2299 Piedmont Avenue, Berkeley, California

PROGRAM

8:15 am **REGISTRATION**

9:15 am **WELCOMING REMARKS**
Farzad Naeim, Strong Motion Instrumentation Advisory Committee (SMIAC)
John Parrish, State Geologist, California Geological Survey

INTRODUCTION
Anthony Shakal, Manager, California Strong Motion Instrumentation Program
Moh Huang, California Strong Motion Instrumentation Program

Session I

Moderator: *Marshall Lew*, AMEC Foster Wheeler and SMIAC

9:30 am **Small-Strain Damping for Ground Response Analysis as Used in Non-Ergodic Hazard Analysis – Lessons from California Recordings**
Kioumars Afshari and *Jonathan Stewart*, UC Los Angeles

10:00 am **Nonlinear Site Response at California Downhole Arrays and Interpretation of Finite Element Simulation Results**
Ramin Motamed, Gangjin Li and Stephen Dickenson, University of Nevada, Reno

10:30 am Break

Session II

Moderator: *Bret Lizundia*, Rutherford + Chekene and SMIAC

11:00 pm **Critical Assessment of Code Torsional Provisions using CSMIP Database of Instrumented Buildings**
Yijun Xiang, Farzad Naeim and *Farzin Zareian*, UC Irvine

11:30 pm **Untangling the Dynamics of Soil-Structure Interaction using Nonlinear Finite Element Model Updating**
Hamed Ebrahimian, Domniki Asimaki, Danilo Kusanovic and Farid Ghahari, Caltech

12:00 pm **Lunch**
(Lunch will be provided)

12:30 pm **Observations from the September 19, 2017 M7.1 Puebla-Morelos Earthquake in Mexico** (invited presentation)
Eduardo Miranda, Stanford University

Session III

Moderator: *Martin Eskijian*, California State Lands Commission and SMIAC

1:00 pm **Investigation of the Spatial Variability of Seismic Input Motions for CSMIP-Instrumented Bridges during the 2014 South Napa Earthquake – The Case of Golden Gate Bridge**
S. Farid Ghahari, Hamed Ebrahimian and *Ertugrul Taciroglu*, UC Los Angeles

1:30 pm **Relationship between Earthquake Ground Motion Intensity Measures and Embankment Dam Deformations**
Richard Armstrong, CSU Sacramento

2:00 pm Break

Session IV

Moderator: Wilfred Iwan, Caltech and SMIAC

2:30 pm **Investigation of Ground Motions from the 2014 South Napa Earthquake Considering Inelastic Structural Response**
Tadahiro Kishida, *Silvia Mazzoni*, Yousef Bozorgnia, Brian Chiou, Robert Darragh, Hamid Haddadi, Robert Kayen, Christopher Markham, Sifat Muin and Walt Silva, UC Berkeley

3:00 pm **Development and Evaluation of Ground Motion Intensities for Record Selection and Scaling for Response History Analyses**
Eduardo Miranda and Hector Davalos, Stanford University

3:30 pm **Adjourn**

SMALL-STRAIN DAMPING FOR GROUND RESPONSE ANALYSIS AS USED IN NON-ERGODIC HAZARD ANALYSIS – LESSONS FROM CALIFORNIA RECORDINGS

Kioumars Afshari and Jonathan P. Stewart

Department of Civil & Environmental Engineering
University of California, Los Angeles

Abstract

We compile a California vertical array database of 21 sites. Weak motion transfer functions derived from data are compared to predictions from 1D ground response analyses performed using three damping models – geotechnical models, models for quality factor (Q) based on seismological inversion, and models derived from the site-specific site diminutive parameter (κ_0). When compared to prior results for KiK-net sites in Japan, the California sites have, on average, improved match of empirical and theoretical transfer function shapes and more event-to-event consistency. Using κ_0-informed damping results in a slightly better fit between predicted and observed transfer functions than alternative damping models.

Introduction

Evaluating the role of local site conditions on ground shaking is an essential part of earthquake ground motion prediction, which can be done using ergodic models or site-specific (non-ergodic) analyses. One-dimensional (1D) simulation of shear waves propagating vertically through shallow soil layers, also known as ground response analysis (GRA), is a common approach for capturing the effects of site response on ground shaking. While site response can include important contributions from the wave propagation mechanics simulated in GRA, site response as a whole is considerably more complex. Processes that can control site response in this context include 1D ground response in combination with additional effects including surface waves, basin effects (including focusing and basin edge-generated surface waves), and topographic effects. Because GRA only simulates a portion of the physics controlling site response, there should be no surprise that it is not always effective at accurately predicting site effects.

Validation and testing of 1D GRA is possible by studying recordings from vertical array sites. They allow for the observation of ground motions from the same source both at the surface and the depth at which the downhole sensor is installed. Therefore, a vertical array directly reveals the effects of site response between surface and downhole instruments. In addition, well characterized vertical array sites, which include a high quality shear wave velocity (V_S) profile and possibly a geotechnical log, allows for validating numerical site response models.

Numerous studies of data from vertical arrays at individual sites have found reasonably good fits of data to GRA results (e.g., Borja et al., 1999; Elgamal et al., 2001; Lee et al., 2006; Tsai and Hashash, 2009; Yee et al., 2013). The KiK-net array in Japan (Aoi et al., 2000) provides

a large inventory of vertical arrays that has been extensively used for validation purposes (Thompson et al., 2012; Kaklamanos et al, 2013, 2015; Zalachoris and Rathje, 2015), although the resolution and quality of the seismic velocity and geotechnical site descriptions is arguable sub-optimal. Nonetheless, when viewed as a whole, these KiK-net data challenge the notion that 1D GRA provides a reliable estimate of site response. Were this result found to be widely applicable, it would upend a good deal of current practice that relies on GRA to estimate first-order site response.

Our objective in this study was to evaluate ground response analysis as a method of predicting non-ergodic (site-specific) site response. We utilize the growing body of vertical array data from California which we compiled into a database described in Chapter 2 of Afshari and Stewart (2017). We use the data to evaluate surface-downhole transfer functions, and we study the goodness of fit between empirical transfer functions (ETF) from observations and theoretical transfer functions (TTF) from 1D GRA. In 1D GRA, we use three different approaches for estimating soil damping as discussed next. This paper extends upon the preliminary results presented in Afshari and Stewart (2015) using more sites and an additional damping model informed by site-specific observations regarding high-frequency spectral decay using the so-called diminutive parameter (κ_0).

Ground Response Analyses Procedures

There are many options for performing 1D GRA. Different procedures for GRA can be used depending on the level of nonlinearity that is expected in the profile. The principal alternatives for GRA are linear (more specifically, visco-elastic), Equivalent-Linear (EL), and Nonlinear (NL) methods. Linear methods require only a shear wave velocity profile, unit weights, and a soil damping profile. Additional soil properties required for EL are relationships for modulus reduction and damping vs. shear strain. The NL procedures require these same inputs, but will often incorporate shear strength and other parameters related to viscous damping and rules for unload-reload relationships.

We model the soil as linearly visco-elastic because almost all of the recordings compiled in our database are not strong enough to cause soil nonlinearity. Therefore, we only perform linear analysis to validate GRA under small levels of ground shaking. We have chosen to use the linear option in the Frequency Domain Analysis module in DEEPSOIL (Hashash et al., 2016) for linear analysis. We applied parameter selection protocols for GRA as given by Stewart at al. (2014). An exception is small strain damping (D_{min}), the selection of which is discussed below.

Alternative Damping Models

Small-strain damping is required in GRA, including those employing linear soil properties. Even under elastic conditions, damping occurs because of the intrinsic damping within soil elements and scattering of waves off of subsurface irregularities (e.g., Rodriguez-Castellanos et al. 2006).

We consider two classes of models for small strain damping in soils, both of which are frequency-independent (hysteretic). The first class of models are collectively referred to as geotechnical models, because they are derived from advanced cyclic testing performed in

geotechnical labs. These models account for intrinsic damping. The second are V_S-based models originally developed from calibration of stochastic ground motion simulations in central and eastern North America. To the extent that the calibration is accurate for a given application, these models incorporate the effects of both intrinsic material damping and scattering.

Material Damping Models

Various geotechnical models relate small-strain damping as measured from geotechnical laboratory cyclic testing, denoted D_{min}^{L}, to various predictor variables related to soil type and confining pressure. We estimate laboratory-based D_{min}^{L} using Darendeli (2001) relations for clays and silts, and Menq (2003) relations for granular soils. The input parameters for the D_{min}^{L} models are plasticity index (*PI*), overconsolidation ratio (*OCR*), and effective stress for Darendeli (2001), and mean grain size (D_{50}), coefficient of uniformity (C_u), and effective stress for Menq (2003). The D_{min}^{L} relations can only be used when geotechnical log and/or description of soil conditions are available for the site.

Models for Combined Material Damping and Wave Scattering Effects

We begin with a brief description of the square-root impedance (SRI) method for predicting site effects (Joyner et al. 1981; Boore 2013). While this method is not directly used for comparison to data in this study, the approach is nonetheless important for the present discussion because it provides the context in which site diminutive parameter κ_0 is used. The SRI method uses the following equation for evaluating amplification of Fourier Amplitude Spectra for a vertical ray path:

$$A_0(f) = \left(\frac{\rho_R V_R}{\overline{\rho}\,\overline{V}} \right)^{0.5} \tag{1}$$

where A_0 is the amplification, ρ_R and V_R are density and shear wave velocity at the reference (downhole condition), and $\overline{\rho}$ and $\overline{V}$ are average density and shear wave velocity for a depth interval corresponding to the top quarter wavelength of the profile. While this method is simple and efficient, it cannot capture the effects of resonance and nonlinearity. Moreover, in the form represented by Eq. (1), it does not include the effects of damping, which is evident by the amplification value at high frequencies approaching a plateau. This plateau feature is unrealistic because actual amplification functions slope downward with frequency at high frequencies beyond the primary modal peaks in the spectrum. Although the shape shown in Figure 1 is strictly applicable to site amplification, similar features are observed in simulated Fourier amplitude spectra using stochastic methods (e.g., Boore, 2003).

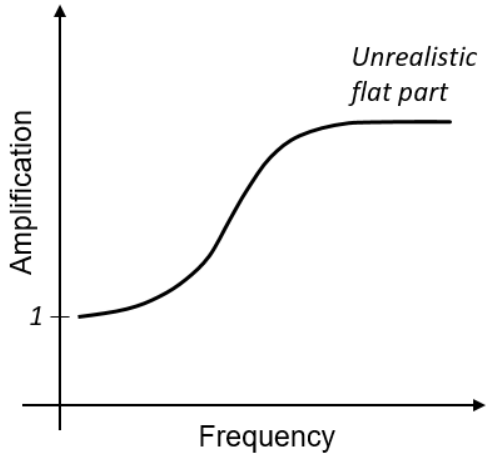

Figure 1. Unrealistic plateau of amplification at high frequencies when using quarter wave length theory without application of diminutive parameter κ.

In order to overcome the problem of unrealistic Fourier amplitude spectral shapes at high frequencies, a spectral decay, or diminutive, parameter (κ) is introduced.

$$X(f) = X_0(f) \times \exp(-\pi\kappa f) \tag{2}$$

where X indicates Fourier amplitude. The effect on spectral shape of applying this parameter is shown in Figure 2. The value of κ applicable to a particular ground motion recording can be partitioned into two components, namely a zero distance κ or site κ (κ_0), and the attenuation with distance ($\kappa_R R$) (adapted from Anderson, 1991):

$$\kappa = \kappa_0 + \kappa_R R \tag{0}$$

where R is the source-site distance, and κ_R is the rate with which the decay parameter (κ) increases with distance, capturing the effects of anelastic attenuation.

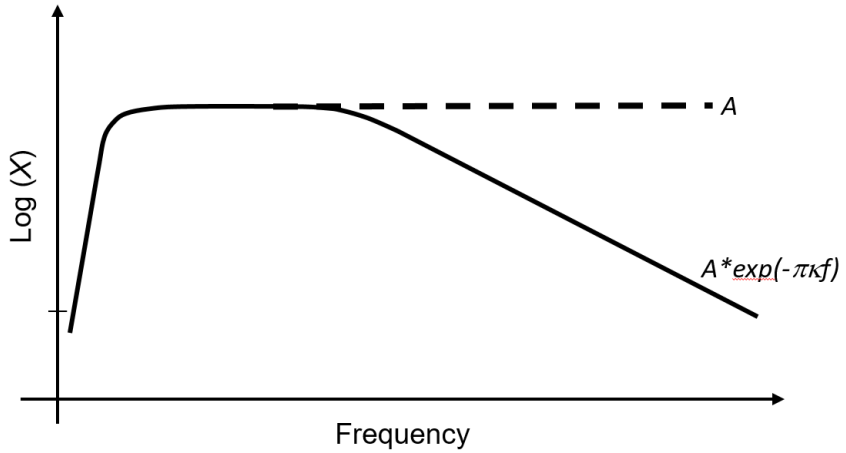

Figure 2. Modifying simulated ground motions at high frequencies by introducing κ.

The contribution of site damping to high frequency attenuation is captured by the κ_0 diminutive parameter (Eq. 3). The κ_0 parameter represents the cumulative effect of damping through the soil column, which is commonly represented by (Hough and Anderson 1988; Chapman et al. 2003; Campbell 2009):

$$\kappa_0 = \int_0^z \frac{dz}{Q_{ef}(z) V_S(z)} \tag{4}$$

where z is the soil column depth and Q_{ef} is the depth-dependent effective material quality factor, representing both the effects of frequency-dependent wave scattering and frequency-independent soil damping. Quantity Q_{ef} can be readily converted to an effective soil damping as follows (Campbell, 2009):

$$D_{eff}(\%) = \frac{100}{2Q_{\text{ef}}} \tag{5}$$

In order to facilitate ground motion prediction in central and eastern U.S., several investigators have developed models for either depth-dependent Q_{ef} or κ_0 in particular regions (e.g., Boore and Joyner 1991, Gomberg et al. 2003, Cramer et al. 2004). Campbell (2009) reviewed many of these studies and proposed a suite of models relating Q_{ef} to V_S, one of which is given by:

$$Q_{ef} = 7.17 + 0.0276 V_S \tag{6}$$

where V_S is in m/s. Eq. (6) is one of four models proposed by Campbell (2009) and has seen application in a number of subsequent studies (Hashash et al., 2014; E. Rathje, personal communication) (more so than the other three models). We choose to use this model over an older model by Olsen et al. (2003) which is intended for long periods (>2 sec). An advantage of this approach for modeling D_{eff} is that it is only based on V_S as an input parameter, and therefore it does not require a geotechnical log. We apply this approach for all 21 sites used in this study.

The third damping model considered in this study takes the site component of κ (i.e, κ_0) from ground motion recordings to adjust values of small-strain damping derived from geotechnical models to represent site-specific effects. Whether such adjustments are effective for ground motion prediction is investigated in the next section.

The expression for κ_0 given in Eq. (4) strictly applies when the full crustal profile is considered in the depth integral. A more practical alternative is to evaluate the site diminutive parameter for reference rock, $\kappa_{0,ref}$, and then modify it for damping through the soil column as (Campbell, 2009):

$$\kappa_0 = \kappa_{0,ref} + \int_0^z \frac{dz}{Q_{ef}(z) V_S} \tag{7}$$

The integral in this case represents the contribution from the geologic column above the reference rock. Note that $\kappa_{0,ref}$ as used in simulations may not match the site condition at the downhole sensor. However, for the present application, we take $\kappa_{0,ref}$ as applying for the

downhole geologic condition. Adopting this definition and using Eq. (5) to convert Q_{ef} to D_{min}, we re-write Eq. (7) as:

$$\kappa_0 = \kappa_{0,ref} + \int_0^z \frac{2D_{eff}(z)}{100} V_S^{-1}(z)dz \quad (8)$$

The vertical array data can be used to estimate the integral in Eq. (8), which in turn can be used to adjust model-based D_{min} to reflect site-specific conditions. The methodology of estimating κ-informed damping is described in Section 3.2.3 of Afshari and Stewart (2017).

Inferences of Site Response from Transfer Functions and Implications for the Effectiveness of Ground Response Analysis

Empirical transfer functions (ETFs) representing site response between the downhole and surface accelerometers are computed from ratios of Fourier amplitudes as follows:

$$H(f) = \frac{Z(f, x_1)}{X(f, x_2)} \quad (9)$$

where $H(f)$ is the ETF, $Z(f,x_1)$ is the surface FAS and $X(f,x_2)$ is the downhole FAS. ETFs are only considered over the usable frequency range based on record processing. The ETF is taken as the geometric-mean of ETFs for the two horizontal components of the recordings (at their as-recorded azimuths) for each site. The results shown subsequently are smoothed through the use of a logarithmic window function proposed by Konno and Ohmachi (1998) with the coefficient for bandwidth frequency (b) equal to 20.

Theoretical transfer functions (TTF) are a direct outcome of linear analysis. In other words, the calculation of TTFs does not require analysis of ground motions and their Fourier amplitudes as in Eq. (9). When time-domain procedures are used, the ground motions must be calculated, their FAS computed, and then TTF can be taken using Eq. (9).

Before proceeding further, it should be pointed out that the ETF (and TTF) represents the surface/downhole ratio in which the surface motion is outcropping and the downhole motion is 'within'. The 'within' term indicates that the motion includes the effects of down-going waves that have reflected from the ground surface, whereas outcropping motions are twice the amplitude of the incident wave due to full reflection at a free-surface.

Transfer Function Comparisons from KiK-Net Array in Japan

Thompson et al. (2012) studied 100 KiK-Net sites in Japan in order to assess the variability in site amplification and the performance of linear 1D GRA. These sites have recorded a large number of surface and downhole recordings. For GRA, they used the program NRATTLE, which is a part of the ground motion simulation program SMSIM (Boore, 2005). NRATTLE performs linear GRA using Thomson–Haskell matrix method (Thomson, 1950; Haskell, 1953). The input parameters for NRATTLE include shear wave velocity (V_S), soil density, and the intrinsic attenuation of shear-waves (Q_S^{-1}) which represents damping. Soil density was estimated from P-wave velocity using the procedures suggested by Boore (2008), and $Q_S^{-1}$was estimated using a grid-search algorithm to optimize the fit to $H(f)$. Note that by

optimizing damping in this manner, Thompson et al. (2012) do not assess the performance of alternative damping models. Moreover, this optimization would not be possible to perform in a forward sense when vertical array recordings from a site are not available.

Thompson et al. (2012) computed ETFs with Eq. (9) using available data meeting certain selection requirements. In order to minimize the potential for nonlinear effects, only records having a ground surface PGA < 0.1 g were selected. In total, 3714 records from 1573 earthquakes were considered for the 100 KiK-net sites. Goodness-of-fit was quantified using Pearson's sample correlation coefficient (r) as a measure of how well the model predictions and the data are correlated. Parameter r quantifies how well the transfer functions align, including the locations and shapes of peaks. Parameter r is insensitive to relative overall levels of amplification. Thompson et al. (2012) calculated the Pearson's sample correlation coefficient for i^{th} earthquake and j^{th} analysis (based on damping estimation approach) as follows for a given site:

$$r_{ij} = \frac{\sum\left(\mathrm{ETF}_i(f) - \overline{\mathrm{ETF}_i}\right)\left(\mathrm{TTF}_j(f) - \overline{\mathrm{TTF}_j}\right)}{\sqrt{\sum\left(\mathrm{ETF}_i(f) - \overline{\mathrm{ETF}_i}\right)^2}\sqrt{\sum\left(\mathrm{TTF}_j(f) - \overline{\mathrm{TTF}_j}\right)^2}} \tag{10}$$

The summations in Eq. (10) are taken over a frequency range with a lower bound f_{min} corresponding to the first peak in the TTF and an upper bound f_{max} that is the minimum of the frequency of the fourth peak of the TTF or 20 Hz. The summation is performed over all frequency points between f_{min} and f_{max}, which are equally spaced in logarithmic units. The mean value of r across all events (r_j) for a given site is denoted $\bar{r}$. A value of $\bar{r} = 0.6$ was taken by Thompson et al. as the threshold for good fit.

Results for the 100 considered KiK-Net sites show that only 18% have a good fit between ETFs and TTFs, indicating 1D GRA fails to provide an accurate estimation of site response for a large majority of KiK-net sites.

A second metric considered by Thompson et al. (2012) concerns the inter-event variability of transfer function ordinates, which they computed as a median value of the standard deviations computed across the frequencies within the range to compute r. Large values of this standard deviation indicate large event-to-event differences in observed site amplification, suggesting potential complexities from 3D geologic structure. The results for full list of 100 sites and a comparison to California data is presented in the next section.

Transfer Function Comparisons for California Vertical Array Data

Using the data set described in Chapter 2 of Afshari and Stewart (2017), we compute ETF ordinates for each of 21 selected California vertical array sites. In this sense our approach is similar to that of Thompson et al. (2012) – we 'cast the net widely' to study site response performance over a wide range of conditions. Unlike several studies conducted since Thompson et al. (2012), we do not screen sites to identify those for which the ETF matches the shape of a TTF; instead we seek to understand how frequently such a match is achieved in relatively weak motion data from California vertical array sites.

We exclude recordings with strong ground shaking (*PGA* at surface instrument > 0.1 g) so as to minimize nonlinear effects. Figure 3 shows histograms of *PGA* and *PGV* for the downhole instrument records used in the present work.

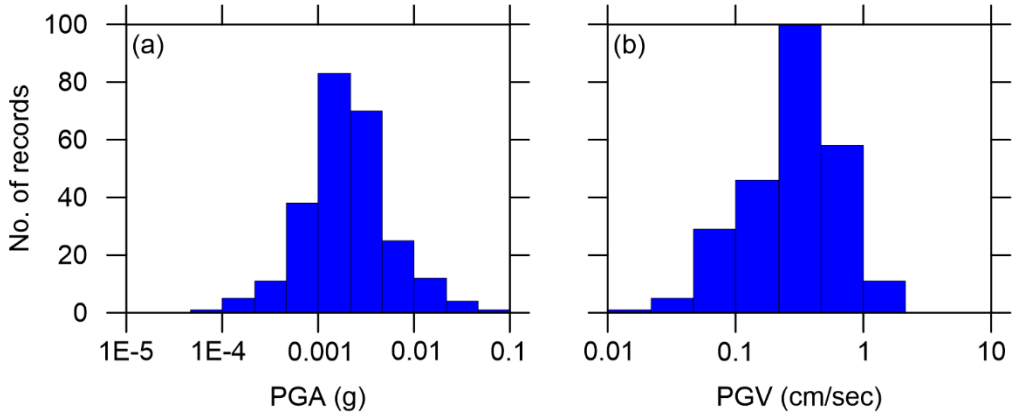

Figure 3. Histograms of PGA (a) and PGV (b) for downhole recordings used in this study

We assume a log-normal distribution for ETF ordinates and compute for each site the median ($\mu_{\ln}$) (equivalent to the exponent of the natural log mean) and the natural log standard deviation of ETF ($\sigma_{\ln}$) at each frequency using all available record pairs.

Theoretical transfer functions (TTFs) are computed by linear visco-elastic 1D GRA in DEEPSOIL (Hashash et al., 2016). As the downhole sensor is recording both up-going and down-going waves, we take the boundary condition at the base of the model as rigid (Kwok et al., 2007). The visco-elastic analysis in DEEPSOIL is performed in the frequency domain, and the transfer function predicted by the model is independent of the input motion. Similar to ETFs, the TTFs are smoothed by Konno and Ohmachi (1998) function with b=20. We utilize alternate approaches for estimating small-strain soil damping as described previously to provide insight and guidance on best practices for selection of effective small-strain damping (D_{eff}). Note that this aspect of our analysis departs from the prior work of Thompson et al. (2012), who back-calculated damping to optimize the ETF-TTF fit.

Figure 4 shows two examples of model-data transfer function comparisons. The match (or lack thereof) of the positions of the first several peaks in ETFs and TTFs are a good indicator of consistency between the transfer functions. In the example of El Centro-Meloland site, the simulations are not able to capture the position of any of the visible five peaks seen in the ETF. This is an indication that 1D GRA is unable to simulate the site response between surface and downhole regardless of the damping model. On the contrary, for the Treasure Island site, the position of all six peaks in the ETF are captured by GRA, which is an indication that the 1D assumption implicit to GRA is valid for this site.

We also consider the quantitative assessment of goodness of fit provided by the Pearson's sample correlation coefficient r (Eq. 10). We use the mean value over all recordings at a given site, $\bar{r}$, which is shown in Figure 5. Generally, sites with qualitatively good fit between ETF and TTF have values of $\bar{r} > 0.6$ (e.g., Treasure Island site in Figure 4) and sites with poor fit have

$\bar{r} < 0$ (e.g., El Centro-Meloland site). Transfer function comparisons for the other 19 vertical array sites are given in Chapter 4 of Afshari and Stewart (2017).

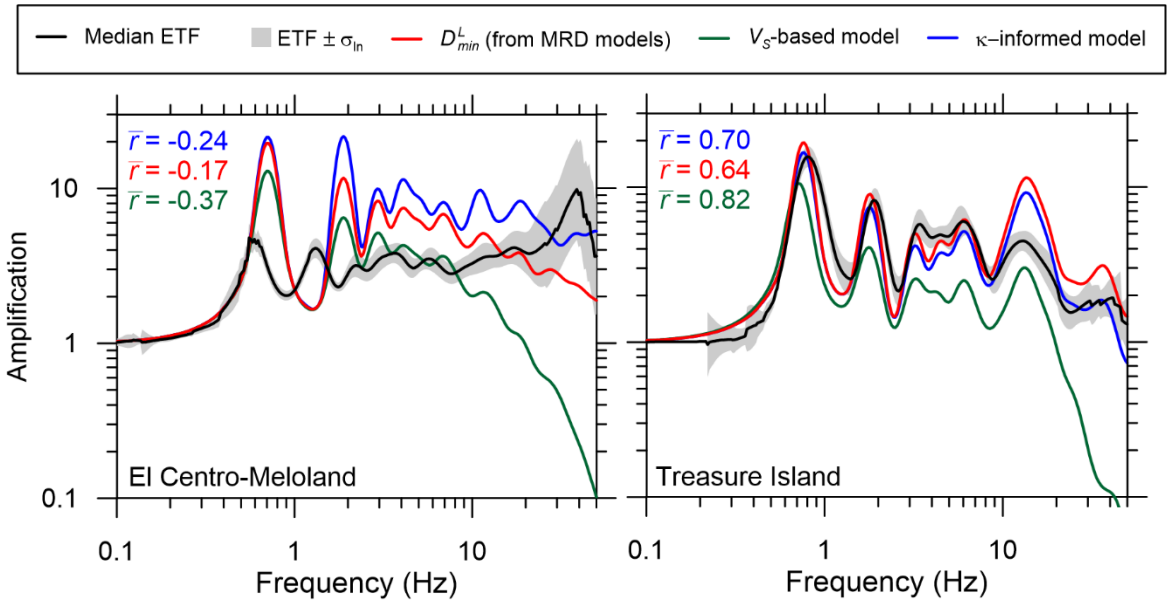

Figure 4. Comparison of ETF and TTFs for El Centro-Meloland and Treasure Island. Values of $\bar{r}$ for each damping model are shown in different colors (red: D^L_{min}, green: V_S-based, blue: κ-informed).

Figure 5 shows histograms of $\bar{r}$ from the California vertical array sites using the three damping models (geotechnical, V_S-based, κ-informed). Also shown for comparison is the distribution from Thompson et al. (2012) for KiK-net sites, although the optimization of damping performed in that study makes the comparison somewhat 'apples-to-oranges', with Japan sites expected to have higher $\bar{r}$ than they would have had without optimization. We see that California sites have higher values of $\bar{r}$ in aggregate, with a higher population median and lower standard deviation. There is also a higher percentage of sites with strong correlation ($\bar{r} >$ 0.6) in comparison to their counterparts for the KiK-net arrays in Japan for all damping models. This suggests that the ability of GRAs to match observation is better for the California vertical arrays than for KiK-net sites. Furthermore, the comparison of $\bar{r}$ histograms for California sites suggests a slight increase in $\bar{r}$ when using the κ-informed model indicating a slightly better performance of the κ-informed damping model in capturing the shape of site response transfer functions.

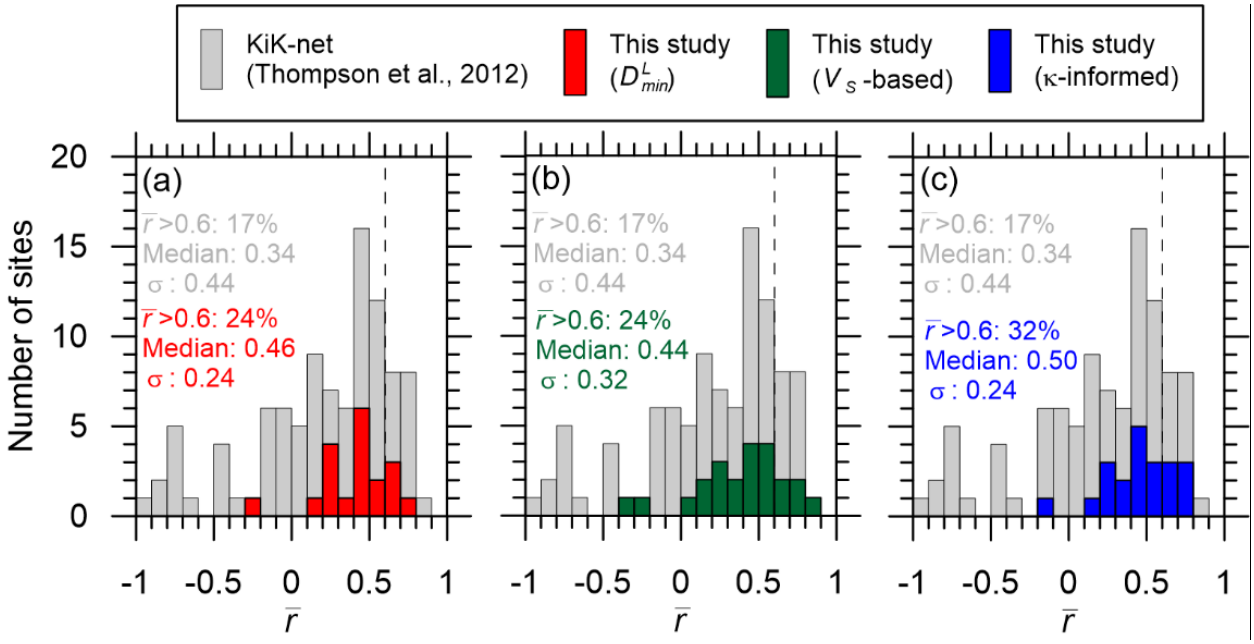

Figure 5. Histograms of $\bar{r}$ for California and KiK-net sites as well as their medians and standard deviations. Values and summary statistics of $\bar{r}$ for each damping model are shown in different colors for California sites (red: D^L_{min}, green: V_S-based, blue: κ-informed model).

As described earlier, Thompson et al. (2012) introduced a metric of ETF variability that is useful to consider in combination with $\bar{r}$ because it quantifies event-to-event variability in observed site response across a particular vertical array. This metric is computed by first taking the natural log standard deviation of ETF ordinates for each of the frequencies considered in the analysis of $\bar{r}$ (i.e., between the lower and upper bound frequencies f_{min} and f_{max}). Then the median across those standard deviations is taken, which is denoted σ^M_{ln}. Figure 6 shows the distribution of σ^M_{ln} for the California vertical array sites, with the values reported by Thompson et al. (2012) for the KiK-net sites also shown for comparison (the method of computation is the same in both cases). The inter-event dispersion is notably smaller for the California sites, with only two (10%) exceeding the value of 0.35 considered as 'high dispersion' by Thompson et al. (2012).

Sites having comparable transfer function shapes and low dispersion have been useful for GRA validations performed in several studies (e.g., Kaklamanos et al. 2015, Zalachoris and Rathje, 2015). To facilitate similar work using California data, Table 1 lists California vertical array sites with $\bar{r} > 0.6$ and $\sigma^M_{ln} < 0.2$ (considering the most optimal outcomes among the damping models).

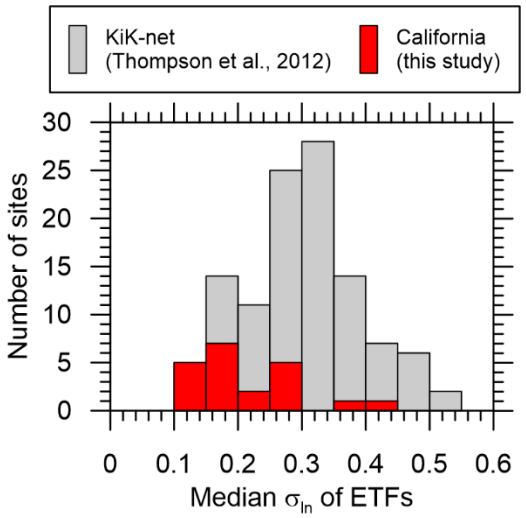

Figure 6. Histogram of ETF between-event standard deviation term σ_{ln}^{M} for California and KiK-net vertical array sites.

Table 1. California vertical array sites with $\bar{r} > 0.6$ and $\sigma_{ln}^{M} < 0.2$ (considering the most optimal outcomes among the damping models)

Site Name	Code #	Optimal $\bar{r}$	Damping model	σ_{ln}^{M}
Benicia-Martinez South	68323	0.79	V_S-based	0.17
Eureka	89734	0.75	V_S-based	0.20
Treasure Island	58642	0.82	V_S-based	0.20
Wildlife Liquefaction Array	NA	0.69	Geotechnical	0.15

Summary and Interpretation of Results

California has one of the most useful inventories of vertical arrays world-wide, when viewed from the perspective of site and ground motion data quality and quantity. We have compiled a database that is used to investigate the effectiveness of the 1D assumption inherent to ground response analysis procedures and to evaluate the relative effectiveness of three alternative damping models.

We find a better fit and smaller ETF dispersion for the California sites as compared to what was found previously by Thompson et al. (2012) for 100 KiK-net sites. This may result from the former mostly being located within large sedimentary basins and relatively flat areas, whereas the later are often on firmer ground conditions (often weathered rock or thin soil over rock) with uneven ground conditions. The geologic conditions at the KiK-net sites are such that horizontal layering of sediments is less likely to be an acceptable assumption, with the site response being strongly influenced by 2D and 3D effects associated with irregular stratigraphy and (in some cases) topography. The 2D and 3D effects in site response in KiK-net sites has been studied by De Martin et al. (2013), who suggests the period and amplitude of site response peaks are significantly sensitive to 2D and 3D effects due to non-horizontal layering. Another possible

factor resulting in a better fit for California sites is the quality of V_S measurements. The vertical arrays in California used in this study have high-resolution suspension logging measurements (with only one exception), while the KiK-net sites are characterized with lower-resolution downhole measurements.

Ground response analyses based on geotechnical models underestimate site attenuation, which has been observed previously and is expected because scattering effects are neglected. The models based on seismological inversion tend to overestimate site attenuation; this conclusion is likely not fully general, but applies to the considered data inventory. Among the three damping models used in this study for GRA, the κ-informed model is found to slightly better predict the shape of site response transfer functions.

Acknowledgments

Funding for this study is provided by California Strong Motion Instrumentation Program, California Geological Survey, Agreement Numbers 1014-961 and 1016-985. This support is gratefully acknowledged. We are appreciative of Tadahiro Kishida and Yousef Bozorgnia for providing access to data processing codes and their efforts in developing data resources used in this study. We also thank Hamid Haddadi of CSMIP for providing weak motion records from the Center for Engineering Strong Motion Data FTP folders, Javier Vargas Ortiz, Bahareh Heidarzadeh, and Jamison Steidl for providing geotechnical logs for vertical arrays sites considered in this project, and Eric Thompson and Adrian Rodriguez-Marek for providing valuable insight on their previous studies involving vertical arrays.

References

Afshari, K. and Stewart, J. P., 2015. Effectiveness of 1D ground response analyses at predicting site response at California vertical array sites, *Proc. SMIP2015 Seminar on Utilization of Strong Motion Data*, California Strong Motion Instrumentation Program, Sacramento, CA.

Afshari, K. and Stewart, J. P., 2017. Implications of California Vertical Array Data for the Analysis of Site Response with 1D Geotechnical Modeling, *A report on research conducted under grant no. 1014-961 from California Strong Motion Instrumentation Program, California Geological Survey.*

Anderson, J. G., 1991. A preliminary descriptive model for the distance dependence of the spectral decay parameter in Southern California, *Bull. Seismol. Soc. Am*. 74, 1969-1993.

Aoi, S. ,Obara, K., Hori, S., Kasahara, K., Okada, Y., 2000. New Japanese uphole–downhole strong-motion observation network: KiK-Net, Seismological Research Letters *Seism. Res. Lett.* 72:239.

Boore, D.M., 2003. Simulation of ground motion using the stochastic method, *Pure and Applied Geophysics*, **160**, 635-675.

Boore, D. M., 2005. SMSIM—Fortran programs for simulating ground motions from earthquakes: Version 2.3—A Revision of OFR 96- 80-A, *Open-File Rpt. 00-509*, U.S. Geological Survey, revised 15 August 2005, 55 pp.

Boore, D.M., 2008. Some thoughts on relating density to velocity <http://quake.wr.usgs.gov/boore/daves_notes/daves_notes_on_relating_density_to_velocity_v1.2.pdf>

Boore, D. M., 2013. The uses and limitations of the square-root-impedance method for computing site amplication. *Bull. Seismol. Soc. Am.* **103**, 2356-2368.

Boore, D. M., and W. B. Joyner, 1991. Estimation of ground motion at deep-soil sites in eastern North America, *Bull. Seismol. Soc. Am.* **81**, 2167–2185.

Borja, R. I., Chao, H.-Y., Montans, F. J., and Lin, C.-H., 1999. Nonlinear ground response at Lotung LSST site, *J. Geotech. Geoenviron. Eng.*, **125**, 187–197.

Campbell, K.W., 2009. Estimates of shear-wave Q and κ_0 for unconsolidated and semiconsolidated sediments in Eastern North America, *Bull. Seismol. Soc. Am*. 99, 2365-2392.

Cramer, C. H., Gomberg, J. S., Schweig, J. S., Waldron, B. A., and Tucker, K., 2004. The Memphis, Shelby Country, Tennessee, seismic hazard maps, *U.S. Geol. Surv.* Open-File Rept. 04-1294.

Darendeli, M. B., 2001. Development of a New Family of Normalized modulus reduction and material damping curves, PhD Thesis, Department of Civil Engineering, University of Texas, Austin, TX.

De Martin, F., Matsushima, S., Kawase, H., 2013, Impact of geometric effects on near- surface Green's functions, *Bull. Seismol. Soc. Am*. **103**, 3289-3304.

Elgamal, A., Lai, T., Yang, Z., He, L., 2001. Dynamic soil properties, seismic downhole arrays and applications in practice, *Proceedings, 4th International Conference on Recent Advances in Geotechnical Earthquake Engineering and Soil Dynamics*, S. Prakash, ed., San Diego, CA.

Gomberg, J., Waldron, B., Schweig, E., Hwang, H., Webbers, A., Van Arsdale, R., Tucker, K., Williams, R., Street, R., Mayne, P., Stephenson, W., Odum, J., Cramer, C., Updike, R., Hutson, S., and Bradley, M., 2003. Lithology and shear-wave velocity in Memphis, Tennessee, *Bull. Seismol. Soc. Am*. **93**, 986–997.

Haskell, N.A., 1953. The dispersion of surface waves on multilayered media. *Bull. Seismol. Soc. Am.*, **72**, 17–34.

Kaklamanos, J., Bradley, B. A., Thompson, E. M., and Baise, L. G., 2013. Critical parameters affecting bias and variability in site-response analyses using KiK-net downhole array data, *Bull. Seismol. Soc. Am.*, **103**, 1733–1749.

Kaklamanos, J., Baise, L. G., Thompson, E. M., and Dorfmann, L., 2014. Comparison of 1D linear, equivalent-linear, and nonlinear site response models at six KiK-net validation sites, *Soil Dyn. Eqk. Eng.*, **69**, 435–460.

Kaklamanos, J., Baise, L. G., Thompson, E. M., Dorfmann, L., 2015. Comparison of 1D linear, equivalent-linear, and nonlinear site response models at six KiK-net validation sites, *Soil Dyn. Earthq. Eng.* 69, 207-215.

Konno, K., and Ohmachi, T. (1998). Ground-Motion Characteristics Estimated from Spectral Ratio between Horizontal and Vertical Components of Microtremor, *Bull. Seismol. Soc. Am.*, **88**, 228–241.

Kwok, A.O., Stewart, J.P., Hashash, Y.M.A., Matasovic, N., Pyke, R., Wang, Z., and Yang, Z. (2007). Use of exact solutions of wave propagation problems to guide implementation of nonlinear seismic ground response analysis procedures, *J. Geotech. & Geoenv. Engrg.*, ASCE, 133 (11), 1385-1398.

Lee, C.-P., Tsai, Y.-B., and Wen, K. L., 2006. Analysis of nonlinear site response using the LSST downhole accelerometer array data, *Soil Dyn. Eqk. Eng.*, **26**, 435–460.

Menq, F. Y., 2003. Dynamic Properties of Sandy and Gravelly Soils, PhD Thesis, Department of Civil Engineering, University of Texas, Austin, TX.

Olsen, K., Day, S., Bradley, C., 2003. Estimation of Q for long-period (> 2 sec) waves in the Los Angeles basin. *Bull. Seismol. Soc. Am.* **93**, 627–638.

Rodriguez-Castellanos, A, FJ Sánchez-Sesma, F Luzon, R Martin, 2006. Multiple scattering of elastic waves by subsurface fractures and cavities, *Bull. Seismol. Soc. Am.* **96**, 1359-1374

Stewart, J.P., Afshari, K., and Hashash, Y. M. A., 2014. Guidelines for performing hazard-consistent one-dimensional ground response analysis for ground motion prediction, *PEER Report No. 2014/16*, Pacific Earthquake Engineering Research Center, UC Berkeley, CA.

Thompson, E. M., Baise, L. G., Tanaka, Y., and Kayen, R. E., 2012. A taxonomy of site response complexity, *Soil Dyn. Earthq. Eng.*, **41**, 32–43.

Thomson, W. T., 1950. Transmission of elastic waves through a stratified solid, Journal of Applied Physics, **21**, 89–93.

Tsai, C. C. and Hashash, Y. M. A., 2009. Learning of dynamic soil behavior from downhole arrays, *J. Geotech. Geoenv. Eng.*, **135**, 745–757.

Yee, E., Stewart, J. P., and Tokimatsu, K., 2013. Elastic and large-strain nonlinear seismic site response from analysis of vertical array recordings, *J. Geotech. Geoenv. Eng.*, **139**, 1789–1801.

Zalachoris, G., and Rathje E. M., 2015. Evaluation of one-dimensional site response techniques using borehole arrays, *J. Geotech. Geoenviron. Eng.*, 10.1061/(ASCE)GT.1943-5606.0001366, 04015053.

NONLINEAR SITE RESPONSE AT CALIFORNIA DOWNHOLE ARRAYS AND INTERPRETATION OF FINITE ELEMENT SIMULATION RESULTS

Ramin Motamed[1], Gangjin Li[1] and Stephen Dickenson[2]

[1] Department of Civil & Environmental Engineering, University of Nevada Reno, Reno, NV
[2] New Albion Geotechnical, Inc., Reno, NV

Abstract

This paper summarizes the results of a recently completed project on the one-dimensional (1D) site response analysis (SRA) of five geotechnical downhole arrays in California which were subjected to both strong and weak earthquake shakings. The arrays were initially assessed in terms of the effectiveness of the 1D SRA using taxonomy classification. Then, SRA was performed utilizing finite element program LS-DYNA to study the site effects at the selected arrays. Lastly, the predictions were compared with the recorded counterparts and the uncertainties of the 1D SRA models were evaluated using two methods namely the Goodness-of-Fit (GOF) and Amplification Factor (AF) residuals. The 1D SRA results of the selected arrays were interrogated on a site-by-site basis and discussions are made on the effectiveness of the employed nonlinear SRA models.

Introduction

This study investigates the influence of local site effects and the soil nonlinear response on the amplification of recorded ground motions at five CSMIP geotechnical downhole arrays where recorded motions exceeded 0.1g. Taxonomy evaluation of the arrays was carried out to inform the expected level of accuracy of the 1D SRA models. Furthermore, LS-DYNA, an advanced Finite Element (FE) program, was utilized to develop soil column models for 1D SRA at these arrays in order to quantify the shortcomings of the 1D approximations on the computed site response. By acknowledging the limitation of the 1D SRA modeling such as: (1) all horizontal boundaries are extended infinitely, and (2) the response is dominated by vertically propagating horizontally polarized shear (SH) waves, we evaluated the accuracy of the calculated response at these arrays. Both strong and weak recorded ground motions were used to perform SRA for each downhole array and the analysis results were compared with the observations at every available downhole sensor depth in order to examine the effectiveness of SRA models in capturing the soil response. On the basis of the analyses performed, we quantified the accuracy of the 1D SRA models and the advantages of the nonlinear soil modeling using two quantitative methods namely the Goodness-of-Fit (GOF) and Amplification Factor (AF) residuals.

Selection of Geotechnical Downhole Arrays

Array Selection Criteria

We carried out a screening procedure through the CSMIP geotechnical downhole arrays with special attention to the ones recorded motions during the 2014 M_w 6.0 South Napa Earthquake to select arrays that met the following criteria:

1. Accelerometers measure bi-directional shaking (i.e. two horizontal components);
2. The array has recorded both small and moderate-to-large amplitude motions (PGA < 0.1 g and PGA > 0.10 g);
3. Recorded ground motions are regarded as free-field motions and are not affected by an adjacent structure;
4. The soil layers are not susceptible to liquefaction and liquefaction has not previously been observed at close proximity to the array;
5. The site geology is relatively simple and a soil column can reasonably represent the subsurface soil behavior (i.e. minor basin or topography effects);
6. Arrays with information on subsurface soil properties such as in-situ test data.

Selected Arrays

Ideally, the selected arrays should have met all the criteria as listed above; however, it is acknowledged that site-specific aspects of the local geology, topography, and level of site characterization will diverge from these criteria to some extent. In most cases, the constraints had to be relaxed for selecting sites. In this study, we eventually identified 5 downhole arrays including (1) Crockett - Carquinez Bridge Geotech Array #1 (CC #1), (2) Crockett – Carquinez Bridge Geotech Array #2 (CC #2), (3) Vallejo - Hwy 37/Napa River E Geo. Array (Vallejo), (4) Eureka Geotechnical Array (Eureka), (5) El Centro - Meloland Geotechnical Array (El Centro). Figure 1 presents the location of these arrays in California. At these sites, PS suspension logging was conducted by the California Department of Transportation (Caltrans) hence shear wave velocity (V_s) and compression wave velocity (V_p) were measured. The site characteristics of the selected arrays are summarized in Table 1. Detailed description of these arrays and the subsurface soil characteristics can be found in Li et al. (2017).

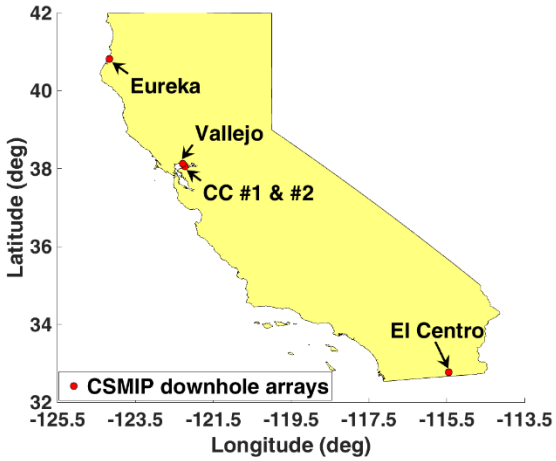

Figure 1. Location map of the selected CSMIP downhole arrays in this study

Table 1. Site characteristics of selected arrays (CESMD)

Station Name	Site Geology	Sensor Depths (m)	$V_{s,30}$ (m/sec)	Site Class (ASCE 7-10)	GWT Depth* (m)	Taxonomy (Site Quality for 1D SRA)
Crockett - Carquinez Br #1	Shallow clay over rock	0, 20.4, 45.7	345	D	4	HP (5)
Crockett - Carquinez Br #2	Shallow clay over soft rock	0, 61, 125	173	D	0.9	LP (2)
Eureka Geotechnical Array	Deep alluvium	0, 19, 33, 56, 136	194	D	1	LG (1)
El Centro - Meloland Geotechnical Array	Deep alluvium	0, 30, 100, 195	182	D	5	LP (3)
Vallejo - Hwy 37/Napa River E	Bay mud	0, 17.9, 44.5	509	C	3	HP (4)

Note: * GWT depth is estimated as the depth where V_p reaches 1500m/sec.

Taxonomy Evaluation of Selected Arrays

In this study, we utilized the site classification scheme (i.e. taxonomy) proposed by Thompson et al. (2012) to quantify the extent of site response complexity at the selected downhole arrays and assess the validity of the 1D site response assumptions. In the proposed taxonomy classification, the sites are classified into four distinct categories, i.e. LG, LP, HP and HG sites. The first letter of the taxonomy notation indicates the inter-event variability (σ) class of empirical transfer functions (ETFs) (H for "high" and L for "low") while the second letter indicates the goodness-of-fit (r) between ETFs and theoretical transfer functions (TTFs) (G for "good" and P for "poor"). The threshold values of σ and r are 0.35 and 0.6, respectively. In order to minimize the potential for nonlinear effects and increase the statistical significance, Thompson et al. (2012) recommended to use at least 10 records with PGA < 0.1g at ground surface for the taxonomy evaluation.

We carried out the taxonomy evaluation of the selected five downhole arrays and Figure 2 illustrates two extreme examples including Eureka as an LG site (i.e. the highest quality array) and the Crockett - Carquinez Br #1 as an HP site (i.e. the least quality array) for 1D SRA studies. The taxonomy designations for all other arrays are listed in Table 1 and the details of our taxonomy evaluation can be found in Li et al. (2017). In this paper, we further discuss the correlations between the taxonomy evaluation outcome and the calculated average residuals at these arrays.

1D Site Response Analysis

Methodology

In this study, Finite Element (FE) program LS-DYNA (LSTC, 2012) was utilized to develop and run 1D SRA models. We acknowledge the constraints of the 1D SRA modeling such as (1) soil layer boundaries are horizontal and extended infinitely in lateral directions, and

(2) modeled seismic waves are limited to the vertically propagated shear waves (i.e. SH waves). Soil column models of the selected arrays were developed in LS-DYNA using solid elements constrained to move in shear and Figure 3 presents two example soil columns. The soil columns were discretized in such a way that the maximum frequency each layer could propagate was as close to 37.5 Hz as possible. The bases of the soil columns were fixed to represent the "within" profiles (Stewart et al., 2008). In the current engineering practice, soil deposits are routinely modeled with lumped mass, springs and dampers for 1D SRA (e.g., DeepSoil, Hashash et al., 2016). Alternatively, SRA modeling with advanced FE programs such as LS-DYNA are capable to represent the effects of multi-directional shaking. In this study, the recorded acceleration data at the deepest downhole sensors of each array were input in both horizontal directions (bi-directional shaking) simultaneously to study the interaction between the horizontal components of the site response.

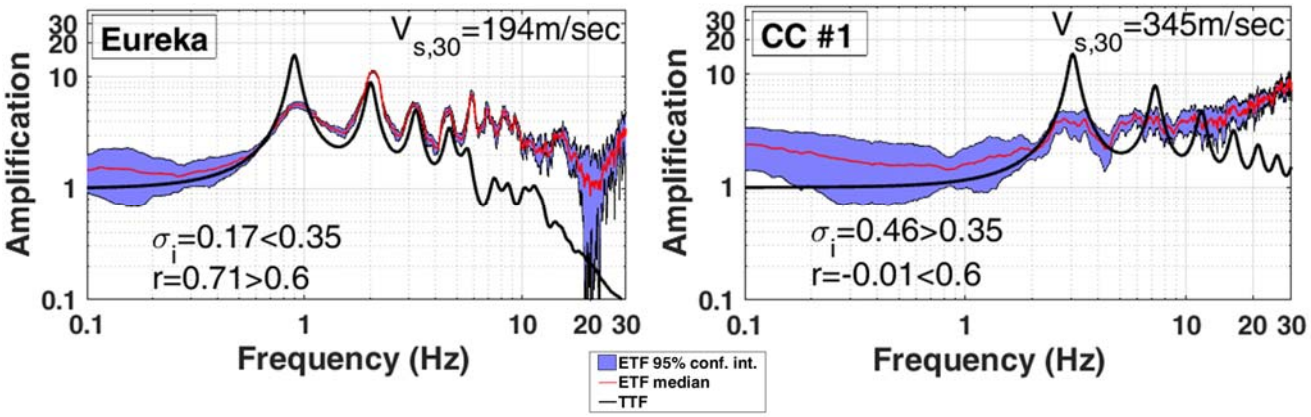

Figure 2. Taxonomy evaluation of Eureka and CC #1

The influence of dynamic stress-strain behavior on computed site response were investigated using two different soil nonlinear models, including general quadratic/hyperbolic backbone curve (Groholski et al., 2016, denoted as GQH hereafter) , modified two-staged hyperbolic backbone curve (Motamed et al., 2016, denoted as MTH hereafter). For all the nonlinear soil models, small strain damping (D_{min}) was applied using the DAMPING_FREQUENCY_RANGE_DEFORM feature in LS-DYNA which provides approximately frequency-independent damping over a range of frequencies to element deformation. D_{min} was set as 2% and 5% for strong and weak shakings in the frequency range of 1~30 Hz, respectively.

Regarding the nonlinear soil models (i.e. GQH and MTH), the MAT_HYSTERETIC_SOIL model was employed to simulate the dynamic response of the soil deposit, which includes an option to adjust soil stiffness based on the level of strain rate. Dynamic soil behavior was characterized by modified two-stage hyperbolic backbone curve for MTH model and general bivariate quadratic equation for GQH model. These two models were developed to properly account for the maximum shear stress in the constitutive model at large strain. Hysteretic damping of soil materials is governed by the loading-unloading relationship as described by Masing rule (Masing, 1926). Rate-dependent effects of clayey soils were accounted for by applying a 5% increase in stiffness per log cycle of plastic strain rate.

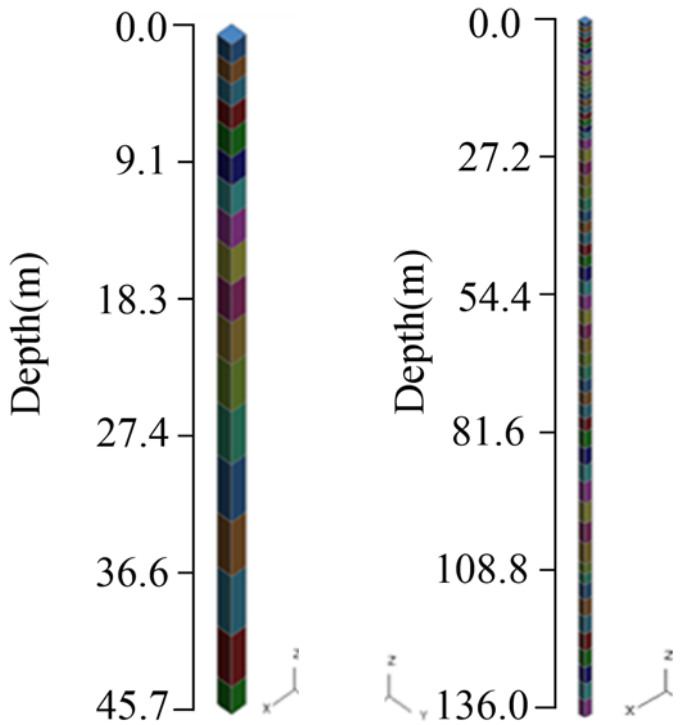

(a) (b)

Figure 3. LS-DYNA soil column models for (a) CC #1 and (b) Eureka

Selection of Ground Motions

For each selected CSMIP downhole array, six individual analyses were performed using input motions that included one moderately strong time history (PGAsurface ≥ 0.1 g) and five low-amplitude motions (PGAsurface < 0.1 g). The processed ground motion time series were downloaded through the CESMD website. In total, 30 ground motions ranging in amplitude from PGA at the surface of 0.004g to 0.98g were utilized in this study. Figure 4 presents the distribution of recorded PGA at ground surface and the site classification of the studied arrays.

Analysis Results and Discussions

The performance of the 1D SRA models varied by site, which is attributed to the combined influence of stratigraphy and dynamic soil properties, and to aspects of the geological conditions at the sites that may not lend themselves to the 1D approximation of wave propagation. This section discusses the 1D SRA results of the two downhole arrays, Eureka and CC #1, which represent the highest and lowest quality predictions, respectively. Due to the page limitation, only the strong shaking analysis is presented for each array. For more details of our analysis results and discussions, please refer to Li et al. (2017)

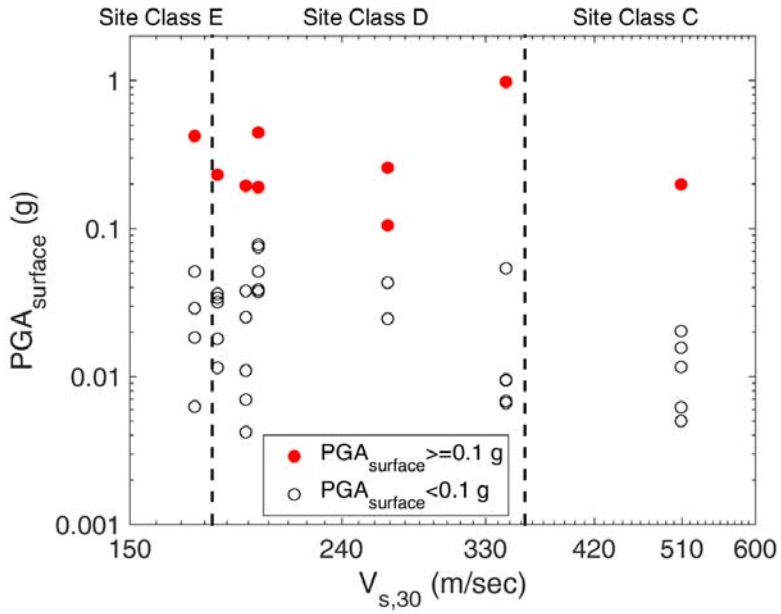

Figure 4. Distributions of PGA at the ground surface versus $V_{S,30}$ for the ground motion records used in this study and the site classes.

Eureka

The 1D SRA analysis results of Eureka subjected to the Ferndale Earthquake (Mw 6.5, 01/09/2010) are presented in Figures 5 and 6. As can be seen in Figure 5, GQH and MTH models fairly well reproduced the soil response for all components at various depths with regard to the 5% damped spectral acceleration (Sa). However, they slightly underestimated the peaks of Sa at surface and 19 m depth for both EW and NS components. Conversely, general overestimation was noticed at all depths (EW and NS components) for the linear elastic model. In addition, Figure 6(a) illustrates that the two nonlinear models underestimated the PGA at all depths while the linear model overestimated PGA at all depths. Figure 6(b) shows that the shear strain level in the soil profile reached as high as about 0.3%, indicating that the soil likely exhibited some nonlinear behavior in response to this strong shaking.

CC #1

The 1D SRA analysis results of CC #1 subjected to the main shock (M_w 6.0, 08/24/2014) of the South Napa Earthquake are plotted in Figures 7 and 8. It is shown in Figures 7 and 8(a) that the 5% damped spectral acceleration (S_a) and PGA predictions of GQH and MTH models reach fairly good agreement with the observations at mid-depth of 20.4 m. However, these two nonlinear models underpredicted 5% damped spectral acceleration (S_a) at period less than 0.4 sec and PGA at surface. In contrast, the linear elastic model overpredicted the soil response at 20.4 m depth while it surprisingly performed much better in capturing the large amplification at surface, especially in the EW direction. The nonlinear soil behavior was not dominant in the soil profile as shown in Figure 8(b) with peak shear strain smaller than 0.1%.

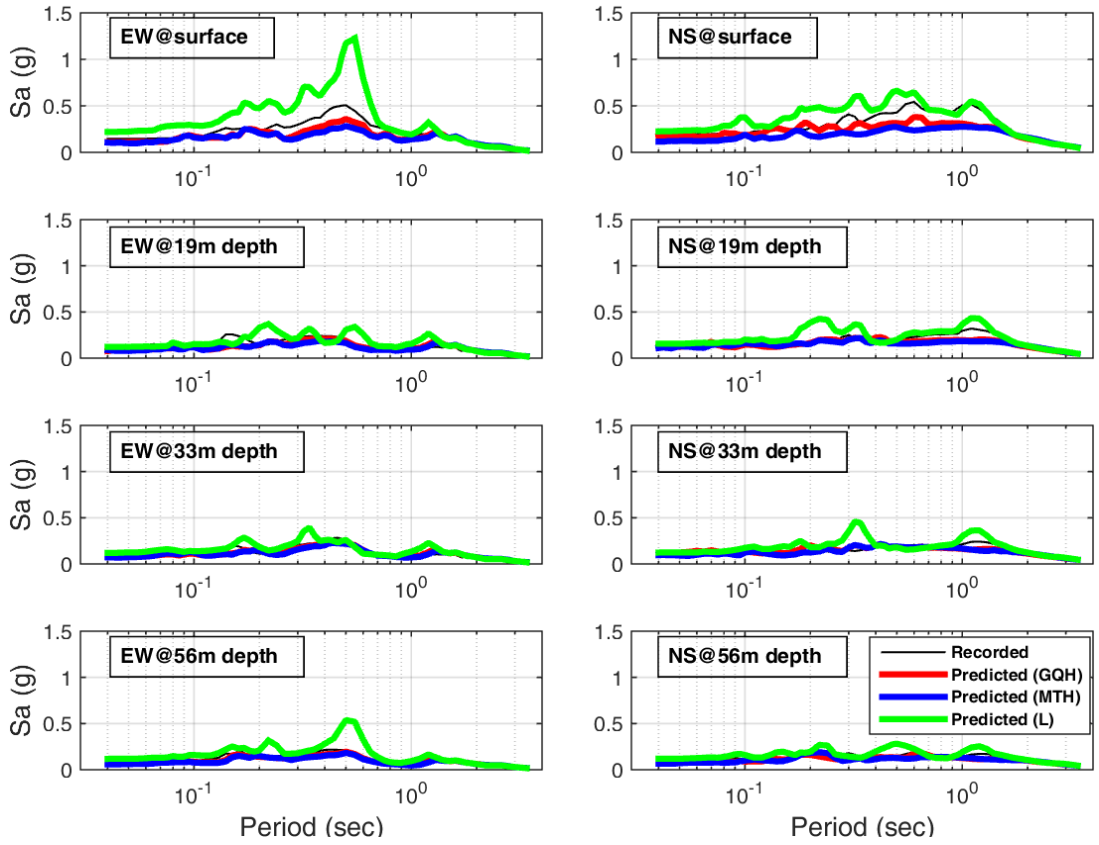

Figure 5. Comparison of measured and predicted 5% damped spectral accelerations at the Eureka array under the shaking of Ferndale Earthquake at different depths.

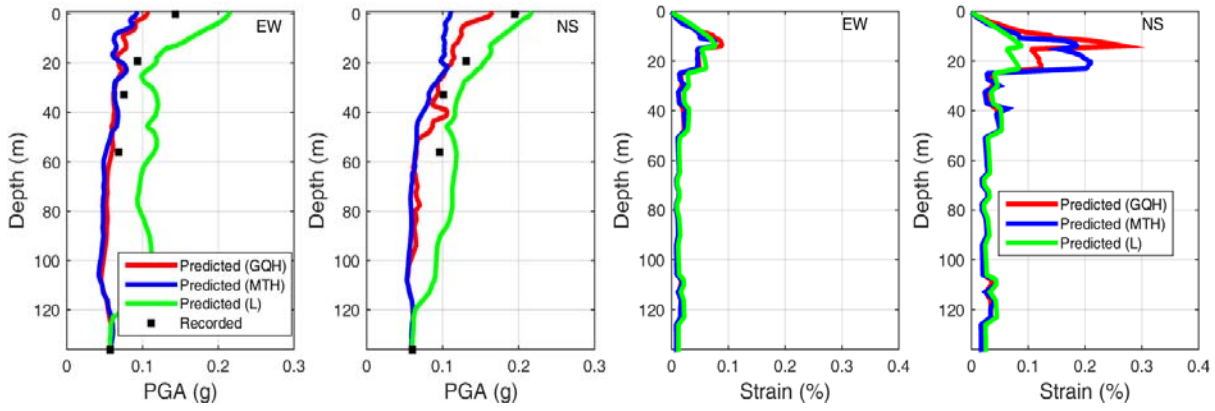

(a) (b)

Figure 6. (a) PGA and (b) max shear strain profiles of Eureka under the shaking of the Ferndale Earthquake.

Quantitative Assessment of 1D SRA Results

In this study, we quantified the accuracy of the different 1D SRA models using two different approaches namely the Goodness-of-Fit methodology proposed by Anderson (2004) and the amplification factor residuals described by Zalachoris and Rathje (2015). These two measures are described briefly hereafter and the results are presented.

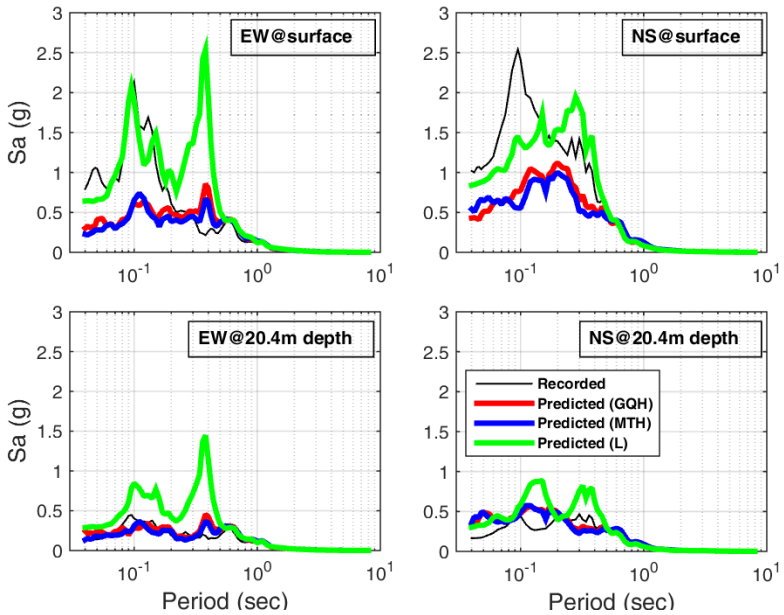

Figure 7. Comparison of measured and predicted 5% damped spectral acceleration of CC #1 under the shaking of South Napa Earthquake mainshock at different depths.

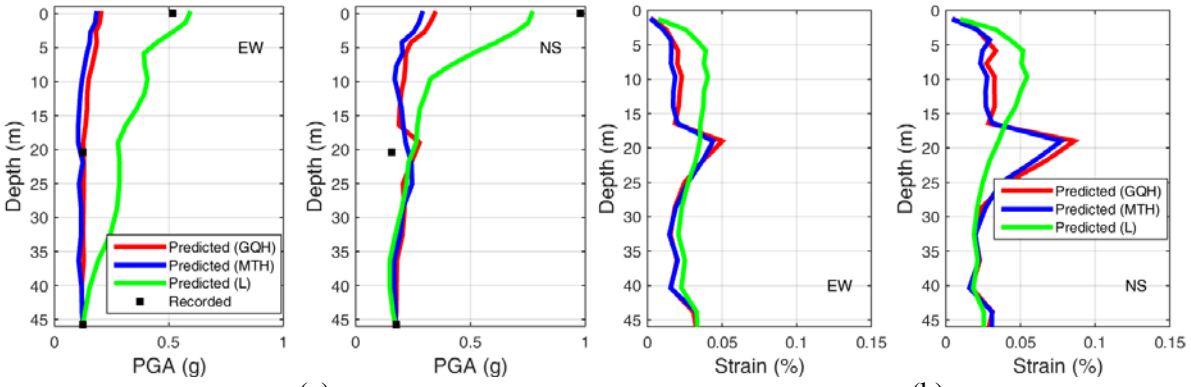

(a) (b)

Figure 8. (a) PGA and (b) max shear strain profiles of CC #1 under the shaking of South Napa Earthquake mainshock.

Goodness-of-fit

Anderson (2004) proposed the Goodness-of-Fit (denoted as GOF hereafter) scoring system to characterize how well synthetic seismographs match the statistical characteristics of observed records using ten different parameters including the peak acceleration, Arias intensity,

Fourier spectrum, acceleration response spectrum, etc. A GOF score below 4 is a poor fit, a score of 4-6 is a fair fit, a score of 6-8 is a good fit, and a score over 8 is an excellent fit. In this study, the GOF for an individual site subjected to a specific shaking is calculated by averaging the GOF at different depths and shaking directions.

We utilized the GOF matrix to evaluate the overall accuracy of the nonlinear (i.e. GQH, MTH) and linear (i.e. L) models across all sites and the results are summarized in Figure 9 which are the mean GOF of the site response models, computed by averaging the GOF across all sites and ground motions. The GOF were also computed using subsets of the pooled GOF corresponding to records with binned γ_{max} (0.01% =<γ_{max} < 0.02%, 0.02% <= γ_{max} < 0.05%, 0.05% ≤ γ_{max}< 0.1% and γ_{max} ≥ 0.1%) and measured $PGA_{surface}$ ($PGA_{surface}$ < 0.05 g, 0.05 g ≤ $PGA_{surface}$ < 0.1 g, 0.1 g ≤ $PGA_{surface}$ < 0.15 g and $PGA_{surface}$ ≥ 0.15 g). As illustrated in Figure 9, the overall quality of the nonlinear SRA models was higher than the linear models (i.e. higher GOF score) and this improvement was more substantial in stronger shakings. We further investigated the correlations between the GOF score and the taxonomy classification which is elaborated hereafter.

Figure 10 presents a summary plot to correlate taxonomy designations with GOF of the nonlinear models for all sites. Each plot was divided by dashed red lines into four subareas representing the taxonomy classification the sites fell under. Besides, the size of the circles in Figure 10 is linearly proportional to the magnitude of the GOF score. The texts adjacent to the circles indicate the actual values of GOF score.

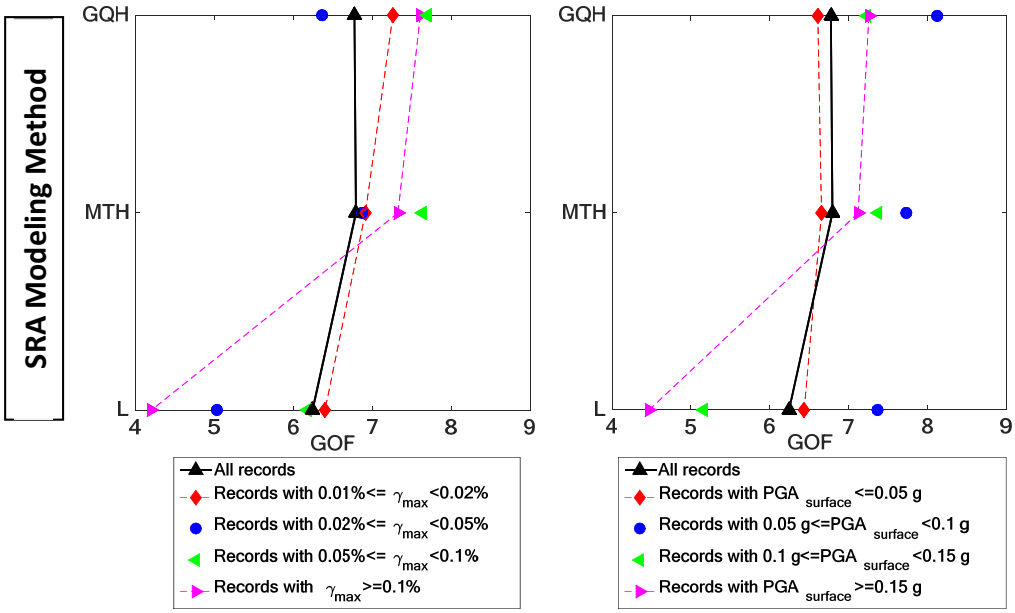

Figure 9. GOF of the 1D SRA models binned for different levels of γ_{max} and PGA at surface.

It is shown that the GOFs of all sites are in between 6 and 8, which implies that a "good fit" was achieved by either GQH or MTH model for the arrays, and illustrates the GOFs of GQH and MTH models for the same site are in good agreement.

In general, as shown on Figure 10, the GOF score becomes larger with low σ or high r for both models. For example, Eureka is classified as a LG site according to the taxonomy scheme with the lowest σ and the highest r among all arrays and thus it yields the highest GOF for both models. Contrarily, CC #1 is designated as a HP site and achieves the lowest GOF with the combined effects of the highest σ and the second lowest r among all sites. This observation indicates that taxonomy designation is in general agreement with the calculated GOF scores for the studied arrays.

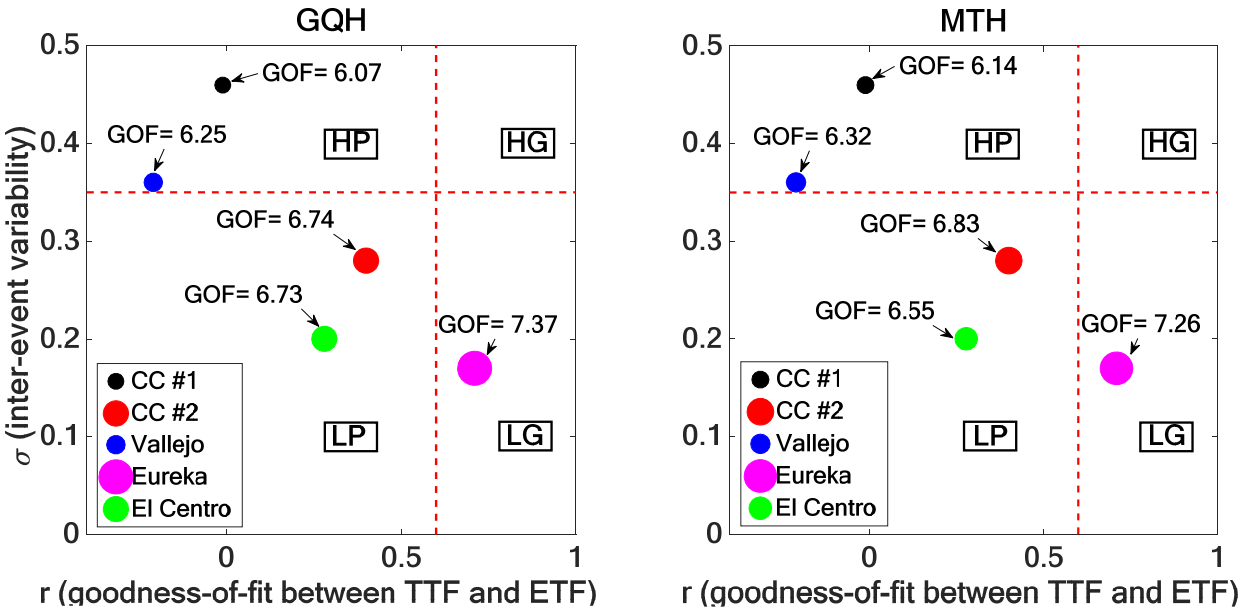

Figure 10. Correlation of taxonomy classification with mean GOF of GQH and MTH models for the CSMIP downhole arrays.

Residual of Amplification Factor

In this study, similar to Zalachoris and Rathje (2015), we quantify the misfit (or bias) as the difference between the natural log of the measured and computed amplification factors (AF) at each period. For the *i*th site and *j*th recording, the residual (R) at period T between the observed amplification factor (AF^{obs}) and the calculated amplification factor (AF^{calc}) is given by Equation 1.

$$R_{i,j}(T) = \ln AF_{i,j}^{obs}(T) - \ln AF_{i,j}^{calc}(T) \quad (1)$$

A positive residual indicates underprediction by the model while a negative residual implies overprediction. A consistent period range (0.04 – 3.0 sec), which was the commonly shared period range of response spectra of all sites and events provided by CSMIP, was utilized to compute the AF residual hereafter.

The analysis results were initially grouped based on their corresponding level of shaking, as depicted by the measured peak acceleration of the surface motions ($PGA_{surface}$). Since the recorded peak ground acceleration at the surface ranges from low (0.004 g) to high (0.98 g), the effect of shaking intensity on the accuracy of the predictions was investigated. Four different

ranges of $PGA_{surface}$ were considered: $PGA_{surface} \leq 0.05$ g, 0.05 g < $PGA_{surface} \leq 0.1$ g, 0.1 g < $PGA_{surface} \leq 0.15$ g and $PGA_{surface} > 0.15$ g.

As seen in Figure 11, the performance of the GQH, MTH and L models strongly depended on the level of shaking, and thus implicitly on the magnitude of the induced shear strains. At low intensity levels, namely for $PGA_{surface}$ less than 0.05 g, there is strong agreement between the observations and the prediction results at all frequencies. A slight underprediction occurs at periods less than 0.2 sec and a slight overprediction at periods greater than 0.2 sec, but still the agreement is fairly good. As the shaking intensity increases, the calculated amplification factor residuals of the site response models deviate from each other, as well as from the observations. In general, the GQH and MTH models moderately underpredicted the amplification at shorter periods while L model strongly overpredicted the amplification over a wide range of periods at high intensity shakings.

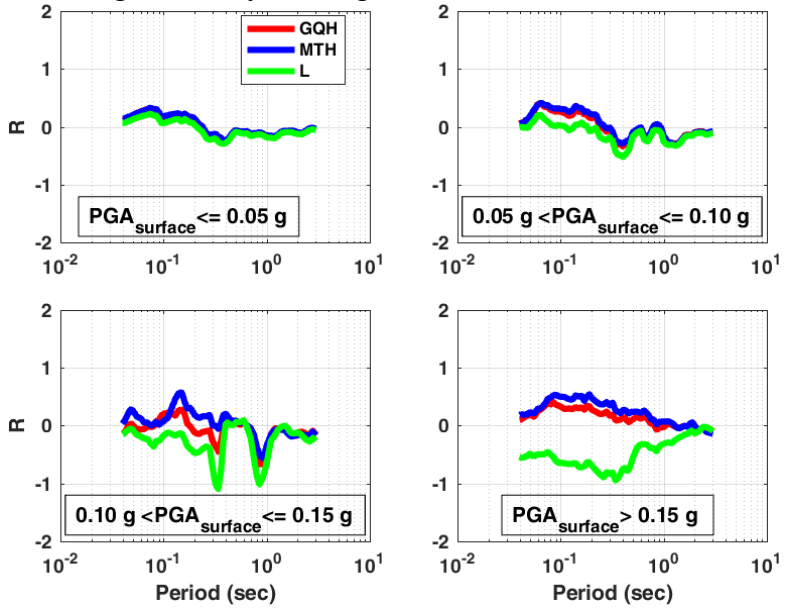

Figure 11. Computed mean residual of amplification factor for all sites at different ranges of measured PGAsurface.

Conclusions

This paper evaluated the taxonomy classification of the five selected CSMIP downhole arrays, hence their quality for 1D SRA studies is ranked. The 1D SRA modeling was performed in LS-DYNA for these arrays to study the effects of subsoil conditions on the amplification of ground motions. Both strong and weak shakings were analyzed for each array and the analysis results were presented.

Overall, nonlinear finite element models for all arrays were capable of reproducing the ground motions fairly well over low frequency range (< 1 Hz) but failed to capture (in most cases underestimated) the components of the motions at intermediate and high frequencies (> 1 Hz). Besides, linear elastic models of arrays in general overestimated the soil response (especially for strong shaking case) and tended to yield intermediate period spectral acceleration peaks caused by resonance of soil profiles. In addition, the nonlinear SRA models typically

resulted in better quality predictions compared to the linear models and this improvement was more significant under strong shakings (PGA > 0.1g).

The outcome of the taxonomy evaluation informed us of the expected level of accuracy at the five studied arrays and our observations were in good agreement with the taxonomy site classification. Among the five arrays studied in detail, Eureka was identified as an LG site (i.e. highest 1D SRA quality rank suggested by the taxonomy scheme) which was consistent with the calculated average GOF and amplification residual at this site. On the other hand, CC#1 was identified as an HP site (i.e. lowest 1D SRA quality rank suggested by the taxonomy scheme) which was again in good agreement with the calculated average GOF and amplification residuals at this site.

We employed two methods to quantify the extent of accuracy of the 1D SRA models using (1) GOF scoring system, and (2) amplification factor residuals and both techniques were found to be useful in comparing the results. The strengths and limitations inherent in the practical application of 1D SRA model demonstrated the following: (i) 1D SRA is applicable for sites where the 1D SRA assumptions are valid, (ii) 1D SRA fails to account for 2D and 3D effects including spatial heterogeneity, nonvertical incidence, basin effects and topographic effects. Considering the presence of complex geologic and topographic conditions at some sites was found to be significant, 1D SRA was not quite effective or accurate in estimating site amplifications. As a means to understand the complexity of site response and the validity of 1D SRA assumptions, it is recommended to evaluate taxonomy class of a specific site prior to performing 1D SRA in engineering practice, if weak ground shakings were recorded at that site.

Acknowledgements

This project was funded by California Strong Motion Instrumentation Program, California Geological Survey. This support is gratefully acknowledged. We also thank Hamid Haddadi and Moh Huang for providing the needed information to undertake this research. We greatly appreciate Abbas Abghari and Caltrans for providing PS suspension logging data of CC #1 and Vallejo as well as geotechnical reports of all three downhole arrays studied in this paper. Discussions with Shahriar Vahdani and Roy Imbsen on subsurface soil conditions at CC #1 and CC #2 were extremely useful which are acknowledged.

References

Anderson, J. G. (2004). Quantitative measure of the goodness-of-fit of synthetic seismograms. *13th World Conference on Earthquake Engineering Conference Proceedings*, Vancouver, Canada, Paper No. 243).

California Engineering Strong Motion Database (CESMD). *www.strongmotioncenter.org*.

Groholski, D. R., Hashash, Y. M., Kim, B., Musgrove, M., Harmon, J., and Stewart, J. P. (2016). Simplified Model for Small-Strain Nonlinearity and Strength in 1D Seismic Site Response Analysis. *Journal of Geotechnical and Geoenvironmental Engineering, 04016042.*

Hashash, Y.M., Groholski, D.R., Phillips, C.A., Park D., and Musgrove M. *DEEPSOIL 6.1*, User Manual and Tutorial. Univ. of Illinois at Urbana-Champaign: Champaign, Illinois, 2016.

Li, G., Motamed, R., and Dickenson, S. (2017). Evaluation of One-Dimensional Multi-Directional Site Response Analyses Using Geotechnical Downhole Array Data. *Earthquake Spectra*. (in press) https://doi.org/10.1193/010617EQS005M

LSTC, 2012. LS DYNA Keyword User's Manual Volumes I & II – Release 971 R.6.1.0. Livermore Software Technology Corporation, Livermore, California.

Masing, G. Eigenspannungen und verfestigung beim messing. *In Proceedings of the 2nd international congress of applied mechanics (Vol. 100, pp. 332-5). sn.*

Motamed, R., Stanton, K., Almufti, I., Ellison, K., & Willford, M. (2016). Improved Approach for Modeling Nonlinear Site Response of Highly Strained Soils: Case Study of the Service Hall Array in Japan. *Earthquake Spectra*, 32(2), 1055-1074.

Stewart, J. P., Kwok, A. O., Hashash, Y. M. A., Matasovic, N., Pyke, R., Wang, Z., & Yang, Z. (2008). Benchmarking of nonlinear seismic ground response analysis procedures. *Rpt. No. PEER-2008, 4.*

Thompson, E. M., Baise, L. G., Tanaka, Y., & Kayen, R. E. (2012). A taxonomy of site response complexity. *Soil Dynamics and Earthquake Engineering, 41*, 32-43.

Zalachoris, G., & Rathje, E. M. (2015). Evaluation of one-dimensional site response techniques using borehole arrays. *Journal of Geotechnical and Geoenvironmental Engineering*, 141(12), 04015053.

CRITICAL ASSESSMENT OF CODE TORSIONAL PROVISONS USING CSMIP DATABASE OF INSTRUMENTED BUILDINGS

Yijun Xiang, Farzad Naeim and Farzin Zareian

Department of Civil & Environmental Engineering
University of California, Irvine

Abstract

This research aims at assessing the validity of accidental torsion provisions in building codes. Uncertainty in stiffness is considered as the main source of possible eccentricity. Monte Carlo simulation is utilized to statistically assess the behavior of nine one-story symmetric-in-plan base systems with nine different translational to rotational period ratios (Ω). Three vibrational characteristics and equivalent design eccentricity are developed and compared with information obtained from CSMIP database. The effect of Ω, plan aspect ratio, and correlation in building stiffness on building displacement amplification due to torsion are investigated. Equivalent design eccentricity is quantified based on these results.

Introduction

Seismic code provisions require that the effect of building torsion during seismic excitation be considered at each floor level. This effect for symmetric-in-plan buildings is captured by exerting the seismic equivalent lateral force of each floor at a distance–equal to 5% of the building's plan dimension perpendicular to the direction of the applied equivalent lateral force–from the center of mass (CM) of the floor diaphragm. Denoted as "accidental torsion," the later represents the effect of discrepancies between the mass and stiffness distribution along the height of the real building, and the effect of rotational component of ground shaking on the structure. In essence, accidental torsion is rooted in the inherent uncertainty of engineering models. Traditionally, analytical methods for seismic response assessment of buildings are incapable of addressing such modeling uncertainty, unless accidental torsion is explicitly built into the analytical model through the so-called 5% rule.

Building code provisions on inclusion of accidental torsion in seismic response assessment of buildings is not limited to symmetric-in-plan structures. Accidental torsion is added to the inherent torsional effects in asymmetric-in-plan buildings, and is explicitly considered in traditional analytical seismic response assessment methods. In contrast, however, the effect of modeling uncertainty that leads to consideration of accidental torsion is dwarfed by the inherent torsional effects in buildings with asymmetric-in-plan. Therefore, its critical to maintain focus on assessing the torsional response of symmetric-in-plan buildings.

This research is built on the results of previous work at CSMIP (De la Llera and Chopra, 1992), and others (e.g. De la Llera and Chopra, 1994, and 1995; Lin et al., 2001; Hernandez and Lopez, 2004; De-la-Colina and Almeida, 2004; Basu et al., 2014) that lend itself to evaluation of code-accidental torsion provisions and its dependence on structural system properties.

Specifically, in an effort similar to what is proposed here, De la Llera and Chopra (1992) concluded–based on motions recorded in three buildings instrumented by CSMIP–that code specified accidental torsion is adequate in representing the torsion in recorded motions. They speculated that it is not necessary to consider accidental torsion in the design of many buildings. We critically evaluate these claims using CSMIP data, and develop expressions for accidental torsion of buildings. The ultimate aim of this study is to develop a set of rational, meaningful, and practical ways to include accidental torsion in seismic response assessment, and improve both the seismic design provisions of building codes (e.g., ASCE, 2010, and 2007) and the practice of performance-based design and retrofit of structures.

Methodology

For a building subject to translational ground motions, the equation of motion can be written as Eq.1-1:

$$\begin{bmatrix} m & 0 & 0 \\ 0 & m & 0 \\ 0 & 0 & I_o \end{bmatrix} \begin{Bmatrix} \ddot{u}_x \\ \ddot{u}_y \\ \ddot{u}_\theta \end{Bmatrix} + \begin{bmatrix} k_{xx} & 0 & k_{x\theta} \\ 0 & k_{yy} & k_{y\theta} \\ k_{\theta x} & k_{\theta y} & k_{\theta\theta} \end{bmatrix} \begin{Bmatrix} u_x \\ u_y \\ u_\theta \end{Bmatrix} = - \begin{Bmatrix} m\ddot{u}_{gx}(t) \\ m\ddot{u}_{gy}(t) \\ 0 \end{Bmatrix} \quad \text{(Eq.1-1)}$$

where $I_o = mr^2$ is the rotational inertia. Theoretically, a building with symmetric plan has zero off-diagonal elements in the stiffness matrix, and the dynamic responses of two translational directions of the system are uncoupled. However, when asymmetric stiffness distribution takes place in a system with nominally symmetric plan, translational ground motion triggers torsional vibration and the deformation along the translational axis is amplified due to torsional effects.

One of the most important parameters that affects torsional behavior of a building is Ω, the ratio of dominant translational period to dominant rotational period. Large Ω values are associated with perimeter frame buildings with large torsional stiffness (Eq.1-2), while small Ω values represent buildings such as core wall systems with low torsional stiffness. Ω values ranging from 0.6 to 1.4 are investigated in this study, which covers most of the building cases.

$$\Omega = \frac{T_{tran}}{T_{rot}} = \frac{\sqrt{m/K_{tran}}}{\sqrt{mr^2/K_{rot}}} \quad \text{(Eq.1-2)}$$

Nine one-story four-VLLR (i.e. vertical lateral load resisting elements) base systems with symmetric plans are developed whose translational period T_{tran} = 1.5sec and Ω = 0.6, 0.7, 0.8, 0.9, 1.0, 1.1, 1.2, 1.3, 1.4, respectively. The deformation of the roof of the base systems subject to one directional earthquake ground motion along the direction of T_{tran}, denoted as δ_b, is merely the translational displacement along that direction due to the symmetric plan of the buildings.

To consider the effect of uncertainty in stiffness of VLLRs, literature review has been conducted to access the variability of element cross section dimensions, second moment of inertia and material strength. Ramsay *et al.* (1979) used Monte Carlo simulation to conclude that deformation of reinforced concrete beams has a coefficient of variation of 0.14, and De la Llera and Chopra (1994) suggested the same value be used as the variation of stiffness of reinforced concrete elements. This approach is under the assumption that force distribution is deterministic (a conservative estimate). Ellingwood and Galambos (1980) investigated probability based load

criterion and Melchers (1987) evaluated reliability of structures, showing that the coefficient of variation of Young's modulus and cross section moment of inertia is approximately 0.06 and 0.05, respectively. Bournonville *et al.* (2004) performed statistical analysis to mechanical properties of reinforcing bars and found that coefficient of variation of reinforcement yield strength ranges from 0.03 to 0.09. ASTM A6 (2005) provides variability of structural element dimensions, and ASTM A992 (2004) provides steel and concrete material strength; according to the ASTM resources, section depth or width has a coefficient of variation ranging from 0.01 to 0.04, and column steel yield stress (Grade 50) has a coefficient of variation of 0.05.

If each dimension is assumed to have a coefficient of variation equal to 0.03, then moment of inertia has a coefficient of variation of 0.06 to 0.09 assuming no correlation and complete correlation between each dimension, respectively. Given the coefficient of variation of Young's modulus is approximately 0.06, coefficient of variation of the stiffness of all structural elements are conservatively equal to 0.14.

A hundred sample Monte Carlo simulations is run for each base system, treating four VLLRs as four normally distributed random variables, with mean values equal to the stiffness of the base system and the coefficient of variation equal to 0.14. Given that the probability of the stiffness of one of the four VLLRs being close to the stiffness of another is high if they are manufactured in batch and produced identically, a correlation coefficient of $\rho = 0.5$ between the stiffness of four VLLRs is assumed. For comparison purposes, $\rho = 0$, which conservatively assumes uncorrelated VLLR stiffness are also used in this study. Forty ground motion are scaled to a low intensity level of S_a=0.06g at a period of 1.5sec to examine linear torsional behavior of the buildings. Therefore, 4000 asymmetric building plan analyses are performed per base system and 36000 analyses are completed in total. These 36000 analyses are repeated for base systems with plan aspect ratios of 1:1, 1:2, 1:4 and 1:8 to account for the effect of building plan dimension, where aspect ratio is defined as the length along the applied ground motion direction to the length perpendicular to the ground motion direction.

Effect of torsional vibration is measured and estimated via the largest amplification in displacement among four corners of the building at the roof level. With asymmetric stiffness distributions, buildings rotate even though the ground motion is applied to the center of mass. Total response is the summation of translational response and rotational response. Three torsional vibration characteristics are developed in Eq.1-3:

$$\alpha_1^i = \frac{max(\delta_{tran}^i + \delta_{rot}^i)}{max(\delta_b)} \quad \text{(Eq.1-3,a)}$$

$$\alpha_2^i = \frac{max(\delta_{tran}^i + \delta_{rot}^i)}{max(\delta_{tran}^i)} \quad \text{(Eq.1-3,b)}$$

$$\alpha_3^i = \frac{max(\delta_{tran}^i)}{max(\delta_b)} \quad \text{(Eq.1-3,c)}$$

$$\alpha_1^i = \alpha_2^i \alpha_3^i \quad \text{(Eq.1-3,d)}$$

α_1^i is the ratio of the peak total response of the i^{th} asymmetric system to the peak translational response of the base system without eccentricity. α_2^i is the ratio of the peak total

response of the i^{th} asymmetric system to the peak translational response of the same i^{th} system. α_3^i is the ratio of the peak translational response of the i^{th} asymmetric system to the peak translational response of the base system. To summarize, α_1^i estimates the total displacement amplification due to stiffness eccentricity compared to a non-eccentric base system; it is the multiplication of α_2^i and α_3^i, where the former estimates the displacement amplification within a certain asymmetric system, and the latter estimates the contribution of pure translational displacement in that asymmetric system.

Torsional vibration characteristics represent the amplification in displacement due to stiffness uncertainty in asymmetric buildings, and those characteristics need to be transferred to a measure of distance representing how far away the equivalent lateral force should be applied to the center of mass to capture the same amount of torsional displacement amplification.

To analyze the displacement amplification caused by eccentric static loading, an eccentric equivalent lateral force is applied to the base system. In comparison, a non-eccentric equivalent lateral force is also applied to the base system right at the center of mass. The ratio between two displacements in these two scenarios demonstrates the amplification due to eccentric push over, as shown in Eq.1-4 and Eq.1-5, where *b* is the dimension of the plan perpendicular to the applied static force, and *e* is the eccentricity in percentage, *eb/2* is the distance from the applied force to the center of mass.

$$\alpha_p = \frac{\delta_p^e}{\delta_p^{ne}} = \frac{{}^{V}/_{K_{trans}} + {}^{Ve}/_{K_{rot}} b/2}{{}^{V}/_{K_{trans}}} \quad \text{(Eq.1-4)}$$

$$V = S_a W/g \quad \text{(Eq.1-5)}$$

An example of displacement amplification from eccentric push over analysis is shown in Figure 1-1: two buildings with plan aspect ratios of 1:1 and 1:8 are subject to eccentric lateral force, nine grey lines represent the linear relationship between displacement amplification and the eccentricity of the applied lateral force. Higher displacement amplification is seen in the building with higher plan aspect ratio, when Ω and lateral force eccentricity are both fixed.

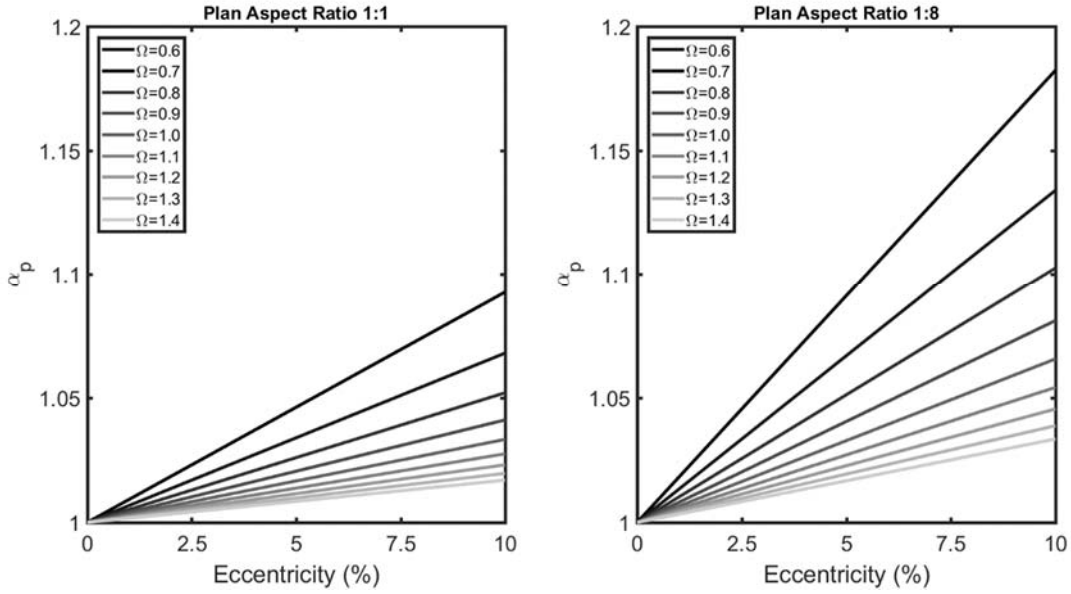

Figure 1-1. Amplification due to eccentric push over for nine base systems

α_1 , which is the ratio of the asymmetric system peak total response to the symmetric system peak translational response, is mapped to the eccentricity in percentage by equating average of α_1 and α_p. In other words, the equivalent eccentricity determines how far away should the equivalent static lateral force be applied from the center of mass to make the symmetric system have as much displacement amplification as an asymmetric system with uncertain VLLRs stiffness and subject to ground motions. Since each Monte Carlo simulation results in one α_1 value, there are 36000 realizations of α_1 for a given plan aspect ratio system. Statistical properties of α_1 database such as median and 75th percentile are mapped to the corresponding equivalent eccentricity, representing different levels of torsion design requirements.

Results

Results of equivalent eccentricities from Monte Carlo simulation are shown in Figure 2-1; observations and conclusions are as follows:

- 5% eccentricity from code provision is larger than the median response from the simulations, as the computed equivalent eccentricity of all systems with translational to rotational period ratio ranging from 0.6 to 1.4 and plan aspect ratio ranging from 1:1 to 1:8 fall below 5%.
- Higher levels of eccentricity (compared to 5%) is required to be applied to a system if confidence levels larger than 50% is of interest.
- Compared to buildings that have large rotational stiffness (Ω larger than 1), buildings that are sensitive to torsion (Ω less than 1) require less equivalent eccentricity at higher confidence level.
- Equivalent eccentricity (displacement amplification) is Ω sensitive. When translational period and rotational period are identical, it reaches its minimum value (almost equal to zero). Equivalent eccentricity displays an M shape over the Ω = 0.6 to 1.4 range.

- Buildings with larger plan aspect ratio do not necessarily have higher equivalent eccentricity, though they have relatively higher displacement amplification α_1 .

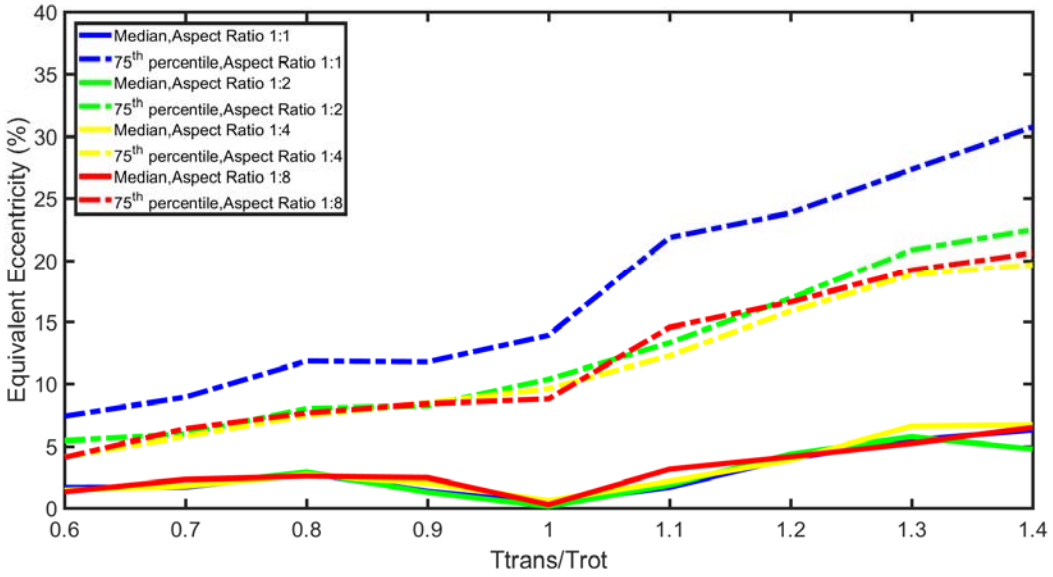

Figure 2-1. Equivalent eccentricity for buildings with Ω ranging from 0.6 to 1.4 and plan aspect ratio ranging from 1:1 to 1:8, using uncorrelated VLLRs stiffness model (ρ = 0)

The effect of VLLRs stiffness correlation on equivalent eccentricity is also studied; sample results are demonstrated in Figure 2-2 for a building with plan aspect ratio of 1:2 and ρ = 0.0 and 0.5. Using the median value of the simulations as the target displacement amplification to compute the equivalent eccentricity, systems with correlated VRRLs stiffness have smaller equivalent eccentricity and correspondingly smaller displacement amplification. This can be explained by the observation that when stiffness of the four VLLRs increase or decrease coherently (i.e. correlation), the level of asymmetricity is reduced and leads to a reduction in displacement amplification. Asymmetricity can be estimated by the off-diagonal element (Eq.2-1) in equation of motion, where *D* is the perpendicular distance between center of mass and VLLRs, k_1 and k_2 are stiffness of VRRLs along X axis.

$$k_{x\theta} = \sum k_i x_i = (k_1 - k_2)D \qquad \text{(Eq.2-1)}$$

Variation in difference between the stiffness of VLLRs decreases when introducing correlation to VLLRs stiffness as shown in Eq. 2-2.

$$\sigma^2_{k_1-k_2} = \sum_{i=1}^{2}\sum_{j=1}^{2}\rho_{ij}\sigma_{k_i}\sigma_{k_j} = \sigma^2_{k_1} + \sigma^2_{k_2} - 2\rho\sigma_{k_1}\sigma_{k_2} \qquad \text{(Eq.2-2)}$$

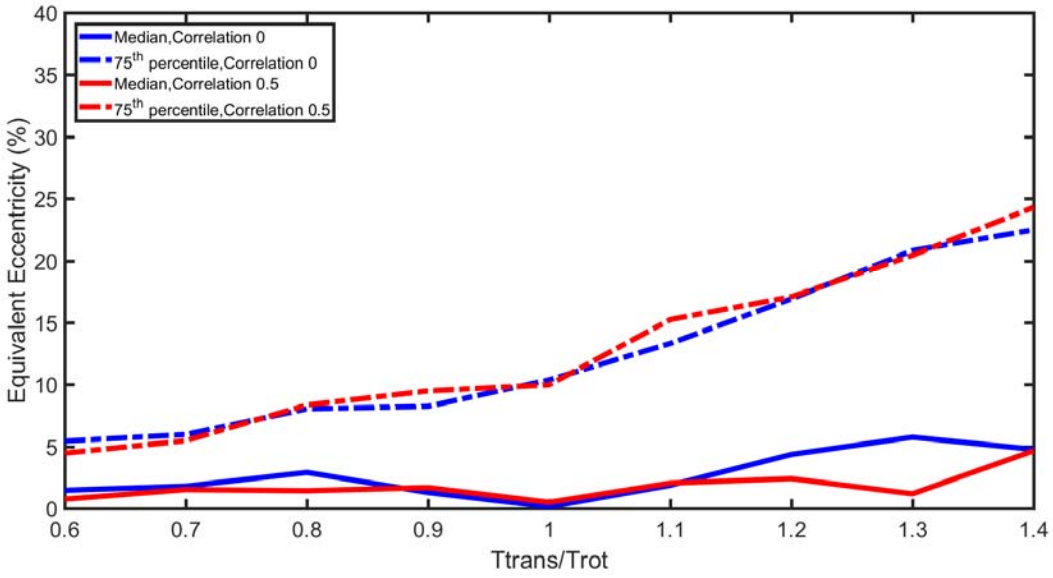

Figure 2-2. Equivalent eccentricity for buildings with Ω ranging from 0.6 to 1.4 and two stiffness correlation ($\rho = 0, \rho = 0.5$), using a plan aspect ratio 1:2 model

The difference between equivalent eccentricity of systems with and without VLLR stiffness correlation diminishes at large quantiles (see Figure 2-2 for the 75% quantile). This numerical issue may happen due to the small amount of total simulation numbers to capture equivalent eccentricity at the tail of its distribution. Nevertheless, equivalent eccentricity associated with uncorrelated stiffness cases are preferred since it provides a more conservative estimate of accidental torsion.

The distribution of three torsional vibration characteristics (α_1 , α_2 and α_3) are plotted in forms of box plots and compared among four systems with different plan aspect ratios. Each box plot shows five quantiles of the data set: top and bottom sides of the blue box show 75 and 25 percentiles; the red bar in the middle of the blue box shows the median; and top and bottom whiskers show an extension equal to 1.5 times the difference between the values associate with 75 and 25 percentiles to the 75 and 25 percentile values respectively. Figure 2-3, Figure 2-4 and Figure 2-5 show the boxplots for α_1 , α_2 and α_3 , respectively. The following observations are drawn from Figures 2-3, 2-4, and 2-5:

- The total amplification is mainly due to translational displacement other than rotational displacement, since no large difference is observed between α_1 and α_3 , and the mean value of α_2 is below 1.05. That reveals the fact that amplification in translational response due to simultaneous decrease in VLLRs stiffness affects the building more than amplification in rotational response due to the difference in stiffness of the opposite VLLRs.
- An increase in plan aspect ratio results in an increase in displacement amplification due to uncertainty in stiffness.

- Buildings with plan aspect ratio of 1:1 have smaller rotational amplification (α_2) compared to other plan aspect ratios.
- In average, total displacement amplification (α_1) is less than 1.05, and is minimized when the building's translational period equals its rotational period.
- Large variance of three vibration characteristics show the importance of extreme cases. Design for confidence levels larger than 50% would result in large values of α_1 , α_2 and α_3 .

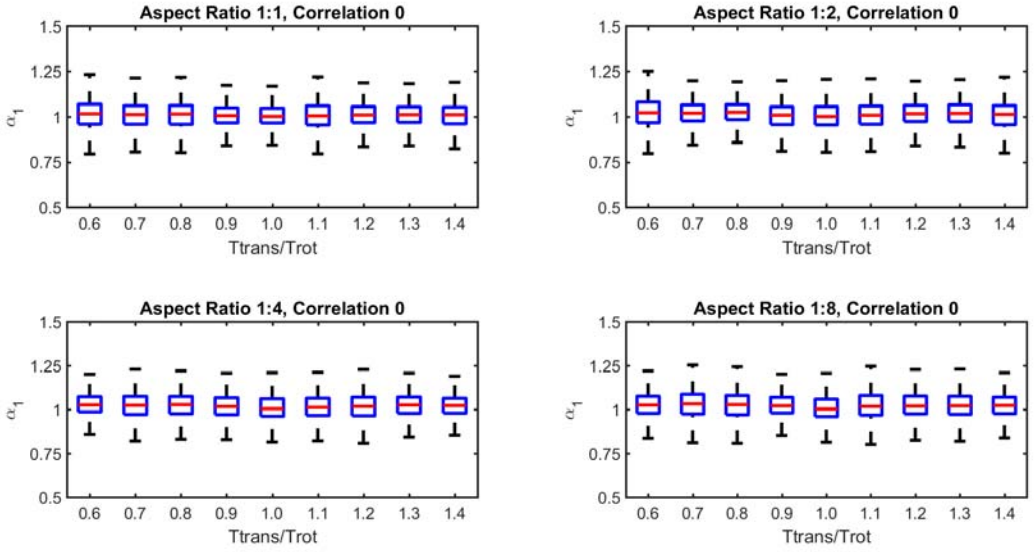

Figure 2-3. Distribution of α_1 for buildings with Ω ranging from 0.6 to 1.4 and plan aspect ratio ranging from 1:1 to 1:8

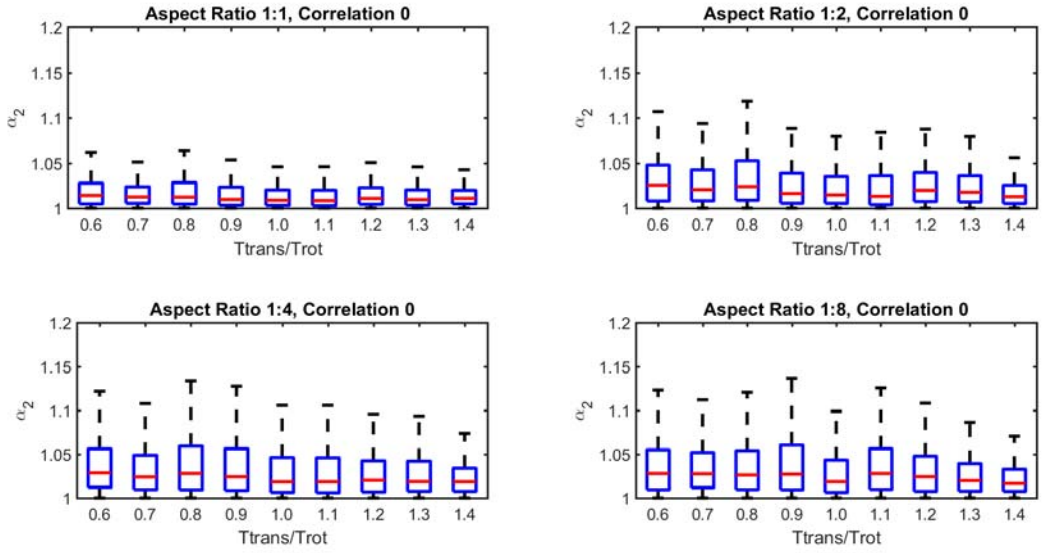

Figure 2-4. Distribution of α_2 for buildings with Ω ranging from 0.6 to 1.4 and plan aspect ratio ranging from 1:1 to 1:8

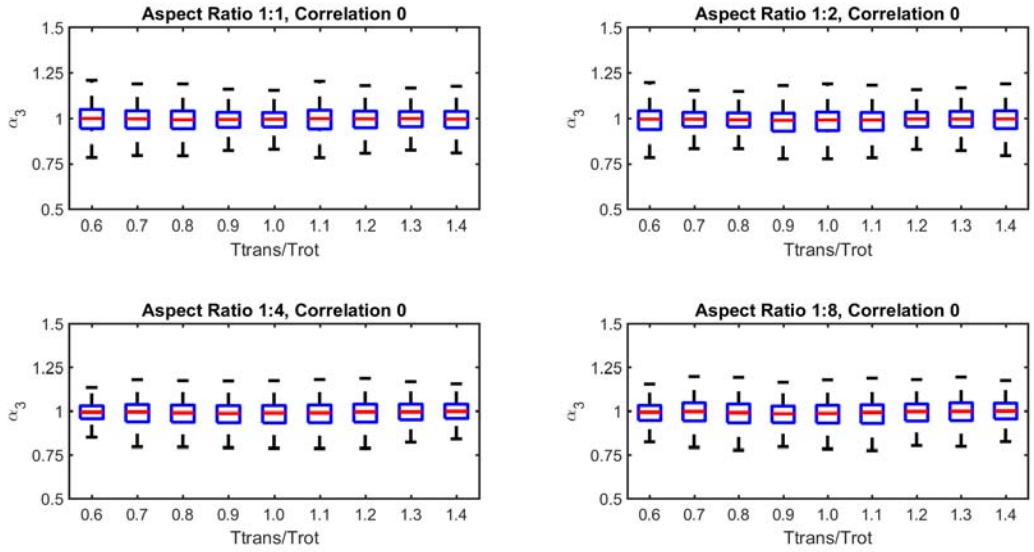

Figure 2-5. Distribution of α_3 for buildings with Ω ranging from 0.6 to 1.4 and plan aspect ratio ranging from 1:1 to 1:8

Validity of simulation results are checked using records from CSMIP database. Three-dimensional system identification techniques (Juang,1997, Van Overschee, 1996, Zhang 2001) are applied to four selected SMRF buildings (combinations of two plan aspect ratio of 1:1 and 1:2, and two levels of building height: high-rise and low-rise) in the CSMIP database to obtain translational to rotational period ratio. α_2 , the ratio of peak total response to peak translational response within an asymmetric system is computed in each of the four selected buildings. Since results of computed displacement amplification can be inaccurate at high noise levels, only those records with PGV (peak ground velocity) larger than 5cm/s are selected. Building information can be found in Table 2-1 and Figure 2-6.

Table 2-1. Selected buildings and ground motions information

Station	Height (ft)	Aspect Ratio (X to Y)	Ground Motion	PGV_x PGV_y (cm/s)	α_{2x} α_{2y}	Ω_x Ω_y
14533	265	1:1	Whittier 87	6.86 4.43	1.03 1.07	1.03 1.11
23516	41.3	1:1.1	Calexico 04Apr 2010	2.50 5.85	1.01 1.01	1.22 1.28
24104	41	1:2	Calexico 04Apr 2010	3.08 1.80	1.01 1.01	1.37 1.36
24569	274	1:2.1	Landers 92	7.63 12.42	1.06 1.02	0.93 0.96

Figure 2-7 shows the vibrational characteristic α_2 versus translational to rotational period ratio Ω of four selected buildings from CSMIP database superposed on the corresponding simulation results. It is notable that due to lack of records for one-story building, none of the selected buildings are one-story systems as the building models used for simulation purpose. However, Chopra (1995) showed that displacement amplification in a multistory building can be approximated by a single-story system with the same Ω as long as it satisfies: 1) The centers of mass of all floors lie on a vertical line; 2) Resisting planes form an orthogonal grid and are connected by a rigid diaphragm at each floor; 3) Lateral stiffness matrices of all resisting frames are proportional to each other. Thus, the displacement amplification of four selected symmetric-in-plan buildings can be approximated by their one-story counterparts.

Figure 2-6. Selected buildings from CSMIP database

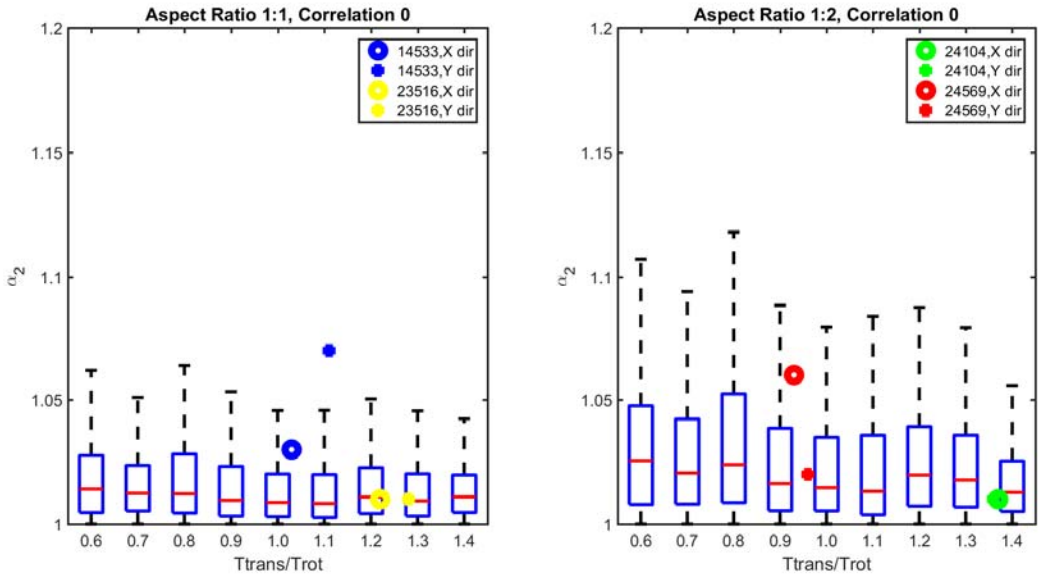

Figure 2-7. Comparison between simulation results and records from four selected buildings in CSMIP database

It can be observed from Figure 2-7 that displacement amplification of low-rises (building ID 23516 and 24104) are close to the median of simulation results. Simulations used in this research take into account VLLRs stiffness uncertainty only, while real-life data contains sources other than stiffness uncertainty that may cause torsional vibration (e.g. uncertainty in mass and location of center of mass). Nevertheless, displacement amplification in low-rise buildings has a good match with simulation results at median level. In high-rises (building ID 14533 and 24569), however, data leans towards higher than 75th percentile amplification in displacement, and more extreme cases can be observed. This shows the need for extending this investigation into models other than one-story systems to study the torsional behavior of high-rises.

Summary and Future work

This research develops statistical information on building vibrational characteristics such as displacement amplification factors and equivalent eccentricity using Monte Carlo simulations of one-story systems. Simulation results are verified using records from CSMIP database. Building properties such as plan aspect ratio, translational to rotational period ratio, correlation between VLLRs stiffness are found to be of great importance for prediction of torsional behavior of a building. Conclusions of this study are as follows:

- Displacement amplification due to torsion is highly affected by Ω. Buildings with a translational period identical to rotational period (Ω =1.0) and buildings who are insensitive to torsion (Ω >1.4) tend to have smallest amplification and are least affected by torsional vibration.
- An increase in plan aspect ratio results in an increase in displacement amplification.
- Correlation between VLLRs stiffness reduces displacement amplification due to torsion.
- To account for accidental torsion, the 5% rule is higher than how much an equivalent eccentricity requires at a median level. But when higher confidence level is preferred, equivalent eccentricity can be larger than 5%.

This study mainly focuses on torsional effect of one-story symmetric-in-plan linear system due to uncertainty in stiffness. Aside from plan aspect ratio and period ratio, building height could be one predictor of displacement amplification (as is demonstrated in Figure 2-7). In future studies, building height and nonlinear behavior will be studied. 4-story, 8-story, 12-story and 20-story building models with bilinear hysteretic materials are built to take into account stiffness and strength uncertainty. These building models can also capture the effect of number of VLLRs along one direction.

References

ASCE-American Society of Civil Engineers (2007). *Seismic rehabilitation of existing buildings*. ASCE/SEI 41-06, Reston, VA.

ASCE-American Society of Civil Engineers (2010). *Minimum Design Loads for Buildings and Other Structures* (ASCE/SEI 7–10). American Society of Civil Engineers: Reston, VA.

ASTM A6 (2005). *Standard Specification for General Requirements for Rolled Structural Steel Bars, Plates, Shapes, and Sheet Piling*. American Standards for Testing and Materials, ASTM International, West Conshohocken, Pennsylvania.

ASTM A992 (2004). *Standard Specification for Structural Steel Shapes.* American Standards for Testing and Materials, ASTM International, West Conshohocken, Pennsylvania.

Basu, D., Constantinou, M., Whittaker, A. (2014). An Equivalent Accidental Eccentricity to Account for The Effects of Torsional Ground Motion on Structures. *Engineering Structures,* 69: 1-11.

Bournonville, M., Dahnke, J. and Darwin, D. (2004). Statistical Analysis of the Mechanical Properties and Weight of Reinforcing Bars. *Structural Engineering and Engineering Materials*. Report 04-1.

De-la-Colina, J., Almeida, C. (2004). Probabilistic Study on Accidental Torsion of Low-Rise Buildings. *Earthquake Spectra*, 20(1):25-41.

De la Llera, JC., Chopra, A. (1992). Evaluation of Code-Accidental Torsion Provisions using Earthquake Records from Three Nominally Symmetric-Plan Buildings. *SMIP92 Seminar Proceedings*.

De la Llera, JC., Chopra, A. (1994). Accidental Torsion in Buildings Due to Stiffness Uncertainty. *Earthquake Engineering and Structural Dynamics*, 23:117-136.

De la Llera, JC., Chopra, A. (1995). Estimation of Accidental Torsion Effects for Seismic Design of Buildings. *Journal of Structural Engineering*, 121(1):102-114.

Ellingwood, B., Galambos, T., MacGregor, J. and Cornell, C. (1980). Development of a probability based load criterion for American National Standard. *Special Publication No.577*, National Bureau of Standards, Washington, DC.

Hernandez, JJ., Lopez, O. (2004). Dependence of Accidental Torsion on Structural System Properties. *Proceedings of the 13th World Conference on Earthquake Engineering,* Vancouver, Canada.

Juang, J. (1997). Identification of Linear Structural Systems using Earthquake Induced Vibration Data. Journal of Guidance, Control, and Dynamics, 20(3):492-500.

Lin, WH., Chopra, A., De la Llera, JC. (2001). Accidental Torsion in Buildings: Analysis versus Earthquake Motions. *Journal of Structural Engineering*, 127(5):475-481.

Melchers, R. (1987). *Structural Reliability: Analysis and Prediction,* Ellis Horwood, Chichester, 1987.

Ramsay, R., Mirza, S., and MacGregor. (1979). Monte Carlo Study of Short Time Deflections of Reinforced Concrete Beams. *ACI*, Vol.76 (897-918)

Van Overschee, P., B. De Moor. (1996). Subspace Identification of Linear Systems: Theory, Implementation, Applications. Springer Publishing.

Zhang, H., Paevere, P., Yang, Y., Foliente, GC., Ma, F. (2001) System identification of hysteretic structures. In Nonlinearity and Stochastic Structural Dynamics, IUTAM Symposium, Chennai, India, 1999 Narayanan S, IyengarRN (eds), Kluwer: Dordrecht, The Netherlands; 289–306.

UNTANGLING THE DYNAMICS OF SOIL-STRUCTURE INTERACTION USING NONLINEAR FINITE ELEMENT MODEL UPDATING

Hamed Ebrahimian[1], Domniki Asimaki[2], Danilo Kusanovic[3] and S. Farid Ghahari[4]

[1] Scientific Research Assistant, Department of Mechanical and Civil Engineering, Caltech
[2] Professor, Department of Mechanical and Civil Engineering, Caltech
[3] Ph.D. Candidate, Department of Mechanical and Civil Engineering, Caltech
[4] Postdoctoral Researcher, Department of Civil and Environmental Engineering, UCLA

Abstract

The dynamic response of a building structure to an earthquake excitation is the result of a complex interaction between the structural system and the underlying and surrounding geology. Since modeling the physics of the coupled soil-structure system is a complex undertaking, the state-of-practice has adopted simplified modeling procedures, such as the substructure method. Nevertheless, these procedures are often empirical and/or based on idealized assumptions, such as linear-elasticity. In this study, our objective is to develop a robust model inversion framework that can be utilized to extract information from the real-world building response measurements to back-calculate the model parameters that characterize the structural response and soil-structure interaction effects.

Introduction

The dynamic response of a building structures to an earthquake excitation is the result of a complex interaction between the structural system and the underlying and surrounding geology. The coupled soil-structure response is a function of seismic waves interacting with the building foundation, the nonlinear structural and geologic material response, and other energy dissipation mechanisms such as friction and viscous damping in the structure and soil. Therefore, the prediction accuracy of structural response quantities depends on the accuracy of the employed numerical model in characterizing these different sources of seismic energy dissipation and the dynamic soil-structure interaction.

Since modeling the physics of the coupled soil-structure system in detail is a complex undertaking, especially for practical design or assessment purposes, the state-of-practice has adopted simplified modeling procedures (e.g., [1], [2]). Soil-structure interaction effects are usually modeled using a substructure approach, where the soil flexibility and energy dissipation are modeled using distributed springs and dashpots [3]. Numerous simplified solutions exist to determine the stiffness and damping coefficients of these elements; solutions that are nonetheless based on idealized and restrictive assumptions. Examples of these assumptions include linear-elastic soil and structural behavior, uniform soil half space (or soil profiles with stiffness gradually varying with depth [4]), canonical foundation geometry, etc. These assumptions and the empirical nature of mechanical analogs such as soil springs and dashpots, could potentially lead to large error margins in predicting the seismic response of real-world building structures, even if the simplified models have demonstrated acceptable accuracy for ideal cases. The

applicability of these models becomes even more questionable for nonlinear response time history analyses. This is due to the fact that the concept of soil impedance functions and the resulting equivalent soil springs and dashpot is mainly based on the premise of linear-elastic response behavior. Nevertheless, the coupled soil-structure system is expected to experience nonlinearity during strong earthquakes – both material and geometrical (e.g., foundation-soil separation during rocking). Thus, the system may deviate substantially from the underlying assumptions that have led to substructure modeling techniques for soil-structure interaction analysis.

On the other hand, modern seismic design and assessment codes are progressively stirring toward nonlinear finite element (FE) modeling and response simulations for predictions of structural and nonstructural seismic demands. In a modern seismic analysis approach, a well-calibrated nonlinear model is required to precisely predict not only the peak values of response parameters, but also the time histories of structural responses. Despite all the advancements made in the field of mechanics-based nonlinear structural modeling, the state-of-practice for modeling structural damping and soil-structure interaction is still based on empirical assumptions. Clearly, there is an inconsistency between the mechanics-based modeling techniques available for structural systems and the underlying assumptions guiding the structural damping and soil-structure interaction modeling. This could result in an "inconsistent crudeness" in state-of-the-art seismic modeling of building structures that this proposal seeks to investigate.

In this study, we do not seek to develop new models of soil springs and dashpots or structural damping. Instead, we seek developing a model inversion framework that can be utilized to extract information from the real-world building response measurements to back-calculate the model parameters that characterize the structural response and soil-structure interaction effects. By repeating this effort for different building case studies and earthquake records in the long run, our objective is to compare the estimation results with the state-of-the-art recommendations, and to provide guidelines on how to improve the state-of-practice structural modeling capabilities.

Model Inversion through Nonlinear FE Model Updating

Suppose that the dynamic response of a building structure is recorded during an earthquake event. To simulate the dynamic response of this building structure, a mechanics-based (linear or nonlinear) FE model is developed. The FE model depends on a set of unknown parameters including inertia properties, damping parameters, soil spring and dashpot parameters, and parameters characterizing the nonlinear material constitutive laws used in the FE model. These parameters are referred to as the model parameters henceforth. Using the recorded input ground acceleration time history and the response of the building, the objective is to identify the best set of unknown model parameters that minimize the discrepancy between FE predicted and measured structural responses. Another objective of is to utilize the measured structural responses to jointly estimate the model parameters and input excitation (i.e., foundation input motion) time history.

In this study, the estimation problem is tackled by updating sequentially (i.e., for several batch of measurement data) the probability distribution function (PDF) of the unknown model parameters (and input excitation) using a Bayesian inference method (e.g., [5], [6]). FE model

updating using the measured input excitation and output response of the structure is referred to as the input-output model updating. Contrarily, in an output-only FE model updating, one or multiple time histories of the dynamic input excitation are also unknown. Therefore, the objective of the sequential Bayesian estimation is to estimate jointly the FE model parameters and the time unknown time history of the base excitation so that the discrepancies between the estimated and measured response quantities are minimized [7].

Background

The time-discretized equation of motion of a nonlinear FE model at time step i ($i = 1 \to k$, where *k* denotes the total number of time steps) is expressed as

$$\mathbf{M}(\boldsymbol{\theta})\,\ddot{\mathbf{q}}_i(\boldsymbol{\theta}) + \mathbf{C}(\boldsymbol{\theta})\,\dot{\mathbf{q}}_i(\boldsymbol{\theta}) + \mathbf{r}_i(\mathbf{q}_i(\boldsymbol{\theta}), \boldsymbol{\theta}) = \mathbf{f}_i(\boldsymbol{\theta}) \tag{1}$$

where $\mathbf{M}(\boldsymbol{\theta}) \in \mathrm{P}^{n_{DOF} \times n_{DOF}}$ = mass matrix, $\mathbf{C}(\boldsymbol{\theta}) \in \mathrm{P}^{n_{DOF} \times n_{DOF}}$ = damping matrix, $\mathbf{r}_i(\mathbf{q}_i(\boldsymbol{\theta}), \boldsymbol{\theta}) \in \mathrm{P}^{n_{DOF} \times 1}$ = history-dependent (or path-dependent) internal resisting force vector, $\mathbf{q}_i(\boldsymbol{\theta}), \dot{\mathbf{q}}_i(\boldsymbol{\theta}), \ddot{\mathbf{q}}_i(\boldsymbol{\theta}) \in \mathrm{P}^{n_{DOF} \times 1}$ = nodal displacement, velocity, and acceleration response vectors, respectively, $\boldsymbol{\theta} \in \mathrm{P}^{n_{\boldsymbol{\theta}} \times 1}$ = FE model parameter vector, $\mathbf{f}_i(\boldsymbol{\theta}) \in \mathrm{P}^{n_{DOF} \times 1}$ = dynamic load vector, and n_{DOF} = number of degrees-of-freedom. In the case of uniform (or rigid) seismic base excitation, $\mathbf{f}_i(\boldsymbol{\theta}) = -\mathbf{M}(\boldsymbol{\theta})\mathbf{L}\ddot{\mathbf{u}}_i^g$ where $\mathbf{L} \in \mathrm{P}^{n_{DOF} \times n_{\ddot{\mathbf{u}}^g}}$ = base acceleration influence matrix, and $\ddot{\mathbf{u}}_i^g \in \mathrm{P}^{n_{\ddot{\mathbf{u}}^g} \times 1}$ denotes the seismic input ground acceleration vector. Using a recursive numerical integration rule, such as the Newmark-beta method [8], Eq. (1) is reduced to a nonlinear vector-valued algebraic equation that can be solved recursively and iteratively in time to find the nodal response vector at each time step. In general, the response of a FE model at each time step is expressed as a function (linear or nonlinear) of the nodal displacement, velocity, and/or acceleration response vectors at that time step. Denoting the response quantity predicted by the FE model at time step *i* by $\hat{\mathbf{y}}_i \in \mathrm{P}^{n_{\mathbf{y}} \times 1}$, it follows that

$$\hat{\mathbf{y}}_i = \mathbf{h}_i\left(\boldsymbol{\theta}, \ddot{\mathbf{u}}_{1:i}^g, \mathbf{q}_0, \dot{\mathbf{q}}_0\right) \tag{2}$$

where $\mathbf{h}_i(...)$ is the nonlinear response function of the FE model at time step *i*. The measured response vector of the structure, $\mathbf{y}_i$, is related to the FE predicted response, $\hat{\mathbf{y}}_i$, as

$$\mathbf{v}_i\left(\boldsymbol{\theta}, \ddot{\mathbf{u}}_{1:i}^g\right) = \mathbf{y}_i - \hat{\mathbf{y}}_i\left(\boldsymbol{\theta}, \ddot{\mathbf{u}}_{1:i}^g\right) \tag{3}$$

in which $\mathbf{v}_i \in \mathrm{P}^{n_{\mathbf{y}} \times 1}$ is the simulation error vector and accounts for the misfit between the measured and FE predicted response of the structure. This misfit stems from the output measurement noise, parameter uncertainty, and model uncertainties. The latter stands for the mathematical idealizations and imperfections underlying the FE model, which result in an inherent misfit between the FE model prediction and the measured structural response [9]. In the absence of model uncertainties, it is assumed here that the measurement noises are stationary, zero-mean, independent Gaussian white noise processes (i.e., statistically independent across

time and measurement channels) [10]. Therefore, the probability distribution function (PDF) of the simulation error in Eq. (3) is expressed as

$$p(\mathbf{v}_i) = \frac{1}{(2\pi)^{n_y/2} |\mathbf{R}|^{1/2}} e^{-\frac{1}{2}\mathbf{v}_i^T \mathbf{R}^{-1} \mathbf{v}_i} \tag{4}$$

in which $|\mathbf{R}|$ denotes the determinant of the diagonal matrix $\mathbf{R} \in \mathrm{P}^{n_y \times n_y}$, which is the (time-invariant) covariance matrix of the simulation error vector (i.e., $\mathbf{R} = E(\mathbf{v}_i \mathbf{v}_i^T)$, $\forall i$).

In an output-only FE model updating problem, the FE model parameter vector ($\boldsymbol{\theta}$) and the time history of the seismic input ground acceleration at each time step ($\ddot{\mathbf{u}}_{1:k}^g$) are unknown and modeled as random variables (the corresponding random variables are denoted by $\boldsymbol{\Theta}$ and $\ddot{\mathbf{U}}_{1:k}^g$, respectively). Using Bayes' rule, the posterior probability distribution of the unknowns can be expressed as

$$p\left(\boldsymbol{\theta}, \ddot{\mathbf{u}}_{1:k}^g \mid \mathbf{y}_{1:k}\right) = \frac{p\left(\mathbf{y}_{1:k} \mid \boldsymbol{\theta}, \ddot{\mathbf{u}}_{1:k}^g\right) p\left(\boldsymbol{\theta}, \ddot{\mathbf{u}}_{1:k}^g\right)}{p\left(\mathbf{y}_{1:k}\right)} \tag{5}$$

where $p\left(\mathbf{y}_{1:k} \mid \boldsymbol{\theta}, \ddot{\mathbf{u}}_{1:k}^g\right) = p(\mathbf{v}_{1:k})$ = likelihood function, $p\left(\boldsymbol{\theta}, \ddot{\mathbf{u}}_{1:k}^g\right)$ = joint prior distribution of the random variables $\boldsymbol{\Theta}$ and $\ddot{\mathbf{U}}_{1:k}^g$, and $p(\mathbf{y}_{1:k})$ = normalizing constant independent of $\boldsymbol{\Theta}$ and $\ddot{\mathbf{U}}_{1:k}^g$. The objective of the output-only FE model updating problem is to estimate jointly the unknown model parameters and the ground acceleration time history such that their joint posterior PDF given the measured response of the structure is maximized, i.e.,

$$\left(\hat{\boldsymbol{\theta}}, \hat{\ddot{\mathbf{u}}}_{1:k}^g\right)_{\mathrm{MAP}} = \underset{\left(\boldsymbol{\theta}, \ddot{\mathbf{u}}_{1:k}^g\right)}{\arg\max}\ p\left(\boldsymbol{\theta}, \ddot{\mathbf{u}}_{1:k}^g \mid \mathbf{y}_{1:k}\right) \tag{6}$$

in which $\mathbf{y}_{1:k} = \left[\mathbf{y}_1^T, \mathbf{y}_2^T, \ldots, \mathbf{y}_k^T\right]^T$ = time history of the measured response of the structure, and MAP stands for the maximum posterior estimate. The estimation uncertainty is quantified by evaluating the parameter estimation covariance matrix at the MAP estimate.

Since the model inversion problem is highly nonlinear, a sequential estimation approach, referred to as the sequential Bayesian estimation method, is used in this study to improve the computational efficiency and convergence rate. In this approach, the estimation time interval is divided into successive overlapping time windows, referred to as the estimation windows. The estimation problem is solved at each estimation window to estimate the posterior PDF of unknown parameters. The first two moment of distribution (i.e., mean vector and covariance matrix) of the parameters are then transferred to the next estimation window and used as prior information. The sequential Bayesian estimation method approach is schematically shown in Figure 1. Two approaches are developed to find the posterior mean vector and covariance matrix of the unknown parameters and from the prior estimates: (i) a FE model linearization approach,

and (ii) an unscented transformation approach. These two methods are described in the next two sections, respectively.

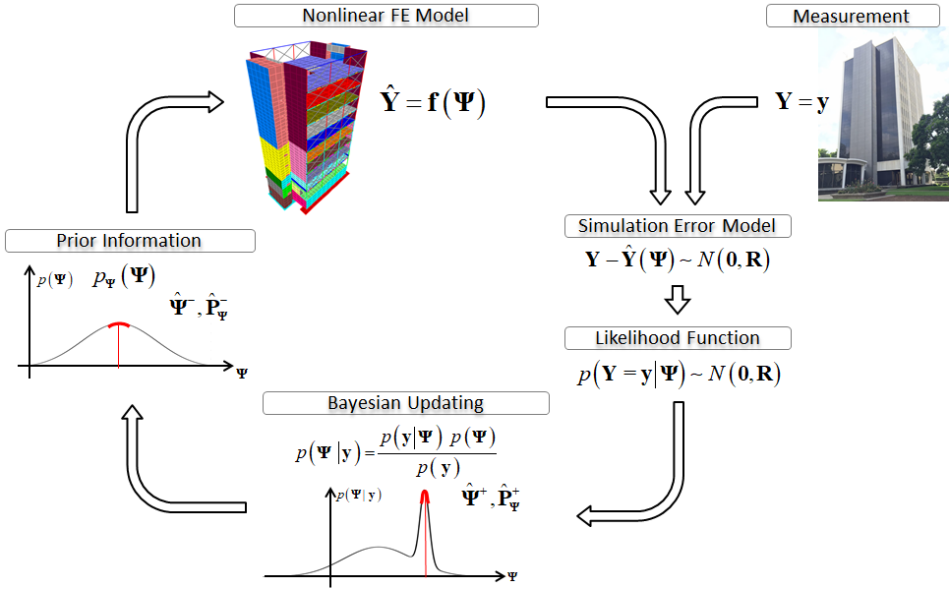

Figure 1: Schematic presentation of the sequential Bayesian FE model updating method.

Sequential Bayesian Estimation using FE Model Linearization

Following Eq. (5) and the sequential estimation logic described above, the natural logarithm of the posterior joint PDF of the FE model parameters and base acceleration time history at the m^{th} estimation window, spanning from time step t_1^m to time step t_2^m, can be derived as

$$\log\left(p\left(\boldsymbol{\theta}, \ddot{\mathbf{u}}^{g,m}_{t_1^m:t_2^m} \middle| \mathbf{y}_{t_1^m:t_2^m}\right)\right) = c + \log\left(p\left(\mathbf{y}_{t_1^m:t_2^m} \middle| \boldsymbol{\theta}, \ddot{\mathbf{u}}^{g,m}_{t_1^m:t_2^m}\right)\right) + \log\left(p\left(\boldsymbol{\theta}, \ddot{\mathbf{u}}^{g,m}_{t_1^m:t_2^m}\right)\right) \tag{7}$$

in which $c = -\log\left(p\left(\mathbf{y}_{t_1^m:t_2^m}\right)\right)$ is a constant. In this equation, the time history of the base acceleration from time step 1 to $t_1^m - 1$, (i.e., $\ddot{\mathbf{u}}^{g}_{1:t_1^m-1}$), is assumed to be deterministic and equal to the mean estimates obtained from previous estimation sequences. For notational convenience, an extended parameter vector at the m^{th} estimation window is defined as $\boldsymbol{\psi}_m = \left[\boldsymbol{\theta}^T, \ddot{\mathbf{u}}^{g,m\ T}_{t_1^m:t_2^m}\right]^T$, where $\boldsymbol{\psi}_m \in \mathrm{P}^{\left(n_{\boldsymbol{\theta}} + t_l \times n_{\ddot{\mathbf{u}}^g}\right)\times 1}$. Since the simulation error is modeled as an independent Gaussian white noise process, the likelihood function is given by

$$p\left(\mathbf{y}_{1:k} \middle| \boldsymbol{\theta}, \ddot{\mathbf{u}}^{g}_{1:k}\right) = \prod_{i=1}^{k} p(\mathbf{v}_i) \tag{8}$$

$$\Rightarrow p\left(\mathbf{y}_{1:k} \mid \boldsymbol{\theta}, \ddot{\mathbf{u}}^{g}_{1:k}\right) = \prod_{i=1}^{k} \frac{1}{(2\pi)^{n_y/2} |\mathbf{R}|^{1/2}} e^{-\frac{1}{2}\left(\mathbf{y}_i - \mathbf{h}_i\left(\boldsymbol{\theta}, \ddot{\mathbf{u}}^{g}_{1:i}, \mathbf{q}_0, \dot{\mathbf{q}}_0\right)\right)^T \mathbf{R}^{-1}\left(\mathbf{y}_i - \mathbf{h}_i\left(\boldsymbol{\theta}, \ddot{\mathbf{u}}^{g}_{1:i}, \mathbf{q}_0, \dot{\mathbf{q}}_0\right)\right)}$$

By substitution of Eq. (8) into Eq. (7) and assuming a Gaussian distribution for the prior joint PDF, it follows that

$$\log\left(p\left(\boldsymbol{\psi}_m \mid \mathbf{y}_{t_1^m:t_2^m}\right)\right) = k_0 - \frac{1}{2}\left(\mathbf{y}_{t_1^m:t_2^m} - \mathbf{h}_{t_1^m:t_2^m}\left(\boldsymbol{\psi}_m, \hat{\ddot{\mathbf{u}}}^{g}_{1:t_1^m-1}\right)\right)^T \tilde{\mathbf{R}}^{-1}\left(\mathbf{y}_{t_1^m:t_2^m} - \mathbf{h}_{t_1^m:t_2^m}\left(\boldsymbol{\psi}_m, \hat{\ddot{\mathbf{u}}}^{g}_{1:t_1^m-1}\right)\right) - \cdots \frac{1}{2}\left(\boldsymbol{\psi}_m - \hat{\boldsymbol{\psi}}_m^{-}\right)^T \left(\hat{\mathbf{P}}_{\psi}^{-}\right)^{-1}\left(\boldsymbol{\psi}_m - \hat{\boldsymbol{\psi}}_m^{-}\right) \tag{9}$$

where k_0 is a constant, and $\hat{\boldsymbol{\psi}}_m^{-}$ and $\hat{\mathbf{P}}_{\psi}^{-}$ are the prior mean vector and covariance matrix of the extended parameter vector at the m^{th} estimation window. $\tilde{\mathbf{R}} \in \mathrm{P}^{(t_l \times n_y)\times(t_l \times n_y)}$ is a block diagonal matrix, in which the diagonals are the simulation error covariance matrix $\mathbf{R}$. To find the MAP estimate of $\boldsymbol{\psi}_m$, the posterior PDF in Eq. (9) is maximized, i.e.,

$$\frac{\partial \log\left(p\left(\boldsymbol{\psi}_m \mid \mathbf{y}_{t_1^m:t_2^m}\right)\right)}{\partial \boldsymbol{\psi}_m} = \mathbf{0} \Rightarrow$$

$$\left(\frac{\partial \mathbf{h}_{t_1^m:t_2^m}\left(\boldsymbol{\psi}_m, \hat{\ddot{\mathbf{u}}}^{g}_{1:t_1^m-1}\right)}{\partial \boldsymbol{\psi}_m}\right)^T \tilde{\mathbf{R}}^{-1}\left(\mathbf{y}_{t_1^m:t_2^m} - \mathbf{h}_{t_1^m:t_2^m}\left(\boldsymbol{\psi}_m, \hat{\ddot{\mathbf{u}}}^{g}_{1:t_1^m-1}\right)\right) - \left(\hat{\mathbf{P}}_{\psi}^{-}\right)^{-1}\left(\boldsymbol{\psi}_m - \hat{\boldsymbol{\psi}}_m^{-}\right) = 0 \tag{10}$$

Eq. (10), which is a nonlinear algebraic equation in $\boldsymbol{\psi}_m$ can be solved using an iterative first order approximation of the FE response function $\mathbf{h}_{t_1^m:t_2^m}\left(\boldsymbol{\psi}_m, \ddot{\mathbf{u}}^{g}_{1:t_1^m-1}\right)$ at $\hat{\boldsymbol{\psi}}_m^{-}$ as

$$\mathbf{h}_{t_1^m:t_2^m}\left(\boldsymbol{\psi}_m, \hat{\ddot{\mathbf{u}}}^{g}_{1:t_1^m-1}\right) = \mathbf{h}_{t_1^m:t_2^m}\left(\hat{\boldsymbol{\psi}}_m^{-}, \hat{\ddot{\mathbf{u}}}^{g}_{1:t_1^m-1}\right) + \left.\frac{\partial \mathbf{h}_{t_1^m:t_2^m}\left(\boldsymbol{\psi}_m, \hat{\ddot{\mathbf{u}}}^{g}_{1:t_1^m-1}\right)}{\partial \boldsymbol{\psi}_m}\right|_{\boldsymbol{\psi}_m = \hat{\boldsymbol{\psi}}_m^{-}} \left(\boldsymbol{\psi}_m - \hat{\boldsymbol{\psi}}_m^{-}\right) + \boldsymbol{H.O.T.} \tag{11}$$

The matrix $\left.\frac{\partial \mathbf{h}_{t_1^m:t_2^m}\left(\boldsymbol{\psi}_m, \ddot{\mathbf{u}}_{g\,1:t_1^m-1}\right)}{\partial \boldsymbol{\psi}_m}\right|_{\boldsymbol{\psi}_m = \hat{\boldsymbol{\psi}}_m^{-}}$ represents the FE response sensitivities with respect to the extended parameter vector, evaluated at the prior mean values of the extended parameter vector, $\hat{\boldsymbol{\psi}}_m^{-}$. This matrix is denoted by **C** hereafter for notational convenience. Substituting Eq. (11) into Eq. (10) and neglecting the higher order terms results in the following (first order approximate) equation for the MAP estimate of $\boldsymbol{\psi}_m$:

$$\hat{\boldsymbol{\psi}}_m^{+} = \hat{\boldsymbol{\psi}}_m^{-} + \left(\mathbf{C}^T \tilde{\mathbf{R}}^{-1}\mathbf{C} + \left(\hat{\mathbf{P}}_{\psi}^{-}\right)^{-1}\right)^{-1} \mathbf{C}^T \tilde{\mathbf{R}}^{-1}\left(\mathbf{y}_{t_1^m:t_2^m} - \mathbf{h}_{t_1^m:t_2^m}\left(\hat{\boldsymbol{\psi}}_m^{-}, \hat{\ddot{\mathbf{u}}}^{g}_{1:t_1^m-1}\right)\right) \tag{12}$$

in which $\hat{\psi}_m^+$ is the updated (or the posterior) mean estimate of ψ_m. It can be shown that the term $\tilde{\mathbf{K}} = \left(\mathbf{C}^T \tilde{\mathbf{R}}^{-1} \mathbf{C} + \left(\hat{\mathbf{P}}_{\Psi}^- \right)^{-1} \right)^{-1} \mathbf{C}^T \tilde{\mathbf{R}}^{-1}$ is similar to the Kalman gain matrix, as used for Kalman filtering [11].

The updated $\hat{\psi}_m^+$ from Eq. (12) is iteratively used as the new point for the linearization of the nonlinear FE model in Eq. (11) to find an improved estimation. This iterative prediction-correction procedure at each estimation window is equivalent to an iterative EKF method for parameter-only estimation [11]. Following the EKF procedure, the prior covariance matrix of the extended parameter vector $\hat{\mathbf{P}}_{\Psi,m}^-$ is updated to the posterior covariance matrix $\hat{\mathbf{P}}_{\Psi,m}^+$ after each prediction-correction iteration. Moreover, it is assumed that both the prior and posterior joint PDF of the extended parameter vector are Gaussian. The updated estimation covariance matrix, can be derived as

$$\hat{\mathbf{P}}_{\psi,m}^+ = E\left[\left(\Psi_m - \hat{\psi}_m^+ \right) \left(\Psi_m - \hat{\psi}_m^+ \right)^T \right] = \left(\mathbf{I} - \mathbf{KC} \right) \hat{\mathbf{P}}_{\psi,m}^- \left(\mathbf{I} - \mathbf{KC} \right)^T + \mathbf{K} \tilde{\mathbf{R}} \mathbf{K}^T \tag{13}$$

Furthermore, to improve the convergence of the iterative prediction-correction procedure, a constant disturbance matrix is added to the posterior covariance matrix at each iteration to provide the prior covariance matrix for the next iteration, i.e.,

$$\hat{\mathbf{P}}_{\Psi,i+1}^- = \hat{\mathbf{P}}_{\Psi,i}^+ + \mathbf{Q} \tag{14}$$

where $\mathbf{Q}$ is a constant diagonal matrix with small positive diagonal entries (relative to the diagonal entries of matrix $\hat{\mathbf{P}}_{\Psi,i}^+$). The matrix $\mathbf{Q}$ is referred to as process noise covariance matrix in the Kalman filtering world. The subscript *i* in Eq. (14) denotes the iteration number.

Sequential Bayesian Estimation using the Unscented Transformation

While the terms $\hat{\mathbf{P}}_{\psi\mathbf{y}}$ = cross-covariance matrix of Ψ and $\mathbf{Y}$, and $\hat{\mathbf{P}}_{\mathbf{yy}}$ = covariance matrix of $\mathbf{Y}$ in are derived by linearizing the nonlinear FE model in the previous section, an unscented transformation (UT) method (e.g., [12], [13]) can also be used to derive the $\hat{\mathbf{P}}_{\psi\mathbf{y}}$ and $\hat{\mathbf{P}}_{\mathbf{yy}}$. UT is a deterministic sampling approach to propagate the uncertainty in Ψ through the nonlinear FE model; thus, circumventing the linearization of the FE model. Therefore, it results in a more accurate estimation of the $\hat{\mathbf{P}}_{\psi\mathbf{y}}$ and $\hat{\mathbf{P}}_{\mathbf{yy}}$, especially for highly nonlinear models. Indeed, using the UT method is at the cost of evaluating the FE model at multiple samples of the vector Ψ; nevertheless, the additional FE computations can be performed in parallel ([14], [15]).

In this approach, the nonlinear FE model is evaluated separately at a set of deterministically selected realizations of the extended parameter vector Ψ, referred to as the sigma points (SPs) denoted by ϑ^j, which are selected around the prior mean estimate $\hat{\Psi}^-$. In this study, a scaled UT based on $(2 \times n_{\Psi} + 1)$ sigma points (i.e., $j = 1, 2, \ldots, (2 \times n_{\Psi} + 1)$) is used, where n_{Ψ} denotes the size of the extended parameter vector. The mean and covariance matrix of

the FE predicted structural response $\mathbf{Y}$, and the cross-covariance matrix of $\mathbf{\Psi}$ and $\mathbf{Y}$ are respectively computed using a weighted sampling method as

$$\bar{\mathbf{y}} = \sum_{j=1}^{2\times n\Psi+1} W_m^j \, \hat{\mathbf{y}}\left(\vartheta^j\right) \tag{15}$$

$$\hat{\mathbf{P}}_{yy} = \sum_{j=1}^{2\times n\Psi+1} W_e^j \left[\hat{\mathbf{y}}\left(\vartheta^j\right) - \bar{\mathbf{y}}\right]\left[\hat{\mathbf{y}}\left(\vartheta^j\right) - \bar{\mathbf{y}}\right]^T + \mathbf{R} \tag{16}$$

$$\hat{\mathbf{P}}_{\Psi y} = \sum_{j=1}^{2\times n\Psi+1} W_e^j \left[\vartheta^j - \hat{\mathbf{\Psi}}^-\right]\left[\hat{\mathbf{y}}\left(\vartheta^j\right) - \bar{\mathbf{y}}\right]^T \tag{17}$$

where W_m^j and W_e^j denote the mean and covariance weighting coefficients, respectively [13]. With this approach, the Kalman gain matrix can be computed and the sequential parameter estimation can be pursued following Eqs. (12) and (13).

FE Model Updating of the Millikan Library Building

The Millikan Library

The Millikan Library is a reinforced concrete shear wall building with a basement level and nine stories above the ground. It is located on the California Institute of Technology (Caltech) campus in Pasadena, and was constructed from 1966 to 1967. Millikan library has been the subject of several studies, especially in the fields of system identification and structural health monitoring. The building is a unique case for soil-structure interaction studies, due to its unique structural and soil properties (Figure 2).

The Millikan Library structure is 43.9 m tall above ground including the roof level. It has a 4.3 m deep basement below the ground level. Except for the first and the roof levels, which are 4.9 m high, all floors are 4.3 m high. The basement is encased by surrounding retaining shear walls. A surrounding precast concrete wall enlaces the roof story to protect the installed mechanical equipment. The lateral force resisting system comprises of shear walls in the NS direction on the east and west sides of the building, and shear walls around the elevator shaft in the north-south and east-west directions. The floor system consist of lightweight reinforced concrete slabs supported by reinforced concrete beams. The foundation system consist of a 1.2 m deep central pad 6 meters below the ground level, and two foundation beams in the north and south sides of the building 5 meters below the ground level. Four stepped beams connect the foundation pad to the north and south foundation beams. This special foundation system acts somehow similar to a rocking chair [16].

FE Model Development

Using the available structural drawings, a detailed FE model of the structural system is developed. We used the graphic-user-interface of SAP2000 software [17] to develop the initial geometry of the model. The SAP2000 model was then transformed to OpenSees [18] using a series of custom-developed Matlab interfaces based on the SAP2000 Application Programming

Interface (API). The developed FE model in OpenSees is nonlinear, with an option to switch to a linear model. The model is based on fiber-section force-based beam-column elements to model beams and columns. Kent-Scott-Park uniaxial material model with linear tension softening is used to model concrete and Giuffré-Menegotto-Pinto material is utilized to model reinforcing steel. A multi-layered nonlinear shell element with damage-plasticity concrete material model [19] is used to model shear walls and slabs. The kinematic interaction of precast claddings on the north and south faces of the building with the structural system are modeled using diagonal brace elements, with an elastic-perfectly plastic material model. The brace elements are assumed to have a rectangular cross section of 0.1 x 0.1 m. By adjusting the elastic modulus and yield strength of their material model, the stiffness and force contribution of the precast panels to the dynamic response of the structure are modeled.

Figure 3 shows the geometry of the model. Different colors in this figure present different section properties used to define the shell (shear wall and slab) and beam-column elements. The model is meshed manually to adjust the size and shape of elements. It consists of 1,885 frame elements, 4,043 shell elements, and 27,526 digress of freedom.

Figure 2: Millikan Library building.

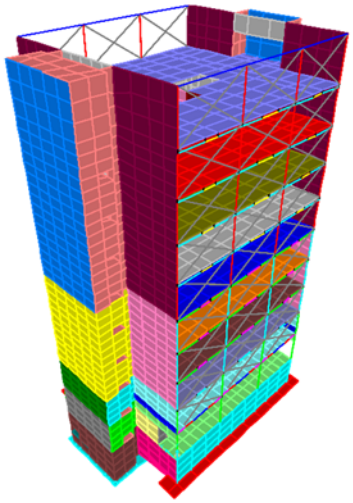

Figure 3: Developed FE model of the Millikan Library structure.

Several earthquake records are available for the Millikan Library. Details about sensor arrangements [20] and recorded earthquake data [16] are available in the literature and are not repeated here for brevity. For the purpose of this study, we used only the 2002 Yorba Linda earthquake record, which is a low-amplitude earthquake (PGA ~ 0.8% g). Although the level of considered earthquake in this study is low and therefore, may not activate the material nonlinearity, the developed model updating process is general and can be used with linear and or nonlinear models regardless of the earthquake intensity.

FE Model Updating using Foundation-Level Input Motions

At this stage, we use the measured acceleration response at the foundation level (i.e., foundation-level input motion) and the measured output response of the structure for the FE model updating. The objective of this input-output model updating is to estimate the unknown

model parameters of the superstructure, regardless of the soil subsystem. For this purpose, we start with an identifiability analysis to determine the most identifiable parameter sets. After selecting the parameter sets, we verify the estimation algorithms using simulated data. Finally, we use the real measurement data to estimate the model parameters.

Model Identifiability and Parameter Selection

Identifiability analysis is an approach to investigate if the unknown parameters can be uniquely estimated from data. To assess the parameter identifiability we used an information-theoretic approach [21] to measure the amount of information contained in measurement data about an unknown model parameter. The entropy gain is used to quantify the amount of information each unknown parameter receives from the measurement data. Comparing the entropy gain between different parameters is used to assess the relative identifiability of parameters. Moreover, the mutual entropy gain between parameter pairs is used to investigate the relative correlation between the parameters. This entropy gain and mutual entropy gain are used to guide the selection of the estimation parameters.

To assess the identifiability of model parameters, first we start with a nonlinear FE model. Twenty different parameters that characterize the material and inertia properties of model are selected, as shown in Table 1. Since the amplitude of the 2002 Yorba Linda earthquake is low, material yielding is not expected and therefore, only the elastic-related material parameters for reinforcing steel are included in the identifiability analysis. On the contrary, since the precast cladding are expected to yield under small inter-story drift ratios, the yield strength of brace elements is included in the analysis.

For a given input motion, the entropy gain for each parameter is a function of the initial (prior) value of the parameter, which is unknown in advance. The incorrect selection of the prior model parameter values can result in an incorrect identifiability assessment. Therefore, without the knowledge of correct parameter values, the identifiability assessment results would not be accurate anyways; but we still expect to have an approximate assessment of the identifiability. Initial material parameter values for steel and concrete are selected based on the material properties reported in the as-built drawings. The distributed floor mass (aside from self-mass of the structural materials) are estimated based on the approximate mass contribution of nonstructural components and live loads, and are in agreement with the building mass reported in [22]. The mass of each precast cladding panel is approximated as 5,000 kg based on Kuroiwa [22]. The stiffness, of the brace elements (used to model the kinematic interaction effects of the claddings) are approximated based on the modal analysis results before and after their installation ([23], [24]). The yield strength of the brace elements is approximated based on the experimental literature on the precast cladding panels (e.g., [25]). It should be noted that the stiffness and strength contribution of precast panels depends highly on the connection and construction details. In the absence of any detailed information about the precast panels in the Millikan Library, we postulated its properties based on engineering judgement. The model parameter values used for identifiability assessment are listed in Table 1.

Table 1: Twenty model parameters used for the first-step identifiability assessment.

Parameter ID	Description	Value
1	Elastic modulus (*Es*) of steel rebar in beams	180 GPa
2	Compressive strength (f'_c) of concrete in beams	27.6 MPa
3	Tensile strength (f'_t) of concrete in beams	1.73 MPa
4	Elastic modulus (*Ec*) of slab concrete in 1st floor	21 GPa
5	Elastic modulus (*Ec*) of slab concrete in 2nd floor	21 GPa
6	Elastic modulus (*Ec*) of slab concrete in 3rd to 5th floors	21 GPa
7	Elastic modulus (*Ec*) of slab concrete in 6th to roof floors	21 GPa
8	Compressive strength (f'_c) of concrete in columns	34.5 MPa
9	Tensile strength (f'_t) of concrete in columns	1.94 MPa
10	Elastic modulus (*Ec*) of shear wall concrete in basement	21 GPa
11	Elastic modulus (*Ec*) of shear wall concrete in 1st story	21 GPa
12	Elastic modulus (*Ec*) of shear wall concrete in 3rd to 5th stories	21 GPa
13	Elastic modulus (*Ec*) of shear wall concrete in 6th to roof stories	21 GPa
14	Elastic modulus (*E*) of brace elements representing the precast claddings	25 GPa
15	Distributed floor mass (*m*) on 1st to 9th floors	400 kg/m^2
16	Distributed floor mass (*m*) on basement floor	200 kg/m^2
17	Distributed floor mass (*m*) on roof	300 kg/m^2
18	Yield strength (f_y) of brace elements representing the precast claddings	140 MPa
19	Mass-proportional Rayleigh damping coefficient	0.1508
20	Stiffness-proportional Rayleigh damping coefficient	0.0038

Figure 4 shows the entropy gain of these twenty parameters. The entropy gain (measured in Nats) is the amount of information that the measurement data (i.e., the model responses herein) carries about each model parameters. It can be seen that the entropy gain of parameters #16 (distributed floor mass on basement floor), and #18 (yield strength of brace elements) is zero, which means that the structural response (for this specific base excitation) is not sensitive to these parameters. Those parameters that have the higher entropy gain are more likely to be identifiable.

Figure 5 shows the mutual entropy gain between the parameter pairs. This figure is used to investigate the dependence between parameters, which is presented with dark colors: darker colors means stronger relative dependence. For example, Figure 5 that there are strong mutual dependence between parameters #9 (Tensile strength of concrete in columns), #10 (Elastic modulus of shear wall concrete in basement), #11 (Elastic modulus of shear wall concrete in 1st story), and #12 (Elastic modulus of shear wall concrete in 3rd to 5th stories). Moreover, there are some competing effects between these parameters and parameters #1 (elastic modulus of steel rebar in beams), #15 (distributed floor mass on 1st to 9th floors), and #17 (distributed floor mass on roof). This plot along with the plot presented in Figure 4 can be used to choose the estimation

parameters. The parameters that gain relatively small amount of information from the measurement dataset, or have strong dependencies on the other estimation parameters can be put aside (i.e., fixed) during the estimation process to enhance the estimation performance.

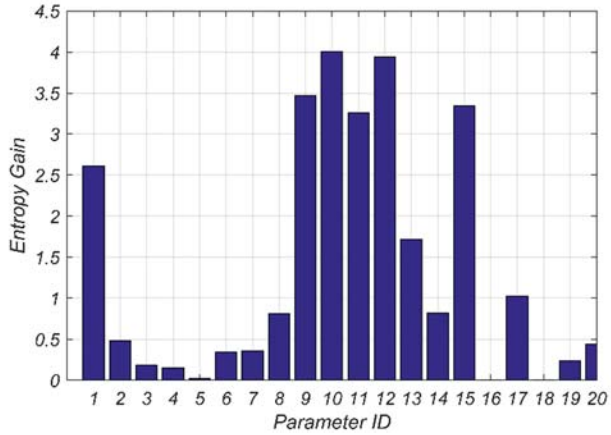

Figure 4: Entropy gain (in Nats) of the twenty model parameters.

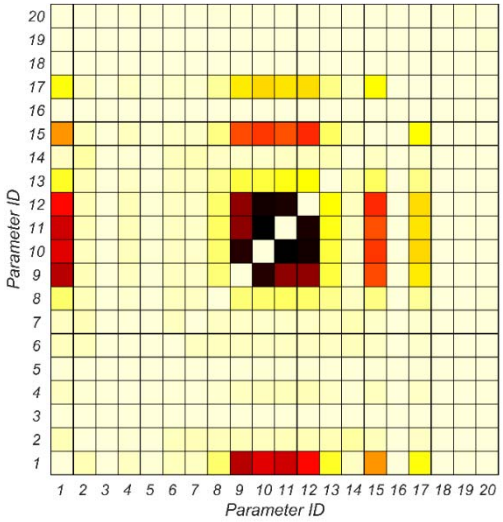

Figure 5: Relative mutual entropy gain between the parameter pairs.

Investigation of these two figures and the FE predicted response of the structure at the component-level reveals that the structure does not experience severe nonlinearity during this earthquake motion. Tensile cracking of concrete is expected in the columns (see parameter #9 in Figure 4), but no yielding is expected. Therefore, we decided to reduce the FE model to a linear elastic model for this earthquake excitation. Based on the presented results, we selected six final parameters to be estimated, as listed in Table 2. The initial (effective) elastic modulus values for concrete in this table are selected to account for tensile cracking under gravity loading.

Table 2: Final selected model parameters for linear-elastic model.

Parameter ID	Description	Value
1	Elastic modulus of brace elements representing the precast claddings (E_{Clad})	25 GPa
2	Elastic modulus of beams and slabs (all floors) (E_{floor})	15.8 GPa
3	Elastic modulus of shear wall and column concrete at 1st and 2nd stories ($E_{W\&C}1$)	22.1 GPa
4	Elastic modulus of shear wall and column concrete at 3rd to roof stories ($E_{W\&C}2$)	22.1 GPa
5	Stiffness-proportional Rayleigh damping coefficient (b)	0.0038
6	Distributed floor mass on 1st to 9th floors (m)	400 kg/m^2

Model Inversion using Recorded Yorba Linda Earthquake Data

After successful verification of the estimation algorithm, we utilize the real data recorded at the Millikan library building during the 2002 Yorba Linda earthquake for the model updating. The six unknown model parameters as introduced before are estimated. The initial and final estimate of parameters along with the final estimated coefficient of variation (COV) are listed in Table 3. Figure 6 shows the time history of the posterior mean and coefficient of variation (COV) of the model parameters, which presents the estimation uncertainties. To evaluate how well the updated model prediction matches the measurement records, Figure 7 compares the measured acceleration response time histories with those estimated using the initial and final estimates of the model parameters. Furthermore, Figure 8 compares the relative root mean square error (RRMSE) of the predicted FE model responses using the initial and final parameter estimates. This figure clearly shows that the model updating process has reduced the RRMSE substantially. Nevertheless, the time history plots in Figure 7 shows non-negligible differences between the estimated and measured response time histories, especially at the middle stories of the building and for the north-south acceleration responses. These differences are most likely due to the incorrect base rocking motions applied on the model. The rocking components of the base motion are calculated using the vertical accelerations recorded at different locations on the foundation level, and the (approximate) horizontal distance between the sensor locations. However, the vertical acceleration data are noisy and moreover, any approximation in determining the sensors' location may result in erroneous estimation of the rocking components of base acceleration. The effects of model uncertainty is another source of error that can contribute to the discrepancies between the estimated and measured structural responses in Figure 7.

Table 3: Initial and final estimate of model parameters using Yorba Linda earthquake data.

Parameter ID	Parameter	Initial Estimate	Final Estimate	Estimated COV (%)
1	E_{Clad}	20 GPa	7.81 GPa	1.60
2	E_{floor}	21 GPa	4.13 GPa	0.81
3	$E_{W\&C}1$	26.7 GPa	16.58 GPa	0.45
4	$E_{W\&C}2$	26.7 GPa	32.06 GPa	0.84
5	b	0.0038	0.0035	1.13
6	m	250 (kg/m^2)	153.84 (kg/m^2)	0.61

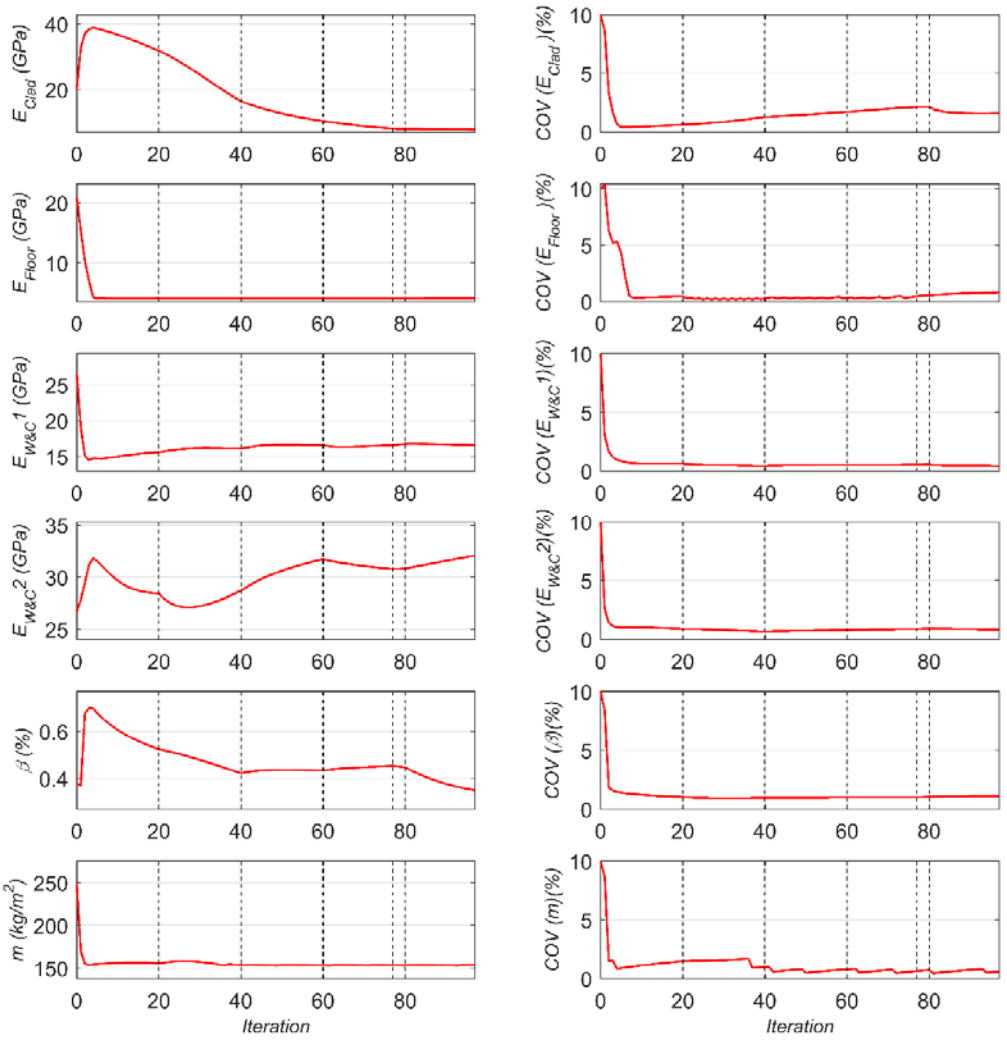

Figure 6: Time histories of the posterior mean (left) and coefficient of variation (COV) (right) of the model parameters estimated from the Yorba Linda earthquake records.

Output-Only Model Inversion

At this stage, we use the updated model of the superstructure, obtained from previous step, and the measured responses of the structure for an output-only FE model updating. The objective is to estimate the foundation input motions (FIMs) and the stiffness and viscosity of the soil springs and dashpots used to model the inertial soil-structure interaction effects. For this purpose, and similar to the previous step, we start with an identifiability analysis to evaluate the sensitivity of the structural response with respect to the soil stiffness and viscosity parameters. Then, we use the real measurement data to estimate the soil parameters.

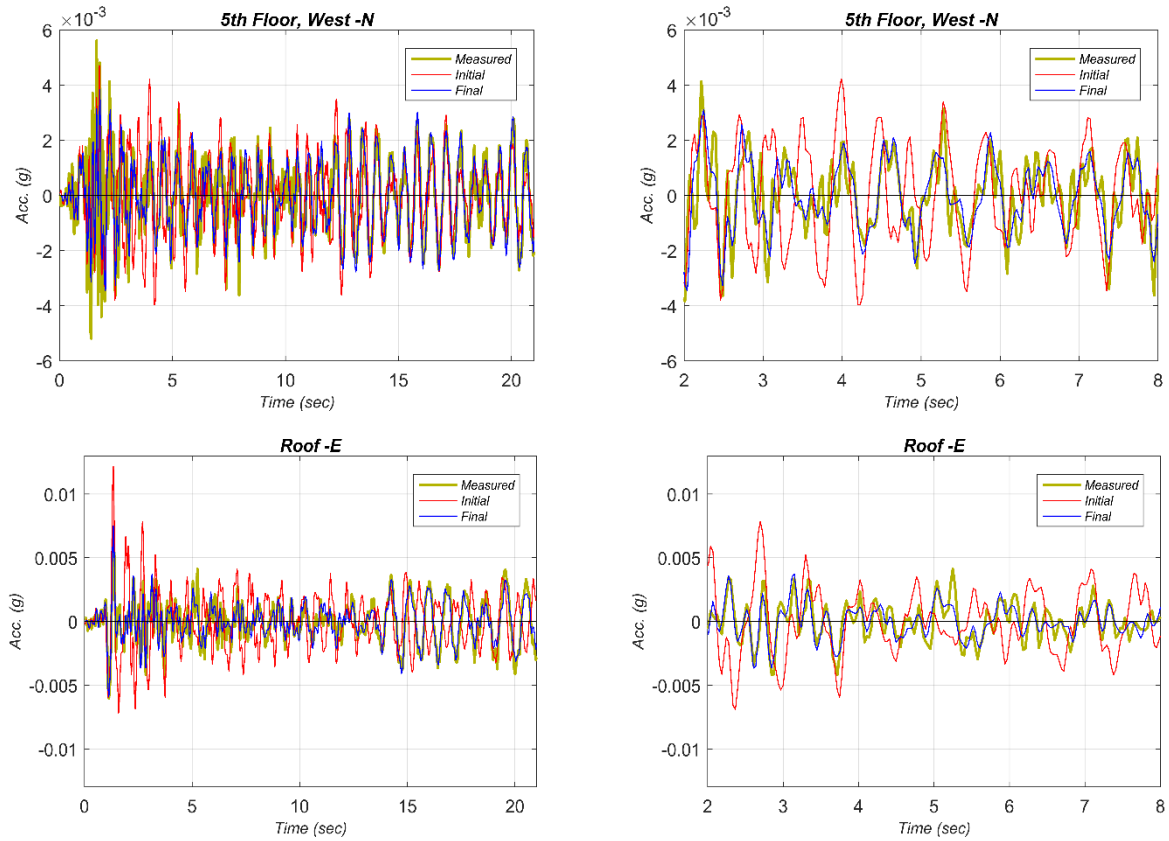

Figure 7: Comparison of the measured structural responses with the structural responses predicted using the initial and final estimate of model parameters.

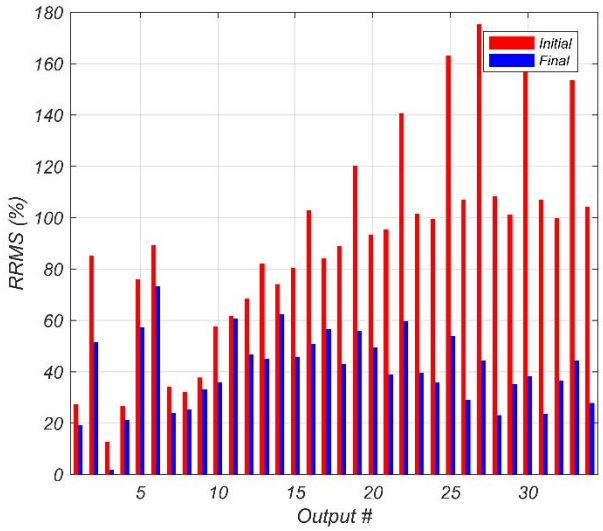

Figure 8: Relative root mean square error (RRMSE) of the FE predicted structural responses using the initial and final estimate of model parameters.

Model Identifiability and Parameter Selection

Distributed linear soil springs and dashpots are included underneath the foundation slab of the updated FE model, obtained from the previous step. Three linear springs and three linear viscous dashpots are modeled independently in x-, y-, and z-direction at each nodal point of the foundation slab. The stiffness of soil springs and viscosity of dashpots are computed using the subgrade modulus (i.e., soil stiffness per unit area), and viscosity modulus (i.e., viscosity of the soil per unit area), respectively, in x-, y-, and z-direction. The spring stiffness is calculated by multiplying the tributary area of the nodal point by the corresponding subgrade modulus. Similarly, the dashpot viscosity is calculated by multiplying the tributary area of the nodal point by the corresponding viscosity modulus.

Six different (unknown) subgrade modulus, namely k_x, k_y1, k_y2, k_z1, k_z2, k_z3, are defined for different foundation regions. These regions and the corresponding subgrade modules are shown Figure 9. Similarly, six (unknown) parameters are used to define the viscosity modulus of soil. The viscosity modulus parameters (c_x, c_y1, c_y2, c_z1, c_z2, c_z3) characterize the viscosity of the soil per unit area, and are specified in Figure 9.

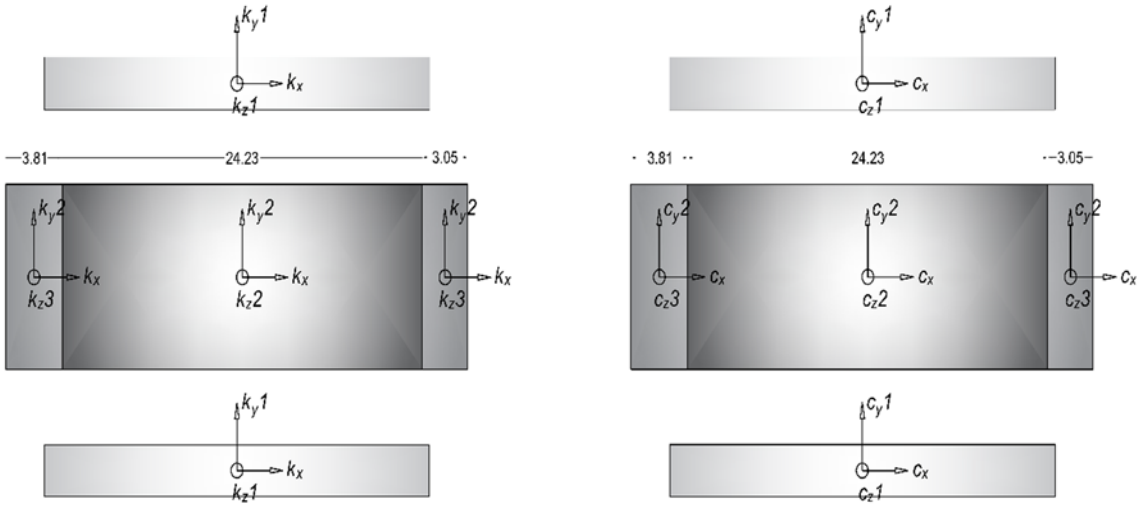

(a) (b)

Figure 9: (a) six unknown subgrade modulus parameters, and (b) six unknown viscosity modulus parameters defined for different foundation regions. The figure shows the foundation plan of the Millikan library including the central pad (at -6 m elevation), and the two foundation beams on the north and south sides (at -5 m elevation).

To assess the identifiability of these twelve soil parameters, we pursue the same identifiability analysis approach presented before. Initial estimate of soil model parameters are assigned following the results presented in [16], and the NIST standard recommendations [3], and are listed in Table 4.

Table 4: Twelve soil model parameters used for the first-step identifiability assessment.

Parameter ID	Description	Initial Estimate	Parameter ID	Description	Initial Estimate
1	k_x	65 MN/m^3	7	c_x	700 kN.s/m^3
2	k_y1	40 MN/m^3	8	c_y1	700 kN.s/m^3
3	k_y2	60 MN/m^3	9	c_y2	700 kN.s/m^3
4	k_z1	25 MN/m^3	10	c_z1	1000 kN.s/m^3
5	k_z2	22.5 MN/m^3	11	c_z2	1000 kN.s/m^3
6	k_z3	37.5 MN/m^3	12	c_z3	1000 kN.s/m^3

Figure 10 shows the entropy gain of the soil parameters. These plots presents the cumulative sensitivity of the FE model response (measured at 34 output channels) to the twelve soil parameters. The small entropy gain of some parameters such as k_y1, c_y1, c_z2, and c_z3 makes them weakly identifiable, and therefore these parameters are removed from the estimation process. Moreover, Figure 11, which shows the mutual entropy gain between the parameter pairs, indicates a strong dependence between k_z1, k_z2, and k_z3. This is not unexpected because the structural response does not include the vertical components of the acceleration (except on the foundation level). Therefore, although the rocking stiffness of the foundation system might be identifiable, its vertical stiffness remains weakly identifiable. By investigating these results, we decide to limit the number of estimation parameters to eight including: k_x, k_y, k_z1, k_z2, k_z3, c_x, c_y, and c_z. The three vertical stiffness are kept for the estimation despite their dependency.

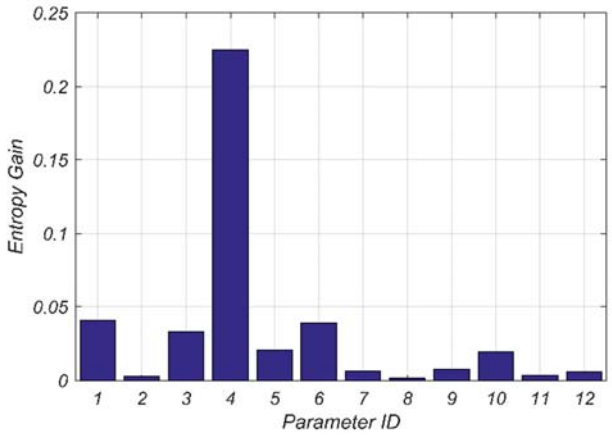

Figure 10: Entropy gain (in Nats) of the twelve soil parameters.

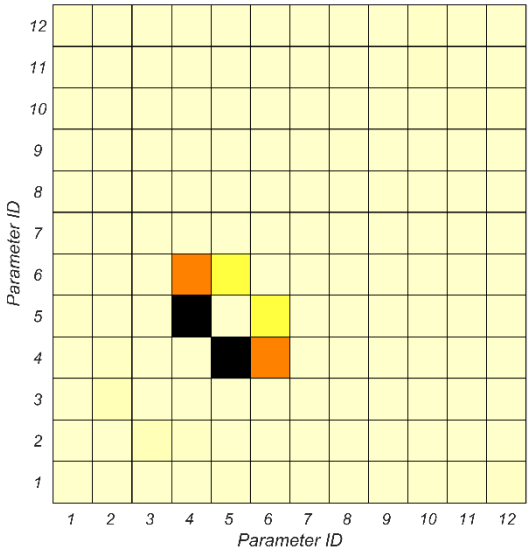

Figure 11: Relative mutual entropy gain between the soil parameter pairs.

Model Inversion using Recorded Yorba Linda Earthquake Data

The real data recorded at the Millikan library building during the 2002 Yorba Linda earthquake are now utilized for an output-only FE model updating to estimate the eight soil

parameters and the three components of the foundation input motion (FIM), namely in EW, NS, and Up directions. The initial and final estimate of parameters along with the estimated coefficient of variation (COV) are listed in Table 5. Figure 12 shows the time history of the three components of the estimated FIM. The estimation uncertainties are quantified through the standard deviation plots presented in this figure. Figure 13 shows the time history of the posterior mean and coefficient of variation (COV) of the soil parameters, which quantifies the estimation uncertainties. The large estimation uncertainties indicate the potential inaccuracy in the final parameter estimates. To evaluate how well the updated model prediction matches the measurement records, Figure 14 compares the measured acceleration response time histories with those estimated using the final estimates of the model parameters. This figure shows a remarkable match between the estimated and measured acceleration responses.

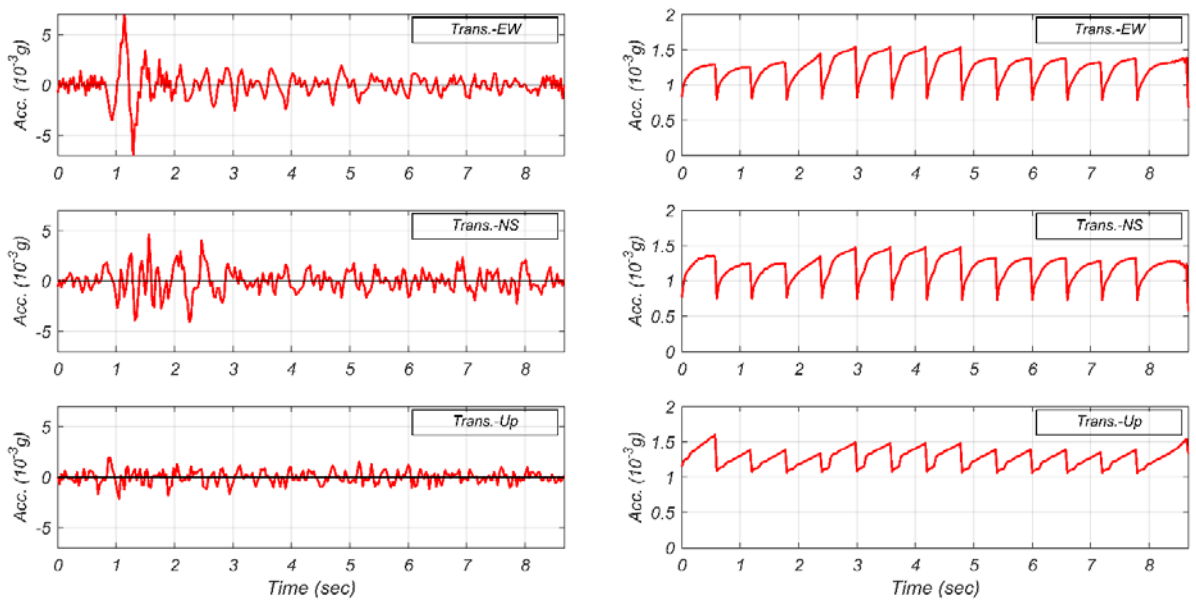

(a) (b)

Figure 12: Estimated foundation input motion (FIM) time history (left) and standard deviation (S.D.) of the estimated FIM time history (right).

Table 5: Initial and final estimates of soil parameters.

Parameter ID	Parameter	Initial Estimate	Final Estimate	Estimated COV (%)
1	k_x	65 MN/m^3	192.1 MN/m^3	19.4
2	k_y	50 MN/m^3	13.0 MN/m^3	40.3
3	k_z1	20 MN/m^3	106.6 MN/m^3	5.4
4	k_z2	22.5 MN/m^3	279.3 MN/m^3	14.4
5	k_z3	37.5 MN/m^3	408.8 MN/m^3	9.7
6	c_x	700 kN.s/m^3	2.4 MN.s/m^3	24.1
7	c_y	700 kN.s/m^3	1.8 MN.s/m^3	7.9
8	c_z	1000 kN.s/m^3	5.9 MN.s/m^3	4.9

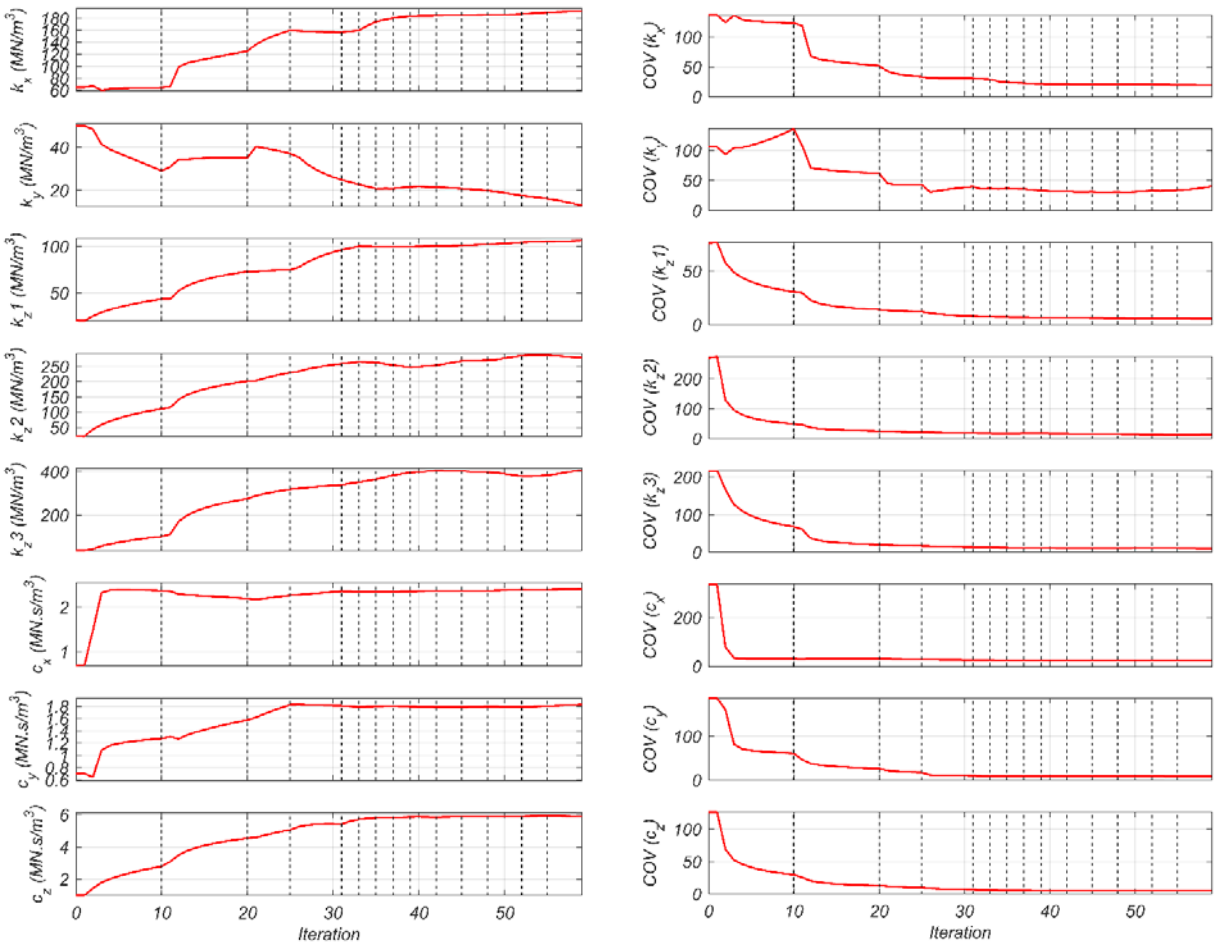

Figure 13: Time histories of the posterior mean (left) and coefficient of variation (COV) (right) of the model parameters estimated from the Yorba Linda earthquake records.

Summary and Conclusions

In this study, we developed a nonlinear FE model updating framework using a sequential Bayesian estimation approach based on the unscented transformation method. The FE model updating algorithm can estimate the unknown model parameters and/or the time history of dynamic input excitation using the measured structural responses. The algorithm can be used for input-output structural model updating (i.e., estimating the unknown model parameters using the foundation level input motion and the output response of the structure), and for output-only model updating (i.e., estimating jointly the unknown model parameters and the time history of input excitation). This capability has been used in this study to estimate the structural model parameters, the stiffness and viscosity of soil subsystem, and the foundation input motions (FIM) for the Millikan library.

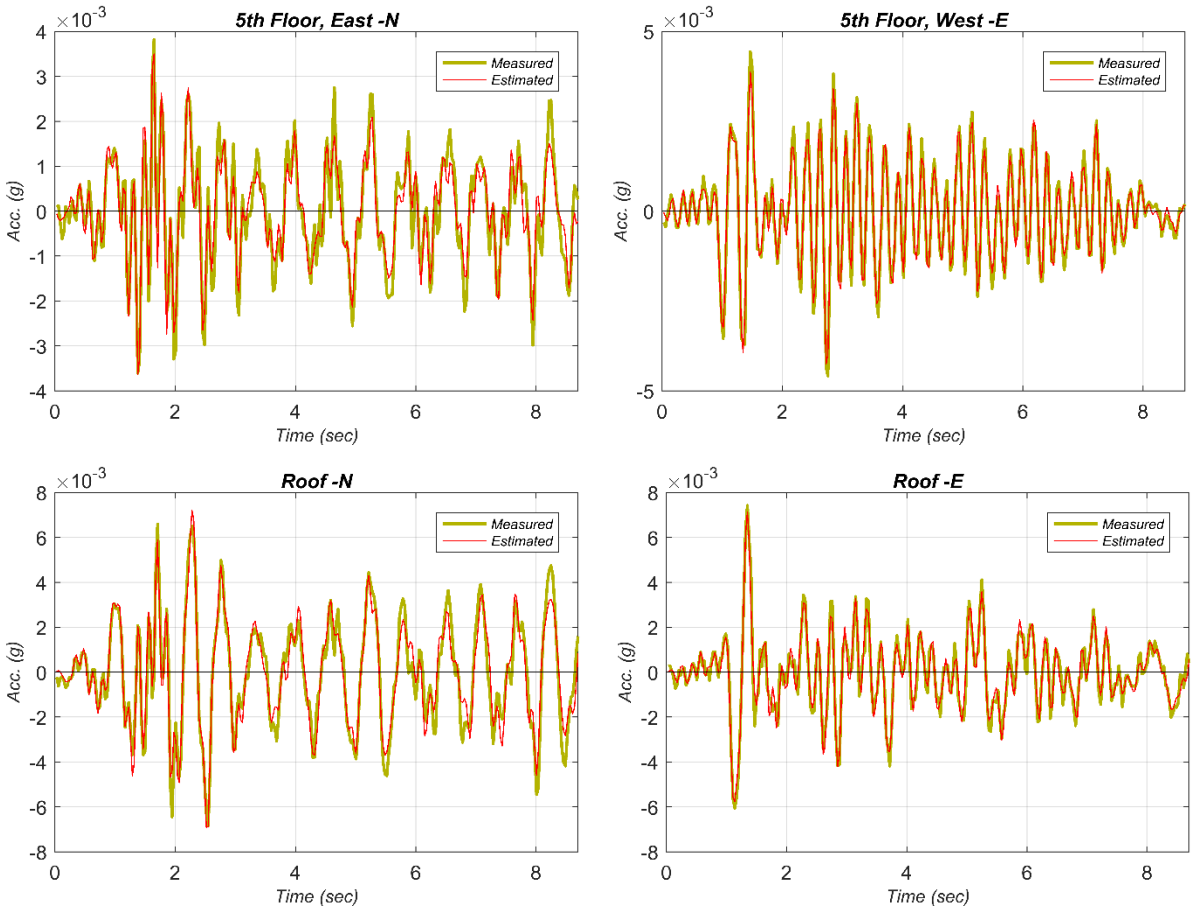

Figure 14: Comparison of the measured structural responses with the structural responses predicted using the final estimate of soil parameters and FIM.

We first developed a detailed FE model of the Millikan library structure. Through an identifiability analysis, we determined the sensitivity of the structural response to various model parameters, and selected a set of parameters that were likely to be identifiable. Since, we used the 2002 Yorba Linda earthquake data, which is a low-amplitude earthquake, we used a linear-elastic FE model of the building structure. At the first step, we performed an input-output model updating to estimate the model parameters related to the structural system. For this purpose, we utilized the foundation motion, measured on the foundation level, and the output response of the structure to estimate six structural model parameters. At the second step, we performed and output-only model updating to estimate the foundation input motions (FIM) and the parameters characterizing the stiffness and viscosity of the soil spring and dashpots. For this purpose, the structural model parameters were fixed at the parameter estimates obtained from the input-output model updating step. Eight soil-related parameters and three components of the FIM were estimated using the recorded response of the structure during the Yorba Linda earthquake.

The objective of this study was to develop, verify, and validate a FE model updating capability that can be used with real-world data. The FE model updating is a tool to integrate

mechanics-based models with measurement data obtained from real world, to reduce the uncertainties in the model and thus, provide more accurate information about the system properties, behavior, and its parameters. The long-term goal of this research initiative is to use this approach for investigating the soil model parameters that are used to model the inertial soil-structure interaction effects.

Acknowledgements

This study was supported partially by the California Geological Survey through Contract # 106-987. This support is gratefully acknowledged. Any opinions, findings, conclusions or recommendations expressed in this study are those of the authors and do not necessarily reflect the views of the sponsoring agency.

References

[1] ASCE, "Minimum Design Loads for Buildings and Other Structures, ASCE/SEI 7-10," American Society of Civil Engineers, Reston, VA, 2010.

[2] PEER, "Guidelines for Performance-Based Seismic Design of Tall Buildings," Pacific Earthquake Engineering Research Center as part of the Tall Buildings Initiative, University of California, Berkeley, CA, 2010.

[3] NEHRP Consultants Joint Venture, "NIST GCR 12-917-21," National Institute of Standards and Technology, Gaithersburg, MD, 2012.

[4] J. M. Roesset, "A review of soil-structure interaction," in *Soil-structure interaction: The status of current analysis methods and research, Rep. No. NUREG/CR-1780 and UCRL-*, Washington, D.C., U.S. Nuclear Regulatory Commission, 1980.

[5] H. Ebrahimian, R. Astroza and J. P. Conte, "Extended Kalman filter for material parameter estimation in nonlinear structural finite element models using direct differentiation method," *Earthquake Engineering and Structural Dynamics,* vol. 44, no. 10, pp. 1495-1522, 2015.

[6] R. Astroza, H. Ebrahimian and J. P. Conte, "Material Parameter Identification in Distributed Plasticity FE Models of Frame-Type Structures Using Nonlinear Stochastic Filtering," *ASCE Journal of Engineering Mechanics,* vol. 141, no. 5, pp. 04014149 1-17, 2015.

[7] H. Ebrahimian, R. Astroza, J. P. Conte and C. Papadimitriou, "Bayesian optimal estimation for output-only nonlinear system and damage identification of civil structures," *Structural Control and Health Monitoring,* vol. in press, 2017.

[8] A. K. Chopra, Dynamics of Structures: Theory and Applications to Earthquake Engineering, Englewood Cliffs, N.J.: Prentice-Hall, 4th Ed., 2012.

[9] J. L. Beck and L. S. Katafygiotis, "Updating Models and their Uncertainties. Part I: Bayesian Statistical Framework," *ASCE Journal of Engineering Mechanics,* vol. 124, no. 4, pp. 455-461, 1998.

[10] J. L. Beck, "Bayesian System Identification based on Probability Logic," *Structural Control and Health Monitoring,* vol. 17, no. 7, p. 825–847, 2010.

[11] D. Simon, Optimal State Estimation: Kalman, H-Infinity, and Nonlinear Approaches, Hoboken, NJ: John Wiley & Sons, 2006.

[12] S. J. Julier and J. K. Uhlmann, "A new extension of the Kalman filter to nonlinear systems," in *11th International Symposium on Aerospace/Defense Sensing, Simulation and Controls*, Orlando, FL, 1997.

[13] E. A. Wan and R. van der Merwe, "The unscented Kalman filter for nonlinear estimation," in *IEEE 2000 Adaptive Systems for Signal Processing, Communications, and Control Symposium*, Lake Louise, Canada, 2000.

[14] R. Astroza, H. Ebrahimian and J. P. Conte, "Batch and Recursive Bayesian Estimation Methods for Nonlinear Structural System Identification," in *Risk and Reliability Analysis: Theory and Application – In Honor of Prof. Armen Der Kiureghian*, Springer, 2016.

[15] R. Astroza, H. Ebrahimian, Y. Li and J. P. Conte, "Bayesian Nonlinear Structural FE Model and Seismic Input Identification for Damage Assessment of Civil Structures," *Mechanical Systems and Signal Processing,* vol. 93, no. 1, p. 661–687, 2017.

[16] S. F. Ghahari, F. Abazarsa, O. Avci, M. Çelebi and E. Taciroglu, "Blind Identification of the Millikan Library from Earthquake Data Considering Soil–Structure Interaction," *Structural Control and Health Monitoring,* vol. 23, pp. 684-706, 2016.

[17] Computers and Structures, Inc., "SAP2000," [Online]. Available: https://www.csiamerica.com/products/sap2000. [Accessed 09 2017].

[18] OpenSees, "Open System for Earthquake Engineering Simulation," [Online]. Available: http://opensees.berkeley.edu/. [Accessed 08 2017].

[19] X. Lu, L. Xie , H. Guan , Y. Huang and X. Lu, "A Shear Wall Element for Nonlinear Seismic Analysis of Super-tall Buildings using OpenSees," *Finite Elements in Analysis and Design,* vol. 98, pp. 14-25, 2015.

[20] CESMD - A Cooperative Effort, "Center for Engineering Strong Motion Data," [Online]. Available: https://www.strongmotioncenter.org/. [Accessed 09 2017].

[21] H. Ebrahimian, "Nonlinear Finite Element Model Updating for Nonlinear System and Damage Identification of Civil Structures," Ph.D. Dissertation, UC San Diego, La Jolla, CA, 2015.

[22] J. Kuroiwa, "Vibration Tests of a Multistory Building," Ph.D. Dissertation, California Institute of Technology, Pasadena, California, 1967.

[23] P. Jenning and J. Kuroiwa, "Vibration and Soil–Structure Interaction Tests of a Nine-Story Reinforced Concrete Building," *Bulletin of the Seismological Society of America,* vol. 3, no. 891-916, p. 58, 1968.

[24] J. Luco, M. Trifunac and H. Wong, "On the Apparent Change in Dynamic Behavior of a Nine-Story Reinforced Concrete Building," *Bulletin of the Seismological Society of America,* vol. 77, no. 6, p. 1961–1983, 1987.

[25] A. Belleri, M. Torquati, A. Marini and P. Riva, "Horizontal Cladding Panels: In-plane Seismic Performance in Precast Concrete Buildings," *Bulletin of Earthquake Engineering,* vol. 14, no. 4, pp. 1103-1129, 2016.

INVESTIGATION OF THE SPATIAL VARIABILITY OF SEISMIC INPUT MOTIONS FOR CSMIP-INSTRUMENTED BRIDGES DURING THE 2014 SOUTH NAPA EARTHQUAKE—THE CASE OF GOLDEN GATE BRIDGE

S. F. Ghahari[1], H. Ebrahimian[2] and E. Taciroglu[1]

[1.]Department of Civil & Environmental Engineering, University of California, Los Angeles
[2.] Department of Mechanical and Civil Engineering, California Institute of Technology

Abstract

This paper presents interim results from a study on the identification of spatial variability in bridge Foundation Input Motions (FIMs) observed during the 2014 South Napa Earthquake. Bridges are especially prone to the spatial variability of ground motions because they extend over relatively long distances. The primary objective of this project has been to develop a framework to identify FIMs from response signals recorded at instrumented bridges, because, in general, FIMs cannot be measured directly. In this progress paper, we present the development and verification of a framework developed for this purpose and its application to a real-life case study—namely, the Golden Gate Bridge. This bridge was chosen, because initial analysis suggested that its behavior is not significantly affected by inertial soil-structure interaction effects, and thus, the identified FIMs could be—at least partially—validated. Results obtained from both verification (identification using simulated response signals) and validation (identification using real-life data) confirmed the applicability of the developed framework, which will be applied to the other long-span bridges affected by the 2014 South Napa Earthquake in a follow-up study.

Introduction

In order to accurately estimate the response of bridge structures under earthquake ground motions, highly detailed and accurate Finite Element (FE) models are necessary; but they are not sufficient by themselves. While presently available commercial/open-source software packages enable accurate response predictions for bridges, our inability to apply physically accurate/consistent input motions remains a major challenge. This issue is even more challenging for long-span bridges due to the *spatial variability* of input motions [1]. In current practice, California Department of Transportation (Caltrans), for example, takes spatial variability into account by computationally producing ground motions at each pier of the bridge using one-dimensional site-response analyses. That is, the seismic motion estimated on the bedrock is transferred to the surface at each pier using specific soil properties at each pier's site. In the presence of kinematic Soil-Structure Interaction (SSI) effects, these Free-Field Motions (FFMs) must also be converted to the so-called Foundation Input Motions (FIMs) (see **Figure 1**). Therefore, while ground motions at the bedrock of the bridge site may be uniform, a long bridge may still experience differing excitations at different piers. This procedure assumes vertically propagating horizontally polarized waves, which is not necessarily true. The deconvolution procedures used for estimating the bedrock motions from ground surface records also introduce various numerical errors (including unrealistically large motions at the bedrock). Conversion of

FFMs into FIMs is another source of potentially significant error, and at the present time, there is no validated procedure to carry out the said conversion.

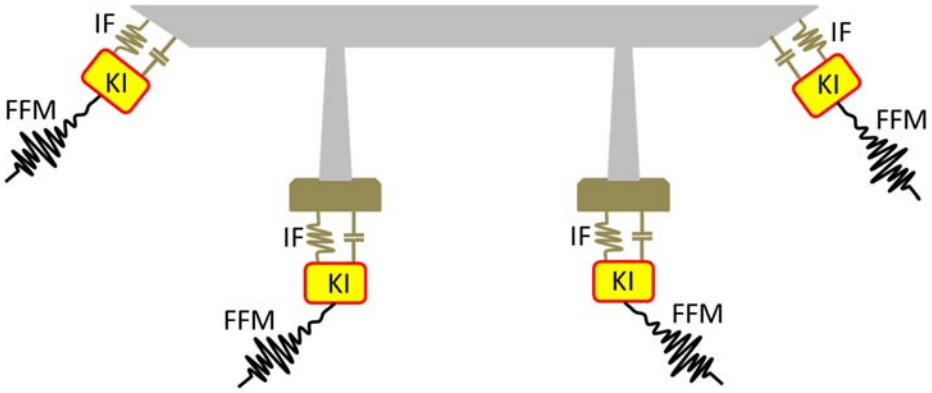

Figure 1. Schematic representation of dynamic analysis of a long bridge.

The back-calculation of FIMs from real-life data is a key capability to study spatial variability effects and to validate (or to refute) new or existing procedures that predict the foundation input motions. In our previous study [2], we showed some evidences of spatial variability in data recorded on the foundation level of bridges during 2014 South Napa earthquake. However, due to possible inertial soil-structure interaction effects, these foundation level measurements may not be representative of FIMs. To resolve this issue, we proposed a framework to recover FIMs from recorded response of bridge structures instrumented through California Strong Motion Instrumentation Program (CSMIP) [3]. In the present paper, we verify and validate the proposed framework through both simulation and real-life data obtained from the Golden-Gate Bridge. There is almost no overlap between this paper and our previous study in SMIP16, so the readers should refer to [2] for more details about the definitions, objective, and overall plan. Also, the methods developed to recover bedrock motion and site effect transfer function from identified FIMs are discussed in [2] which are not discussed here for the sake of space. Details of these methods can be found in [4] and [5].

Data Selection

As mentioned above, this project will use data recorded during the 2014 South Napa earthquake. To be able to select earthquake data sets in systematic way, a Matlab [6] toolbox, called CSMIP-BRIDGE, is developed, which is able to connect to the Center for Engineering Strong Motion Data (CESMD)[1] [7], collects meta data of all bridges instrumented through CSMIP. An overview of this toolbox is shown in **Figure 2**. Current version of this toolbox has a database which can be updated manually by the user. Also, there is search form through which bridges with specific characteristics can be identified. As seen in **Figure 2**, currently there are 81 instrumented bridges in the database. 17 of the 80+ instrumented bridges recorded the South Napa earthquake. In our previous study [2], we described a process through which 7 bridges (CSMIP 68184, 68185, 68322, 68682, 58632, 58700, and 67771) can be subject of the current

[1] www.strongmotioncenter.org

project based on some criteria like level of vibration, sensor distribution, having nearby FFM, etc.

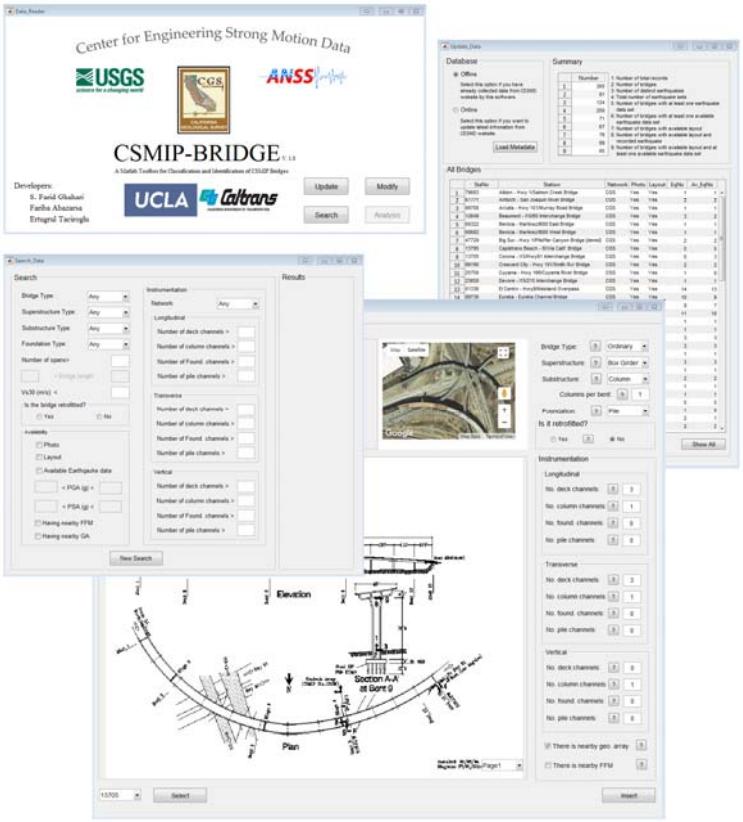

Figure 2. CSMIP-BRIDGE toolbox.

Identification Method

Our objective is to estimate jointly the model parameters and the time history of the foundation input motions (FIMs) using the recorded dynamic response of a bridge structure during an earthquake. For this purpose, we adopted the output-only Extended Kalman Filter (EKF) presented by Huang et al. [8] in our SMIP16 paper [2]. We successfully verified that approach through a simple 39-DOF synthetic example shown in **Figure 3** where 6 parameters of the structure (modules of elasticity of the deck beam, two Rayleigh damping parameters, and three soil-foundation springs) along with three FIMs were unknown. We were able to identify unknown parameters and FIMs with measured response simulated at only five locations as shown in **Figure 4** and **Figure 5**, respectively. However, that method is not suitable for real-life structures that exhibit significant nonlinearities (material and/or geometry). In the present study, we have developed a joint parameter and input estimation approach based on the unscented Kalman filtering method [9]. The estimation approach is briefly described in this section.

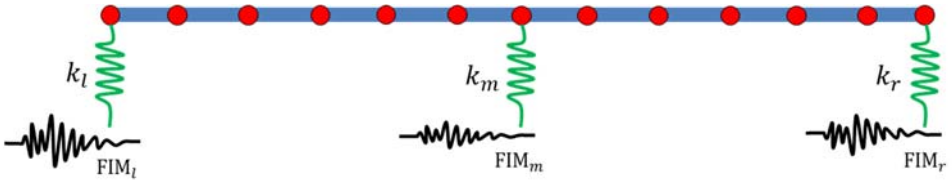

Figure 3. Synthetic bridge model with multiple support excitation.

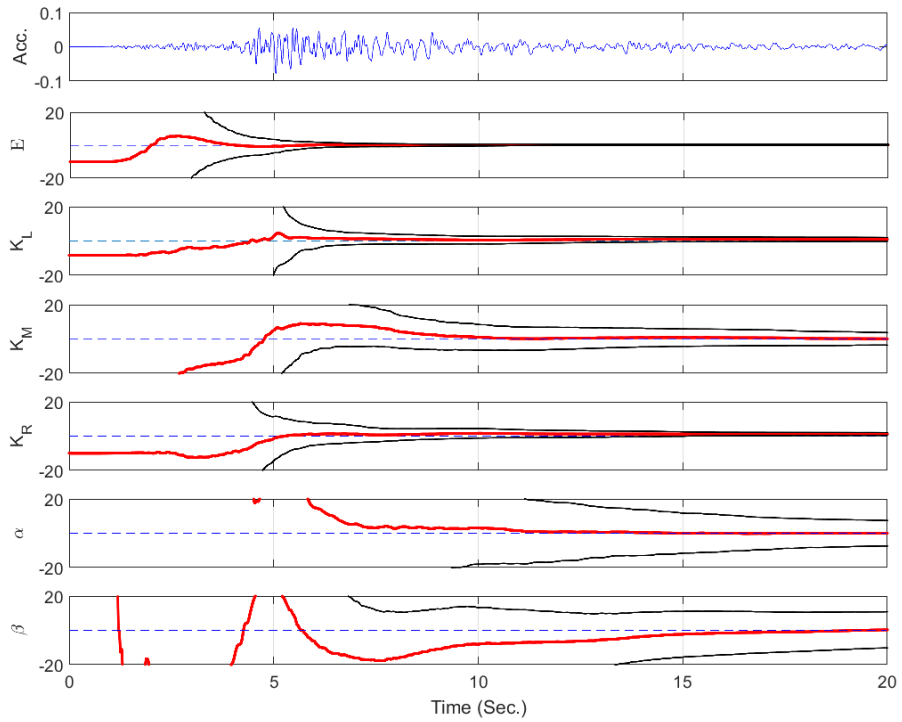

Figure 4. Error convergence rate.

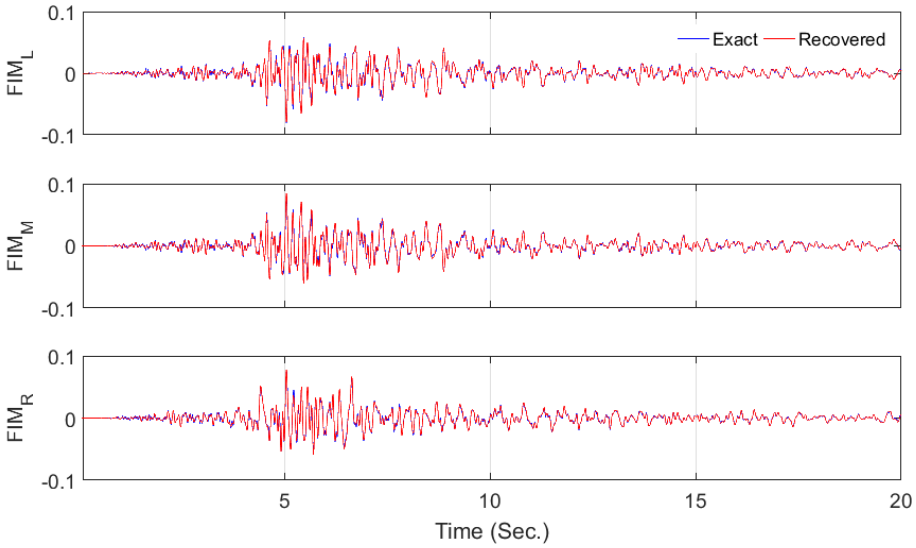

Figure 5. Comparison between exact and identified FIMs.

The response of the Finite Element (FE) model of a bridge structure at each time step to a multi-support earthquake excitation can be expressed as a (nonlinear) function of the model parameter vector, $\boldsymbol{\theta}$, and the time history of the base input motions, $\ddot{\boldsymbol{u}}_{1:i}^{g}$, i.e.,

$$\widehat{\boldsymbol{y}}_i = h_i\left(\boldsymbol{\theta}, \ddot{\boldsymbol{u}}_{1:i}^{g}\right), \tag{1}$$

where $h_i(.)$ is the nonlinear response function of the FE model at time step i, encapsulating all the dynamics of the model from time step 1 to i. The measured response vector of the structure, $\boldsymbol{y}_i$, is related to the FE predicted response, $\widehat{\boldsymbol{y}}_i$, as

$$\boldsymbol{v}_i\left(\boldsymbol{\theta}, \ddot{\boldsymbol{u}}_{1:i}^{g}\right) = \boldsymbol{y}_i - \widehat{\boldsymbol{y}}_i\left(\boldsymbol{\theta}, \ddot{\boldsymbol{u}}_{1:i}^{g}\right), \tag{2}$$

in which $\boldsymbol{v}_i \in \mathrm{R}^{n_y \times 1}$ is the simulation error vector and accounts for the misfit between the measured and FE predicted response of the structure. The simulation error is ideally modeled as a zero-mean Gaussian white noise vector (i.e., $\boldsymbol{v}_i \sim N(\mathbf{0}, \mathbf{R})$) by neglecting the effects of modeling error [10]. The objective of the estimation problem is to find the estimates of the unknown parameter vector, i.e., $\boldsymbol{\psi}_i = \left[\boldsymbol{\theta}^T, \ddot{\boldsymbol{u}}_{1:i}^{g\ T}\right]^T$, for which the discrepancies between the measured and FE predicted responses are minimized in a probabilistic sense. Since the estimation problem is highly nonlinear, a sequential estimation approach is used in this study to improve the estimation efficiency. In this approach, the time domain is divided into successive overlapping time windows, referred to as the estimation windows. The estimation problem is solved at each estimation window to estimate the unknown parameter vector. Assume that the m-th estimation window spans from time step t_1^m to time step t_2^m. Therefore, the unknown parameter vector at this estimation window is defined as $\boldsymbol{\psi}_m = \left[\boldsymbol{\theta}^T, \ddot{\boldsymbol{u}}_{t_1^m:t_2^m}^{g,m\ T}\right]^T$, where $\boldsymbol{\psi}_m \in \mathrm{R}^{(n_{\boldsymbol{\theta}} + t_l \times n_{\ddot{\boldsymbol{u}}^g}) \times 1}$, in which $t_l = t_2^m - t_1^m$ is the estimation window length, and $n_{\ddot{\boldsymbol{u}}^g}$ is the number of unknown components of the base input motions. The unknown parameter vector, $\boldsymbol{\psi}_m$, is estimated using a parameter-only Kalman filtering method. To this end, the unknown parameter vector is modeled as a random vector, the evolution of which is characterized by a Gaussian Markov process – also known as a random walk. Then, a state space model is set up, in which the state equation governs the evolution of the random parameter vector and the measurement equation corresponds to the discrepancies between the measured and FE predicted structural responses [11], i.e.,

$$\boldsymbol{\psi}_{m,k+1} = \boldsymbol{\psi}_{m,k} + \boldsymbol{\gamma}_{m,k}, \tag{3}$$

$$\boldsymbol{y}_{t_1^m:t_2^m} = \widehat{\boldsymbol{y}}_{t_1^m:t_2^m,k+1}\left(\boldsymbol{\psi}_{m,k+1}\right) + \boldsymbol{v}_{t_1^m:t_2^m,k+1}, \tag{4}$$

in which $\boldsymbol{\gamma}_{m,k} \sim N(\mathbf{0}, \mathbf{Q})$, $\boldsymbol{v}_{t_1^m:t_2^m,k+1} \sim N(\mathbf{0}, \widetilde{\mathbf{R}})$, where $\widetilde{\mathbf{R}} \in \mathrm{R}^{(t_l \times n_y) \times (t_l \times n_y)}$ is a block diagonal matrix, whose block diagonals are the simulation error covariance matrix $\mathbf{R}$. In Eqs. (3) and (4), k denotes the iteration number. As can be observed, the estimation process at each estimation window is iterative, i.e., the mean vector and covariance matrix of the unknown parameter vector is iteratively updated based on the discrepancies between the time histories of the measured and estimated responses.

An Unscented Kalman Filtering (UKF) method is used to update the unknown parameter vector at each iteration. In this method, the nonlinear FE model is evaluated separately at a set of

deterministically selected realizations of the unknown parameter vector, which are referred to as the sigma points (SPs) denoted by $\boldsymbol{\vartheta}^j$. The sigma points are selected around the prior mean estimate $\widehat{\boldsymbol{\psi}}^-$. In this study, a scaled Unscented Transformation (UT) based on $2n_{\boldsymbol{\psi}}+1$ sigma points (i.e., $j = 1,2,\ldots,2n_{\boldsymbol{\psi}}+1$) is used, where $n_{\boldsymbol{\psi}}$ denotes the size of the extended parameter vector. The mean and covariance matrix of the FE predicted structural responses, and the cross-covariance matrix of $\boldsymbol{\psi}$ and $\boldsymbol{y}$ are respectively computed using a weighted sampling method as

$$\overline{\boldsymbol{y}} = \sum_{j=1}^{2n_{\boldsymbol{\psi}}+1} W_m^j \, \widehat{\boldsymbol{y}}_i\left(\boldsymbol{\vartheta}^j\right), \tag{5}$$

$$\widehat{\mathbf{P}}_{\boldsymbol{yy}} = \sum_{j=1}^{2n_{\boldsymbol{\psi}}+1} W_e^j \left[\widehat{\boldsymbol{y}}_i\left(\boldsymbol{\vartheta}^j\right) - \overline{\boldsymbol{y}}\right]\left[\widehat{\boldsymbol{y}}_i\left(\boldsymbol{\vartheta}^j\right) - \overline{\boldsymbol{y}}\right]^T + \mathbf{R}, \tag{6}$$

$$\widehat{\mathbf{P}}_{\boldsymbol{\psi y}} = \sum_{j=1}^{2n_{\boldsymbol{\psi}}+1} W_e^j \left[\boldsymbol{\vartheta}^j - \widehat{\boldsymbol{\psi}}^-\right]\left[\widehat{\boldsymbol{y}}_i\left(\boldsymbol{\vartheta}^j\right) - \overline{\boldsymbol{y}}\right]^T, \tag{7}$$

where W_m^j and W_e^j denote weighting coefficients [12]. Now, the UKF prediction-correction procedure can be employed to estimate the posterior parameter mean vector $\widehat{\boldsymbol{\psi}}^+{}_{m,k+1}$ and covariance matrix $\widehat{\mathbf{P}}^+_{\boldsymbol{\psi},m,k+1}$ at each iteration. The identification algorithm is summarized in **Table 1**.

Table 1. Identification algorithm for joint estimation of the model parameters and the FIM time history.

1. Set the estimation window length t_l, and the start and end points of each estimation window.
2. Set the initial mean vector and covariance matrix of the unknown parameter vector as
$$\widehat{\boldsymbol{\psi}}^+{}_0 = \left[\widehat{\boldsymbol{\theta}}_0{}^T, \ddot{\boldsymbol{u}}^{g,0}_{t_1^0:t_2^0}{}^T\right]^T, \text{ and } \mathbf{P}^+_{\boldsymbol{\psi},0} = \begin{bmatrix} \widehat{\mathbf{P}}_{\boldsymbol{\theta\theta},0} & \mathbf{0} \\ \mathbf{0} & \widehat{\mathbf{P}}_{\ddot{\boldsymbol{u}}^{g,0}} \end{bmatrix}.$$
3. Define the process noise covariance matrix $\mathbf{Q}$ and the simulation error covariance matrix $\mathbf{R}$. Set up matrix $\widetilde{\mathbf{R}}$.
4. For the m-th estimation window:
   - 4.1. Retrieve the posterior estimates of the mean vector and covariance matrix of the unknown parameter vector from the last estimation window (i.e., $\widehat{\boldsymbol{\psi}}^+{}_{m-1}$, and $\mathbf{P}^+_{\boldsymbol{\psi},m-1}$). Set up $\widehat{\boldsymbol{\psi}}^+{}_{m,0}$ and $\mathbf{P}^+_{\boldsymbol{\psi},m,0}$ based on $\hat{\boldsymbol{\psi}}^+_{\boldsymbol{m}-1}$ and $\mathbf{P}^+_{\boldsymbol{\psi},m-1}$.
   - 4.2. Iterate (k = 1, 2, …):
     - a. Set $\widehat{\boldsymbol{\psi}}^-{}_{m,\mathrm{k}+1} = \widehat{\boldsymbol{\psi}}^+{}_{m,\mathrm{k}}$, $\mathbf{P}^-_{\boldsymbol{\psi},m,k+1} = \mathbf{P}^+_{\boldsymbol{\psi},m,k} + \mathbf{Q}$.
     - b. Generate sigma points. Run the FE model for $(2n_{\boldsymbol{\psi}}+1)$ sigma points. Derive $\overline{\boldsymbol{y}}$, $\widehat{\mathbf{P}}_{\boldsymbol{yy}}$, and $\widehat{\mathbf{P}}_{\boldsymbol{\psi y}}$ using Eqs. (5)-(7).
     - c. Compute the Kalman gain matrix: $\mathbf{K} = \widehat{\mathbf{P}}_{\boldsymbol{\psi y}}\left(\widehat{\mathbf{P}}_{\boldsymbol{yy}}\right)^{-1}$.
     - d. Find the corrected estimates of the mean vector and covariance matrix of the unknown parameter vector:
       $\widehat{\boldsymbol{\psi}}^+{}_{m,\mathrm{k}+1} = \widehat{\boldsymbol{\psi}}^-{}_{m,\mathrm{k}+1} + \mathbf{K}\left(\boldsymbol{y}_{t_1^m:t_2^m} - \overline{\boldsymbol{y}}\right)$, $\mathbf{P}^+_{\boldsymbol{\psi},m,k+1} = \mathbf{P}^-_{\boldsymbol{\psi},m,k+1} - \mathbf{K}\left(\widehat{\mathbf{P}}_{\boldsymbol{yy}} + \widetilde{\mathbf{R}}\right)\mathbf{K}^T$.
     - e. Check for convergence: if $\left|\widehat{\boldsymbol{\psi}}^+{}_{m,k+1} - \widehat{\boldsymbol{\psi}}^+{}_{m,k}\right| < 0.02 \times \widehat{\boldsymbol{\psi}}^+{}_{m,k-1}$ or $k+1 > 10$, then move to the next estimation window ($m = m + 1$, go to step 4); otherwise, iterate again at the current estimation window ($k = k + 1$, go to step 4.2).

Verification and Validation

To verify and validate output-only identification method, we use both simulated and real-life data obtained from the Golden Gate Bridge (GGB), respectively. GGB is chosen for this pilot study because it was the only bridge with structural drawings available to us at the present time. Also, we expected to have negligible inertial SSI effects due to the flexibility of the bridge, so foundation responses would be representative of FIMs and thus could be used to validate the identified FIMs.

The Structural System

The Golden Gate (**Figure 6**) is a strait that connects he San Francisco Bay to the Pacific Ocean. The GGB is a suspension bridge over Golden Gate, which connects San Francisco to Marin County. GGB was the longest (main span) suspension bridge in the world until 1964. It has been also declared one of the wonders of the modern world by the American Society of Civil Engineers (ASCE).

Figure 6. Golden Gate.

The GGB was completed and opened to traffic on May 28, 1937 [13]. The total length of the GGB from abutment to abutment is 2737 m (8981 ft), with other detailed dimensions of the bridge as shown in **Figure 7**. Summarizing from [14], the structural system is briefly reviewed here (Geometrical and mechanical properties of these elements can be fund, for example, in [15], [16] and not discussed here for brevity). As a suspension bridge, the GGB consists of several structural systems. To have a visual understating, **Figure 8** is presented. The approach viaducts are of steel girder, truss and arch construction. Anchorage blocks (south one is not shown in **Figure 8**), piers, and pylons are of reinforced concrete construction. The towers, deck, and cables (main cable and hangers) are of steel construction. The towers are funded directly on the underlying rock. The deck, which was originally of reinforced concrete and replaced by orthotropic steel plate at the center and reinforced concrete sidewalks in 1980's, is carried on floor beams every 25 ft. These beams are connected to stiffening trusses at both sides. In original construction, stiffening trusses were connected to each other with only a top lateral bracing system. Later, in 1950's, a bottom lateral bracing system was added to make the roadway

supporting system a closed box and consequently reduce deck's torsion/twist. The entire mentioned stiffening system is suspended every 50 ft with hangers on each side, were replaced in 1970's. The main span is fixed laterally and vertically to the towers at its both ends, has a limited amount of free movement in the longitudinal direction, and fully released for rotation at its both ends through joints.

While the GGB has experienced several retrofit stages as mentioned above, prompted by the 1989 Loma Prieta earthquake, the GGB, Highway and Transportation District[2] initiated a series of studies of the bridge which concluded necessity of a massive retrofit including [17]:

- installation of dampers between the stiffening trusses and the towers,
- replacement of one-quarter of the stiffening truss lateral braces with new ductile members,
- stiffening of the bridge towers to prevent undesirable plate buckling,
- strengthening of the bridge piers,
- strengthening of the saddles supporting cables on the tops of the towers,
- strengthening of the wind-locks connecting the suspended structure and the towers,
- and strengthening of the pedestals supporting the orthotropic deck.

The retrofit started in 1997 and was initially planned to be ended in 2012, which was later changed several times (lately to 2021). Retrofit carried out in three phases due to several factors like level of vulnerability, provided fund, and traffic closure. In Phase 1 (1997-2002), the Marin (North) approach viaduct was retrofitted. In Phase 2 (2002-2007), San Francisco (South) approach viaduct, anchorage housing, arch, and pylons were retrofitted. Phase 3 (2008-2021) was conducted in two sub phases A and B. In Phase 3A (2008-2014), North Anchorage housing and pylon were retrofitted. In Phase 3B, main suspension span, main towers, South tower pier and fender is going to be retrofitted. This phase is the most challenging part and mainly due to this reason the completion date of retrofit project has been extended to 2021. Another reason for such extension was to increase the strength of the bridge against factors beyond earthquakes, like terrorism attacks. As a summary, details of the retrofit measures conducted at each phase are shown in **Figure 9**.

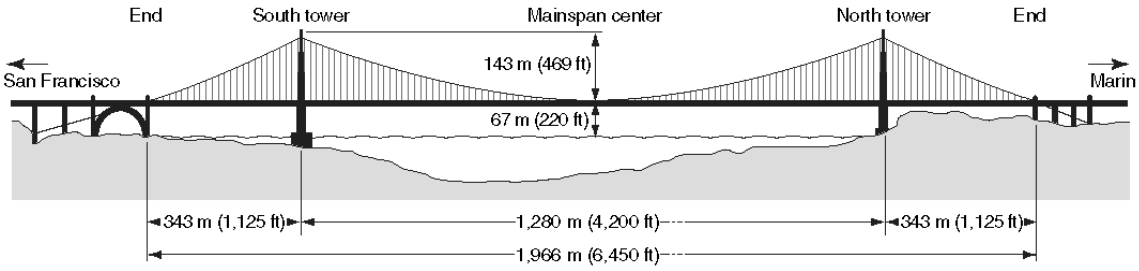

Figure 7. Dimensions of the bridge [18].

[2] This is a special district of the state of California formed in 1928.

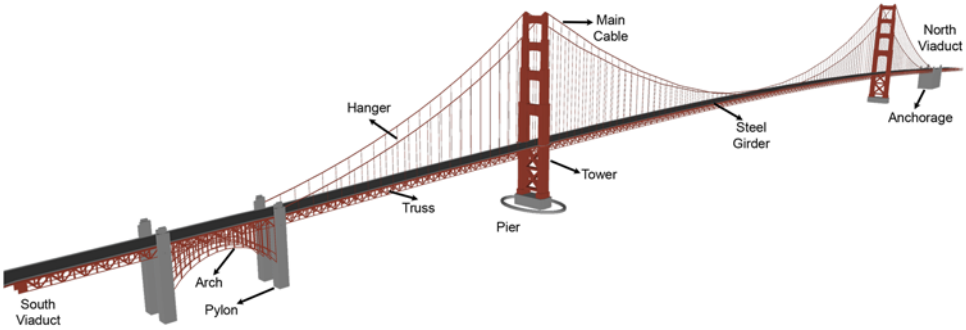

Figure 8. Various parts of the GGB (3D model is taken from Google Earth).

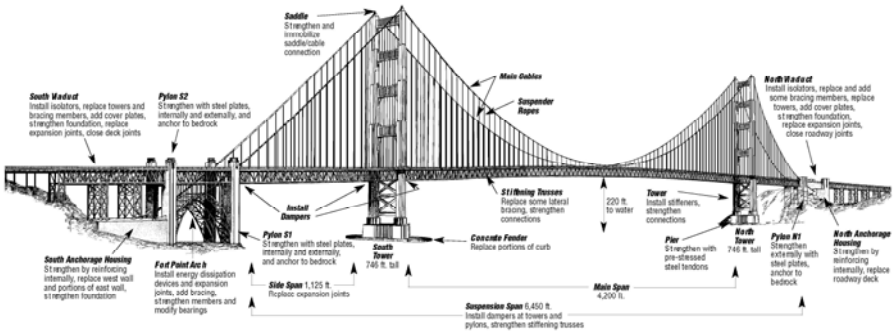

Figure 9. GGB retrofit measures (http://goldengatebridge.org/projects/retrofit.php).

Prior Identification Studies

The oldest study on vibration-based identification of the GGB goes back to 1947 when Nishkian measured vertical movement of the bridge deck during its operation [19]. Later, Vincent carried out similar measurements using more accurate sensors and compared real-life data and model prediction [20], [21]. He used data recorded in a 15 years period by suspended mass accelerometers and identified first asymmetric, first and second symmetric vertical natural frequencies of the deck as 0.095, 0.125, and 0.158 Hz, respectively. He also reported torsional frequency of deck as 0.20 Hz. The rate of studies (not specifically on system identification topic) on this bridge got accelerated in 90's. Tanaka and Davenport [22] re-examined data used by Vincent [20]. They also experimentally tested a taut-strip model in laboratory under wind turbulence and concluded that at low speed wind first asymmetric mode is the dominant one. Abdel-Ghaffar and Scanlan [15], [16] conducted extensive experimental investigations on the bridge to determine natural frequencies, mode shapes, and damping ratios from ambient data. They used spectral peak picking for natural frequency identification, cross-spectrum analysis for mode shape identification, and half-power bandwidth method for damping ratio estimation. They could identify 20 vertical, 18 torsional, 33 lateral, and 20 longitudinal modes of the suspended span in the frequency range of 0 to 1.5 Hz and 20 longitudinal, 15 torsional, and 11 lateral modes of the towers in the frequency range of 0 to 5 Hz.

Pakzad et al. [23] designed and implemented a scalable wireless sensor network and used it for modal identification of GGB from ambient data collected in summer of 2006. They limited their analysis to modes below 5 Hz. As they used wireless sensor network, they could measure vibration using various instrumentation layouts. Through their study, it is clearly understood that

for such large and flexible structure, identification could be subjected to spatial aliasing[3] if the number of measurement nodes is small. Based on their results, first vertical, transverse and torsional modes are at 0.106, 0.228, and 0.230 Hz, respectively, where all these modes are asymmetric [24]. This valuable dataset were later used several times for verification and validation of some identification methods and frameworks. For example, Pakzad et al. [25] verified the performance of the distributed modal identification approach through this dataset. Chang and Pakzad [26] verified their modified Natural Excitation Technique (NExT) using same data. Also in 2014, same data was analyzed by Matarazzo and Pakzad [27] through pseudo mobile sensing data[4] and they used structural identification using expectation maximization (STRIDE) [28] to identify modal properties of the GGB from ambient data. Their results were as accurate as those identified before [24].

In 2012, Çelebi [18] carried out an extensive study on the GGB. He analyzed data recorded during three weak earthquakes (Bolinas 1999, Yountville 2000, and Alum Rock 2007). He employed spectral analysis [29] for output-only and Auto-Regressive with eXogenous input (ARX) [30] for input-output identification purposes. This study is the first one in which modal characteristics are identified from earthquake data. He filtered out frequencies below 0.05 and above 50 Hz. While this study provides us with precious information, it suffers from some definiteness. It is done before 2014 South Napa earthquake. Amplitude spectra are not a reliable method for identification of earthquake data, while input-out ARX technique suffers from the fact that it cannot consider multiple support excitations. Even under uniform excitation assumption, any input-output identification technique gives us modal characteristics between only input and output locations. So, any flexibility provided by boundaries, like soil, is excluded.

Recorded Earthquake Data

Following the 1989 Loma Prieta earthquake, it was recommended to instrument large bridges in the California [31]. The seismic instrumentation was planned in 1992 by the CSMIP and the GGB, Highway and Transportation District in cooperation with an appointed seismic instrumentation advisory board [3]. In 1995 (prior to retrofit), 72 accelerometers (15 on the north viaduct and anchorage housing; 33 on the suspension bridge; 22 on the south viaduct and anchorage housing and Fort Arch; 3 at the south free-field; 3 at a downhole under the south viaduct) and 4 relative displacement sensors were installed [32]. After completion of the Phase 1 of the retrofit, 18 sensors were installed on the north viaduct and anchorage housing and a geotechnical array with 6 sensors was installed near the north viaduct. Finally, 22 more sensors were added after completion of the Phase 2. The current locations[5] of the sensors on the suspension bridge are shown in **Figure 10**.

[3] This is not explicit conclusion of that study, and is concluded by this paper's authors based on the results presented in [23]. Also, the term spatial aliasing is not a common term in signal processing.
[4] Pseudo mobile sensing data is the data without actually implementing mobile sensor network and is extracted directly from a fixed sensor data matrix provide that the paths of the mobile sensors are known.
[5] Last update: 10/31/2016

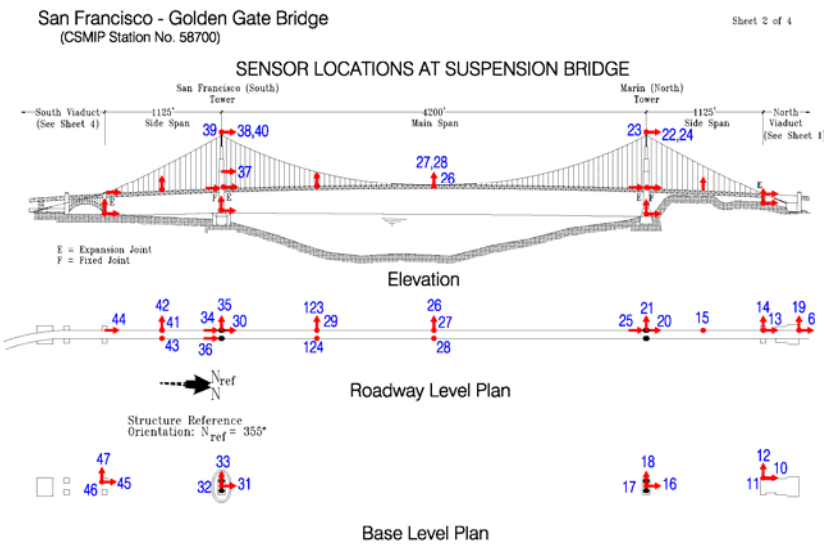

Figure 10. Locations of strong-motion sensors on the suspension span of the Golden Gate Bridge (www.strongmotioncenter.org, last accessed 1/1/2017).

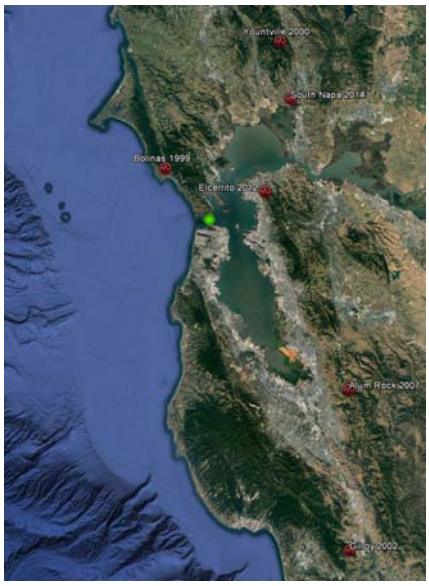

Figure 11. Geographical distribution of earthquake centers around the Golden Gate Bridge.

Several earthquakes have been recorded by the GGB instrumentation system by today (see, **Table 2** and **Figure 11** for these earthquakes' properties and geographical distribution around the GGB); however, a few of them are publicly available through the CESMD. As it will be discussed in the next section, earthquake data up to 2007 are already studied by Çelebi [18]. Herein, we only study the latest earthquake, i.e., 2014 South Napa earthquake. Note that data of Elcerrito earthquake is not available in CESMD. As it can be seen in **Table 2**, Peak Structural Acceleration (PSA) is highest in the South Napa earthquake in comparison with other prior earthquakes.

Table 2. Earthquakes recorded by GGB instrumentation system (Last update: 1/1/2017)

Earthquake	Date/Time UTC	Magnitude	Depth (km)	Epicentral Dist. (km)	PGA (g)	PSA (g)
Bolinas	8-17-1999/1:06	4.5 (Mw)	7.0	20.6	0.020	0.112
Yountville	9-3-2000/8:36	5.0 (Mw)	5.0	62.1	0.009	0.039
Gilroy	5-13-2002/05:00	4.9 (Mw)	7.6	122.5	0.010	0.071
Alum Rock	10-30-2007/03:04	5.4 (Mw)	9.2	75.5	0.012	0.036
Elcerrito	3/5/2012/13:33	4.0 (ML)	9.2	19.6	0.016	0.084
South Napa	8-24-2014/10:30	6.0 (Mw)	11.3	46.7	0.012	0.181

Due to very sparse instrumentation (**Figure 10**) it is crucial to limit frequency band to prevent phenomenon we can call it spatial aliasing. As it was described in the previous section, due to the size and flexibility of the system, there are many modes in the original frequency range of data (0-50 Hz). So, using such sparse instrumentation it would almost impossible to distinguish modes. As an example, first 8 mode shapes of the suspension part which are identified from ambient signals through dense instrumentation by Abdel-Ghaffar [15] are redrawn in **Figure 12**. On this figure, available sensors deployed through CSMIP which could measure bridge response during 2014 South Napa earthquake are shown by red circles. In the

best scenario, we could be only able to identify mode shapes as displayed by red solid lines. As it can be seen from this figure, there is no meaningful difference between first symmetric and fourth asymmetric modes shapes through available sensors, for example. Or, AS3 and S4 mode shapes are very similar to each other. Note that these modes are all lowest modes and the similarity of mode shapes will highly increase for higher modes. As Blind Modal Identification (BMID) method [33]–[36], which will be used later to identify modal properties from output signals, relies heavily on linear independency of mode shapes, we have to eliminate higher modes from our analysis. Therefore, we apply a low-pass filter to only keep a few fundamental modes. As studied by Pakzad and Fenves [24], there are, for example, 15 vertical modes below 1 Hz, so we filter out frequencies higher than this value. Also, due to low frequency errors observed in the signals, frequencies below 0.05 Hz are also filtered out through high-pass filter. Recorded acceleration signals on the suspension part are shown in **Figure 13** in which all records are shown with same scale. Also, first 20 seconds of the signals are not shown, because there is no significant motion. As this figure shows response of the deck in the vertical direction and longitudinal and transverse vibration of the towers have highest level of motion.

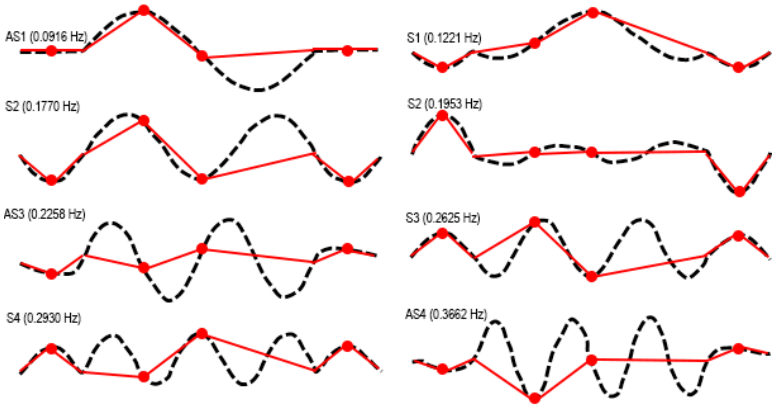

Figure 12. Mode shapes identified from ambient testing [15] (black curves), permanent sensors (red circles), and identifiable mode shapes (red lines).

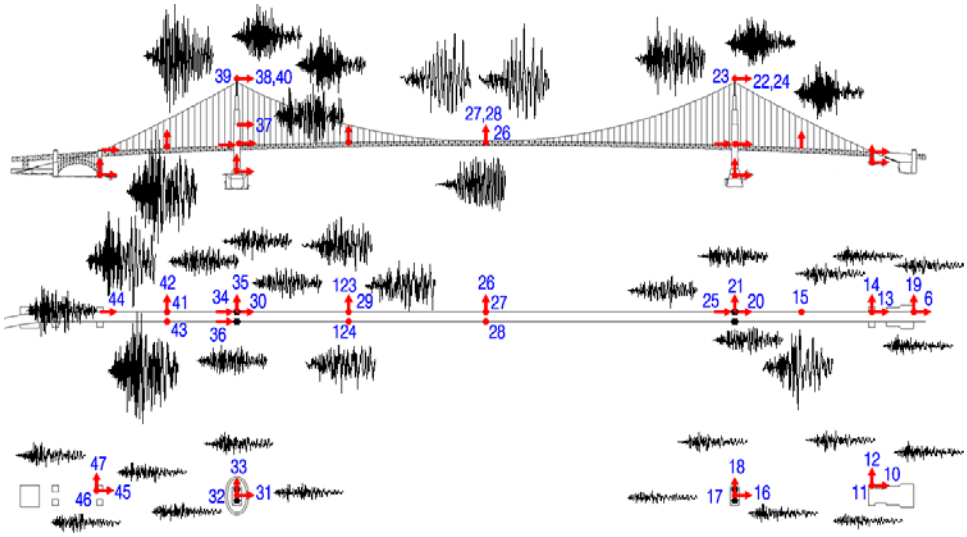

Figure 13. Recorded acceleration signals on the suspension part of the GGB.

To make sure that the frequency range of under study contains most energy content of the signals, maximum displacement responses after filtering are normalized with original values and shown in **Figure 14**. As it can be seen, this ratio is higher than 0.8 for most of the channels. Specifically, for those channels recorded on suspension part (foundation, deck, and tower levels), this value is close to 0.9. Note that those few cases with value less than 0.8 are related to low frequency errors which are removed through high-pass filtering.

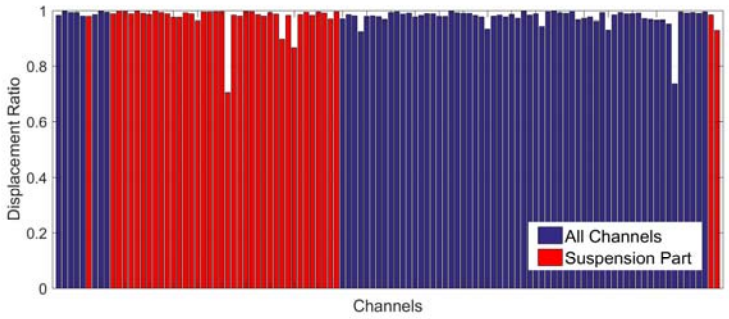

Figure 14. Ratio of after filtering maximum displacement values to the original values.

As will be discussed later, material nonlinearity will not be included in the model. Herein, we carried out a visual observation on observed dominant frequencies to make sure that there is no significant nonlinearity in the system. To do so, we present time-frequency representation [37] of a few signals. As a first example, time-frequency representation of CH27+CH28 (vertical movement of the mid-span) is presented in subplot (b) of **Figure 15**(left). Acceleration time history of the signal is also shown in subplot (a). As it can be seen, a very dominant frequency at 0.3067 Hz with a minor contribution from 0.6733 Hz is observed in this figure. High level of energy of the 0.3067 Hz component may mask contribution of other components. To resolve this issue, time history is scaled by its instantaneous amplitude as described in [38]. This figure is shown in subplot (c) of **Figure 15**(left). Interestingly, two other frequencies appear now. During first ~20 seconds, bridge is vibrating in its fundamental mode ~0.1333 Hz due to ambient excitations. After arriving seismic waves, higher modes at 0.3067, 0.6733, and 0.8867 Hz get excited, while mode at 0.3067 persistently exists by the end of the record.

Figure 15(right) presents same graphs for deck's torsional vibration estimated through CH27-CH28. Again, through time-frequency representation and with help of amplitude scaling, it is possible to observe contribution of different modes at different time instants. At the very beginning, a mode at 0.3333 Hz is dominant, then mode at 0.2333 Hz gets dominated for 20 seconds until the arrival of severe seismic waves. After a short period of time in which a higher frequency of 0.8133 Hz is present, most part of the signal is affected by a mode at 0.5733 Hz.

Frequencies named at two paragraphs above can be labeled according to the prior studies and frequency closeness. These labels are shown in **Table 3** and are deduced from Abdel-Ghaffar's experimental study [15].

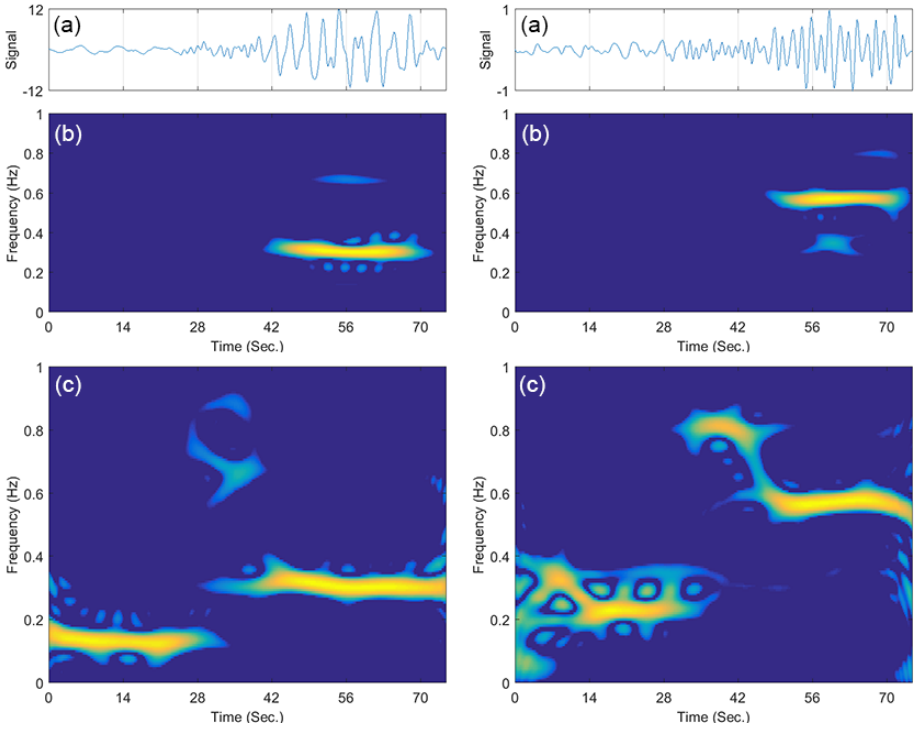

Figure 15. Time and time-frequency representation of CH27+CH28 (left) and CH27-CH28 (right).

Table 3. Labels of the modes observed in **Figure 15** [15].

Frequency (Hz)	0.1333	0.2333	0.3067	0.3333	0.6733	0.5733	0.8133	0.8867
Mode	VS1	TS1	VS4	TS2	VS7	TS4	TS6	VS9

V: Vertical; T: Torsional; S: Symmetric

One of the main objectives of this study is to investigate any spatial variability in bridge's FIMs. This bridge has sensors on its foundation level, so foundation response could be FIMs provided that there is no inertial soil-structure interaction effect. Let's assume that there is no inertial SSI effects and assume foundation response as FIM. In the absence of any spatial variability, input excitation experienced by the ridge at its all piers must be similar with only possible phase delay effect. To check the similarity between two signals, say $s_i[n]$ and $s_j[n]$, sample cross-covariance index is employed here [29], which is calculated as

$$c_{ij}[k] = \frac{1}{N}\sum_{n=0}^{N-k}(s_i[n]-\bar{s}_i)\ \left(s_j[n+k]-\bar{s}_j\right) \quad 8)$$

where $k = 0, 1, \cdots, N-1$, and N is number of time samples. $\bar{s}_i$ and $\bar{s}_j$ indicate the mean of two signals. It is also possible to calculate $c_{ij}[k]$ for negative lags, which are indeed obtained by changing the i and j sub-indices at the summation above. $c_{ij}[k]$ is usually normalized with the square-root of $c_{ii}[0]$ and $c_{jj}[0]$ to keep the value of covariance between -1 and 1. This normalized value is termed the *cross-correlation* in time series analysis. A cross-correlation

equal to −1 or +1 denotes two signals are identical except with a time lag, whereas a cross-correlation close to zero means that that they are not similar.

Figure 16 shows $c_{ij}[k]$ versus tame lags for $i, j =$ CH47, CH33, CH 18, and CH12, which are four transverse channels at four piers. Peak value of the cross-correlation is depicted by using a vertical dashed line and the absolute value of time lag corresponding to these peaks are written on each subplot. Several significant observations are deduced from this figure. First, all peak values are at negative time lags showing that if there is wave propagation, it is from North (Marin) to South (San Francisco) direction. Second, the peak level of correlation is very low between all pairs of channels, showing there is significant incoherency [39]. Third, assuming plane waves with similar incident angle, the average value of the surface apparent wave velocity obtained by dividing horizontal distance between each two channels by these time lags is around 4400 m/s.

Similar figures for Longitudinal and Vertical channels are produced but not shown for the sake of space. For Longitudinal direction, channels 45, 31, 16, and 10, and for the Vertical direction channels 46, 32, 17, and 11 are used. It was observed that similar comments can be made on these directions two. If we calculate the surface apparent wave velocity corresponding to the observed delays, it could be around 6000 and 7000 m/s for longitudinal and vertical directions, respectively. It is noteworthy to mention that estimation of the delay through cross-correlation gives us an average of the group delay if the medium of the wave propagation is dispersive.

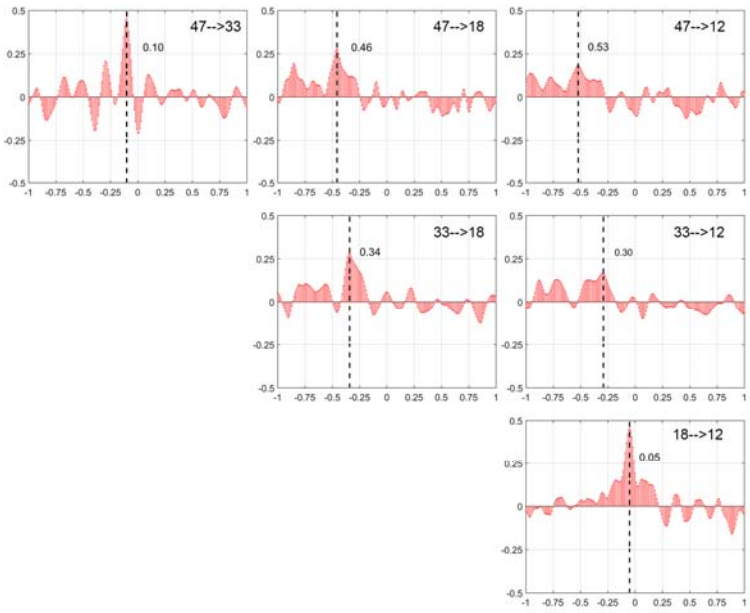

Figure 16. Cross-correlation among acceleration channels on the foundation level in Transverse direction. Horizontal axes are time lags (in seconds) and vertical axes are cross-correlation.

Numerical Modeling

Up to the knowledge of the authors, first numerical study on the GGB was carried out by Baron et al. [40] in 1976. They created linear 2D (with 278 nodes) and 3D (with 120 nodes) models to investigate dynamic behavior of the bridge in longitudinal-vertical and transverse-

torsional directions, respectively. Both models were fixed at the towers' bases. Static, eigenvalue, and time history analyses were carried out in this study. The model was excited under both uniform and multiple support excitations. However, only wave passage effect was considered. Also, a Rayleigh damping matrix with mass and stiffness proportional factors of 0.04805 and 0.0065 were used.

Abdel-Ghaffar [41] was one of pioneering researchers who studied dynamic response of suspension bridges. He employed frequency-domain random vibration approach to analyze GGB under multi-support excitations. Both vertical (induced by vertical and longitudinal excitations) [42], [43] and lateral [44], [45] earthquake-induced response of the GGB under multiple support excitations were studied. 2D linearized Finite Element models developed by Abdel-Ghaffar which were later used in several studies [15], [16] consisted of 283 beam elements with 193 movable nodes, resulting in a system with 1146 degrees of freedom. Axial tension effects of the cables were included by the addition of a geometric stiffness matrix to the elastic stiffness matrix [46]. In the most fundamental symmetric and ten asymmetric vertical, torsional, and transverse modes, there was a very good agreement between numerical and experimental mode shapes and natural frequencies. He also showed that his simpler 2D models work as accurately as 3D model developed by Baron et al. [40].

As mentioned earlier, after 1989 Loma Prieta earthquake, a series of studies for the purpose of seismic evaluation and possible retrofit were initiated. The district engaged T. Y. Lin International (TYLI) to perform these evaluation studies [47], while sub-consultants Imbsen & Associates, Inc. (IAI) and Geospectra, Inc. (GI) were also engaged. The 3D model of the main bridge used in that evaluation had been originally developed for TYLI's Transit Feasibility study [48]. This model was composed of 9933 frame elements connecting 4775 nodes, which was reduced by using a super-element formulation such that the total number of active degrees of freedom was around 4000 [14]. Similar to Abdel-Ghaffar's studies, dynamic loads and responses was regarded as disturbances to the dead-load configuration, so the analysis problem was linearized with response respect to the dead-load state of the structure. Also, geometrical nonlinearity was considered by using geometric stiffness matrices. This global model went under several analyses including linearized time history analysis under multiple-support earthquake excitation. In addition to this global model, several more detailed linear and nonlinear analyses were carried out by local modes, e.g., tower-to-pier connection. Results of these studies were later published in several papers and reports [17], [49]–[54]. In a very recent work, Game et al. [55] created a 3D model of the GGB in Strand7 [56]. While they kindly shared their model with us, the model was not accurate in geometry and details.

In the present study, a new 3D model is created. To create such model with highest accuracy in geometry, the geometry was taken from Google Earth which was already shown in **Figure 8**. This model was taken to the ABAQUS [57] to convert faces and lines to a 3D model with solid elements. This model is shown in **Figure 17**(a). A model with solid elements is computationally very expensive and cannot be used in output-only identification framework described in the previous section. Hence, solid elements were replaced with structural elements in SAP2000 [58], which is shown in **Figure 17**(c). To create this model, publicly available details [13] on this bridge, sample of which is shown in **Figure 17**(b), were taken into account along with all quantitative and qualitative description found in other researcher's studies reviewed in prior sections. Finally, to take advantage of parallel processing, this SAP2000 model was transformed to OpenSEES [59] using a Matlab [6] interface developed by the authors, which

uses SAP Application Programming Interface (API) to communicate to SAP2000. This Matlab code enables us to repeat the process for any other structure. The final OpenSEES model is

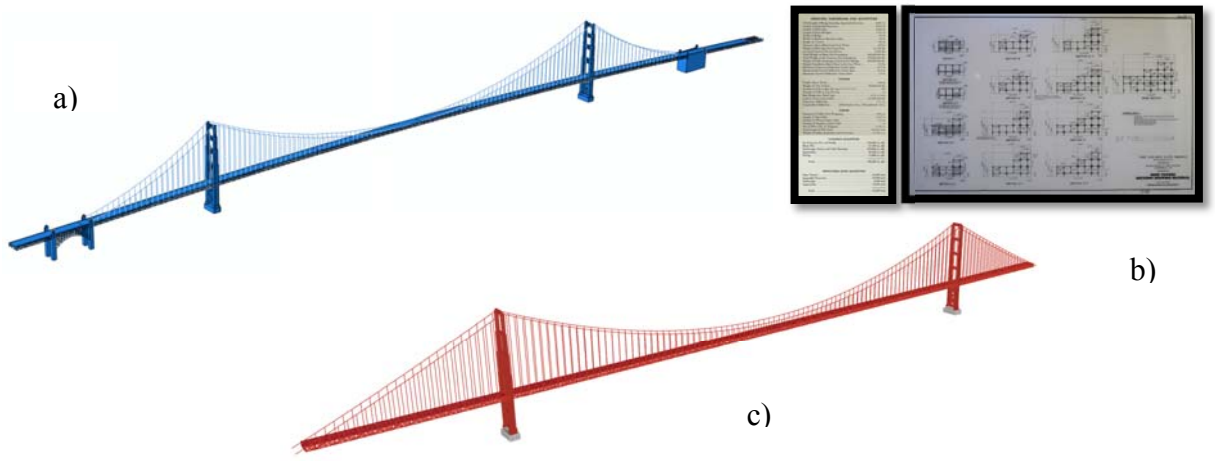

shown in **Figure 18**.

Figure 17. (a) Abaqus model, (b) samples of available structural details, and (c) SAP2000 model.

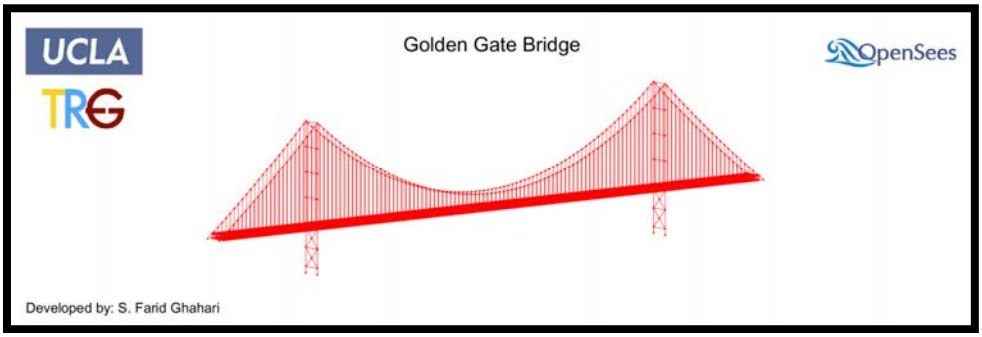

Figure 18. OpenSEES model of the GGB.

The OpenSEES model is composed of more than 20000 Degrees-Of-Freedom (DOFs) with more than 8000 frame elements and 2000 area elements. In the original SAP2000 model, cables and hangers were modeled as cable elements and main cables' geometry was determined iteratively such that after imposing dead load they have internal stress and maximum sag as reported by Abdel-Ghaffar [15]. In the OpenSEES, cables and hangers are modeled using Co-rotational truss element with material which can accept initial stress. While there is no material nonlinearity (except zero compression in cables and hangers) in the model, geometrical nonlinearity was considered, because it is crucial for suspension bridges.

Identifiability

The first step in any identification is to figure out possible sources of uncertainties and identifiability of these uncertainties. As we did not have access to the actual details of the GGB and also this bridge experiences several retrofit stages during its life as reviewed in prior sections, almost all material properties are uncertain. In addition, all connections (like spans'

connections to the towers) and boundaries (like soil-abutment and soil-foundation systems) are modeled by appropriate linear springs with expected values which must be updated through identification process. Also, parameters of Rayleigh damping (the best possible strategy for damping modeling right now) are considered as other potential updating parameters.

In total, there are 66 parameters which are potential candidates for the updating along with FIMs. However, it is not needed/possible to consider all of these parameters in the identification process. Through two sifting steps, the number of updating parameters is much reduced as follows. In the first step, it was identified which parameters have indeed value and which are free or fixed. For example, according to the structural drawings and prior studies, towers do not have relative translation with respect to the main and side spans, so we fixed these connections and excluded them from identification process. Assuming non-fixed connections makes the modal properties of the model deviate from what reported in previous studies. While it is expected not to have significant inertial SSI effects (based on this fact we choose GGB to be able to validate FIMs, indeed), we considered translational and rotational springs of soil-foundation systems as unknowns. However, values of these springs' stiffnesses must be very low to make these springs effective, which are not physically meaningful with respect to the GGB's properties. So, we fixed them too. We also excluded initial tension in cables and hangers, because they have been already considered by applying gravity loads. Based on these facts, 28 parameters out of initial 66 parameters can be potential updating parameters, which are listed in **Table 4**. However, all of these parameters might not be identifiable through available instrumentation layout. To specify identifiability of these parameters, which is second sifting step, we carried out sensitivity analysis to calculate total information for each parameter θ_i as [60]

$$\mathrm{I}_i = \sum_{j=1}^{m} \left(\frac{\partial y_j}{\partial \theta_i}\right)^2 \quad \text{for} \quad i = 1 \dots 28 \tag{9}$$

where $\partial y_j / \partial \theta_i$ is the sensitivity of response at j-th channel with respect to the θ_i and m is the number of all recorded channels. We perturbed θ_i around its nominal value and used Finite Difference to calculate $\partial y_j / \partial \theta_i$. **Figure 19**(a) shows information entropy for all these 28 parameters. Assuming a threshold of 1, for example, 7 parameters are the most informative parameters. This figure shows that from this model and instrumentation layout, it is not possible to infer any reliable information about abutment's springs, mainly because it is a very flexible bridge.

Even, not all of 7 parameters can be uniquely identified. By looking at mutual information among parameters shown in **Figure 19**(b), it is seen that some parameters are highly correlated with each other. For example, Modulus of elasticity of Chords is correlated with modulus of elasticity of diagonal Bars. So, we fix one (diagonal Bar's) of them and consider the other one as updating parameter (Chord's). Also, because Hanger's and deck's modules of elasticity are also highly correlated with diagonal bar's modules of elasticity, we also fix them.

Finally, we have 4 important parameters (Tower's, Cable's, Chord's, and Bottom Bracing's modules of elasticity) which are identifiable through the present instrumentation layout. While damping parameters are not very informative in comparison with respect to others, we consider them too, because they do not have any correlation with others. So, we carry out the identification with 6 unknown parameters along with 6 time-series of FIMs (3 components at

each pier). We assume same FIMs in south and north abutments as south and north piers, respectively.

Table 4. Candidate parameters after first sifting step.

No.	Element	Parameter
1	Bottom Bracing	Elastic Modules
2	Cable	Elastic Modules
3	Chord	Elastic Modules
4	Deck	Elastic Modules
5	Diagonal Bar	Elastic Modules
6	Floor Beam	Elastic Modules
7	Hanger	Elastic Modules
8	Kneebrace	Elastic Modules
9	Top Bracing	Elastic Modules
10	Tower	Elastic Modules
11	Track Girder	Elastic Modules
12	Transverse Strut	Elastic Modules
13	Vertical Rod	Elastic Modules
14	Vertical Bar	Elastic Modules
15	South Tower-South Side Span	Spring Stiffness, M2
16	North Tower-North Side Span	Spring Stiffness, M2
17	South Abutment	Spring Stiffness, P
18	South Abutment	Spring Stiffness, V2
19	South Abutment	Spring Stiffness, V3
20	South Abutment	Spring Stiffness, T
21	South Abutment	Spring Stiffness, M2
22	North Abutment	Spring Stiffness, P
23	North Abutment	Spring Stiffness, V2
24	North Abutment	Spring Stiffness, V3
25	North Abutment	Spring Stiffness, T
26	North Abutment	Spring Stiffness, M2
27	Damping	Alpha
28	Damping	beta

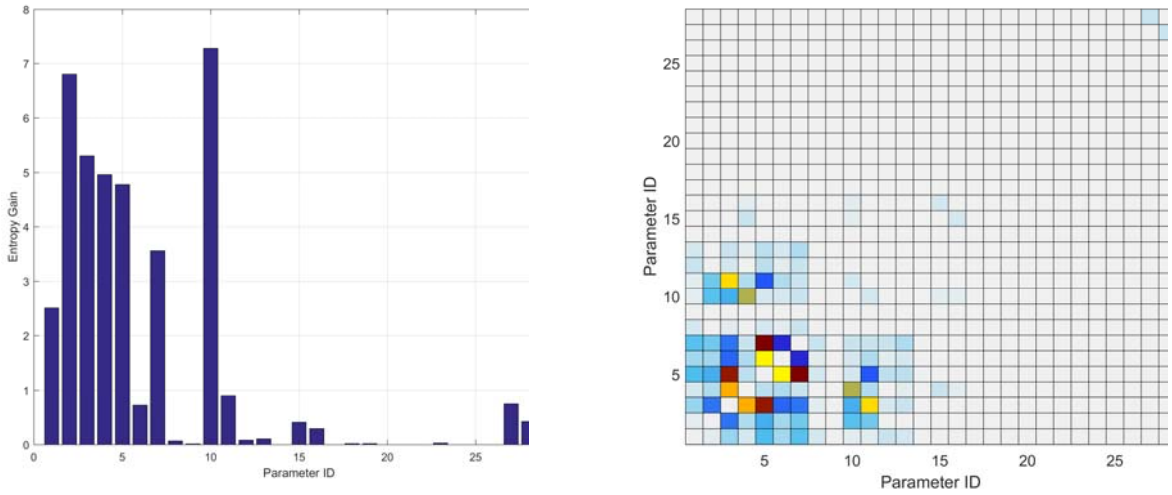

(a) Information entropy (b) Mutual information

Figure 19. Identifiability analysis. (a) information entropy for each parameter, (b) mutual information among parameters, and (left) list of parameters.

Identification Results

Verification: Simulation Data

Before applying the proposed identification method on the real-life data, it is crucial to verify it through simulated data. The proposed method is able to work for a wide range of applications from linear to nonlinear or input-output to output-only cases. As an initial test, we used it for input-output identification. Such input-output identification is quite useful in real world, because one way to consider soil-structure interaction effects is to modify input motions to include feedback inertia effect. In other words, it is possible to exclude compliance beyond a location by imposing prescribed motion at that location. For example, Shirkhande and Gupta [61] followed same approach to estimate response of the GGB using a fixed-base model. In addition, even complexity of the output-only identification could decrease if an input-output identification using foundation-level measurement carried out first to estimate superstructure's parameters while soil-foundation parameters. Of course this approach is only applicable if there is measurement on the foundation level.

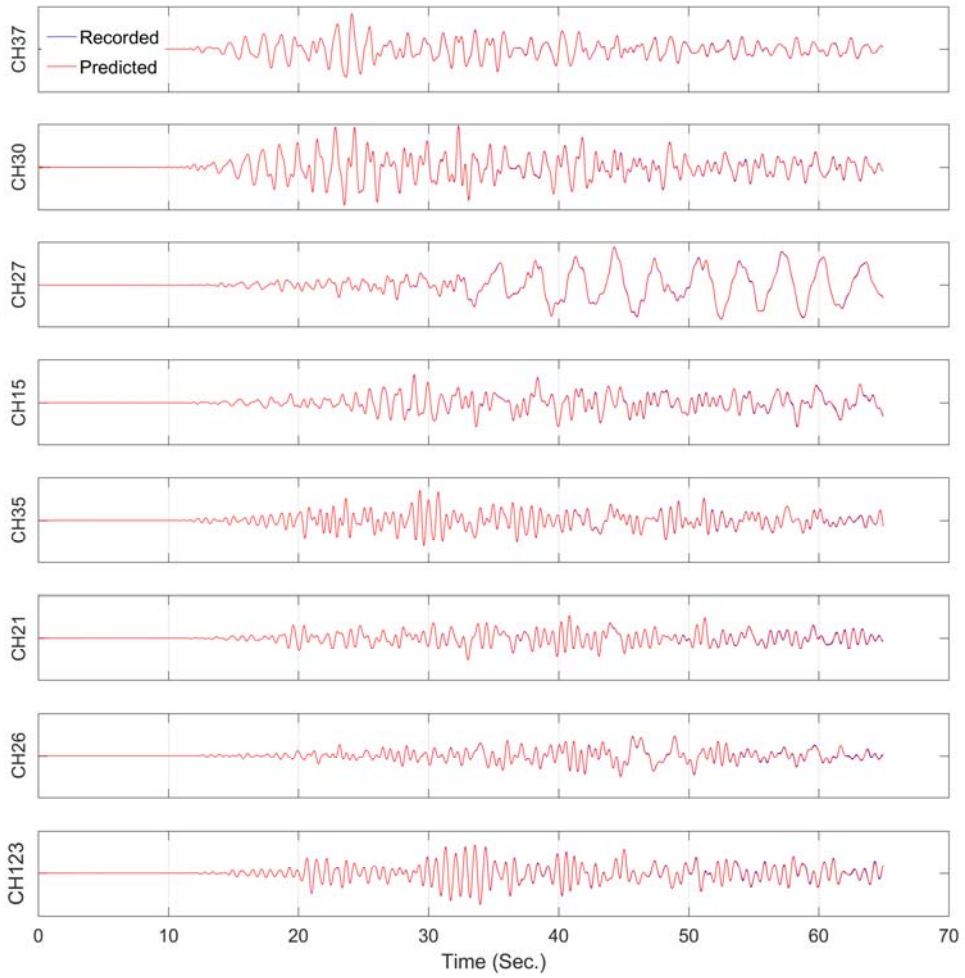

Figure 20. Comparison between recorded (simulated) and predicted acceleration responses at select channels.

We applied this input-output identification on the simulated data of the GGB. **Figure 20** shows comparison between recorded (synthetically simulated) and predicted (at the last iteration of the last updating step) responses at some selected channels. As seen, prediction is perfect. While we assumed 50% initial error in all 6 parameters, final results show 0.03%, 0.04%, 0.23%, 1.59%, 2.38%, and 13.76% error at the end of updating process. As expected, damping parameters are not identified as accurate as others in which stiffness proportional factor is more erroneous, which is in agreement with **Figure 19**(a).

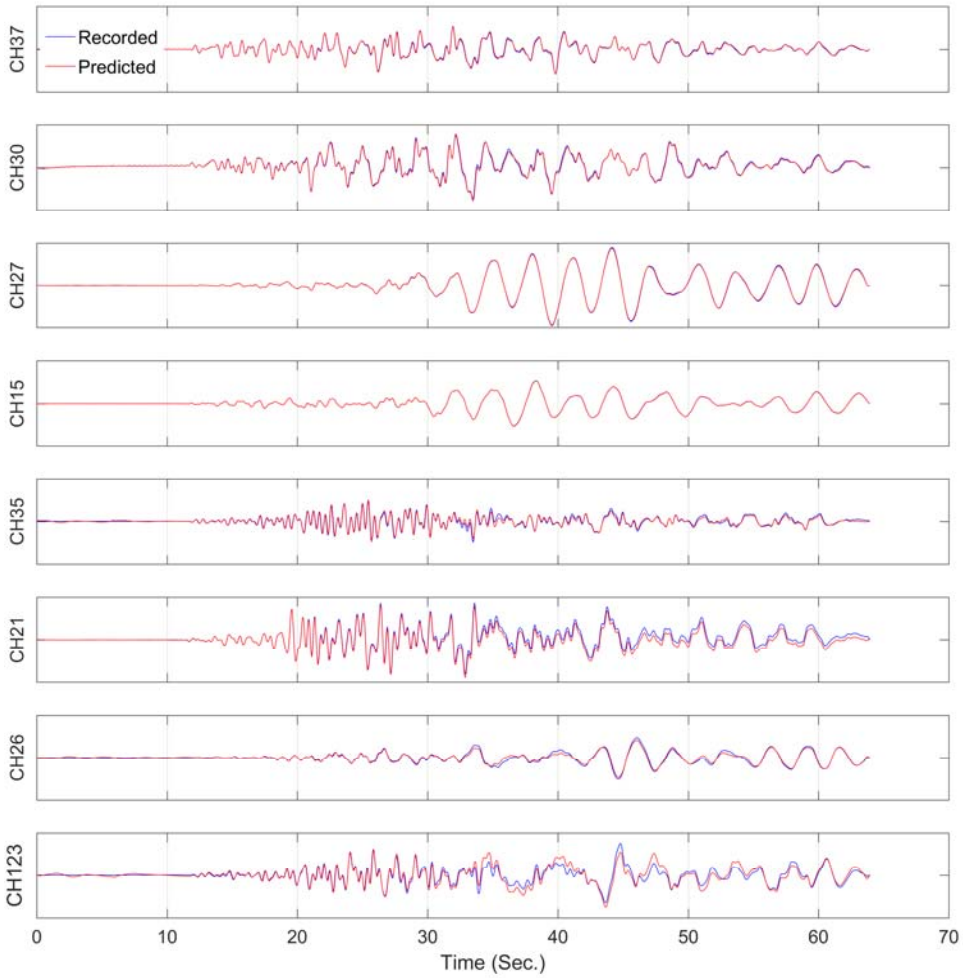

Figure 21. Comparison between recorded (simulated) and predicted acceleration responses at select channels.

While it is possible to use information obtained in the input-output identification step to reduce parameters uncertainty in the output-only identification, we do not use it, because response of the foundations/abutment might not be recorded at all piers in real-life. Therefore, we carry out output-only identification while all 6 parameters along with FIMs are unknown. Assuming an initial error of 20% we obtained 4.28%,0.25%, 0.56%, 23.94%, 6.78%, and 3.25% for Towers', Cables', Chord's, Braces' modules of elasticity, and mass and stiffness proportional damping coefficients, respectively. While all results are acceptable and expected, identification algorithm was not successful to find modules of elasticity of bottom bracing. Comparison between recorded and predicted responses at some selected channels is shown in **Figure 21**[6]. As seen, while one of parameters is not identified accurately, predicted responses are very close to the recorded ones.

Finally, the most important identification results are FIMs. The identified FIM in the transverse direction on the South pier is shown in **Figure 22** along with its exact counterpart. As this figure shows, the input motion is identified with a very good accuracy especially in time

[6] We used different damping values in output-only simulation, so response signals are not identical to Figure 20.

windows with high levels of excitation. The other FIMs are also identified with the same level of accuracy, which are not shown here for brevity.

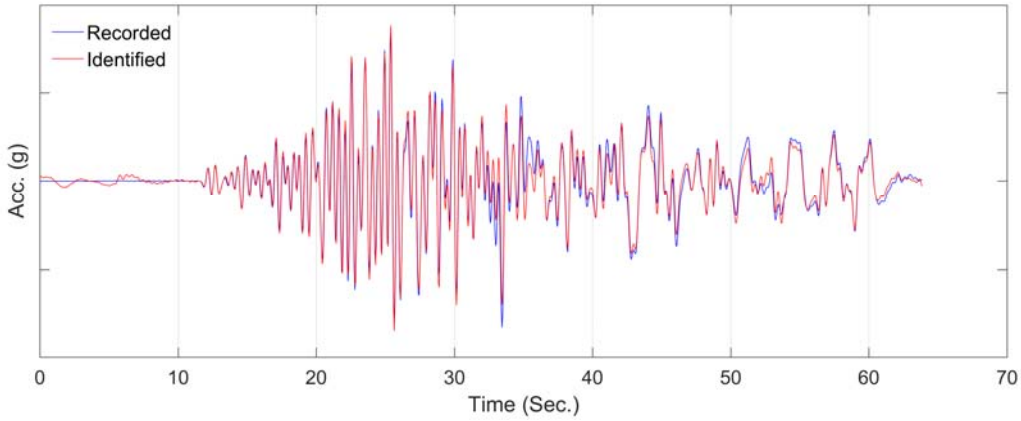

Figure 22. Comparison between exact and identified FIM in transverse direction on the South pier.

Validation: Real-Life Data

Herein, we replace simulated signals with their real-life recorded counterparts and carry out input-output and output-only identification as carried out in the previous section. **Figure 23** compares recorded and predicted acceleration responses at some selected channels in the input-output identification. As expected, results are not as good as synthetic data. However, the level of accuracy varies among channels. Predicted responses at channels 37, 30, 35, and 21 are very close to the real-life data. All these channels are on the towers or very close to the towers. Response prediction at the Channel 15 is acceptable, although there are some high frequency components which are not captured in the prediction. The major discrepancies are observed at channels 26, 27, and 123. All these channels are on the main span. Several reasons could be possible source of such inconsistencies. First off, we did not have access to all details of the bridge, so there could be some modeling uncertainties in addition to parameter uncertainties. Secondly, responses at these channels are highly affected by the other co-existing excitations like due to wind and moving vehicles, which are not considered here. Finally, we modeled damping through the Rayleigh method, which might not be able to accurately model damping for all modes. This could be significant for the main-span channels, because many modes are contributing to these signals, while channels on the tower mostly contain only a few fundamental modes of the system.

While we considered wide boundaries for the updating parameters, all modules of elasticities are identified around $2 \times 10^{11}\ N/m^2$ except those of the bottom bracings, which are around $2.5 \times 10^{11}\ N/m^2$. This indicates that perhaps the dimensions of bottom bracing elements were underestimated in the model. Identified Rayleigh damping parameters are both around 0.1.

Predicted responses and one of identified FIMs obtained in output-only identification are shown in **Figure 24** and **Figure 25**, respectively. As seen, the similarity level between recorded and predicted responses is close to what we observed for the input-output case (**Figure 23**) while here FIMs are also identified. One of the identified FIMs is shown in **Figure 25**. Assuming that what is recorded on the foundation is true FIM (inertial SSI is negligible), these two signals are

quite similar, but the amplitude of the identified FIM is higher than the recorded foundation response. The authors believe that this is because level of input excitation is compromised with overall damping of the system. This issue could be addressed in future by introducing damping more specifically, especially when system is going under nonlinear behavior. In other words, by parametrizing sources of damping, e.g., backbone curves of plastic hinges, relationship there would be no linear relationship between input, damping, and response, so both input and damping could be identified more accurately.

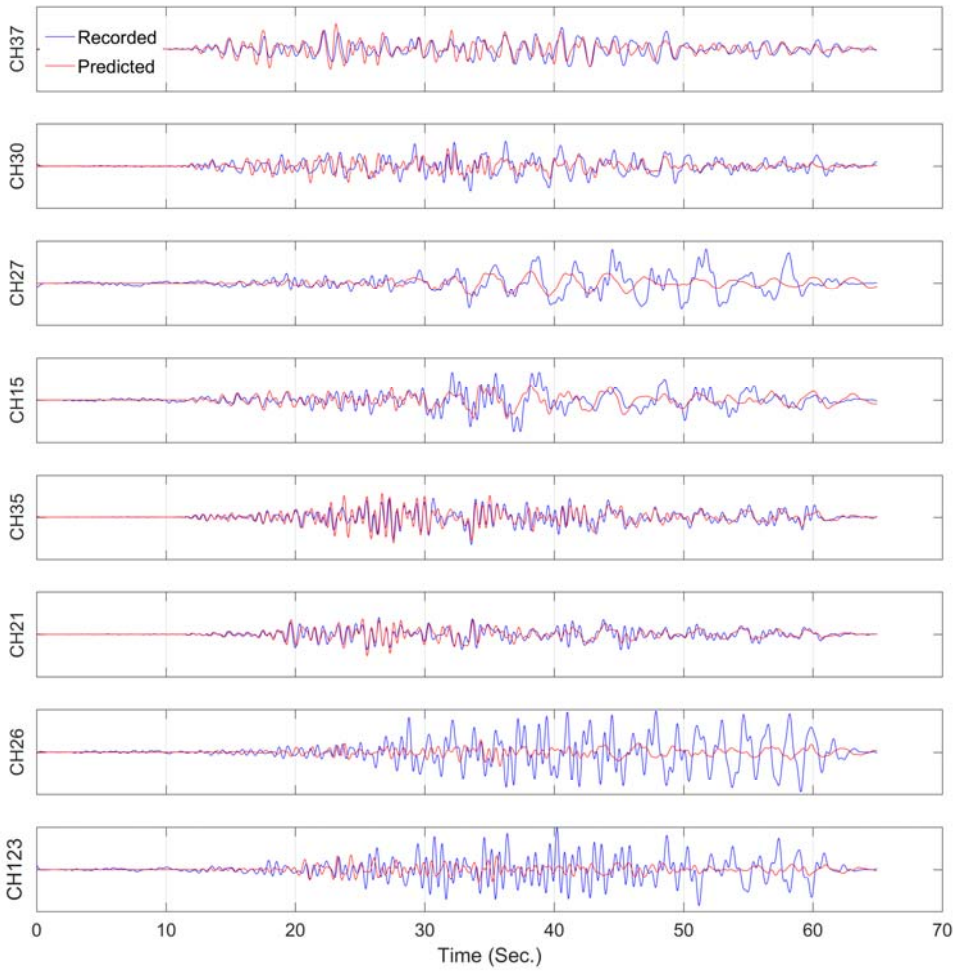

Figure 23. Comparison between recorded and predicted acceleration responses at select channels.

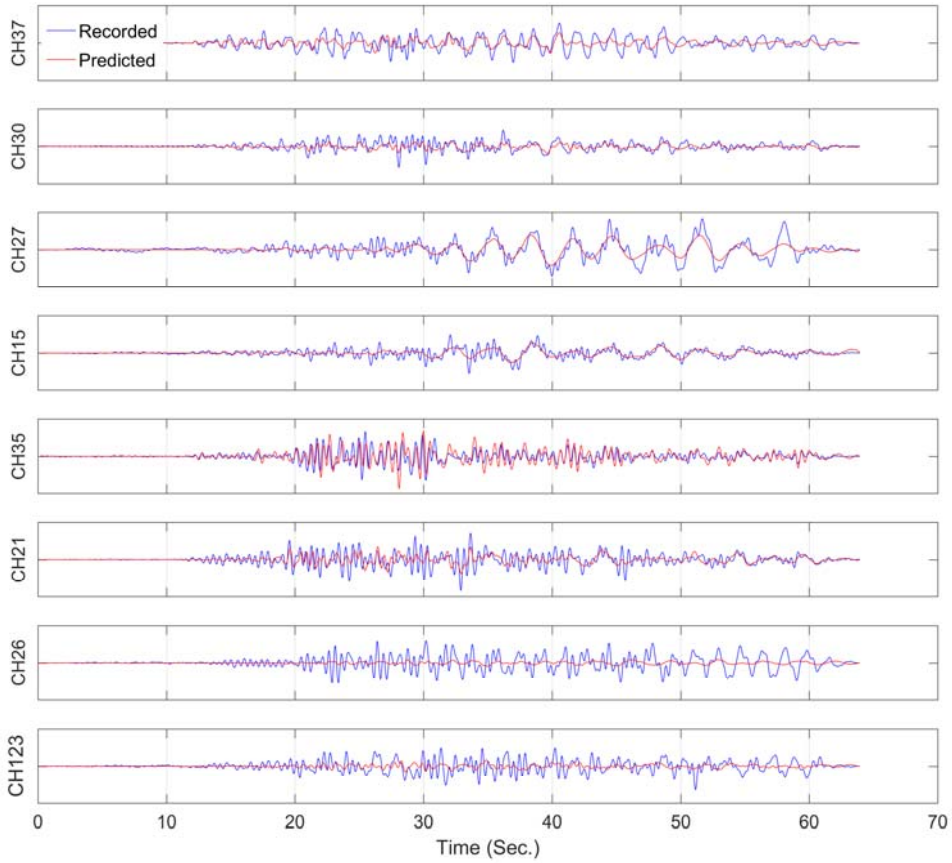

Figure 24. Comparison between recorded and predicted acceleration responses at select channels.

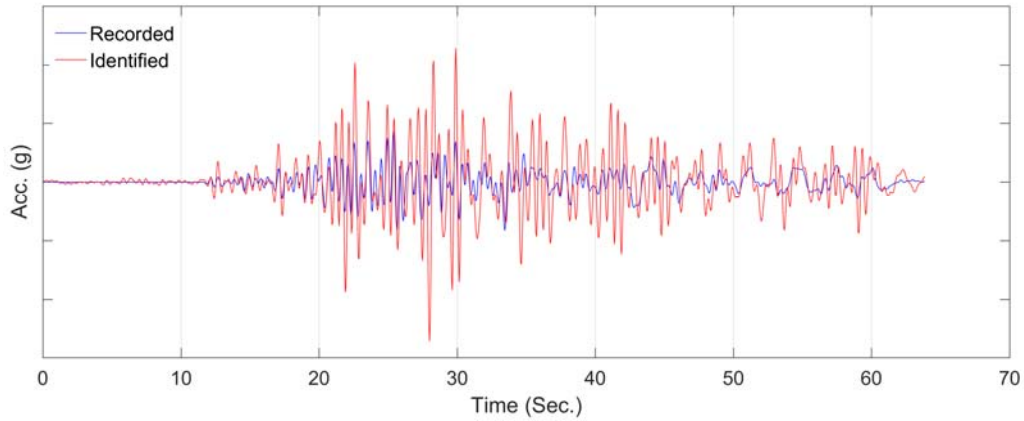

Figure 25. Comparison between recorded foundation response and identified FIM in transverse direction on the South pier.

Conclusions

This study presented a verification and validation study whose objective is to quantify the spatial variability in bridge Foundation Input Motions (FIMs) using data recorded during the 2014 South Napa Earthquake. This aspect comprised the development and verification of two distinct (and new) methods. The first of these was an output-only system identification method that yields time-history estimates of FIMs at all bridge piers from accelerations recorded on the bridge. The second was a blind channel identification method that enables the identification of local site effects at each pier provided that all FIMs are caused by a single excitation source and the kinematic interaction is similar at all piers. The second method was presented in our first phase of study at SMIP16. The applicability of the second method—i.e., the output-only identification method—was tested in the present paper through an extensive study on both simulated and real-life data from the Golden Gate Bridge. The results of this study showed that the proposed framework is able to recover FIMs from sparsely measured responses of a complex bridge. To the best of our knowledge, this is the only study in which multiple FIMs are identified with real-life recordings from a bridge structure.

Acknowledgement

The authors would like to acknowledge Dr. Celebi from USGS, and Prof. Asimaki from Caltech for their valuable comments and help. Also, Dr. D'Auria from UCLA Institute for Digital Research and Education helped us to carry out analyses on UCLA Hoffman cluster, which is appreciated. The work presented in this manuscript was funded, in part, by the California Geological Survey (Contract No. 1014-963) and by the California Department of Transportation (Grant No. 65A0450). Any opinions, findings, conclusions or recommendations expressed in this material are those of the authors and do not necessarily reflect the views of the sponsoring agencies.

References

[1] A. Zerva and V. Zervas, "Spatial variation of seismic ground motions: An overview," *Appl. Mech. Rev.*, vol. 55, no. 3, p. 271, 2002.

[2] E. Taciroglu and S. F. Ghahari, "Identification of spatial variability in bridge foundation input motions: Theoretical basis," in *Proceedings of SMIP16 Seminar on Utilization of Strong-Motion Data*, 2016.

[3] A. F. Shakal, C. D. Petersen, A. B. Cramlet, and R. B. Darragh, "CSMIP near-real-time strong motion monitoring system: Rapid data recovery and processing for event response," in *Proceedings SMIP95 Seminar on Seismological and Engineering Implications of Recent Strong-Motion Data, Huang, MJ, Ed*, 1995.

[4] S. F. Ghahari, F. Abazarsa, C. Jeong, A. Kurtulus, and E. Taciroglu, "Blind identification of site effects and bedrock motions from surface response signals," *Soil Dyn. Earthq. Eng.*, 2017 (under review).

[5] E. Ghahari, S.F., Abazarsa, F., Taciroglu, "Probabilistic Blind Identification of Site Effects from Ground Surface Signals," *Bull. Earthq. Eng.*, 2017 (under review).

[6] MATLAB, Online manual—*Components*, vol. 3, no. 7, p. 750, 2004.

[7] CESMD, "Center for Engineering Strong Motion Data," 2017. [Online]. Available: http://strongmotioncenter.org/. [Accessed: 01-Jan-2017].

[8] H. Huang, J. N. Yang, and L. Zhou, "Adaptive quadratic sum-squares error with unknown inputs for damage identification of structures," *Struct. Control Heal. Monit.*, vol. 17, no. 4, pp. 404–426, 2010.

[9] R. Astroza, H. Ebrahimian, Y. Li, and J. P. Conte, "Bayesian nonlinear structural FE model and seismic input identification for damage assessment of civil structures," *Mech. Syst. Signal Process.*, vol. 93, pp. 661–687, 2017.

[10] H. Ebrahimian, R. Astroza, J. P. Conte, and R. A. de Callafon, "Nonlinear finite element model updating for damage identification of civil structures using batch Bayesian estimation," *Mech. Syst. Signal Process.*, pp. 1–29, 2016.

[11] S. Haykin, *Kalman Filtering and Neural Networks*, vol. 5, no. 3. 2001.

[12] S. J. Julier, "New extension of the Kalman filter to nonlinear systems," in *Proceedings of SPIE*, 1997, pp. 182–193.

[13] J. B. Strauss and C. E. Paine, *The Golden Gate bridge: report of the chief engineer to the Board of directors of the Golden Gate Bridge and Highway District, California, September, 1937*. Golden Gate Bridge, Highway and Transportation District, 1938.

[14] M. A. Ketchum and C. Seim, *Golden Gate bridge seismic evaluation*. TY Lin International, 1990.

[15] A. M. Abdel-Ghaffar and R. H. Scanlan, "Ambient vibration studies of golden gate bridge: I. Suspended structure," *J. Eng. Mech.*, vol. 111, no. 4, pp. 463–482, 1985.

[16] A. M. Aabdel-Ghaffar and R. H. Scanlan, "Ambient Vibration Studies of Golden Gate Bridge: II. Pier-Tower Structure," *J. Eng. Mech.*, vol. 101, no. 4, pp. 483–499, 1985.

[17] T. J. Ingham, S. Rodriguez, M. N. Nader, F. Taucer, and C. Seim, "Seismic retrofit of the golden gate bridge," in *Proc., National Seismic Conf. on Bridges and Highways: Progress in Research and Practice*, 1995.

[18] M. Çelebi, "Golden Gate Bridge response: A study with low-amplitude data from three earthquakes," *Earthq. Spectra*, vol. 28, no. 2, pp. 487–510, 2012.

[19] L. H. Nishkian, "Vertical vibration recorders for the Golden Gate Bridge," *Bull. Seismol. Soc. Am.*, vol. 37, no. 2, pp. 81–88, 1947.

[20] G. S. Vincent, "Golden Gate bridge vibration studies," *Trans. Am. Soc. Civ. Eng.*, vol. 127, no. 2, pp. 667–701, 1962.

[21] G. S. Vincent and M. Labse, "Correlation of predicted and observed suspension bridge behavior," *Trans. Am. Soc. Civ. Eng.*, vol. 127, no. 2, pp. 646–666, 1962.

[22] H. Tanaka and A. G. Davenport, "Wind-Induced Response of Golden Gate Bridge," *J. Eng. Mech.*, vol. 109, no. 1, pp. 296–312, 1983.

[23] S. N. Pakzad, G. L. Fenves, S. Kim, and D. E. Culler, "Design and Implementation of Scalable Wireless Sensor Network for Structural Monitoring," *J. Infrastruct. Syst.*, vol. 14, no. 1, pp. 89–101, 2008.

[24] S. N. Pakzad and G. L. Fenves, "Statistical Analysis of Vibration Modes of a Suspension Bridge Using Spatially Dense Wireless Sensor Network," *J. Struct. Eng.*, vol. 135, no. 7, pp. 863–872, 2009.

[25] S. N. Pakzad, G. V. Rocha, and B. Yu, "Distributed modal identification using restricted auto regressive models," *Int. J. Syst. Sci.*, vol. 42, no. 9, pp. 1473–1489, 2011.

[26] M. Chang and S. N. Pakzad, "Modified Natural Excitation Technique for Stochastic Modal Identification," *J. Struct. Eng.*, vol. 139, no. 10, pp. 1753–1762, 2013.

[27] T. J. Matarazzo and S. N. Pakzad, "Modal identification of golden gate bridge using pseudo mobile sensing data with STRIDE," in *Dynamics of Civil Structures, Volume 4*, Springer, 2014, pp. 293–298.

[28] T. J. Matarazzo and S. N. Pakzad, "STRIDE for structural identification using expectation maximization: iterative output-only method for modal identification," *J. Eng. Mech.*, vol. 142, no. 4, p. 4015109, 2016.

[29] J. Bendat and A. Piersol, *Engineering applications of correlation and spectral analysis*. 1993.

[30] L. Ljung, "System Identification: Theory for the user," *Englewood Cliffs*, 1987.

[31] G. W. Housner and C. C. Thiel Jr., "Competing against time: report of the Governor's Board of Inquiry on the 1989 Loma Prieta earthquake," *Earthq. Spectra*, vol. Vol. 6, no. 4, p. 681–711. Nov., 1990.

[32] M. Huang, P. Hipley, and A. Shakal, "Seismic Instrumentation of Toll Bridges in California," in *Sevnetgh National Seismic Conference on Brdiges and Highways, Oakland, Californa, Paper*, 2013, p. P10.

[33] S. F. Ghahari, F. Abazarsa, M. A. Ghannad, and E. Taciroglu, "Response-only modal identification of structures using strong motion data," *Earthq. Eng. Struct. Dyn.*, vol. 42, no. 8, 2013.

[34] S. F. Ghahari, F. Abazarsa, M. A. Ghannad, M. Celebi, and E. Taciroglu, "Blind modal identification of structures from spatially sparse seismic response signals," *Struct. Control Heal. Monit.*, vol. 21, no. 5, 2014.

[35] F. Abazarsa, F. Nateghi, S. F. Ghahari, and E. Taciroglu, "Extended blind modal identification technique for nonstationary excitations and its verification and validation," *J. Eng. Mech.*, vol. 142, no. 2, 2016.

[36] S. F. Ghahari, F. Abazarsa, and E. Taciroglu, "Blind modal identification of non-classically damped structures under non-stationary excitations," *Struct. Control Heal. Monit.*, 2016.

[37] François Auger, P. Flandrin, P. Gonçalvès, and O. Lemoine, "Time-Frequency Toolbox for Use with Matlab - Reference Guide," *October*, pp. 1995–1996, 1996.

[38] M. ?elebi, Y. Hisada, R. Omrani, S. F. Ghahari, and E. Tacirogluc, "Responses of two tall buildings in Tokyo, Japan, before, during, and after the M9.0 Tohoku earthquake of 11 March 2011," *Earthq. Spectra*, vol. 32, no. 1, 2016.

[39] A. Der Kiureghian, "A Coherency Model for Spatially Varying Ground Motions," *Earthq. Eng. Struct. Dyn.*, vol. 25, no. August 1995, pp. 99–111, 1996.

[40] F. Baron, M. Arikan, and R. E. Hamati, *The effects of seismic disturbances on the Golden Gate Bridge*. University of California, College of Engineering, Earthquake Engineering Research Center, 1976.

[41] A. M. Abdel-Ghaffar and E. E. R. Laboratory, "Dynamic analyses of suspension bridge structures," 1976.

[42] A. M. Abdel-Ghaffar and L. I. Rubin, "Vertical seismic behaviour of suspension bridges," *Earthq. Eng. Struct. Dyn.*, vol. 11, no. 1, pp. 1–19, 1983.

[43] A. M. Abdel-Ghaffar and R. G. Stringfellow, "Response of suspension bridges to travelling earthquake excitations: Part I. Vertical response," *Int. J. Soil Dyn. Earthq. Eng.*, vol. 3, no. 2, pp. 62–72, 1984.

[44] A. M. Abdel Ghaffar and L. I. Rubin, "Lateral Earthquake Response of Suspension Bridges," *J. Struct. Eng.*, vol. 109, no. 3, pp. 664–675, 1983.

[45] A. M. Abdel-Ghaffar and R. G. Stringfellow, "Response of suspension bridges to travelling earthquake excitations: Part II-lateral response," *Int. J. Soil Dyn. Earthq. Eng.*, vol. 3, no. 2, pp. 73–81, 1984.

[46] A. M. Abdel-Ghaffar, R. H. Scanlan, and J. Diehl, *Analysis of the dynamic characteristics of the Golden Gate Bridge by ambient vibration measurements*. Princeton University, 1985.

[47] C. Seim and S. Rodriguez, "Seismic performance and retrofit of the Golden Gate bridge," in *Structural Engineering in Natural Hazards Mitigation:*, 1993, pp. 133–138.

[48] C. Seim and M. Ketchum, "Golden Gate Bridge Mass Transit Feasibility Study, Golden Gate Bridge, Highway and Transportation District, San Francisco, California," 1990.

[49] S. Rodriguez and T. J. Ingham, "Seismic protective systems for the stiffening trusses of the Golden Gate Bridge," in *Proceedings of the National Seismic Conference on Bridges and Highways*, 1995.

[50] M. Nader and T. J. Ingham, "Seismic Retrofit of the Towers of the Golden Gate Bridge," in *Proceedings of the National Seismic Conference on Bridges and Highways, San Diego, CA, December*, 1995.

[51] R. Imbsen and R. Schamber, "Seismic retrofit of the north approach viaduct of the Golden Gate Bridge," *Transp. Res. Rec. J. Transp. Res. Board*, no. 1688, pp. 154–162, 1999.

[52] M. I. Gürelli and C. L. Nikias, "EVAM: An Eigenvector-Based Algorithm for Multichannel Blind Deconvolution of Input Colored Signals," *IEEE Trans. Signal Process.*, vol. 43, no. 1, pp. 134–149, 1995.

[53] Y. Nakamura, A. Der Kiureghian, and D. Liu, *Multiple-support response spectrum analysis of the Golden Gate Bridge*, vol. 93, no. 5. Earthquake Engineering Research Center, University of California, 1993.

[54] R. A. Dameron, R. S. Dunham, and J. C. Castro, "Nonlinear analysis and experimental validation of a stiffening truss chord of the golden gate bridge," in *Computing in Civil Engineering (New York)*, 1994, no. 2, pp. 1106–1114.

[55] T. Game *et al.*, "Full dynamic model of Golden Gate Bridge," in *AIP Conference Proceedings*, 2016, vol. 1762, no. 1, p. 20005.

[56] Strand7, "Strand7 Finite Element Analysis System." Strand7 Software Sydney, Australia, 2007.

[57] Hibbitt, Karlsson, and Sorensen, *ABAQUS/standard User's Manual*, vol. 1. Hibbitt, Karlsson & Sorensen, 2001.

[58] S. V CSI, "8, 2002. Integrated Finite Element Analysis and Design of Structures Basic Analysis Reference Manual," *Comput. Struct. Inc., Berkeley, California, USA*, 2010.

[59] F. McKenna, "OpenSees: a framework for earthquake engineering simulation," *Comput. Sci. Eng.*, vol. 13, no. 4, pp. 58–66, 2011.

[60] J. G. Reid, "Structural Identifiability in Linear Time-Invariant Systems," *IEEE Trans. Automat. Contr.*, vol. 22, no. 2, pp. 242–246, 1977.

[61] M. . Shrikhande and V. K. Gupta, "Dynamic soil-structure interaction effects on the seismic response of suspension bridges," *Earthq. Eng. Struct. Dyn.*, vol. 28, no. 11, pp. 1383–1403, 1999.

RELATIONSHIP BETWEEN EARTHQUAKE GROUND MOTION INTENSITY MEASURES AND EMBANKMENT DAM DEFORMATIONS

Richard J. Armstrong

Department of Civil Engineering
California State University, Sacramento

Abstract

The relationship between earthquake ground motion characteristics and embankment dam deformations is currently being investigated through a ground motion study using two validated non-linear deformation (NDA) embankment models. Presented in this paper are: (1) NDA results for one of the dams in this study, Lenihan Dam, against the 1989 Loma Prieta earthquake, and (2) current results of the ground motion study with this NDA model. The paper ends with major conclusions and plans for future work.

Introduction

In a seismic hazard assessment of an embankment dam, the ground motion intensity measure deemed important to the dam must first be identified (e.g., spectral acceleration, SA; peak ground velocity, PGV; and arias intensity, AI). Following this identification, the potential distribution of each intensity measure can be predicted using ground motion prediction equations. The actual design target level of one or more of these intensity measures can then be determined through deterministic or probabilistic seismic hazard analyses. One method of setting the design target level is the conditional mean approach, which is described in detail for use in dam engineering by Armstrong (2017). In this approach, a single intensity measure that relates well to embankment-dam response—called the conditioning intensity, IM^*—is selected, and the value is set based on the hazard level defined. The values of the other intensity measure targets are then selected according to the value of this conditioning intensity measure and other statistical considerations. When the conditional mean approach is used, it is important for the conditioning intensity measure, IM^*, to relate well to the engineering demand parameter (EDP) of interest—for example, vertical crest deformation—because the expectation is that as IM^* increases, so should the EDP. More specifically, as stated by Kramer (2008), IM^* should be unbiased, consistent, robust, efficient, and sufficient.

Previous studies have investigated the relationship between ground motion intensity measures and embankment or slope deformation. Based on these studies, it has been suggested that for stiff embankment dams in which significant strength loss is not expected, the SA at the first-mode period of the structure relates well with embankment deformations. However, for embankment dams founded on liquefiable alluvium, other non-SA intensity measures have been found to relate better to embankment deformations (Beaty and Perlea 2012)—such as AI; cumulative absolute velocity, CAV; and $\sqrt{AI \cdot D595}$, where $D595$ is the duration between 5% and 95% AI. These studies, however, have been based on relatively simplified Newmark-type

sliding block analyses with large ground motion databases (e.g., Bray and Travasarou 2007, Saygili and Rathje 2007) or on non-linear deformation analyses shaken with significantly smaller sets of ground motions (Beaty and Perlea 2012).

In a current project—supported by the California Department of Conservation, California Geological Survey, Strong Motion Instrumentation Program, Agreement 1016-988—data from strong ground motion recordings from two embankment dams during the 1989 Loma Prieta earthquake are being used to validate each non-linear deformation analysis model for subsequent use in assessing the relationship between earthquake ground motion characteristics and embankment dam deformations. Currently, a suite of over 700 ground motions is being used in this assessment. It is anticipated that at the completion of this project, this work will provide significant additional insight into the relationship between ground motion characteristics and embankment dam deformations.

The purpose of this paper is twofold: (1) to present NDA results for one of the dams in this study, Lenihan Dam, against the 1989 Loma Prieta earthquake, and (2) to present current results of the ground motion study with this NDA model. The paper will begin with a detailed description of the validation of the NDA of Lenihan Dam to the 1989 Loma Prieta earthquake, followed by a description of the ground motion database used and an initial evaluation of the results. The paper will end with conclusions and plans for future work.

Background

Lenihan Dam

James J. Lenihan Dam (or, simply, Lenihan Dam, which is sometimes called Lexington Dam) is a zoned earthfill dam that was constructed across Los Gatos Creek in 1952 (Figures 1 and 2). The dam impounds Lexington Reservoir, which has a maximum capacity of 19,044 acre-feet at the spillway elevation of 653 feet (TGP 2012). The crest of the dam is at elevation 673 feet, with an embankment height of 195 feet measured from the lowest point of the foundation rock to an embankment height of 207 feet measured from the lowest point of the downstream toe. The zoned earthfill dam is composed of upstream and downstream shells, core, and drainage zones. The core is further divided into an upper and lower core to reflect differences in material properties. The upstream shell and upper core material were obtained from the same borrow source. The upstream shell is generally composed of gravelly clayey sands to sandy clays, while the upper core is composed of gravelly clayey sand to clayey gravel. The lower core came from another borrow source with the material being generally classified as highly plastic sandy clays to highly plastic silty sands-sandy silts. The downstream shell, obtained from a third borrow source, consists mainly of gravelly clayey sand to clayey gravels. No classification information is available for the drain material. The embankment materials were constructed on Franciscan Complex bedrock, without a foundation seepage cutoff or grout curtain. Instrumentation of Lenihan Dam includes survey monuments, piezometers, inclinometers, seepage weir, and strong ground motion accelerometers.

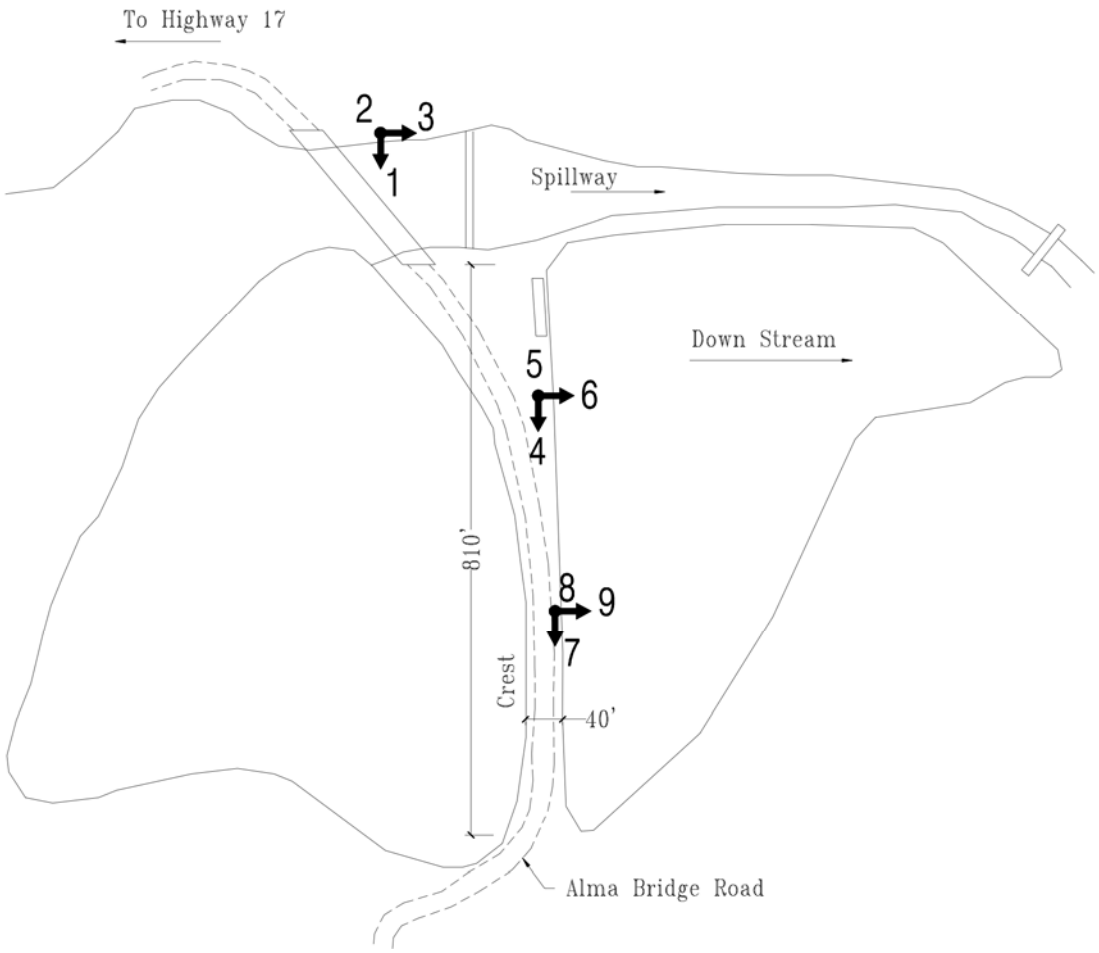

Figure 1. Plan view of Lenihan Dam with locations of strong motion instruments (from Center for Earthquake Strong Ground Motion).

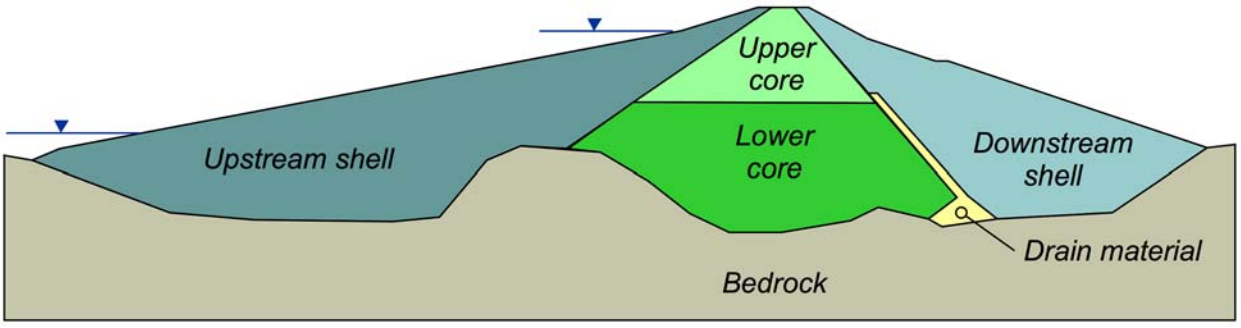

Figure 2: Design cross-section with reservoir level of 556 feet during the 1989 Loma Prieta Earthquake and at the spillway elevation of 653 feet.

Loma Prieta Earthquake

The M = 6.9 Loma Prieta earthquake occurred along a segment of the San Andres fault on October 17, 1989. The epicenter of this earthquake event was located 13 miles from Lenihan Dam. At the time of the earthquake, the reservoir was at around elevation 556 feet – 97 feet below the spillway. During this earthquake, strong ground motion instruments located at the left abutment and on the crest measured the dynamic response of the dam. Due to the strong shaking, the embankment crest deformed horizontally around 3 inches downstream and approximately 10 inches vertically downward, resulting in longitudinal and transverse cracking at the dam site (Hadidi et al. 2014).

Analysis of the strong ground motion data is provided in Figure 3 in terms of the SA, ratio of the crest SA to abutment SA, peak ground velocity (PGV), AI, and $D595$. The results shown in Figure 3 correspond to the strong ground motion recording in the transverse directions (directions "3", "6", and "9" in Figure 1). Peak ground acceleration (PGA) changed from 0.44g at the abutment to between 0.38g and 0.45g along the crest. The most significant increase in acceleration corresponded to a spectral period of 1 second, which roughly represents the natural period of the dam.

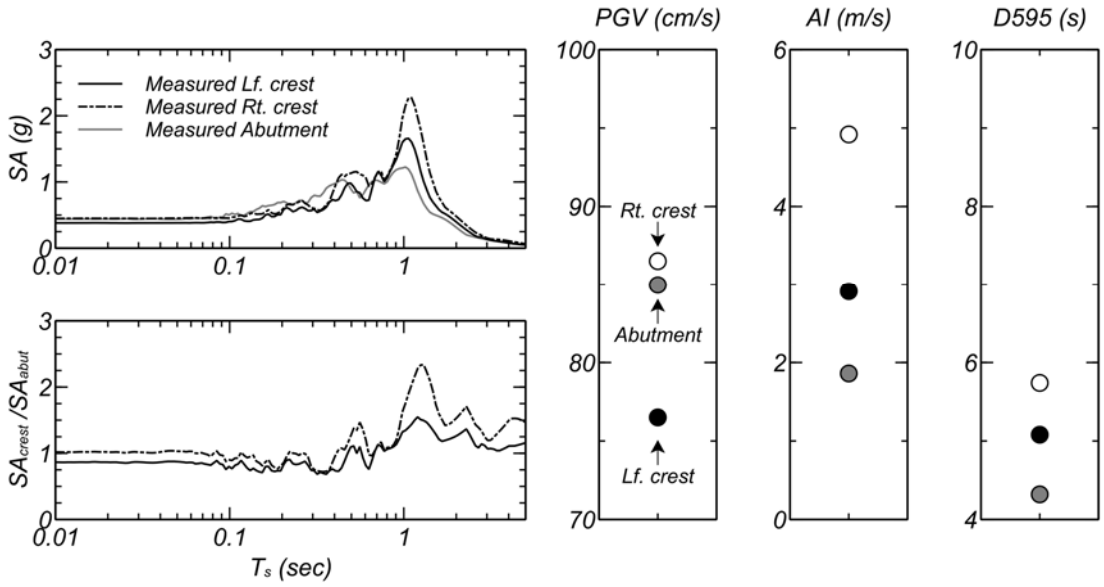

Figure 3: Measured ground motion characteristics in transverse direction during the 1989 Loma Prieta earthquake.

Non-linear Deformation Analysis of Lenihan Dam

Analysis Approach

Numerical Analysis Details

The NDA was conducted using the commercial program FLAC (Itasca Consulting Group, 2016). This program uses an explicit solution scheme and is well suited for performing deformation analyses with non-linear material response, large geometry changes, and instability. The explicit solution satisfies the equations of motion at each nodal mass for every time step. The numerical mesh used in the NDA is shown in Figure 1. The element size was selected to accurately transmit motion frequencies up to at least 10 hertz.

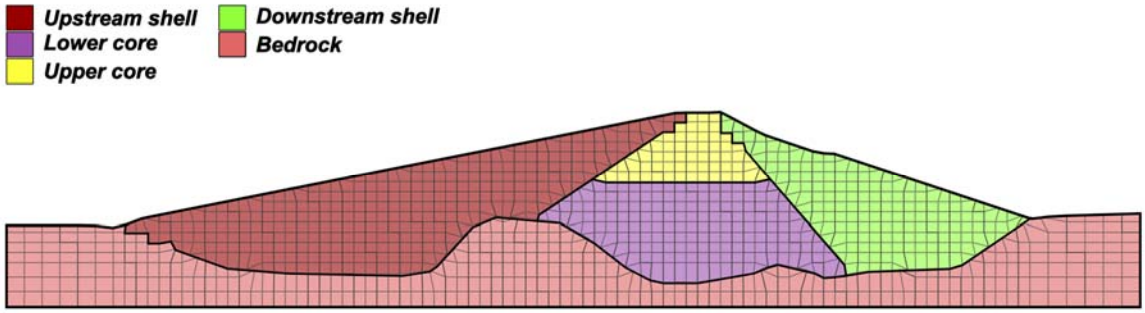

Figure 4: Numerical mesh.

Constitutive Modeling Approach

The UBCHYST constitutive model (Byrne and Naesgaard, 2011) was used to model the expected non-linear soil response during the 1989 Loma Prieta earthquake. The UBCHYST model captures, with increased shear strain, the reduction of shear modulus and increase in hysteretic damping. The UBCHYST is essentially an extension of the Mohr-Coulomb model with a tangent shear modulus that is a function of the developed stress ratio and other modification factors. Up to 11 input parameters can be set to control various aspects of the UBCHYST constitutive model response. Of those 11 input parameters, the following five parameters were modified in these analyses: maximum shear modulus (G_{max}) and bulk modulus, cohesion (S), hysteretic parameter (n), and hysteretic parameter (R_f). The first three input parameters are also inputs into the elastic-perfectly plastic Mohr-Coulomb model, while the last two input parameters help to define the hysteretic behavior of UBCHYST. Of n and R_f, n was found to have the most significant effect on the hysteretic behavior. As a result, R_f was simply set to the recommended default value of 0.98, and n was used to adjust the constitutive model response to capture the desired dynamic soil element behavior. In particular, the expected dynamic soil behavior was defined through the G/G_{max} and ξ curves developed by Vucedic and Dobry 1991 (termed here VD91).

The input parameter n was selected by comparing the calculated G/G_{max} and ξ of single element simple shear simulations to those values from VD91. In performing these simulations, it

was found that n as well as the ratio of the shear strength to maximum shear modulus (S/G_{max}) both significantly affect the calculated value of G/G_{max} and ξ. Because the goal was to have a single target G/G_{max} and ξ for each material in the embankment, and S/G_{max} will change throughout the embankment, it was then necessary to define a relationship between between n and S/G_{max}. To accomplish this, a large suite of single element simple shear simulations was conducted with UBCHYST, with varying values of n and S/G_{max}; further, a statistical relationship was developed between n and S/G_{max} so that all numerical elements, regardless of S/G_{max}, would result in the same target curve from VC91. Specifically, it was found that for the target shear modulus and damping curves from PI = 15 and PI = 30 used in VC91, the necessary relationship between n and S/G_{max} was $n = 2300 \times S/G_{max}$ for PI = 15 and $n = 1300 \times S/G_{max}$ for PI = 30.

An example of the dynamic simple shear response of UBCHYST using this technique is shown in Figure 5. For this example, the ratio between the S to G_{max} was 8x10^{-4}, a range consistent with the NDA model of the embankment. To reasonably match the VD91 for PI = 30, for example, n = 1.04. As highlighted in Figure 5, UBCHYST is capable of matching the G/G_{max} curve up to around a shear strain of 0.001, after which the reduction in G/G_{max} is over-predicted. For the ξ curve, the UBCHYST model is able to match the curve up to a shear strain of approximately 0.0002, after which the model predicts hysteretic damping significantly larger than what would be expected from VD91. The highlighted shortcomings of UBCHYST are primarily due to its basis on the Mohr-Coulomb model formulation.

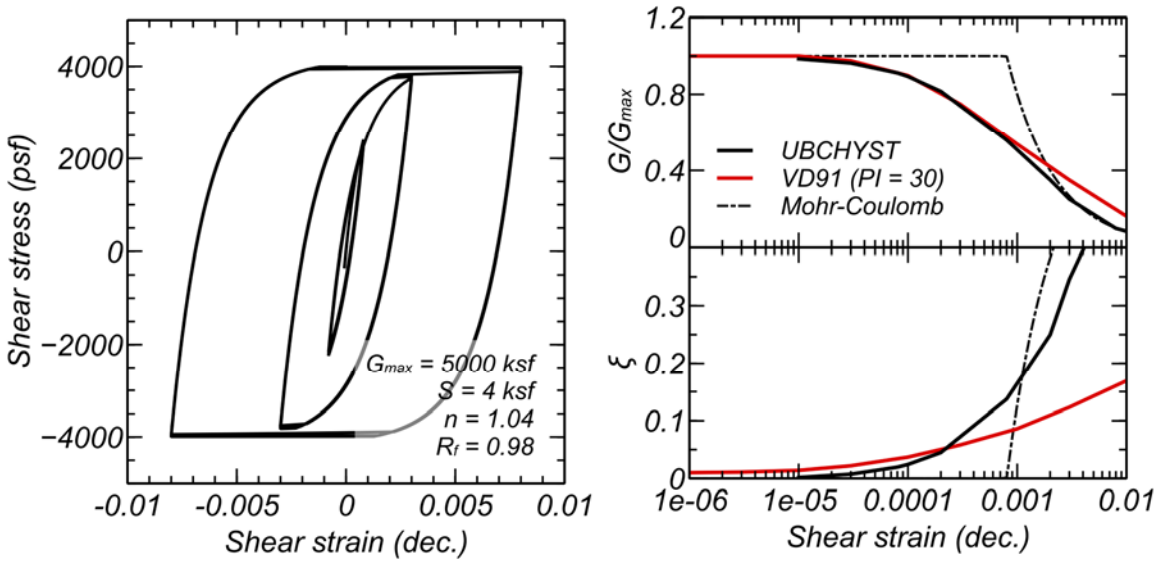

Figure 5. Stress-strain and resulting G/G_{max} and ξ curves for UBCHYST. Comparison to Vucedic and Dobry 1991 (VD91) with PI = 30 and the Mohr-Coulomb model.

Material Property Characterization

Over the years, multiple site investigation programs have been conducted at Lenihan Dam. The most recent such program took place in 2012 by TGP (TGP, 2012). When defining material properties based on this site investigation information, the material characterization completed by TGP and summarized in the work by Hadidi et al. 2014 was used extensively to define material properties. The primary difference between the material properties found here and those used by Hadidi et al. 2014 was the modeling of the variation of shear strength with effective stress. In this work, the shear strength was defined as $S = b' + \sigma' \tan\beta'$ for drained strength and $S = b + \sigma' \tan\beta$ for undrained strengths where $\sigma' = \left(\sigma'_x + \sigma'_y\right)/2$, with the values of intercepts and slopes defined in Table 1 below. These strength envelopes are based directly on the triaxial strength data.

Based on geophysical investigation data, the variation in G_{max} was defined in terms of the vertical effective stress (σ'_y) at 1 atm, V_{s1}, and the exponent m with $G_{max} = \rho {V_s}^2 = \rho \times \left(\left(V_{s1}/\sigma'_y\right)^m\right)^2$. Note that the rock beneath the soil embankment had a γ = 140 psf, V_s = 4500 ft/s. The value of n from the UBCHYST model was determined to match the target G/G_{max} and ξ curve for VD91 with a PI = 30 for the lower core, and the target G/G_{max} and ξ curve for VD91 with a PI = 15 for all other embankment soils. A small proportion of Rayleigh damping was included for the embankment material and rock to capture small strain damping characteristics as well as to reduce numerical noise.

Table 1. Key material parameters used in NDA

Parameters	Upstream shell	Downstream shell	Upper core	Lower core
γ (psf)	138	140	132	124
V_{s1} (ft/s)	1305	1550	1190	680
m	0.5			
β' (deg.)	31.3	29.8	30.1	23.3
b' (psf)	50		0	
β (deg.)	28.8	18.8	27.9	19.3
b (psf)	1020	1570	960	1090
R_f	0.98			
$n^{(A)}$	$2300 \times S/G_{max}$			$1300 \times S/G_{max}$

Notes (A): variation n defined for lower core chosen to match G/G_{max} and ξ curve for PI = 30 from VD91, and variation of n for other embankment material chosen to match G/G_{max} and ξ curve for PI = 15 from VD91.

Establishment of Pre-earthquake Stresses and Boundary Conditions

The pre-earthquake state-of-stress affects both initial conditions for the dynamic analysis and the value of shear strength, which is a function of the effective stress. Total stresses for the embankment were estimated by sequentially adding rows of elements of the mesh and solving for static equilibrium with each new row of elements. This process was continued for the entire embankment. The goal of this process was to roughly mimic the actual construction process.

A seepage analysis was used to model the pore water pressures in the embankment immediately before the 1989 Loma Prieta earthquake. Note that prior to the 1989 Loma Prieta earthquake, several years of below-average rainfall occurred. This resulted in a reservoir level of 506 feet, significant lower than the spillway elevation of 653 feet. Due to the low permeabilities in the embankment, the pore water pressure would slowly respond to this lower reservoir level. Modeling this non-steady state seepage condition could not be achieved using a steady-state seepage analysis with the reservoir at the level of either 506 feet or 653 feet.

In an attempt to reasonably model these non-steady state seepage conditions, the approach used was first to model the steady-state seepage conditions corresponding to the reservoir of 653 feet, and then to lower the reservoir to 506 feet and rerun the analysis until the pore water pressure in the embankment was lowered to the values similar to those measured prior to the 1989 Loma Prieta earthquake. For the initial steady-state seepage conditions corresponding to the reservoir at 653 feet, values of the horizontal and vertical permeability were adjusted until the calculated total head reasonably corresponded to values measured at Lenihan Dam for the piezometer recordings when the reservoir was near the same elevation. Note that the piezometer reading used to evaluate the reasonableness of the non-steady state seepage analysis with the reservoir at 506 feet were based both on actual piezometer readings at the time of the 1989 Loma Prieta earthquake (represented by blue square symbols in Figure 6) and on recent piezometer readings with a previous reservoir response similar to that which occurred before the 1989 Loma Prieta earthquake. Specifically, the piezometer readings from December 2008 were seen to have a previous reservoir response as before the 1989 Loma Prieta earthquake, and the piezometer data from this time was used (represented by blue circle symbols in Figure 6). As seen in Figure 6, by comparison of the calculated and total heads, the seepage model was able to reasonably capture the distribution of total heads.

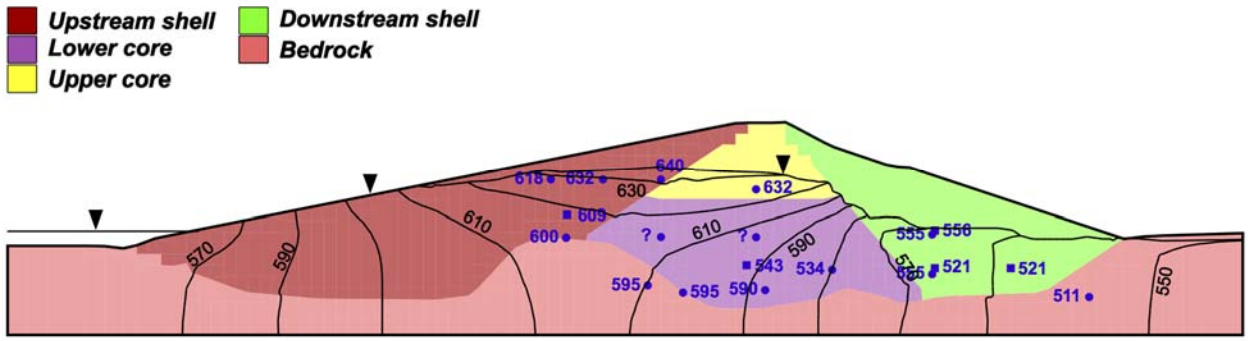

Figure 6. Comparison of calculated and target total heads.

Dynamic Analysis Results

Dynamic analyses were conducted with the transverse acceleration time history from the 1989 Loma Prieta earthquake applied directly at the base of the numerical model. To model the elastic half space below the numerical model, numerical dashpots are added and the velocity time history of the abutment record is converted to a shear stress time history based on the stiffness properties of the rock.

As an initial evaluation of the NDA results, the calculated and measured time histories are shown in Fig. 7 in terms of the SA at the crest, the ratio of the crest SA to abutment SA, and the PGV, AI, and $D595$ computed at the crest. As highlighted by these results, the NDA was able to capture reasonably well key aspects of the observed site response (e.g., SA_{crest}/SA_{abut}) as well as other peak response characteristics (PGA, PGV, and AI) and duration ($D595$).

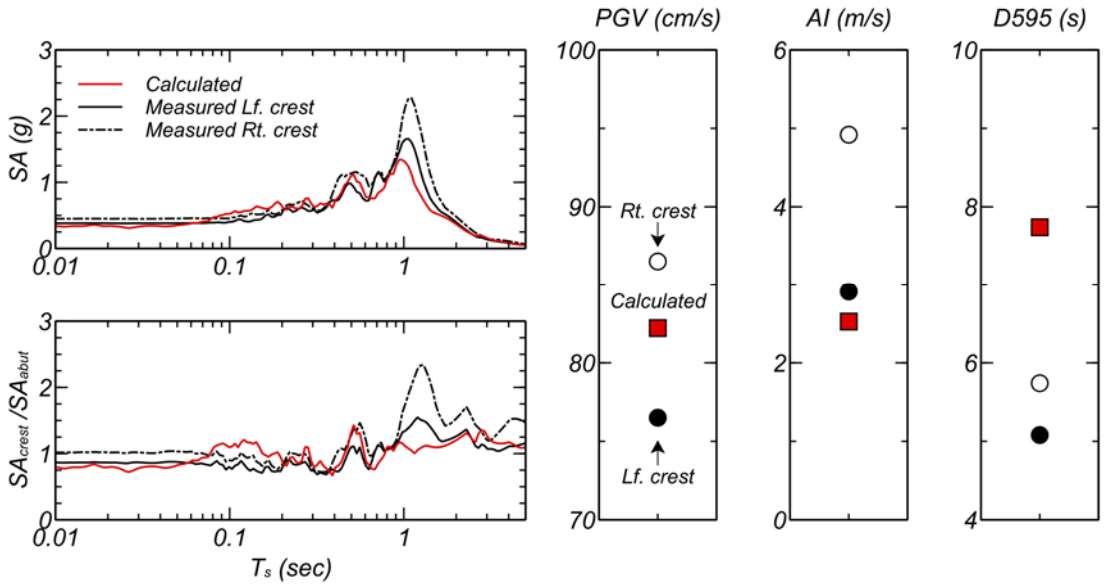

Figure 7: Summary of the calculated and measured dynamic responses at the embankment crest.

In terms of computed deformations, the final crest displacements computed with the NDA were similar to those measured. In particular, the final horizontal displacement (DXF) was 0.27 feet, compared to the measured horizontal displacement between 0.10 and 0.25 feet; and the final vertical displacement (DYF) computed was 0.45 feet, compared to the 0.61 to 0.85 feet measured.

The computed distribution of the shear strains is shown in Fig. 9(a) in terms of the shear strain increment defined as $\frac{1}{2}\sqrt{(\varepsilon_x-\varepsilon_y)^2+4\varepsilon_{xy}^2}$. Localized areas of high shear strain increment are shown in both the upstream and downstream shells, producing the typical circular-type localized failure surfaces expected with slope instability. The computed distributions of horizontal and vertical displacement are shown in Figures 9(c) and (d), respectively, and are relatively consistent with the pattern of deformations and cracks observed. For example, the region where DXF changes from positive to negative corresponded to high volumetric strain extension (Figure 9(b)) and corresponded directly to the location of longitudinal cracking observed following the Loma Prieta earthquake.

Overall, the NDA was able to reasonably capture the dynamic characteristics from the 1989 Loma Prieta earthquake as well as the magnitude and distribution of displacements. The NDA model of Lenihan dam was then used to further explore the relationship between embankment dam deformations and earthquake shaking in the ground motion study.

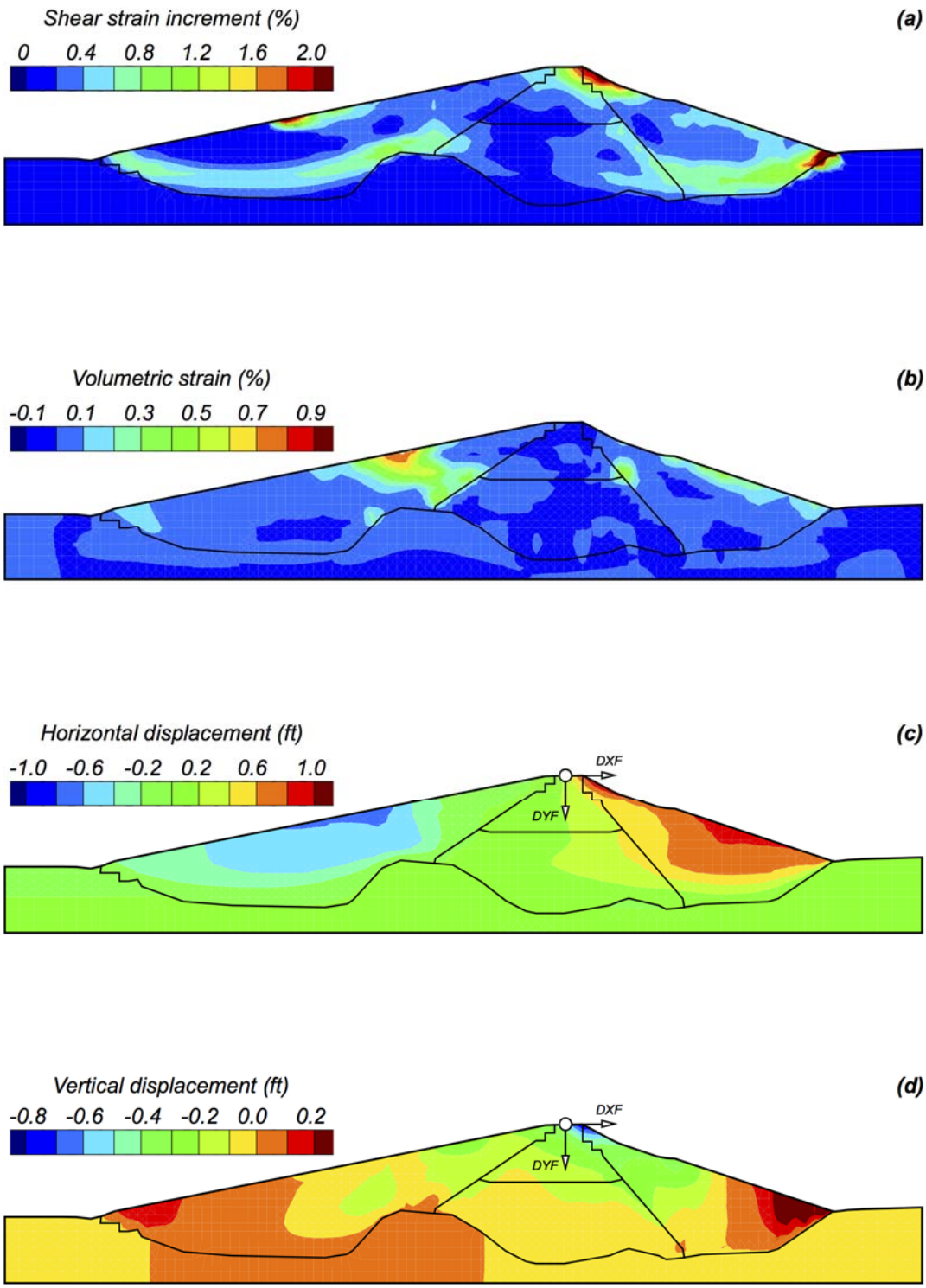

Figure 9: Computed deformations in terms of shear strain increment (a), volumetric strain (b), horizontal displacement (c), and vertical displacement (d).

Numerical Analysis Ground Motion Study

Characteristics of Ground Motion Database

The ground motion database used with the NDA model of Lenihan dam was similar to that used previously in Armstrong (2016). These ground motions were based on the NGA-West1 database with source-to-site distance less than 30 km, similar to many dams in California. For this work, only ground motions based on earthquake events with $M \geq 6$ were used, because it was expected that strong shaking for earthquake events less than 6 would not produce appreciable deformations and therefore would not be particularly useful to evaluate the relationship between embankment deformation and earthquake ground shaking characteristics. For each station, both orthogonal components of the measured strong ground motion acceleration were used if available.

A total of 716 ground motion recordings were found to satisfy this criteria, with distributions of strong ground motion intensity measures of PGA, PGV, AI, and $D595$ shown in Figure 7. Referencing the abutment motion from the 1989 Loma Prieta earthquake with a PGA = 0.44g, PGV = 85.0 cm/s, AI = 1.86 m/s, and $D595$ = 4.32 s, it is seen that the ground motions in this database have ground motion intensity measures that extend from less than to greater than the values measured in the Loma Prieta earthquake. Therefore, it is expected that the resulting deformation will go from negligible to values greater than those observed in the Loma Prieta earthquake. Future plans are to include ground motions from the NGA-West-2 database to augment those in this database, especially those with high ground motion intensity measure values.

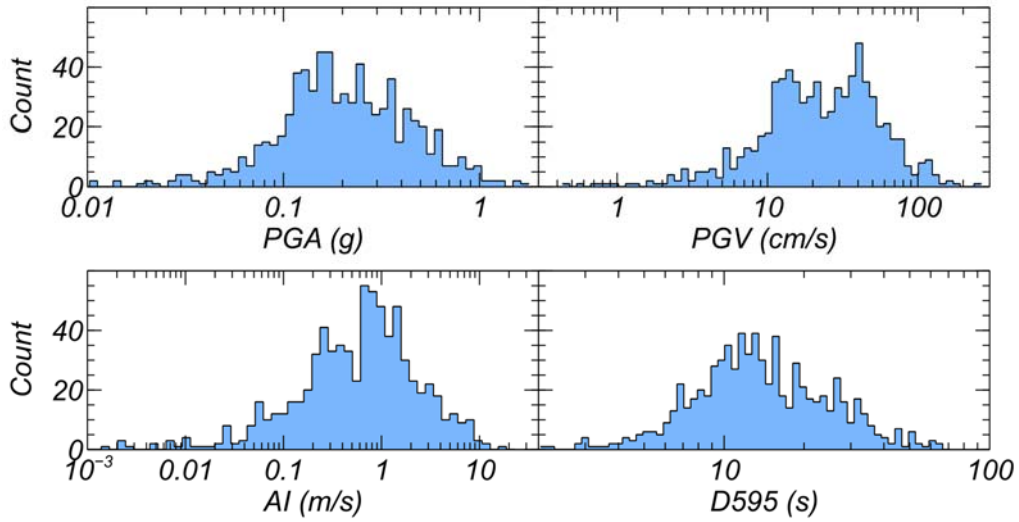

Figure 10. Distribution of ground motion intensity measures.

Numerical Analysis Results

Analyses of the NDA model of Lenihan Dam were conducted with the 716 ground motion time histories described above. The NDA model used was identical to that of Lenihan Dam, except that the reservoir level used was that for a spillway elevation of 653 feet. For each analysis, time histories at key locations were stored, as well as the final solved state of the NDA model.

In this evaluation, the trends between the ground motion intensity measures (IMs) at the base of the model to key engineering demand parameters (EDP) are compared. The ground motion intensity measures computed were PGA, PGV, AI, cumulative absolute velocity (CAV), $D595$, and SA at 200 equal logarithmic increments of spectral period between 0.1 and 30 seconds. The engineering demand parameters computed were peak and final horizontal crest displacement, DXP and DXF, and the peak and final vertical crest displacement, DYP and DYF. Note that in computing these displacements, the displacement was computed relative to the base of the model. Also, the absolute value of the peak and final vertical crest displacement were chosen because the logarithm would otherwise be undefined. Further, only analyses resulting in non-negligible deformation, defined here as a value of DXP, DXF, DYP, or DYF greater than 0.1 feet, were included. This reduced the NDA results to be compared from 716 to 504.

An initial evaluation of the relationships between the embankment crest deformation and ground motion intensity measures is shown in Figure 11 (note that only SA at a selection of spectral periods is included). In each plot, the log_{10} of the IM is compared to the log_{10} of the EDP. The magnitude of the IMs and EDPs have been removed for clarity in comparing plots. A linear trend line is included in each plot, as well as a density ellipse to represent visually the correlation relationship between the IM and EDP. As seen in Figure 11, the ability of each IM to relate to an EDP varies significantly. PGA, AI, and SA at shorter spectral periods related best to the EDPs. Other intensity measures—such as PGV, CAV, and SA—at higher spectral periods still related to the EDPs, but not as strongly as with PGA, AI, and SA at short spectral periods.

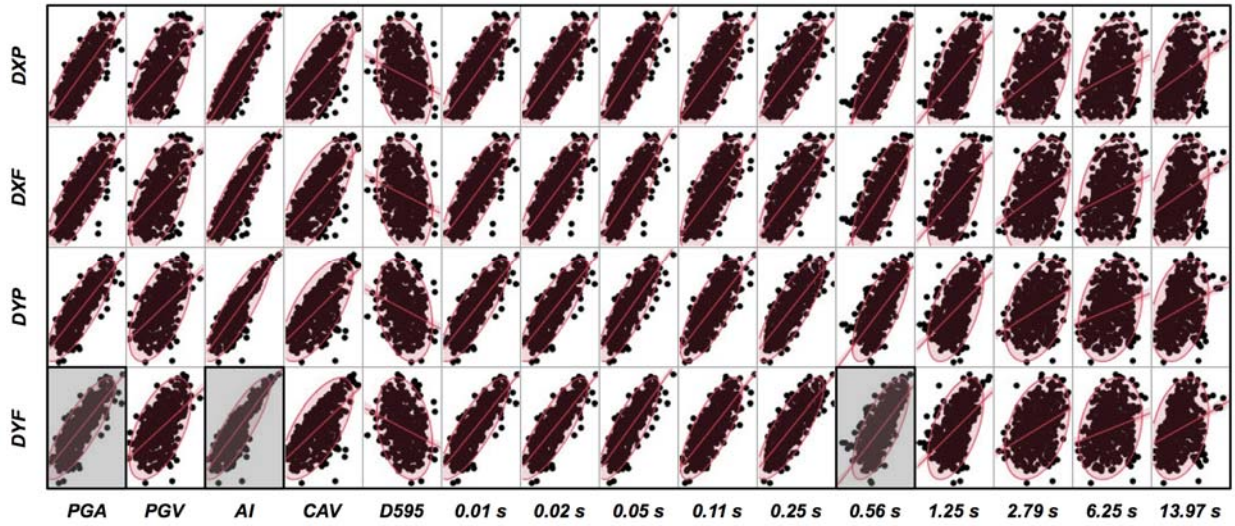

Figure 11. Comparison of IMs and EDPs (all axes are logarithmic).

A closer inspection of the relationship between AI, PGA, and $SA(0.56)$ and DYF shown in Figure 11 is provided in Figure 12. AI and PGA were chosen because AI ranked first and PGA second in order of goodness-to-fit with DYF. SA at a spectral period of 0.56 s was selected because it laid within the expected range of the period of the embankment for many of the analyses. As in Figure 11, a linear trend line is included. Also included in Figure 12 is the magnitude and distribution of DYF and each of the three IMs as well as the standard deviation from the simple bivariate regression analysis.

As highlighted in Figure 12, the relationship between AI and DYF and then PGA and DYF resulted in the lowest standard deviation; therefore, for this particular model, AI, then PGA were the most efficient prediction of this EDP. Therefore, in terms of selecting a conditioning intensity measure for the NDA model of this dam, AI appears to be the preferred IM. It is important to note that the observed relationship between embankment deformations and ground motion intensity measures here is based only on the NDA model of Lenihan Dam. Plans for additional ground motions, more detailed statistical evaluations, and a second validated NDA model will be helpful in better defining the relationship between ground motion intensity measures and embankment dam deformations.

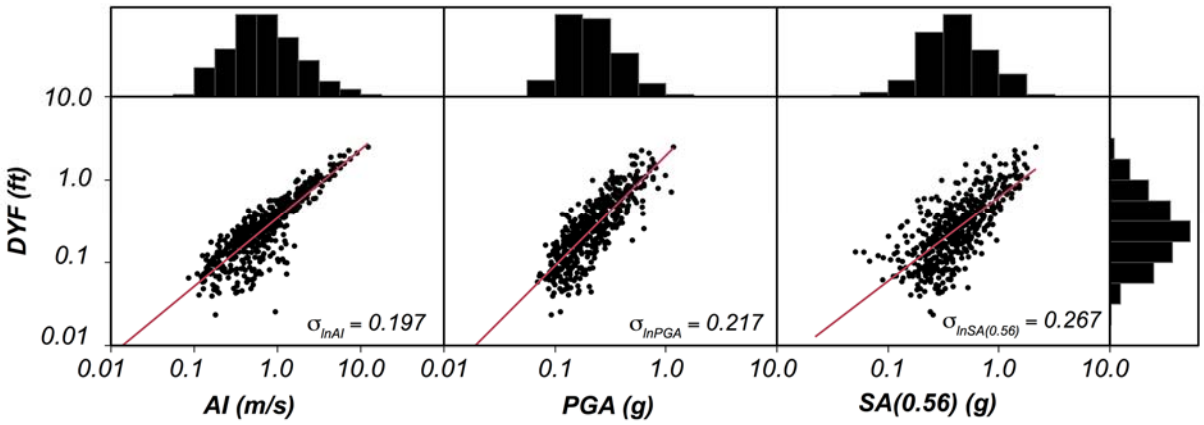

Figure 12. Comparison of intensity measures and engineering demand parameters.

Conclusions

The measured strong ground motion data at Lenihan Dam during the 1989 Loma Prieta earthquake provided a useful case-history to assess the capabilities of current NDAs. With the analysis approach described, the NDAs were able to capture reasonably well key dynamic characteristics such as the surface acceleration response spectra and the magnitude and pattern of permanent deformations. Using the NDA model for Lenihan Dam, additional analyses with the 716 ground motions provided insight into the relationship between ground motion intensity measures and embankment dam deformation. For the NDA model used, AI was found to relate best with embankment dam deformations, followed by PGA and then SA at short spectral periods. Plans to use additional ground motions, to perform more detailed statistical evaluations, and to include a second validated NDA model will be helpful in better defining the relationship between embankment dam deformations and ground motion intensity measures. The second NDA model to be included is of Anderson Dam. This dam was also shaken during the Loma Prieta earthquake, with multiple strong ground motion recordings available. Development of this NDA model is ongoing. Note that for Anderson Dam at the design loading earthquake levels, liquefaction of portions of the embankment and foundation material is expected; thus, this dam model will provide a useful comparison to Lenihan Dam, which had no liquefaction concerns. Ground motions from the NGA-West-2 database will be added to the database currently used and will provide improved insight into the relationship between ground motion intensity measures and embankment dam engineering demand parameters.

Acknowledgements

This work was supported by the California Department of Conservation, California Geological Survey, Strong Motion Instrumentation Program, Agreement 1016-988. The funding provided is greatly appreciated. The work and comments by Howard Yoon and Dr. Dong Soon Park as it relates to this project were particularly valuable.

References

Armstrong R.J. (2016). Procedure for selecting and modifying earthquake motions to multiple intensity measures. *Soil Dynamics and Earthquake Engineering*. 89.

Armstrong R.J. (2017). Use of the conditional mean for improved prediction of ground motion intensity measures for embankment dams. Proceedings, *2014 Annual United States Society of Dams Conference*.

Beaty M.H., and Perlea V.G. (2012). Effect of ground motion characteristics on liquefaction modeling of dams. *ASCE GeoCongress*.

Bray J.D., and Travasarou T. (2007). Simplified procedure for estimating earthquake-induced deviator slope displacement. *Journal of Geotechnical and Geoenvironmental Engineering*, 133(4), 381–92.

Byrne, P.M. and Naesgaard, E. (2010). Personal Communications. UDM Version: 5d. https://www.itascacg.com/udms/ubchyst (Accessed 10/16/17).

Hadid, R., Moriwaki, Y., Barneich, J., Kirby, R., Mooers, M. (2014). Seismic deformation evaluation of Lenihan Dam under 1989 Loma Prieta Earthquake. *Tenth U.S. National Conference on Earthquake Engineering*, Frontiers of Earthquake Engineering.

Itasca Consulting Group. (2016). FLAC, fast lagrangian analysis of continua, user's guide, version 8.0, Itasca Consulting Group, Minneapolis.

Kramer S.L. (2008). Performance-based earthquake engineering: opportunities and implications for geotechnical engineering practice. *Geotechnical Earthquake Engineering and Soil Dynamics IV*, D. Zeng, M. Manzari, and D. Hiltunen, eds., Geotechnical Special Publication No. 181, ASCE, NY.

Makdisi, F.I., Chang, C.Y., Wang Z.I., and Mok C.M. (1991). Analysis of the Recorded Response of Lexington Dam During Various Levels of Ground Shaking, Proc. Of the Seminar on Seismological and Engineering Implications of Recent Strong Motion data, SMIP, California Division of Mines and Geology, 1991. □

Saygili G and Rathje E.M. (2007). Empirical predictive models for earthquake-induced sliding displacements of slopes. *Journal of Geotechnical and Geoenvironmental Engineering*, 134(6), 790–803.

Terra / GeoPentech. (2012). Lenihan Dam, Site Characterization, Material Properties and Ground Motion (Report No. LN-3), Prepared for Santa Clara Valley Water District.

Vucetic, M. and Dobry, R. (1991). Effect of soil plasticity on cyclic response. *Journal of Geotechnical Engineering Division*, 117(1), 89-107.

INVESTIGATION OF GROUND MOTIONS RECORDED DURING THE 2014 SOUTH NAPA EARTHQUAKE CONSIDERING INELASTIC STRUCTURAL RESPONSE

Tadahiro Kishida[1], Silvia Mazzoni[1], Yousef Bozorgnia[1], Brian Chiou[2], Robert Darragh[3], Hamid Haddadi[4], Robert Kayen[5], Christopher Markham[6], Sifat Muin[1] and Walt Silva[3]

1. Pacific Earthquake Engineering Research Center, UC Berkeley
2. California Department of Transportation. Sacramento
3. Pacific Engineering and Analysis, El Cerrito
4. California Geological Survey, Sacramento
5. US Geological Survey, Menlo Park and UC Berkeley
6. Exponent, Oakland

Abstract

The 2014 South Napa mainshock caused significant damage in the Northern California Bay Area. Time series from a foreshock, mainshock, and three aftershocks were collected from various agencies. These were processed following the Pacific Earthquake Engineering Research Center (PEER) standard data-processing methods, and a ground-motion database was developed. Metadata such as fault style, source-to-site distance, average shear wave velocity in the top 30 m (V_{s30}), and basin depth were collected. Shear wave velocity profiles were also measured by the Spectral Analysis of Surface Wave Dispersion (SASW) technique at selected strong-motion stations. These datasets were combined in the ground motion database and compared to the Ground Motion Models (GMMs) from the NGA-West2 studies to evaluate the regional attenuation of these events. Time series at two geotechnical downhole array sites were also collected from 29 earthquakes to calculate apparent wave velocities from wave travel times and empirical transfer functions to understand wave amplification. Characteristics of pulse-like records from the South Napa and NGA-West2 databases were also analyzed to compare near-fault regions between these databases. The influence of pulse-like records was also investigated using inelastic response spectra to understand the damage potential on structures. These observed ground-motion characteristics are summarized in this study. The data produced in this study can be used to generate fragility curves that account for the presence of a pulse in the record.

Introduction

The **M**6.0 South Napa earthquake occurred on August 24, 2014. The epicenter was located approximately 9 km south of the city of Napa in northern California. Residential structures and wineries surrounding this area were significantly damaged. After the earthquake, PEER summarized various preliminary observations, in which the following ground motion characteristics were described (Kishida et al. 2014a). In a comparison of the ground motion attenuation from the South Napa earthquake with the median NGA-West2 GMMs (e.g. Campbell and Bozorgnia 2014), the attenuation rate was higher from the South Napa event especially for relatively high-frequency 5%`damped PSA. Baltay and Boatwright (2015) observed similar trends and noted that the northern California Bay Area has stronger attenuation compared to the average value of attenuation in the GMMs. To confirm these observations, the ground motion

database was expanded by collecting the time series from one foreshock and three aftershocks of the South Napa mainshock. The shear wave velocity profiles were also measured by the Spectral Analysis of Surface Wave Dispersion (SASW) technique at selected strong-motion stations. Combining these data, a ground motion database was developed to evaluate the regional attenuation in the northern California Bay Area. The second characteristic observation was that two geotechnical downhole arrays operated by the California Strong Motion Instrumentation Program (CSMIP) in partnership with California Department of Transportation (Caltrans) (CE68206 and CE68259) located on the south side of the Carquinez Bridge (I-80) recorded PGAs of approximately 1g and 0.42g, respectively, during the 2014 South Napa mainshock. The hypocentral distance was approximately 20 km; hence the observed PGAs were unusually high compared to GMMs. These high PGAs were explained after the earthquake with potential causes such as local site effects, soil–structure interaction effects, or possible basin effects (Kishida et al. 2014a, Çelebi et al. 2015). Çelebi et al. (2015) analyzed the recorded time series and concluded that these large PGAs were caused by local site effects. To further understand wave propagation at the two downhole arrays, time series from 29 previous earthquakes also were collected from the Center for Engineering Strong Motion Data (CESMD 2014). Using this database, apparent wave velocities and empirical transfer functions (ETF) were calculated between sensors at different depths in the downhole arrays from wave travel times and ratios of Fourier amplitude spectrum (FAS), respectively. The third characteristic was that pulse-like motions were observed in the velocity time series at several stations in near fault region. These large velocity pulses were observed during mainshock especially in the forward directivity direction (Kishida et al. 2014a). These pulses could possibly be related to the extensive damage observed at structures and wineries in the city of Napa. To understand these effects, we evaluated all the time series in the database for pulse characterization and compared these to the NGA-West2 database to define the region with potential damage from pulse-like velocity time histories. We also investigated the inelastic response spectra of the pulse-like waveforms to understand the pattern of observed damage during 2014 South Napa mainshock.

Ground Motion Database

Table 1 is the catalog of processed earthquakes in the South Napa sequence developed in this study. The moment magnitudes (**M**) were obtained from Northern California Earthquake Data Center (NCEDC). Hypocenter locations were similarly obtained from NCEDC using the double-difference method as described in Waldhauser and Ellsworth (2000). Time series were obtained from CESMD, Incorporated Research Institutions for Seismology (IRIS), NCEDC, and the California Department of Water Resource (CDWR). Approximately 1,350 records have been processed and filtered following the standard PEER data processing methods (Chiou et al. 2008, Ancheta et al. 2013) to provide uniformly processed time series, PSA at various dampings and Arias Intensity. Instrument corrections were also applied when the response of sensors was not directly proportional to acceleration. A time window for data processing was selected following the recommendations of previous studies (Goulet et al. 2014, Kishida et al. 2014b). An acausal Butterworth bandpass filter was applied after reviewing the FAS shape and the signal-to-noise ratio between the S-wave and the pre-event noise window (when available) on a component-by-component basis (e.g. Darragh et al. 2004, Chiou et al. 2008, Boore et al. 2012). 5%-damped PSA were calculated at selected frequencies for all processed time series following Ancheta et al. (2013). The metadata from all the processing steps were also stored in the database such as record start time, location of station, time window locations, and applied high-pass and low-pass

filter corner frequency. For approximately 500 stations in the database, estimates of V_{s30} were obtained from SASW performed for this study, the NGA-West2 study (Seyhan et al. 2014), or approaches that followed methodologies in the study by Seyhan et al. (2014) and Wills et al. (2015). The depths to bedrock were obtained from the USGS study (Aaggard et al. 2010). Directivity parameters were also obtained for the mainshock following the approach by Chiou and Youngs (2014) that used the finite fault model of Dreger et al. (2015).

Figures 1(a) – 1(c) show the attenuation of PGA, PSA(1.0s) and PSA(3.0s) with closest distance (R_{rup}) for the South Napa earthquake mainshock. The median of the four GMMs by Abrahamson et al. (2014), Boore et al. (2014), Campbell and Bozorgnia (2014), and Chiou and Young (2014) are also shown. At PGA, the median GMM prediction fits well to the observations at shorter distances (R_{rup} < 20 km), whereas it tends to over-predict as distance increase. At PSA of 1.0 and 3.0 s, the median prediction slightly underestimated the data at shorter distances, but fits better at greater distances. Baltay and Boatwright (2015) observed similar trends and explained that the over-prediction of high frequency at greater distance was due to the stronger regional attenuation in this area of northern California. Figures 1(d)-1(f) shows the residuals plotted on a regional map. Positive residuals become prominent in the region north of the mainshock epicenter as period increases. Figures 1(g)-1(i) show the residuals against delta DPP which was the directivity indicator used by Chiou and Youngs (2014). Clear directivity effects were observed in these figures for PSA(3.0s). These effects become unclear as period decreases. Baltay and Boatwright (2015) similarly observed positive correlations with residuals against DPP. Figures 1(j) – 1(l) show the attenuation of PGA with closest distances (R_{rup}) for the three aftershocks. Stronger attenuation with distance were also observed for all three events compared to the median GMM with R_{rup}.

Table 1. Catalog for the South Napa earthquake sequence in the PEER Database

Earthquake Name	Origin Time (Year-Mo-DyTHr:Mn:Sc)	Latitude (°N)	Longitude (°E)	Depth (km)	**M**
Foreshock	2014-08-05T12:40:01	38.2557	-122.323	8.20	3.03
Mainshock	2014-08-24T10:20:44	38.21517	-122.312	11.12	6.02
Aftershock1	2014-08-24T12:47:12	38.23833	-122.343	8.439	3.60
Aftershock2	2014-08-26T12:33:16	38.1785	-122.301	12.577	3.90
Aftershock3	2014-08-31T08:56:20	38.23583	-122.329	9.55	3.24

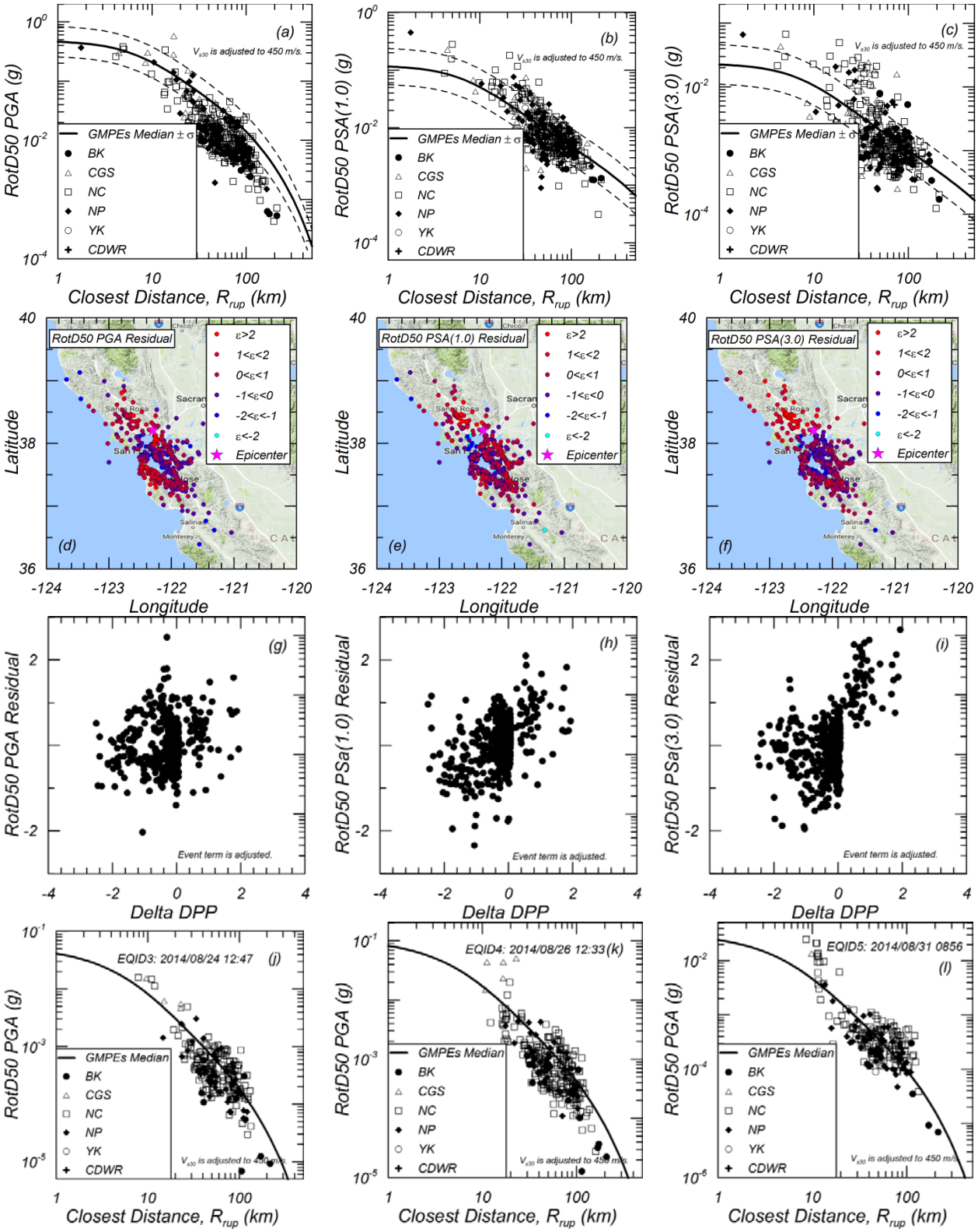

Figure 1. Variations in (a) PGA, (b) PSA(1.0s), (c) PSA(3.0s) against Rrup, variations in residuals of (d)PGA, (e) PSA(1.0s) and (f)PSA(3.0s) on a map, variations in residuals of (g) PGA, (h) PSA(1.0) and (i) PSA(3.0) against Delta DPP for 2014 South Napa mainshock, variations in PGA for three aftershocks (j)EQID3, (k) EQID4, and (l) EQID5 against R_{rup}.

Site Characterization of Strong-Motion Stations by SASW

SASW were performed at 15 strong-motion stations. Table 2 lists these stations, which were selected based on the several factors such as number of recordings in the database, the significance of the strong shaking during the mainshock, and velocity information available in NGA-West2 site database (Seyhan et al. 2013). Figure 2 show pictures of a typical SASW layout. Figure 3 shows an example of the surface wave dispersion curves produced by SASW at the geotechnical downhole array at the south end of the Carquinez Bridge. Surface waves were generated by a truck and recorded by a linear array of seismometers. Figure 4 shows the comparison of the V_s profile from SASW to the suspension logging results from CSMIP (CESMD 2014). These two V_s profiles agree well at depth, while the SASW method provides V_s measurements to the surface.

Table 2. Station list of Vs measurements by SASW

Station Name	Network	Station ID	Latitude (°N)	Longitude (°E)	# of records
Napa - Napa College	CGS	68150	38.270	-122.277	4
Green Valley Road	NC	NGVB	38.280	-122.216	4
Huichica Creek	NC	NHC	38.217	-122.358	5
Lovall Valley Loop Rd	NC	N019B	38.301	-122.402	4
Oakmont	NP	1835	38.442	-122.607	4
Martinez	NP	1847	38.0130	-122.134	4
Glen Ellen	NP	1848	38.367	-122.524	4
McCall Drive, Benicia, CA	NC	C032	38.083	-122.158	5
Main St, Napa, CA	NP	N016	38.299	-122.285	5
Vallejo_FD	NP	1759	38.108	-122.256	2
Napa; Fire Station No. 3	NP	1765	38.330	-122.318	2
NMI	NC	NMI	38.076	-122.259	2
Sonoma	NP	1829	38.290	-122.461	3
Old Carquinez Bridge north free-field	CGS	68184	38.0675	-122.226	1
Carquinez Bridge Geotechnical Array	CGS	68206	38.056	-122.226	3

Figure 2. Example pictures of SASW testing equipment

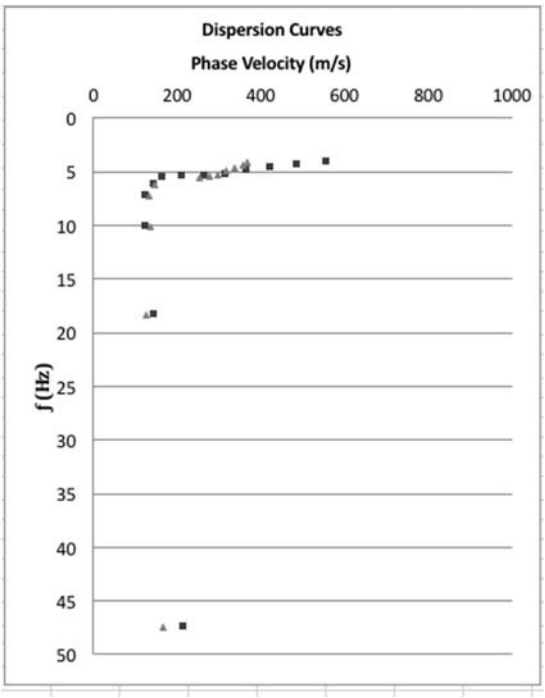

Figure 3. Surface wave dispersion curves at Carquinez Bridge Geotechnical Array (68206)

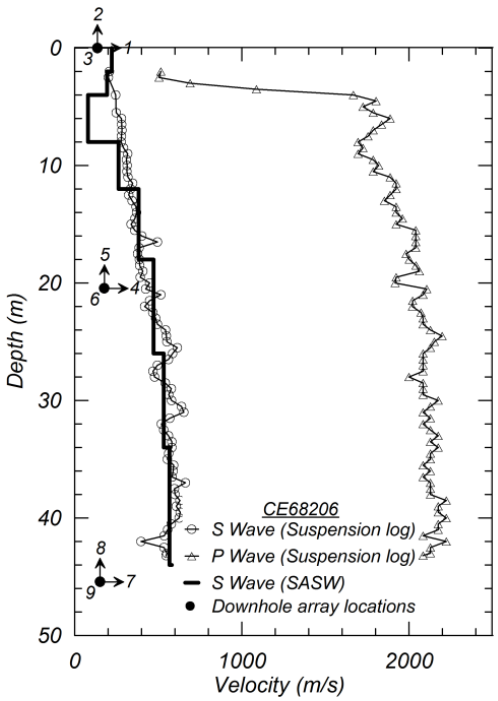

Figure 4. Comparison of the SASW Vs profile with suspension logging results

Carquinez Bridge Geotechnical Array Recordings

The Carquinez Bridge geotechnical array (CE68206) recorded peak ground acceleration of approximately 1.0g at ground surface during 2014 South Napa earthquake. To understand this observation downhole records were collected and processed from 29 previous earthquakes at this array and the nearby CE68259 array. The apparent wave velocities between sensors at depth and empirical wave amplification were estimated. Table 3 lists these earthquakes for which magnitude ranged from 2.2 to 6.0.

Apparent Wave Velocities

Apparent V_s and V_p were calculated between downhole recordings by computing wave travel times. Two analyses were conducted to calculate these velocities. The first was cross-correlation method (CCM) (e.g. Elgamal et al. 1995), and the second was the normalized input-output method (NIOM) (Haddadi and Kawakami, 1998). Incident P- and S-wave-travel times were only considered in the analyses. Figure 5a shows the comparison of apparent wave velocities with field measurements for both of the geotechnical arrays. It shows reasonable agreement between apparent wave velocities and field measurements, where 91% of velocity measurements from CCM and NIOM were within ±30% of the measured velocity. Figure 5b shows the same dataset, however, the x-axis is the difference in apparent velocities between CCM and NIOM methods. The data with large differences between apparent and measured wave velocities also have large differences between the values from CCM and NIOM. Therefore, these data were removed from further analyses when the differences between CCM and NIOM were

greater than 30%. This screening process reduced the percentage of erroneous data (i.e. the difference greater than 30% from the measured velocity) from 9% to 2%.

Table 3. Earthquakes recorded at geotechnical downhole arrays (CE68206 and CE68259)

Earth quake Name	Origin Time (Year-Mo-DyTHr:Mn:Sc)	Earthquake Location	Latitude (°N)	Longitude (°E)	Depth (km)	**M**
1	2006-08-03T03:08:12.86	Glen Ellen	38.3635	-122.589	8.55	4.5
2	2006-12-21T03:12:28.76	Berkeley	37.85717	-122.245	8.643	3.6
3	2007-03-02T04:40:00.75	Lafayette	37.8965	-122.111	15.981	4.23
4	2007-07-20T11:42:22.36	Oakland	37.804	-122.193	5.262	4.2
5	2007-10-31T03:04:54.81	Alum Rock	37.4335	-121.774	9.741	5.45
6	2008-06-04T02:29:04.15	Green Valley	38.24183	-122.184	10.065	3.96
7	2008-09-06T04:00:15.25	Alamo	37.862	-122.008	16.328	4.1
8	2011-01-08T00:10:16.74	Seven Trees	37.28717	-121.658	9.593	4.1
9	2011-08-24T16:57:44.12	San Leandro	37.74517	-122.151	8.632	3.38
10	2011-10-20T21:41:04.26	Berkeley	37.857	-122.253	7.989	3.95
11	2011-10-21T03:16:05.26	Berkeley	37.86083	-122.257	7.939	3.84
12	2011-10-27T12:36:44.46	Berkeley	37.86666	-122.261	7.99	3.62
13	2012-02-16T02:09:14.05	Crockett	38.07667	-122.233	8.827	3.55
14	2012-02-16T17:13:20.58	Crockett	38.07817	-122.234	8.247	3.54
15	2012-03-16T02:56:49.65	Crockett	38.07367	-122.23	7.464	2.48*
16	2014-01-14T04:18:17.60	Vallejo	38.0985	-122.238	8.157	2.76*
17	2014-04-28T21:53:24.41	Vallejo	38.093	-122.253	8.024	2.23*
18	2014-08-24T10:20:44.07	American Canyon	38.21517	-122.312	11.12	6.02
19	2014-08-24T12:47:12.55	Napa	38.23833	-122.343	8.439	3.6
20	2014-08-26T00:02:34.67	Napa	38.24033	-122.341	6.927	2.79*
21	2014-08-26T12:33:16.84	American Canyon	38.1785	-122.301	12.577	3.9
22	2014-08-26T12:35:52.99	American Canyon	38.17567	-122.307	11.473	2.7*
23	2014-08-26T13:12:19.96	American Canyon	38.17933	-122.297	10.006	2.71*
24	2014-08-31T08:56:20.83	Napa	38.23583	-122.329	9.55	3.24
25	2014-09-01T01:41:14.29	American Canyon	38.17717	-122.31	9.141	2.47*
26	2014-09-04T10:56:23.17	American Canyon	38.18033	-122.303	10.937	2.93*
27	2014-09-29T07:17:01.22	American Canyon	38.177	-122.303	11.711	2.5*
28	2015-04-01T14:07:47.16	San Pablo	37.97017	-122.352	4.85	2.67*
29	2015-04-02T07:06:03.87	San Ramon	37.792	-121.987	9.89	3.61

*Magnitude is obtained from Md.

Apparent V_s were calculated by varying the azimuthal angles (rotated by 1°) from the two horizontal time series. Figures 6(a) and (b) show the variation in apparent V_s near the ground surface with azimuthal angle for CE68206 and CE68259, respectively. The results show the clear negative correlation of apparent velocities with the PGA along the rotated azimuthal angle in the mainshock. Figure 7(a) and (b) show the variation of apparent wave velocity with PGA for the two geotechnical arrays from all the earthquakes. It shows that the wave velocity decreases near the ground surface as PGA increases, which may indicate nonlinear soil behavior due to strong shaking. ETFs are also calculated at CE68206 and CE68259 and compared with the theoretical transfer functions (TTF) in Figure 8(a) and (b), respectively. The figure shows good agreement between these two transfer functions, especially for the resonance modes, although the amplification factors are different between these due to differences in damping. During the South Napa mainshock, there is a clear broadening of resonance periods near 6-10 Hz at CE68206.

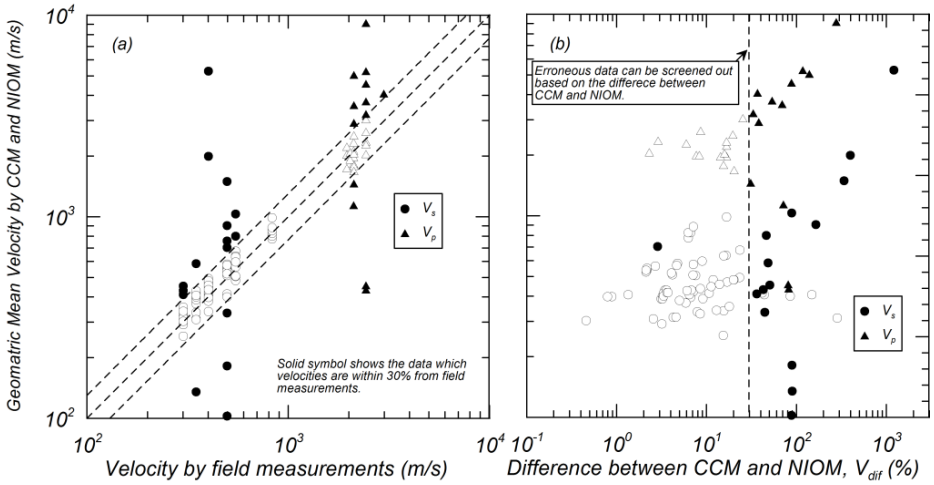

Figure 5. Comparison of apparent wave velocities (a) with field measurements (b) between CCM and NIOM.

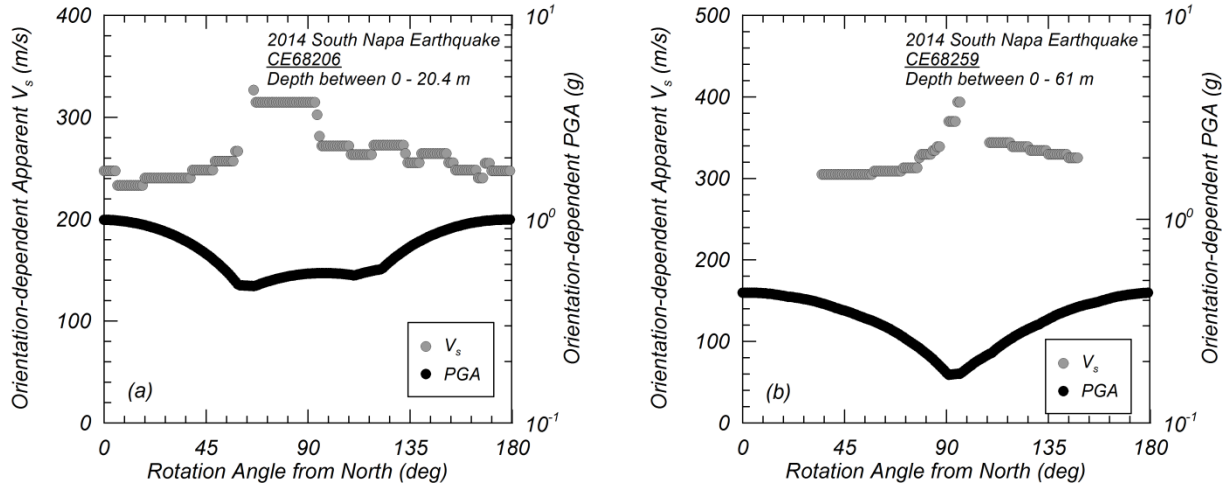

Figure 6. Variation in apparent V_s depending on rotation angle with PGA at (a) CE68206 and (b) CE68259 during the 2014 South Napa earthquake.

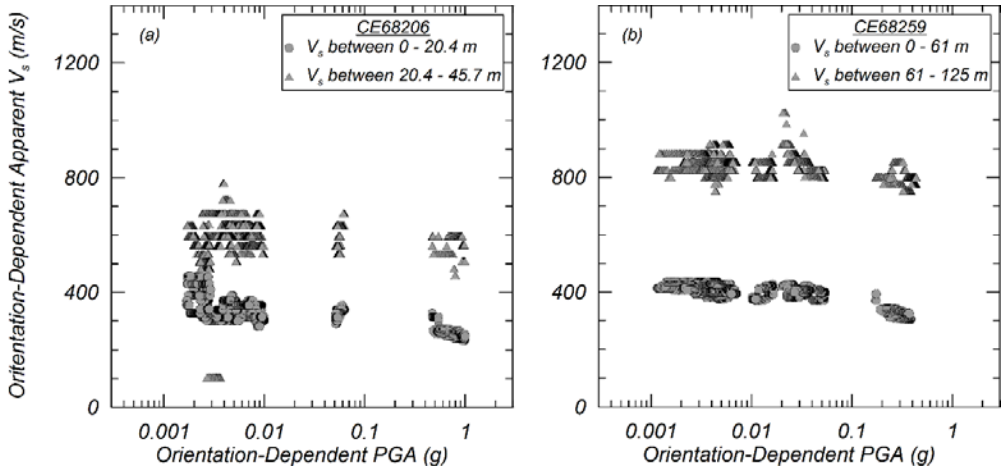

Figure 7. Variation in apparent V_s against PGA at (a) CE68206 and (b) CE68259.

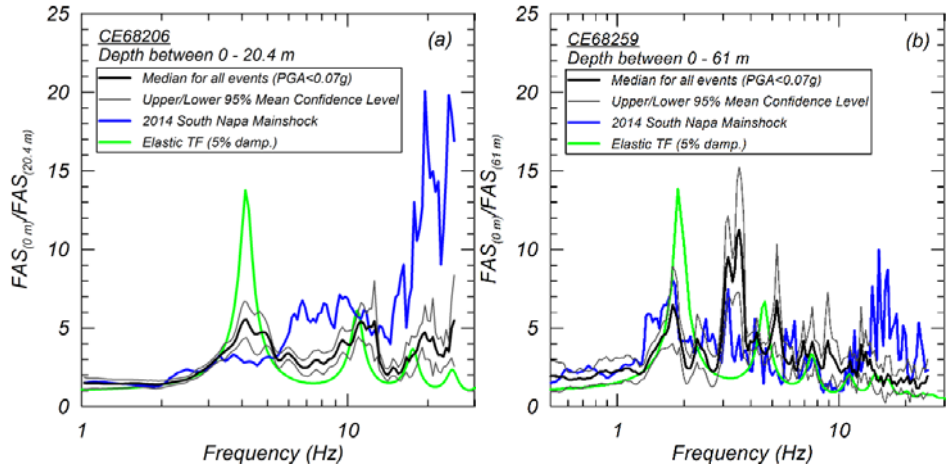

Figure 8. Empirical transfer functions at (a) CE68206 and (b) CE68259.

Identification of Velocity Pulses for Near-Fault Records

Pulses in the velocity time history were observed at near fault stations during the mainshock of the 2014 South Napa earthquake (Kishida et al. 2014a). After the development of the ground motion database, the entire database was analyzed to identify pulse-like records. The methodologies developed by Hayden et al. (2014) and Shahi and Baker (2014) were implemented and compared. Table 4 shows a summary of the recordings identified as pulse-like records in South Napa database; all pulse-like recordings were from the mainshock. A pulse was identified at 7 stations by at least one of the two methods. Differences exist in the calculated pulse period as well as the pulse azimuth (i.e., azimuth of max pulse and azimuth of max peak-to-peak for the Shahi and Baker 2014 and Hayden et al. 2014 methods, respectively) presented in Table 4.

Figure 9 shows example velocity time series, which were identified as pulse-like recordings by both methods. The time series were rotated to the azimuthal angle in which the pulse characteristics were identified. This figure shows maximum velocities of approximately 80 cm/s and clear velocity pulses in both recordings. Figure 10 shows the locations of the stations

where the pulse-like records were identified by either method. Most of the stations were located in the forward directivity region of the fault rupture (e.g. Dreger et al. 2015), whereas the Vallejo – Broadway & Sereno recording site was located in the backward directivity region. The Vallejo – Broadway & Sereno station has a calculated pulse period less than 1.0 s for both methods whereas the other stations in the forward directivity region have pulse periods greater than 1.0 s. The distribution of stations in Figure 10 largely overlaps the station distributions with large positive residuals of PSA (3.0s) in Figure 1(f).

Pulse-like recordings were strongly related to directivity effects in these plots. Similar identifications of pulse-like recordings were performed for the NGA-West2 database (Ancheta et al. 2013). Figure 11 shows scatter plot (R_{rup} versus **M)** of identified pulse-like recordings in the South Napa and NGA-West2 databases. The pulse-like recordings were observed generally within R_{rup} less than 10 km for **M** 5. There was a trend for R_{rup} to increase as **M** increases which could be used to define the near-fault region for design practice.

Table 4. Pulse Identification for recordings from the 2014 South Napa Mainshock

		Hayden et al. (2014)			Shahi and Baker (2014)		
Station Name	RSN	Pulse Identified	Azimuth of Max PPV* (°)	Pulse Period (s)	Pulse Identified	Azimuth of Max Pulse (°)	Pulse Period (s)
Napa College	51	No	160	1.6	Yes	154	2.0
Huichica Creek	89	Yes	171	5.5	Yes	166	2.8
Lovall Valley Loop Rd.	212	Yes	61	3.8	Yes	69	3.6
Fire Station No. 3	217	Yes	62	3.8	Yes	29	4.4
Main St. Napa	219	Yes	56	3.4	No	60	3.9
Atlas Peak	702	Yes	103	2.0	No	177	2.4
Vallejo - Broadway & Sereno	1318	Yes	45	0.6	No	50	0.6

* PPV = Peak-to-Peak Velocity (Hayden et al. 2014)

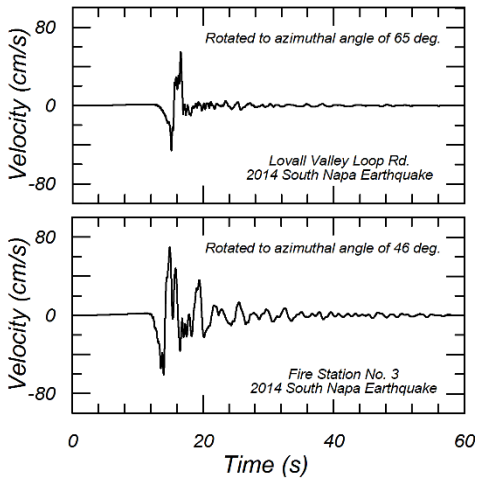

Figure 9. Example of pulse-like time series recorded in the South Napa mainshock.

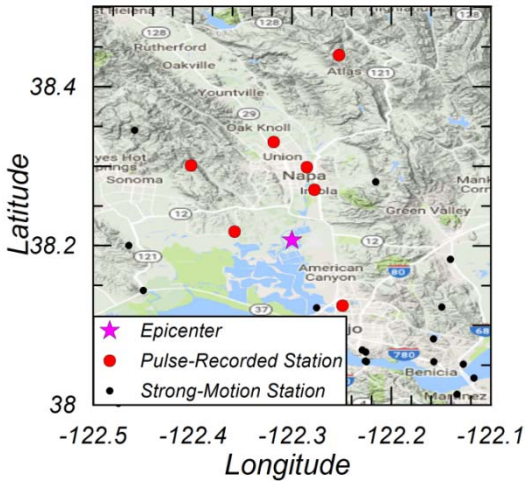

Figure 10. Locations of stations with pulse-like records identified in the 2014 South Napa mainshock.

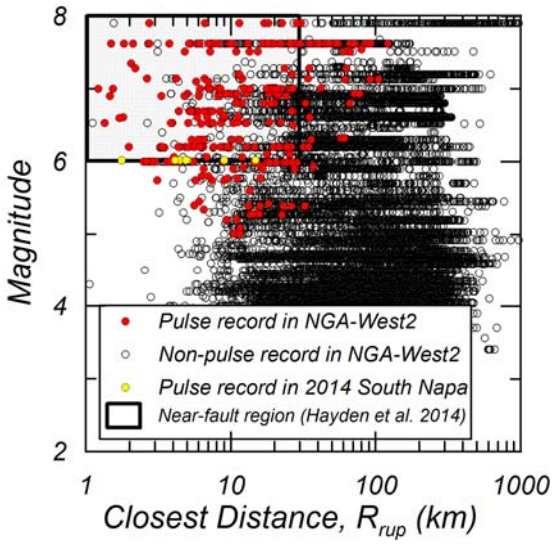

Figure 11. Distribution of pulse-like recordings in the NGA-West2 and South Napa database

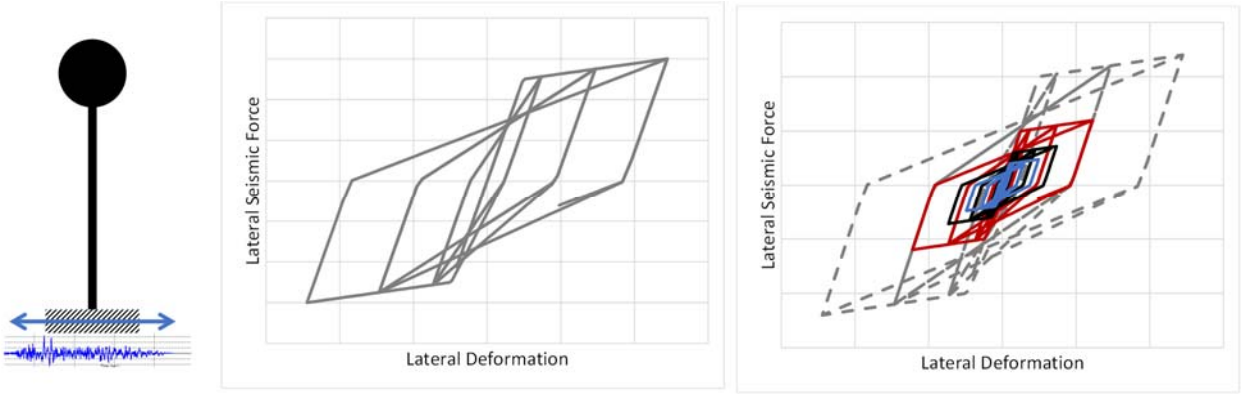

Figure 12. Inelastic-Response Model

Pulse-Motion Characteristics by Inelastic Spectra

Inelastic response spectra were computed for the pulse motions to determine whether the presence of the pulse affected the response of an inelastic system and whether the period shift associated with inelasticity affected the response. The generalized inelastic SDOF model that was used in the analysis is shown in Figure 12, with the analyses performed using OpenSees (McKenna, 1997). This generalized model is consistent with what is assumed in ASCE 7-16. This model was chosen because it represents the critical characteristics of inelastic response – nonlinearity, hysteresis, strength and stiffness degradation due to cycling and ductility. The inelastic spectra were computed for a range of periods and strengths, as shown in Figure 12.

The strength parameter that was used in the analysis is the Estimated-Strength Reduction Factor, Rd, defined as the ratio between the elastic lateral-force demand for design (2/3 MCE_R) and the yield strength of the structure, Vy. This value is equivalent to a combination of the strength-reduction factor R and the strength-amplification factor Ω used in design. (Rd Range:

0.5-10) (Rd >1: structure will yield below 2/3 MCE_R, Rd <1: structure will remain elastic below 2/3 MCE_R). It is important to note that with this definition of Rd, the estimated yield strength of the structure is defined as a function of the site-specific design spectrum. The MCE_R spectrum was computed for each recording station. A graphical representation of the effect of Rd on the design spectra is shown in Figure 13. Because inelastic response of very-stiff structures may yield questionable results, the inelastic spectra were computed for a period range between 0.1 and 10 seconds.

The spectral displacement computed in the inelastic response spectra was normalized to a ductility value to make a graphic comparison over all periods. The inelastic-spectra for two recording stations, "Napa College, RSN 51, JB Dist=3.1 km" and "Lovall Valley Loop Rd, RSN 212, JB Dist=5.0 km", are shown in Figure 14 and 15, respectively, because they display interesting response characteristics. The Napa College record has a pulse at a period between 1 and 2 seconds. This pulse is identified by both identification methods and is evident in the elastic response spectrum, in the Fault-Parallel direction, as shown in Figure 14, top-left figure. The remaining graphs in the figure plot the displacement ductility versus initial elastic period for the Fault-Normal and Fault-Parallel directions, as well as for the azimuth direction for both the Hayden and Shahi pulse characterizations. Each of these inelastic spectra plots the response for different cases of Estimated-Strength Reduction Factor. Figure 14 show that the pulse shape is identified for the cases where the response is near yield (ductility=1, Rd<2). However, for the cases of larger strength reduction, the pulse shape is no longer observed and high ductility demands are evident in all periods below 3 seconds.

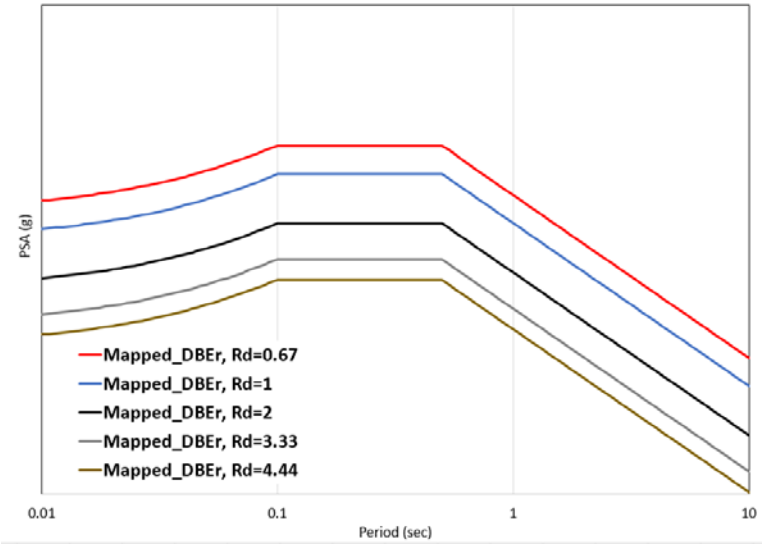

Figure 13. Inelastic Design Spectra

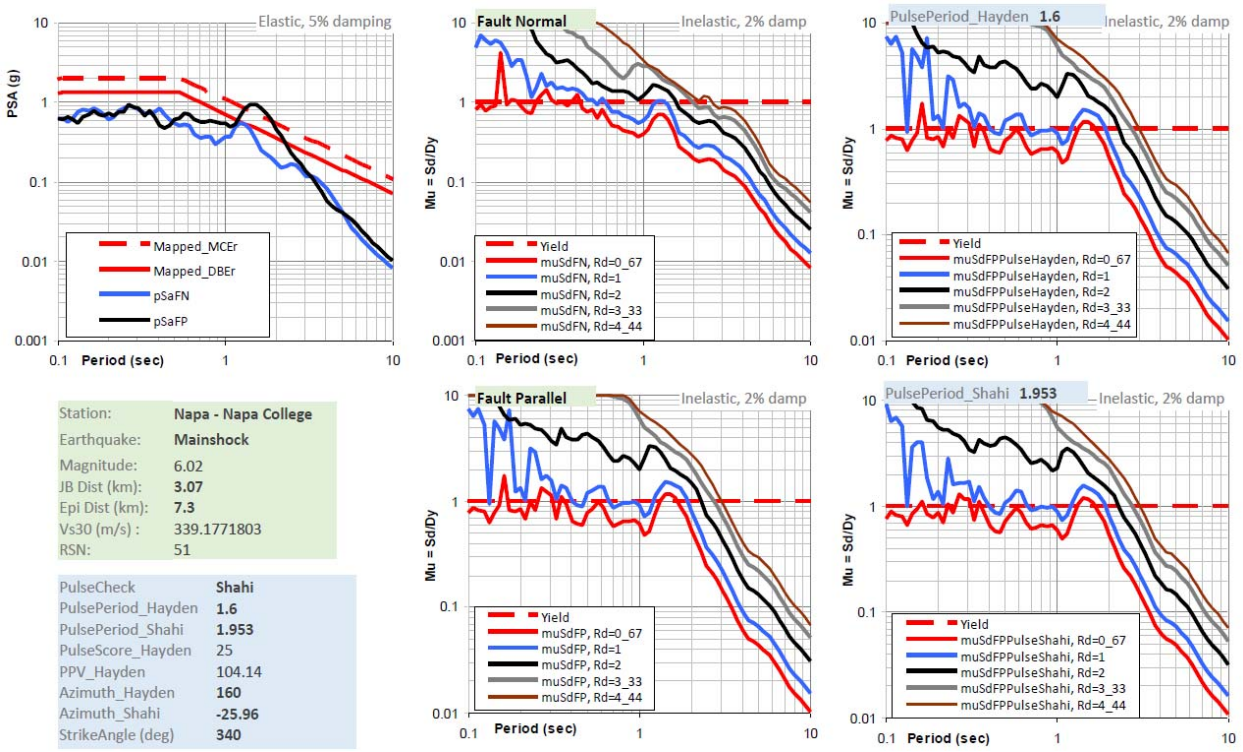

Figure 14. Inelastic Spectra for Napa College, RSN 51, JB Dist=3.1 km

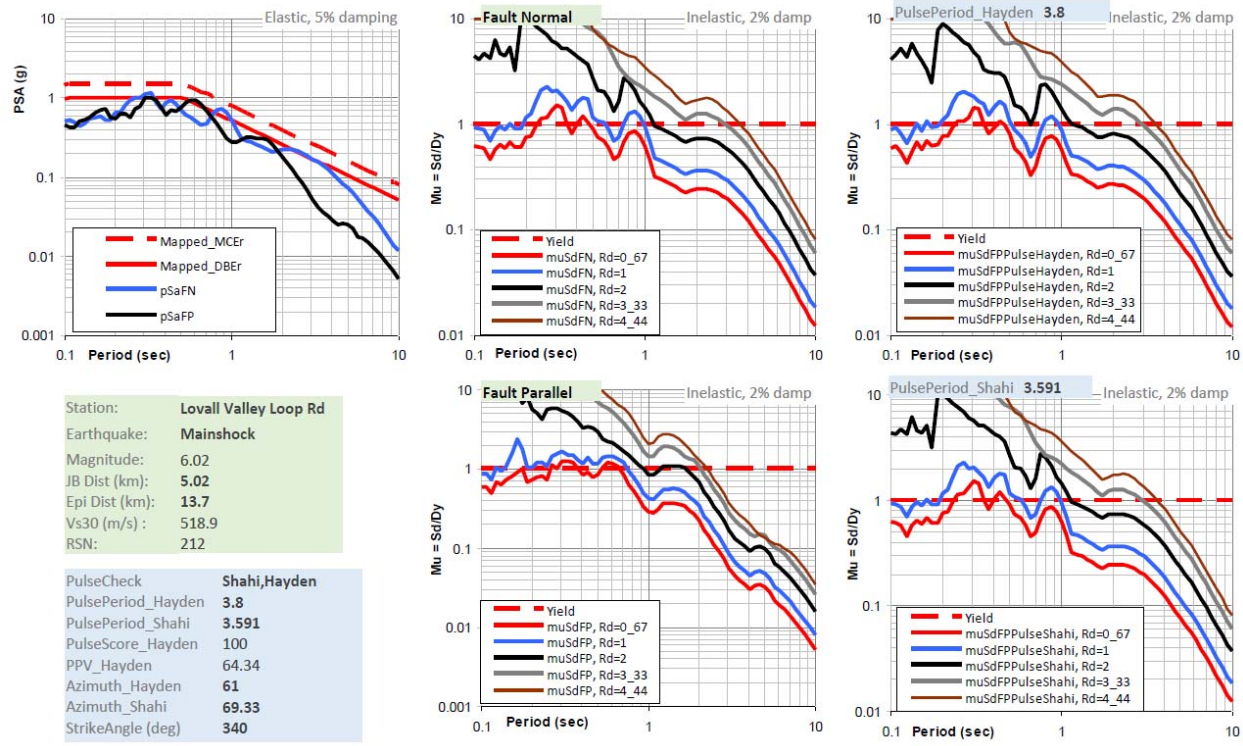

Figure 15. Inelastic Spectra for Lovall Valley Loop Rd, RSN 212, JB Dist=5.0 km

The inelastic spectra for the Lovall Valley Loop Rd record show that the pulse at between 3 and 4 seconds, identified by both methods and observed in the Fault-Normal response, does affect the inelastic response in that period range. The low levels of ductility demand for the cases of the structures with the lowest strength, however, indicate that the pulse does not cause collapse of the structure, unless its ductility capacity is very low. An evaluation of all inelastic response spectra, however, do indicate that the structures at highest risk at the shorter-period structures. This assessment needs to be verified through a rigorous comparison with the response of records without pulse characteristics.

Effect of Pulse-Presence in Inelastic Demands

The larger-magnitude records from the Napa Earthquake were combined with records from the PEER NGAWest-2 Ground-Motion Database with similar magnitude and distance characteristics. The two sets of ground-motion records were flagged based on whether they had a pulse or not, irrespective of the orientation of the pulse, and a record was considered to have a pulse if it me either of the velocity-pulse definitions was met. The records were used in the as-recorded orientation and in the Fault-Normal and Fault-Parallel. As a result, four time histories were used for each database record.

The inelastic models presented in the previous section, with a spectrum of elastic periods and lateral-strength capacities, were subjected to the large number of ground motions. For each SDOF analysis, the inelastic displacement ductility demand was computed as the ratio between the maximum displacement and the structure's yield displacement. When this ductility demand is computed versus the elastic pseudo-spectral acceleration of the record at the same period (including the scale factor), we can observe the effects of the presence of a velocity pulse in the record, as shown for different Effective-Strength Ratios in Figure 16 and Figure 17, Rd=4.44 and Rd=2.0, respectively. The data show a methodology for determining the effects of the velocity pulse. There are cases where there are cases where there is a bias toward a higher ductility demand in records containing a pulse, but for the case 1D analysis, such as this one, it is important to determine a consistent azimuth for the pulse for better record classification. It is worth noting that the effect of the pulse is observed even in the response of systems with a low elastic period, as expected when period elongation is taken into account.

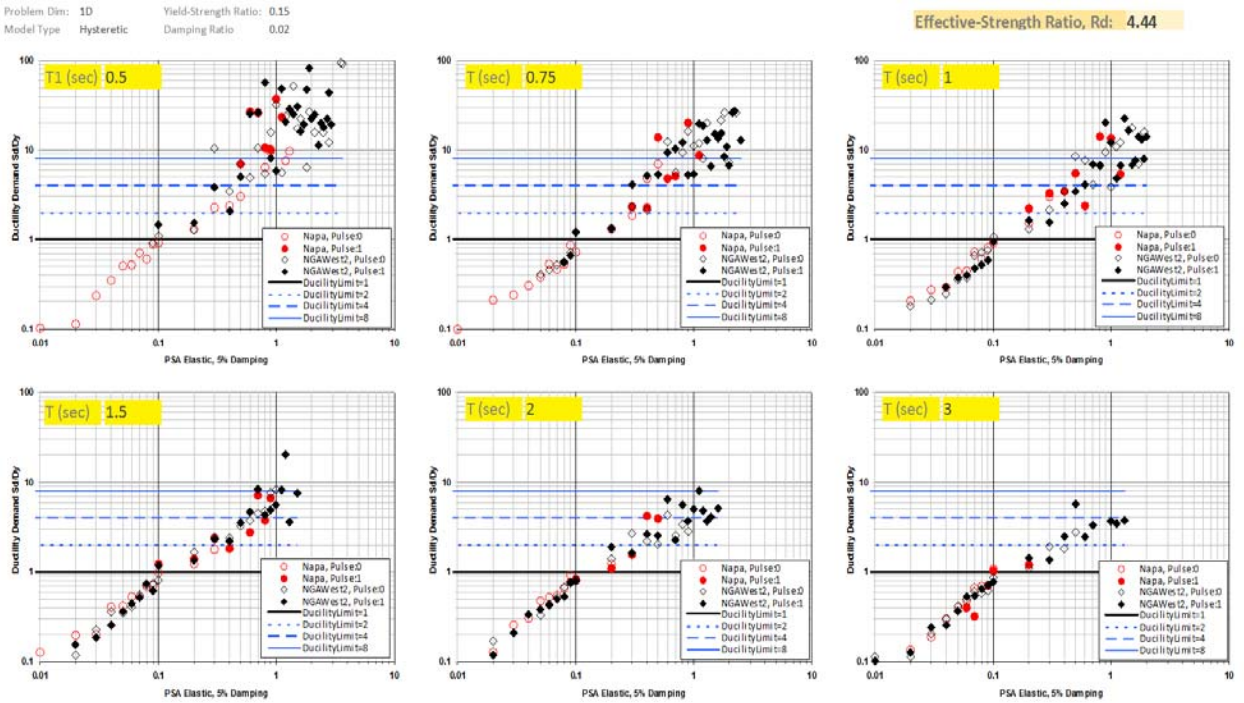

Figure 16. Effect of Velocity Pulse on Ductility Demand vs. Elastic Spectral Ordinate, Rd=4.44

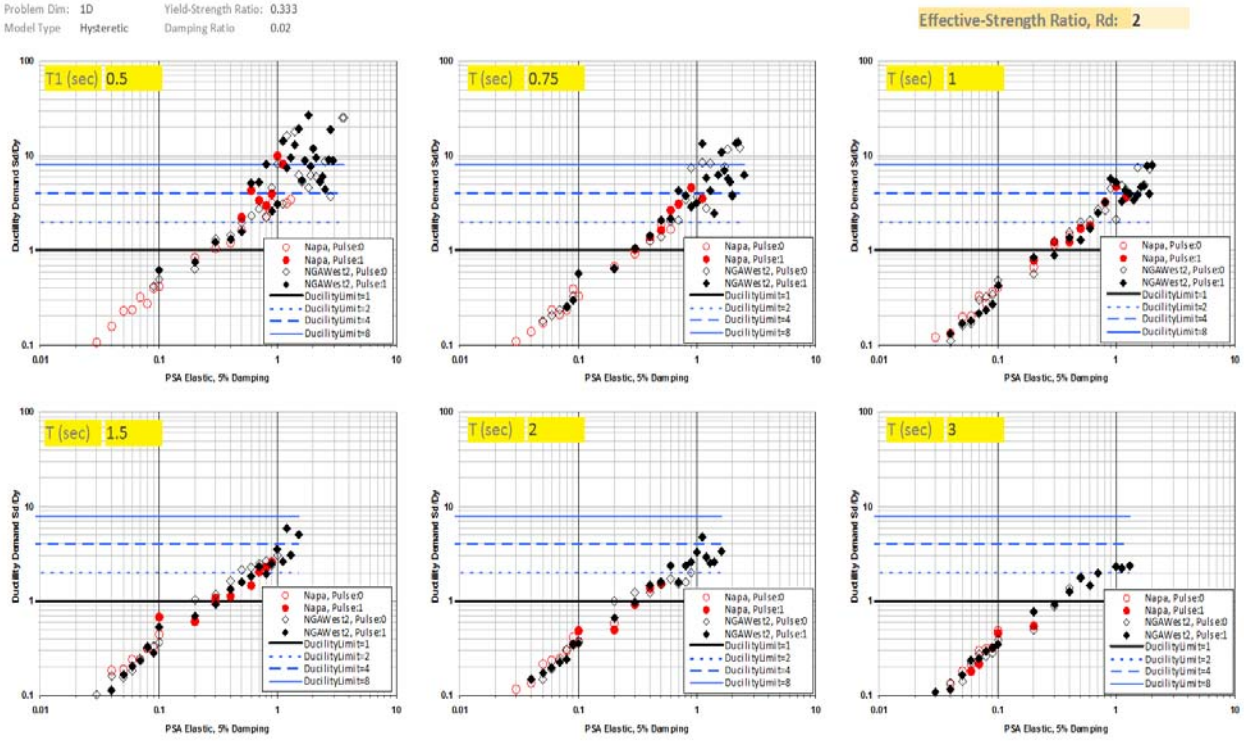

Figure 17. Effect of Velocity Pulse on Ductility Demand vs. Elastic Spectral Ordinate, Rd=2.0

Conclusions

Ground motion characteristics of the 2014 **M**6.0 South Napa earthquake have been investigated. The ground motion database was developed by collecting the time series from one foreshock, mainshock and three aftershocks from various agencies. Shear wave velocity profiles were also measured by the Spectral Analysis of Surface Wave Dispersion (SASW) technique at 15 selected strong-motion stations. Combining these data, a ground motion database was developed, and compared to GMMs in NGA-West2 studies. The results show the stronger attenuation of PGA for these events compared to the median of NGA-West2 models, indicating regional attenuation in this region of northern California Bay Area is greater than predicted by the average GMM. This observation was similar to those by Baltay and Boatwright (2015). The study also reviewed time histories from the two geotechnical downhole arrays operated at the south side of the Carquinez Bridge (I-80), which recorded PGAs of approximately 1g and 0.42g, respectively, during the 2014 South Napa mainshock. The apparent wave velocities computed from the downhole arrays show the clear reduction in V_s during mainshock, indicating that reduction of soil stiffness occurred due to strong shaking. The ETFs were also computed from downhole records and compared to the TTF from V_s profiles. The comparison shows good agreement of resonance periods especially at CE68206, where the maximum PGA of 1g was recorded. The ETF also shows the clear broadening of resonance periods at CE68206 during mainshock, which is consistent to the reduction of V_s in apparent wave velocities. Therefore, evaluations based on one-dimensional wave propagation reasonably explain the downhole array observations in mainshock, which is consistent with the results of Çelebi et al. (2015). The pulse-like velocity time series were investigated by using Hayden et al. (2014) and Shahi and Baker (2014) approaches and utilizing the South Napa and NGA-West2 databases developed in this study. In the South Napa earthquakes, 7 records from mainshock are identified as pulse-like, where most of these stations were located in the forward directivity region. The pulse periods estimated by these two methods were mainly between 2.0 – 4.4 s. The distributions of these stations were consistent with the regions where the positive residuals were observed for PSA(3.0s) compared with GMMs from NGA-West2 studies. The comparison of near-fault regions by pulse-like records between South Napa earthquake and NGA-West2 database also showed that these are reasonably consistent, and increase as magnitude increases. Inelastic response spectra for the recorded ground motions can be used to gain further insight into the expected response of structures with different stiffness (period) and strength characteristics. With a more consistent definition of the pulse azimuth, further studies beyond the scope this project are recommended so that the inelastic-response analyses can be used to compute fragility functions that take into account the presence of a velocity pulse.

Acknowledgements

The project acknowledges Tony Shakal and Moh Huang (CSMIP) for providing the suspension profiles, boring logs and numerous discussions. The assistance by Tom Shantz, Caltrans, who assisted with access at the Carquinez Bridge SASW sites is greatly appreciated. The authors also acknowledge Prof. Stewart and Dr. Gutierrez for providing V_{s30} estimates, and Dr. Aagaard for basin depths at strong-motion stations. The project is funded by CSMIP and the California Department of Transportation and those funds are gratefully acknowledged. The views and conclusions contained in this document are those of the authors and should not be interpreted as necessarily representing the above organizations

References

Aagaard B.T., Graves R.W., Rodgers A., Brocher T.M., Simpson R.W., Dreger D., Peterson N.A., Larsen S.C., Ma S., Jachens R.C. (2010). Ground-motion modeling of Hayward fault scenario earthquakes, Part II: Simulation of long-period and broadband ground motions, Bull. Seismol. Soc. Am., 100(6): 2945–2977.

Abrahamson, N. A., Silva, W. J., and Kamai, R., 2014. Summary of the Abrahamson, Silva, and Kamai NGA-West2 ground-motion relations for active crustal regions, Earthquake Spectra 30, 1025–1055.

Ancheta, T. D., Darragh, R. B., Stewart, J. P., Seyhan, E., Silva, W. J., Chiou, B. S.J., Wooddell, K. E., Graves, R. W., Kottke, A. R., Boore, D. M., Kishida, T. Donahue, J. L. (2013), "PEER NGA-West2 Database", Pacific Earthquake Engineering Research Center, PEER Report 2013/03.

Baltay, A. S. and Boatwright, J. (2015). Ground-Motion Observations of the 2014 South Napa Earthquake, Seismological Research Letters Volume 86, Number 2A, doi: 10.1785/0220140232.

Boore, D. M., A. Azari Sisi, and S. Akkar (2012). Using pad-stripped acausally filtered strong-motion data, Bull. Seismol. Soc. Am. 102 751-760.

Boore, D.M., J.P. Stewart, E. Seyhan, and G.M. Atkinson (2014). NGA-West 2 equations for predicting PGA, PGV, and 5%-damped PSA for shallow crustal earthquakes, Earthquake Spectra 30, 1057-1085.

Bozorgnia, Y., Abrahamson, N. A., Atik, L. A.,Ancheta, T. D.,Atkinsone, G. M., Baker, J. W.,Baltay, A., Boore. D. M.,Campbell, K. W., Chiou, B. S.-J.,Darragh, R., Day, D., Donahue, J., Graves. R. W., Gregor, N., Hanks, T., Idriss, I. M., Kamai, R., Kishida, T., Kottke, A., Mahin, S. A., Rezaeian, S., Rowshandel, B., Seyhan, E., Shahi, S., Shantz, T., Silva, W., Spudich, P., Stewart, J. P., Watson-Lamprey, J., Wooddell, K., and Youngs, T. (2014). "NGA-West2 Research Project". Earthquake Spectra, EERI, August 2014, Vol. 30, No. 3, pp. 973-987.

Campbell, K. W., and Bozorgnia, Y., (2014). NGA-West2 ground motion model for the average horizontal components of PGA, PGV, and 5%-damped linear Response Spectra, Earthquake Spectra 30, 1087–1115.

Çelebi, M., Ghahari, S. F. and Taciroglu, E. (2015), Unusual Downhole and Surface Free-Field Records Near the Carquinez Strait Bridges during the 24 August 2014 Mw 6.0 South Napa, California, Earthquake, Seismological Research Letters Volume 86, Number 4. doi: 10.1785/0220150041.

CESMD (Center for Engineering Strong Motion Data) (2014), http://www.strongmotioncenter.org/ (last accessed September 2016).

Chiou, B. S.-J., and Youngs, R. R., (2014). Update of the Chiou and Youngs NGA ground motion model for average horizontal component of peak ground motion and response spectra, Earthquake Spectra 30, 1117–1153.

Chiou, B., Darragh, R., Gregor, N., and Silva, W. (2008), NGA project strong-motion database, Earthquake Spectra, Vol. 24, No. 1, pp. 23–44.

Darragh B, Silva W, Gregor N (2004) Strong motion record processing procedures for the PEER center. In: Proceedings of COSMOS workshop on strong-motion record processing. Richmond, California, pp 1–12.

Dreger, D. S., Huang, M.-H., Rodgers, A., Taira, T. and Wooddell, K. (2015), Kinematic Finite-Source Model for the 24 August 2014 South Napa, California, Earthquake from Joint Inversion of Seismic, GPS, and InSAR Data, Seismological Research Letters Volume 86, Number 2A, pp327-334, doi: 10.1785/0220140244.

Elgamal, A. W., Zeghal, M., Tang, H. T. and Stepp, J. C., "Lotung Downhole Array. I: Evaluation of Site Dynamic Properties", J. Geotech. Engrg., 1995, 121(4): 350-362.

Goulet, C. A., Kishida, T., Cramer, C. H., Darragh, R. B., Silva, W. J., Hashash, Y. M. A., Harmon, J., Stewart, J. P., Wooddell, K. E., Youngs R. R. (2014), "PEER NGA-East Database", Pacific Earthquake Engineering Research Center, PEER Report 2014/09.

Haddadi, H. R. and Kawakami, H. (1998), Modeling Wave Propagation by using Normalized Input-Output Minimization (NIOM) Method for Multiple Linear Systems, Doboku Gakkai Ronbunshu, Vol. 1998 (1998) No. 584 P 29-39

Hayden, C. P., Bray, J. D. and Abrahamson, N. A. (2014), Selection of Near-Fault Pulse Motions, J. Geotech. Geoenviron. Eng., 2014, 140(7): 04014030.

Kishida, T., Kayen, R.E., Ktenidou, O.-J., Silva, W.J., Darragh, R.B. and Watson-Lamprey, J. (2014b), PEER Arizona Strong-Motion Database and GMPEs Evaluation, Pacific Earthquake Engineering Research Center, University of California, Berkeley, CA, PEER Report 2014/09.

Kishida, T., Wang, S., Mazzoni, S., Markham, C., Lu, Y., Bozorgnia, Y., Mahin, S, Bray, J., Panagiotou, M., Stewart, J., Darragh, R., Abrahamson, N., Hollenback, J., Gutierrez, C., Chiou, B., Muin, S., Dreger, D. (2014a), "PEER Preliminary Notes and Observations on the August 24, 2014, South Napa Earthquake, 1. Strong motion records", Pacific Earthquake Engineering Research Center, PEER Report 2014/09.

Seyhan E, Stewart JP, Ancheta TD, Darragh RB, Graves RW (2014): NGA-West2 Site Database. Earthquake Spectra, 31(3), 1007-1024.

Shahi, S. K. and Baker, J. W. (2014), An Efficient Algorithm to Identify Strong-Velocity Pulses in Multicomponent Ground Motions, Bulletin of the Seismological Society of America, Vol. 104, No. 5, pp. 2456–2466.

Waldhauser, F. and Ellsworth, W. L. (2000), A Double-Difference Earthquake Location Algorithm: Method and Application to the Northern Hayward Fault, California, Bulletin of the Seismological Society of America, 90, 6, pp. 1353–1368, December 2000.

Wills, C. J., Gutierrez, C. I., Perez, F. G. and Branum, D. M. (2015), "A Next Generation VS30 Map for California Based on Geology and Topography", Bulletin of the Seismological Society of America, Vol. 105, No. 6, pp. –, December 2015, doi: 10.1785/0120150105.

DEVELOPMENT AND EVALUATION OF GROUND MOTION INTENSITIES FOR RECORD SELECTION AND SCALING FOR RESPONSE HISTORY ANALYSES

Eduardo Miranda and Héctor Dávalos

John A. Blume Earthquake Engineering Center
Dept. of Civil and Environmental Engineering
Stanford University, Stanford, CA

Abstract

This study evaluates several possible parameters used to quantify the intensity of grouns motions and its correlation with strong nonlinear structural response and collapse. In particular, it compares the dispersion of structural collapse capacities obtained using four different ground motion intensity measures (IMs): (1) $Sa(T_1)$; (2) $Sa(T_1)$ adjusted using ε; (3) an IM consisting spectral acceleration averaged over a period range (Sa_{avg}); and (4) a new IM termed filtered incremental velocity (*FIV*). Results suggest that $Sa(T_1)$ is the least efficient IM whereas Sa_{avg} and *FIV* are the best IM parameters. Additionally, this paper investigates the influence that record scaling has on estimating probabilities of collapse of SDOF and MDOF systems. Results suggest that a systematic bias is introduced by scaling ground motions and that the bias is strongly dependent on the period of vibration and the lateral strength of the system.

Introduction

The use of nonlinear response history analyses is starting to become more common in structural engineering practice due to the adoption of Performance Based Earthquake Engineering, PBEE. This type of analysis is believed to be the most reliable analytical tool to estimate the seismic performance of a structure.

The process of selection and scaling of ground motions using an intensity measure (IM) is of paramount importance as it will influence the accuracy with which the structural response is estimated. Even when some guidelines suggested to assemble a ground motion set using records with causal parameters that are consistent with those that control the desired design spectrum, early studies conducted by Prof. Cornell and his students (Bazzurro and Cornell 1994, 2002; Bazzurro et al. 1998; Jalayer and Cornell, 2003; Luco and Cornell, 2007; Shome et al., 1998) pointed out that selecting records based on causal parameters requires a very large number of ground motions in order to provide adequate results. The reason behind this is the associated significant record-to-record variability in the structural response. Therefore, they proposed to use the five percent damped spectral acceleration at the fundamental period of the structure, $Sa(T_1)$, as the IM and to scale the records to the same spectral ordinate when computing the structural response. By following this procedure, they observed a reduction in record-to-record variability and, therefore, reduced the number of ground motions required to achieve a certain level of error in the estimate of the response. After analyzing a couple multiple-degree-of-freedom (MDOF) structures, they noted that scaling records to the same value of $Sa(T_1)$ lead to an average reduction of 40% in the dispersion of peak interstory drift ratios when compared to the results

obtained from records selected based on a relatively narrow range of M_w and source-to-site distances.

One important shortcoming of the use of S*a*(T_1) as the intensity measure is that its efficiency rapidly decreases as the level of nonlinearity in the structure increases. Thus, several researchers have proposed alternative IMs. For example, Baker and Cornell (2005) proposed the use of a vector IM that consists of $Sa(T_1)$ and the ground motion parameter ε. The ground motion parameter ε is defined as the number of logarithmic standard deviations a pseudo acceleration spectral ordinate of ground motion deviates from the median ordinate predicted by a ground motion prediction equation (GMPE). They observed that ε could be used as a *proxy* to the spectral shape and when used together with $Sa(T_1)$ it could lead to an improved estimate of the seismic response of a structure.

Taking advantage of the bias reduction in structural responses that is obtained when ε is considered. Haselton et al. (2009) proposed a simplified procedure for correcting the collapse capacity of a structure when the spectral shape is not considered in the selection of the records by applying an ε-dependent correction factor. Their method uses a general ground-motion set, selected without regard to ε values, and then corrects the calculated structural response distribution to account for the mean ε expected for the specific site and hazard level. This procedure, which has now also been incorporated into the ATC-63 project and the FEMA P-695 document (FEMA, 2009), avoids having to consider the joint probability distribution of $Sa(T_1)$ and ε. Unfortunately, the procedure focuses on correcting the bias and not in the reduction of the variability/dispersion of the collapse intensities. As a matter of fact, and contrary to popular belief, considering ε does very little in terms of reducing the record-to-record variability and therefore the vector IM consisting on $Sa(T_1)$ and ε remains *a relatively inefficient intensity measure*. This means that it does not lead to a significant reduction in dispersion and hence, although it corrects the bias, it still requires a large number of response history analyses in order to estimate the response of the structure with an acceptable level of confidence.

The reason why the consideration of ε does not lead to a significant reduction in dispersion is because ε is not a direct measure of spectral shape but only a proxy as a single spectral ordinate relative to the intensity measured by a ground motion prediction model cannot provide a measure of spectral shape. Moreover, several studies have shown that ε is ineffective in accounting for spectral shape in the case of near-fault pulse-like ground motions (Baker and Cornell, 2008; Bojorquez and Iervolino 2011). In fact, Haselton et al. (2009) when proposing their approximate method to consider the effect of ε explicitly wrote in their paper: "*the approach proposed in this paper should not be applied to near-fault motions with large forward-directivity velocity pulses*". This is very important because this type of ground motions is precisely the one that is more likely to produce the collapse of structures.

As clearly demonstrated by Shome et al. (1998), having an intensity measure that is strongly correlated with strong nonlinear deformations and collapse of structures has enormous practical consequences for structural engineers. Namely, the level of record-to-record variability achieved in the level of structural response is related to the number of records that the engineer must use for obtaining a reliable estimate of the structural response. In particular they noted the required number of ground motions, n, required to estimate the median structural response within a factor of X (e.g., ± 0.1) with 95% confidence would be given by

$$n = 4\left(\frac{\beta}{X}\right)^2 \quad (1)$$

where β is the level of dispersion in the response when using a certain intensity measure IM expressed as the logarithmic standard deviation. From this equation it can be seen that for the same level of desired accuracy, the reduction in the necessary ground motions is proportional *to the square* of the reduction in dispersion. This is extremely important because there is a considerable computational effort involved in each nonlinear response history analysis.

Besides analyzing the efficiency of *Sa* and $Sa(T_1)+\varepsilon$, in this study we propose a couple of new intensity measures. The first one is called Sa_{avg} which is based on averaged spectral accelerations but taking into account spectral ordinates that correspond to periods that are both shorter and longer than the fundamental period of the structure. The second IM is termed *FIV* and is based on a period-dependent version of the incremental velocity (IV) originally proposed by Anderson and Bertero (1985). Note that this new IM is not based on the concept of spectral shape but rather on time-domain features of a ground motion.

The objectives of this study are: (1) the assessment of current and recently proposed intensity measures that are well correlated with strong nonlinear behavior and the collapse of structures. In particular, the proposed study develops a new ground motion intensity measure (IM) that has a better correlation with large inelastic deformations in structures and with collapse than the correlation provided by intensity measures being used today, namely, $Sa(T_1)$, or the more recently proposed vector IM consisting of $Sa(T_1)$ and ε; and (2) the evaluation of scaling bias using $Sa(T_1)$ in structural response of degrading systems, specially focusing in the estimation of the probability of collapse of a structure. In case a bias is introduced, this study will identify the situations in which it is more critical and the use of scale factors should be limited.

Structural Model and Ground Motion Records for the Efficiency Evaluation

MDOF system

The structure used in this study is a four-story steel special moment frame building with reduced beam sections designed by Lignos et al. (2012) according to the 2003 International Building Code and the 2005 AISC seismic provisions. The design base shear coefficient is V/W = 0.082. The first three modal periods of the structure are T_1 = 1.33s, T_2 = 0.43s and T_3 = 0.22.

The nonlinear behavior of the structure is characterized by concentrated plasticity elements at the ends of beams and columns whose hysteretic behavior is governed by a bilinear response with a modified version of the Ibarra-Medina-Krawinkler (IMK) deterioration model calibrated for steel moment frame structures (Ibarra et al. 2005, Lignos et al. 2010). All the nonlinear analyses are conducted using OpenSees (McKenna 2009).

Ground motion records

The ground motions were selected from the Center for Engineering Strong Motion Data (strongmotioncenter.org) and the PEER Next Generation Attenuation NGA2 database (Ancheta et al. 2014) without any special consideration on spectral shapes. The 265 selected records have

magnitudes varying between 6.93 and 7.62, while the Joyner-Boore distance range is between 0 and 27km, and correspond to recordings from stations located on NEHRP site class C or D.

The ground motion set used in this study is a subset of the *MRCD137* set used by Eads et al. (2014) but some records were excluded when the scale factors that were required to trigger collapse exceeded a value of 20. Additionally, the two components of the Lamont 375 Station during the 1999 Duzce earthquake were also excluded due to extremely unusual high-frequency content. For the complete list and main information of the records used, the reader is referred to the final report of this project in the SMIP17 seminar webpage or Eads et al. (2014).

Structural Model and Ground Motion Records for the Scaling Factor Bias Evaluation

SDOF systems

Two 5%-damped SDOF systems with -3% postelastic stiffnesses were used in the analyses. The short period SDOF corresponded to a system with a period of vibration of 0.25s and the long period system corresponded to an SDOF with a period of 1.50s.

The lateral strength was varied using strength reduction factors, R, defined as

$$R = \frac{m \cdot S_a}{F_y} \tag{2}$$

where m is the mass of the system, F_y is its lateral yielding strength and S_a is the pseudo acceleration spectral ordinate. Depending on the SDOF, R factors ranged between 1.5 and 6.

MDOF systems

This study considers two MDOF systems whose structural system consists of reinforced concrete (RC) special moment frames (SMF) designed by Haselton and Deierlein (2007a). The first MDOF is a two-story building with a fundamental period of vibration T_1 = 0.63s and the second is a four-story building with a fundamental period of vibration T_1 = 1.12s. For detailed description of the design of these structures the reader is referred to Haselton et al. (2007a).

The hysteretic behavior of the ends of the beam and column connections is governed by a modified Ibarra-Medina-Krawinkler model calibrated for RC structures (Ibarra et al., 2005, Haselton et al., 2007b). All the analyses were conducted using OpenSees (McKenna 2009).

Ground motion records

The ground motions used were also selected from strongmotioncenter.org and the PEER Next Generation Attenuation NGA2 database (Ancheta et al. 2013).

SDOF systems

For each SDOF system under study, two sets of 30 ground motions were assembled depending on the scale factors that were needed to reach the intensity of the target spectrum.

This target spectrum corresponds to the MCE level from a NEHRP site class C location in downtown Palo Alto, CA (37.452°N, -122.151°W).

The first set, Set A, corresponds to ground motions whose pseudo acceleration spectral ordinate is similar to that of the target scenario, that is, the scale factors required to reach the target intensity are between 0.5 and 1.5. This set will be also called "unscaled set" and will be used as the benchmark set. The second set, Set B, corresponds to ground motions whose pseudo acceleration spectral ordinate has a value in the neighborhood of 1/10 of the spectral ordinate of the target scenario such that the scale factors required for these records to reach the target intensity are between 7.5 and 12.5. This set will be also called "scaled set".

MDOF systems

For each MDOF system under study, three sets of 50 ground motions were assembled depending on the scale factors that were needed to reach the intensity at the fundamental period of vibration of the MDOF of the same target spectrum used for the SDOF systems.

The first set, Set A, corresponds to ground motions whose pseudo acceleration spectral ordinate is similar to that of the target scenario, that is, the scale factors required to reach the target intensity are between 0.5 and 1.5. This set will be also called "unscaled set" and will be used as the benchmark set. The second set, corresponds to ground motions whose pseudo acceleration spectral ordinate has a value in the neighborhood of 1/5 of the spectral ordinate of the target scenario such that the scale factors required for these records to reach the target intensity are between 4.5 and 5.5. This set is called Set B. Finally, the third set corresponds to ground motions whose pseudo acceleration spectral ordinate has a value in the neighborhood of 1/10 of the spectral ordinate of the target scenario such that the scale factors required for these records to reach the target intensity are between 9.5 and 10.5. This set is called Set C.

For the complete list and main information of all the records used for each SDOF and MDOF systems, the reader is referred to the final report of this project in the SMIP17 seminar webpage.

Ground Motion Intensity Measures

This section evaluates the dispersion on the collapse intensities of the four-story steel structure subjected to the 265 ground motion records using different intensity measures. The intensity measures that will be considered are:

a) $Sa(T_1)$
b) $Sa(T_1)$ combined with the correction using spectral shape proxy ε
c) $Sa_{avg}(T_1)$ as proposed by Eads et al. (2015).
d) A newly developed intensity measure called *FIV3*.

The efficiency of the IMs, defined as the level of variability in the structural responses from a set of records having the same intensity level (Luco and Cornell, 2007), will be evaluated by comparing the logarithmic standard deviation, σ_{lnIM} of the estimated collapse intensities.

Sa(T_1)

Given that the most commonly used intensity measure is *Sa(T_1),* we first proceeded to compute the collapse capacities of the structure using this IM. Figure 1 shows the spectral acceleration *Sa*(T_1) by which 265 earthquake ground motions need to be scaled to in order to produce the collapse of the structure. It can be seen that the ground motions intensities, when characterized by *Sa*(T_1), exhibit a very large record-to-record variability with some ground motions producing the collapse of the structure when the record is scaled to a spectral ordinate of 0.51g at T_1 = 1.33s while others need to be scaled to spectral ordinates as large as 3.25g to produce the collapse of the structure. Also shown in the figure is the median collapse intensity which for this structure is 1.0g, the 5 percentile (ground motion intensity at which only 5% of the ground motions produce collapse in the structure) and 95 percentile (ground motion intensity at which 95% of the ground motions produce collapse). In this case the intensity corresponding to the 95 percentile (2.41g) is 4.47 times larger than the intensity corresponding to the 5 percentile (0.54g) indicating a large variability of the ground motion intensity required to produce collapse. The corresponding logarithmic standard deviation, σ_{LnSa} , equals to 0.39. This figure demonstrates the high variability that exists when one is trying to characterize the collapse potential of the structure under a large set of ground motions using a relatively inefficient intensity measure such as *Sa(T_1)*.

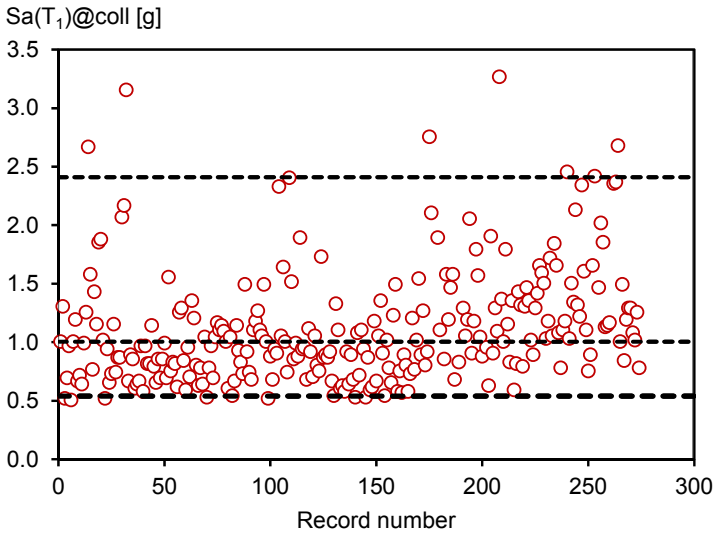

Figure 1. Spectral accelerations at the fundamental period of vibration, Sa(T_1), by which the ground motions need to be scaled to in order to produce the collapse.

Sa(T_1) corrected by ε

Figure 2 presents a plot of the natural logarithm of the *Sa*(T_1) by which the 265 earthquake ground motions need to be scaled to in order to produce the collapse of the building under study as a function of the corresponding ε values. Also shown in the figure is a linear fit regressed to the data. As illustrated in the figure, and as previously noted by Baker and Cornell (2005), the collapse intensity tends to increase as the ε value increases.

The collapse intensities measured using $Sa(T_1)$ were corrected by applying the procedure proposed by Haselton et al. (2009) to account for the effect of ε. This procedure consists in decreasing the intensity producing collapse for records with ε's larger than the target ε and by increasing the intensity producing collapse for records with ε's smaller than the target ε. For this structure designed for a site in Los Angeles, the target ε equals 1.8 (Eads et al., 2014) and it corresponds to the ground motion intensity that has the highest contribution to the mean annual frequency of collapse computed via a collapse deaggregation. Please note that instead of using the Haselton et al. generic slope recommendation that is based on their buildings, here we apply the slope that is specific to this structure.

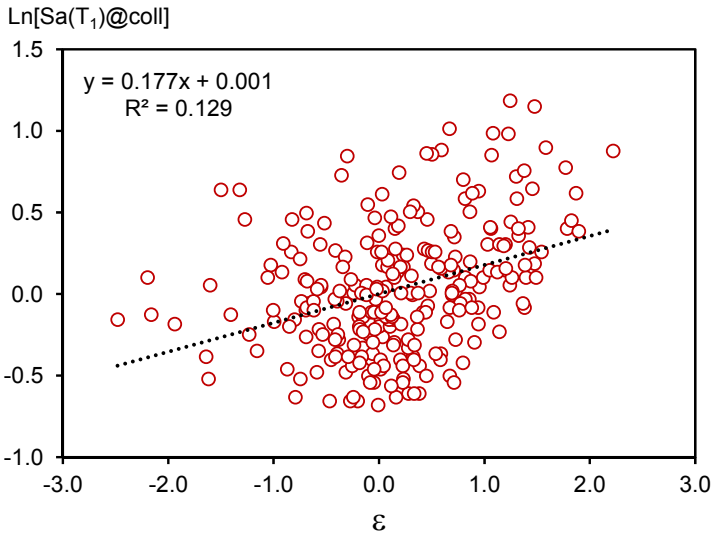

Figure 2. Natural logarithm of the spectral accelerations at the fundamental period of vibration, $Sa(T_1)$, by which the ground motions need to be scaled to in order to produce the collapse plotted as a function of the ε of each record.

The corrected collapse intensities as a function of ε are presented in figure 3. As expected, the bias (the slope of the linear trend) has now been fully eliminated, but a large dispersion remains. Again 5, 50, and 95 percentiles, which are 0.74g, 1.34g, and 3.03g, respectively, are also plotted in the figure with horizontal dashed lines. By comparing figures 1 and 3 it can be seen that, as previously mentioned, considering ε can correct the bias in the median collapse capacity but does not lead to a significant reduction in dispersion. As a matter of fact, for this structure the ratio of corrected collapse intensities corresponding to 95 percentile to 5 percentile equals to 4.1 which is slightly smaller than the ratio of the two percentiles prior to correction for ε which was 4.47. The corresponding logarithmic standard deviation does reduce after the correction is applied to consider the effect of ε, but the reduction is minimal as it only reduces from 0.39 to 0.36. This corresponds to a reduction of approximately 6.6%.

From this results it is seen that while the vector IM comprised by $Sa(T_1)$ and ε can potentially eliminate the bias in the estimation of the median collapse capacity of the structure, it does not lead to a significant reduction in record-to-record variability/dispersion which is a desirable characteristic when nonlinear time history analyses are to be conducted.

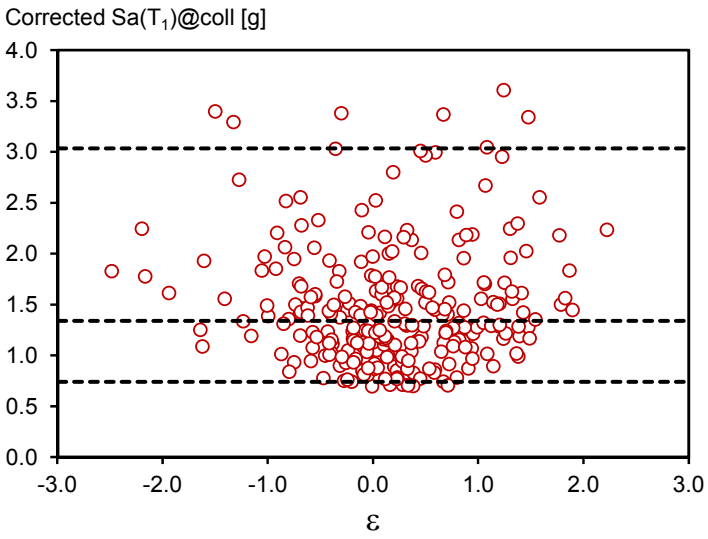

Figure 3. Spectral accelerations that produce collapse in the four-story steel building after correction to take into account the target ε of each record.

Sa_{avg}

The general idea of considering spectral ordinates in a range of periods as a way to measure the damaging potential of an earthquake can be traced back almost a century. Studies conducted by Benioff (1934) and Housner (1952) can be thought as early attempts to consider spectral ordinates from a wide range of periods as an intensity measure.

To the best of our knowledge, Kennedy et al. (1984) conducted the first study that recommended to use a period-dependent range in the averaging of spectral ordinates. They considered the average spectral value between the fundamental period of vibration of the structure (T_1) and a lengthened period. In their study, they noted that the relationship between this average value and the value of $Sa(T_1)$ had an important influence in the nonlinear response of structures. They actually observed a reduction in the variability of their results, which they attributed to the smoothing effect of averaging compared to the use of a single ordinate. More recently, several researchers (e.g. Bianchinni et al. (2009), Bojórquez and Iervolino (2010, 2011), Tsantaki et al. (2012), DeBiasio et al. 2014) have evaluated different pseudo-acceleration averaging schemes focusing on ranges between T_1 and a lengthened period based on the assumption that as the structure degrades, the period of vibration increases. All these studies found a reduction in the dispersion of structural responses when compared to $Sa(T_1)$.

Eads et al. (2014; 2015) were the first studies that recommended to consider periods shorter than T_1 in the averaging range of spectral ordinates. They proposed to use the geometric mean of Sa ordinates between $[0.2 \cdot T_1 - 3 \cdot T_1]$ based on the fact that pulses in the ground motion control the spectral shape of the spectrum at both sides of T_1. This report uses the Sa_{avg} definition proposed by Eads et al. (2015) to evaluate the collapse intensities of the four-story steel structure under study.

Results in figure 3 show the 265 Sa_{avg} values that produce the collapse of the four-story steel MRF structure. The 5, 50 and 95 percentiles, which are 0.49g, 0.70g and 1.08g,

respectively, are also plotted in the figure with horizontal dashed lines. By comparing the record-to-record variability in this figure with that in figures 1, 5, 9, 13, and 17, it can be seen that a significant reduction in dispersion is produced when using the proposed IM. In this case the ratio of the collapse intensities corresponding to 95 percentile to 5 percentile is now 2.21 while this ratio was 4.47 for the case in which $Sa(T_1)$ alone was used as an IM or 4.10 when the vector IM comprised on $Sa(T_1)$ and ε was used. The corresponding logarithmic standard deviation for the proposed scalar IM is 0.21 which is 45% smaller and 41% smaller than the case in which $Sa(T_1)$ alone was used and when $Sa(T_1) + \varepsilon$ was used, respectively. These reductions in dispersion mean that for the same level of confidence in the structural response, one needs to use approximately 31% to 35% of the number of records that would be required when using $Sa(T_1)$ and $Sa(T_1)$ and the correction using ε, respectively.

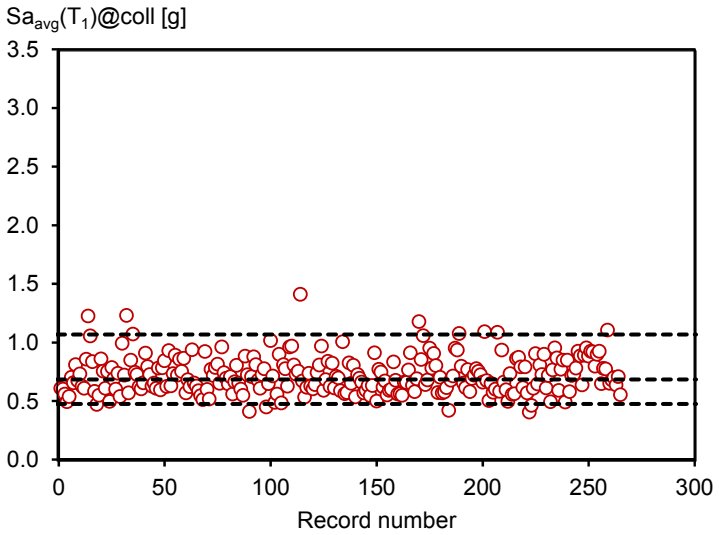

Figure 3. Sa_{avg} intensities by which the ground motions need to be scaled to in order to produce the collapse of the four-story steel structure.

FIV

The filtered incremental velocity, *FIV*, is also based on the concept of incremental velocity, but instead of just focusing on acceleration pulses with large areas, *FIV* is a period dependent intensity measure, hence capturing different intensities for structures with different periods of vibration. The fact that this IM is period dependent and computed from a filtered time acceleration time series aids *FIV* in capturing in a better way damaging pulses for different structures as it focuses on pulses with durations that can induce large inelastic incursions in the structure and disregard high frequency spikes that, depending on the fundamental period of vibration, the structure might not significantly respond to. Moreover, instead of considering only the period-dependent acceleration pulse segment with the largest area, *FIV* considers several pulse segments in the same side of the accelerogram that have the largest area and therefore are more related to large inelastic excursions and structural collapse. Note that *FIV* does not exactly capture the complete damaging acceleration pulses but rather attempts to capture damaging pulse segments. The parameters of *FIV* were determined after several iterations considering variations on the time duration used in the area summation, the number of pulses, and the type and order of the filter.

Figure 4 presents the *FIV* collapse capacities computed. The dashed lines represent the 5, 50, and 95 percentiles with correspond to 253.9cm/s, 359.6cm/s, and 567.8cm/s, respectively. The ratio of the collapse intensities corresponding to 95 percentile to 5 percentile for *FIV3* is 2.23 and the corresponding logarithmic standard deviation for the proposed scalar IM is 0.20 which is 47% smaller and 44% smaller than the case in which $Sa(T_1)$ alone was used and when $Sa(T_1) + \varepsilon$ was used, respectively. Reductions in the logarithmic standard deviation of *FIV* with respect the one computed using $Sa(T_1)$ and $Sa(T_1) + \varepsilon$ mean that by using *FIV*, one needs to use approximately only 27% to 31% of the number of records that would be required when using currently recommended IMs in order to achieve the same level of confidence.

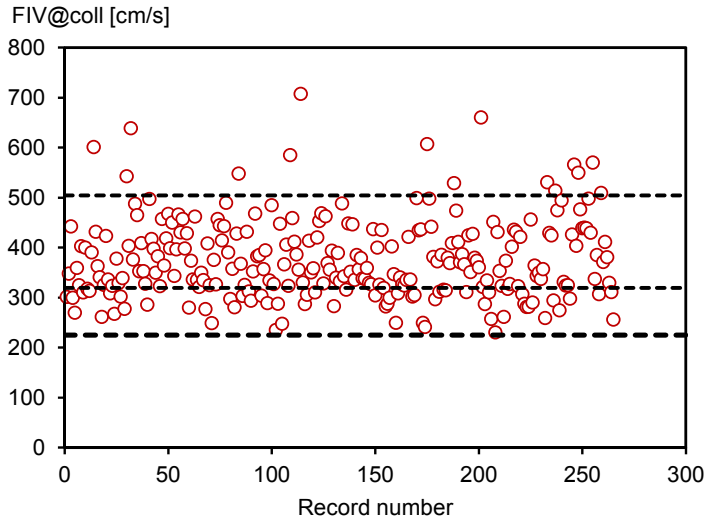

Figure 4. FIV intensities by which the ground motions need to be scaled to in order to produce the collapse of the four-story steel structure.

Figure 5 presents the normalized collapse capacities using $Sa(T_1)$, $Sa(T_1)$ adjusted by considering the spectral shape proxy ε, using Sa_{avg}, and using *FIV*. As it has been mentioned, the reduction in dispersion achieved by either Sa_{avg} or *FIV* is remarkable.

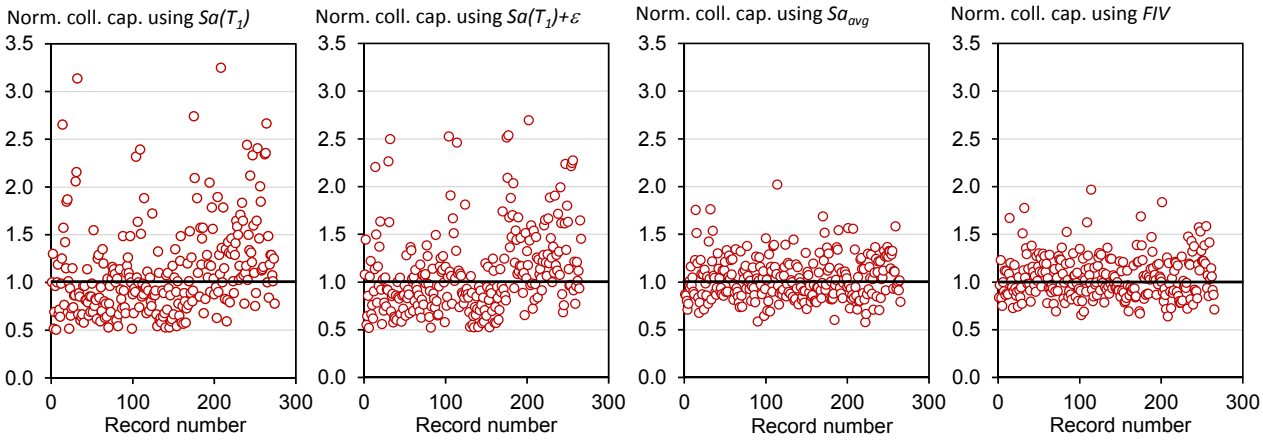

Figure 5. Normalized collapse capacities using different IMs. From left to right: $Sa(T_1)$, $Sa(T_1)$ adjusted using ε, $Sa_{avg}(T_1)$, FIV3.

Scaling factor bias evaluation

The use of scale factors is undoubtedly the most common approach to conduct nonlinear time history analyses at different intensities. The scaling process consists of scaling the acceleration time series until the desired level of the intensity measure is reached. This IM is usually the 5%-damped pseudo acceleration spectral ordinate at the fundamental period of vibration of the structure, $Sa(T_1)$.

Several studies have found contradictory conclusions regarding a possible bias in structural responses that can be introduced by the use of scaling factors. While several assert that the bias in fact exists (e.g., Watson-Lamprey and Abrahamson, 2006; Luco and Bazzuro, 2007; Baker 2007) others have found little evidence to support that claim (e.g., Shome et al., 1999; Iervolino and Cornell, 2005; Zacharenaki et al., 2014).

The following subsections evaluate the scaling factor bias using degrading SDOF and MDOF systems.

SDOF systems

Short period SDOF

The comparison of the median spectrum from the "scaled" and "unscaled" sets is presented in figure 6 which shows a clear difference in the median spectral shapes from both sets. The higher ordinates at all periods (except $T = 0.25$s) mean that, on average, there is a higher content of all frequencies in the records from Set B which might lead to larger structural responses. This observation is in agreement with those previously reported in Luco and Bazzurro (2007) and Baker (2007).

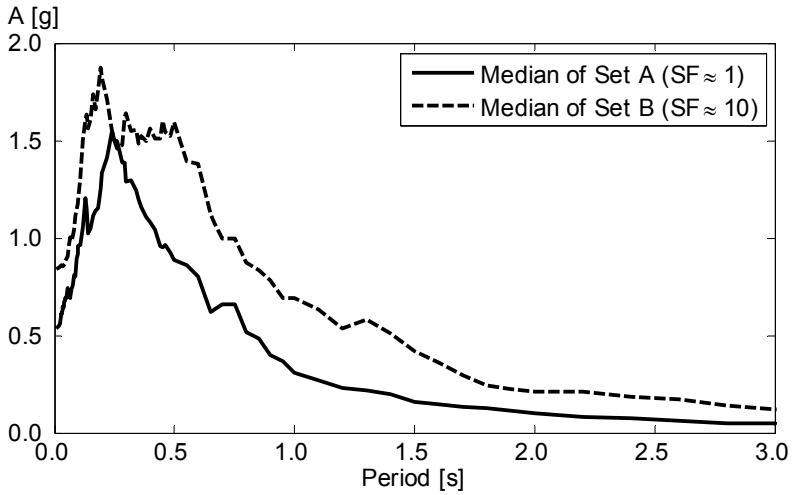

Figure 6. Median Spectra from both ground motion sets used for the T_n=0.25s SDOF

Figure 7 presents the inelastic displacements of the short period SDOF having different strength reduction factors and a positive postelastic stiffness equal to -3% subjected to all records from both sets. This negative postelastic slope is used to capture dynamic instability (Miranda

and Akkar, 2003). Whenever no record caused collapse, the information presented is the same as in figure 7, but when some record triggered collapse, the corresponding probabilities of collapse of each set are reported. In these cases, the dots at the horizontal dashed red lines represent the collapsing cases. Similar conclusions can be made from the results of the degrading SDOF in the sense that the fraction of ground motions that cause collapse in the Set that requires scale factors around 10 is significantly higher than the fraction of collapses obtained using Set A (i.e., ground motions with scale factors close to one). As an example, consider the $T = 0.25$s SDOF with $R = 2.5$, if one uses the Set with scale factors close to one, the probability of collapse (*P(C)*) is equal to zero whereas it corresponds to 23% if the records from Set B are used. Similarly, the probability of collapse for the $T = 0.25$s SDOF having a $R = 4$ equals 30% if the records from Set A are used and 63% if one uses the records with scale factors around 10, that is, Set B.

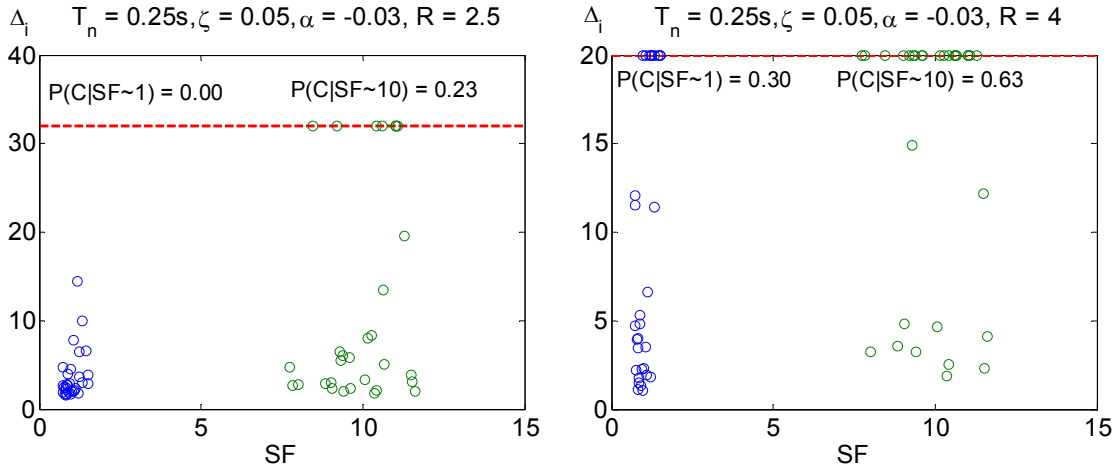

Figure 7. Inelastic displacements of a T=0.25s SDOF with several R factors and α=-3% when subjected to the MCE intensity (blue: SF between 0.5 and 1.5; and green: SF between 7 and 13). The collapse displacement is represented with a horizontal red dashed line.

Long period SDOF

The comparison of the median spectrum from each Set is presented in figure 8 where the difference in the median spectral shapes from both sets is clear. As it was the case for the shorter period SDOF, the higher ordinates at all periods (except $T = 1.5$s) mean that, on average, there is a higher content of all frequencies in the records from Set B and this might lead to larger structural responses.

The results from the degrading SDOF with $T = 1.5$s are presented in figure 9. In this case, there is a bias in the estimation of inelastic displacements and probabilities of collapse introduced by the use of scale factors. The bias in inelastic displacements seems to increase with reductions in the lateral strength of the system. As it was the case for the shorter period SDOF, important overestimations in structural responses are obtained when the Set with scale factors close to 10 is used.

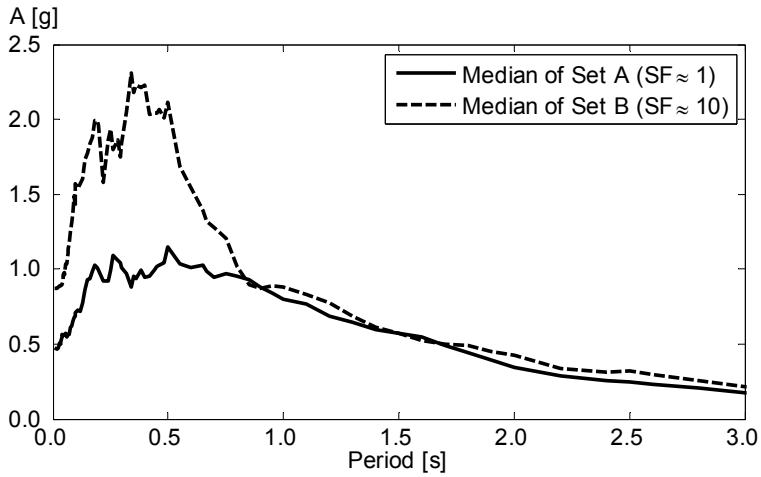

Figure 8. Median Spectra from both ground motion sets used for the T_n=1.5s SDOF

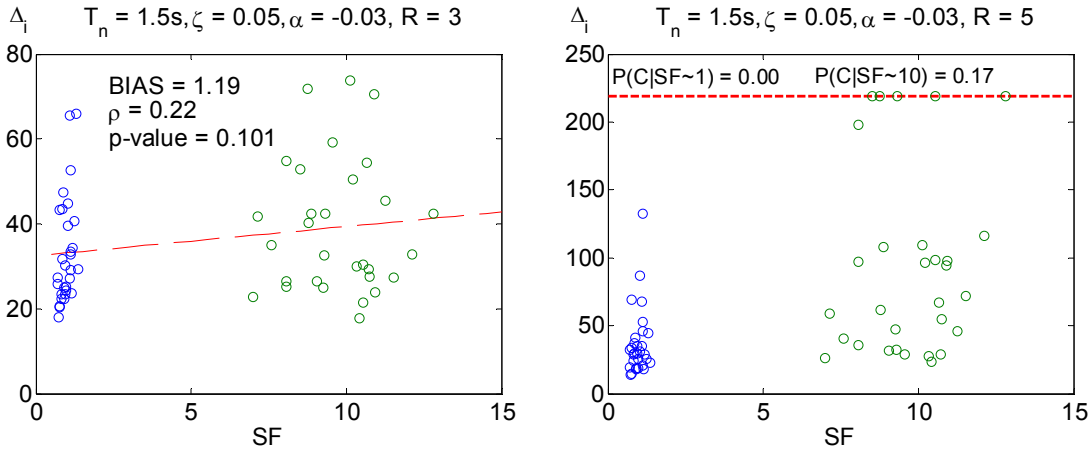

Figure 9. Inelastic displacements of a T=1.5s SDOF with several R factors and α = -3% when subjected to the MCE intensity (blue: SF between 0.5 and 1.5; and green: SF between 7 and 13). The collapse displacement is represented with a horizontal red dashed line.

MDOF systems

Figure 10 presents the median spectra of each of the three Sets used in the evaluation of a possible bias introduced by the use of scale factors. Recall that Set A requires scale factors of approximately 1, Set B scales factor of approximately 5, and Set C scale factors of approximately 10 to reach the target intensity. Panel a) presents the median spectra of each set before scaling and Panel b) presents the median spectra of each set normalized by the spectral ordinate at T_1 = 0.63s. As it was the case for the SDOF systems, these median spectral shapes also reflect the fact that records that have low spectral ordinates and therefore have to be scaled by larger factors to reach the target intensity, have a higher high- and low-frequency content than records whose intensity was already in the neighborhood of the target intensity.

Figure 11 presents the maximum interstory drift ratio (IDR) of the structure when subjected to the 50 ground motions of each set at a target intensity of $Sa(T_1)$ = 1.13g. Results plotted over the red dashed line indicate ground motions that triggered collapse. It is seen that the probability of collapse increases as the scale factors used in the ground motions increase. One

could estimate that the structure has an 18% chance of collapsing at the MCE intensity if scale factors around 10 are used when the 'true' probability of collapse equals only 4%. Even when scale factors of approximately 5 are used to reach the target intensity, the probability of collapse is overestimated by more than a factor of 2.

The second MDOF under study is a four-story structure with a period of vibration of 1.12s. Figure 12 presents the median spectra of each of the three Sets used in the scaling factor bias evaluation. Panel a) presents the median spectra of each set before scaling and Panel b) presents the median spectra of each set normalized by the spectral ordinate at T_1 = 1.12s. Again, the median spectral shapes show that records that originally have low spectral ordinates end up having a higher high- and low-frequency content after scaling than records whose intensity was close to the target intensity which in this case corresponds to 0.8g.

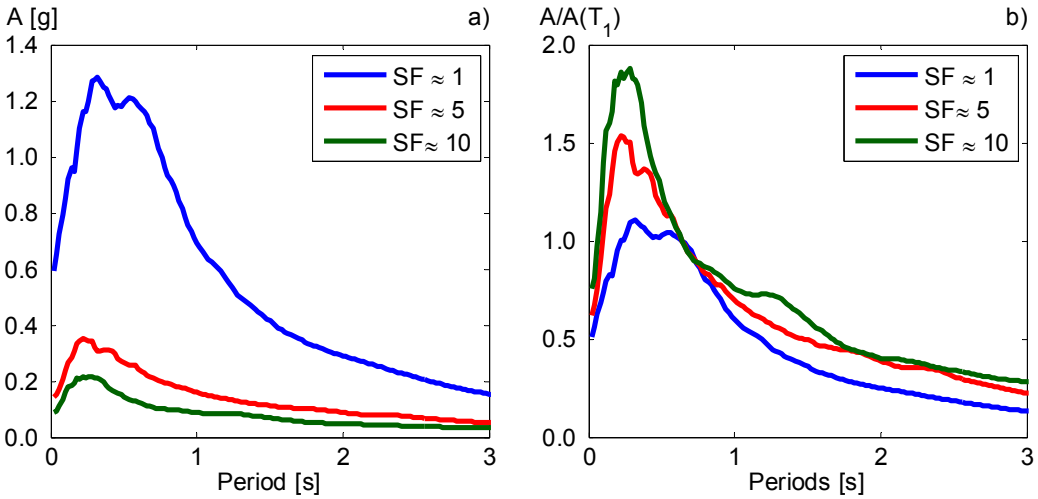

Figure 10. (a) Median spectra of the three sets used for the T_n = 0.63s MDOF without scaling; and (b) Normalized median spectra of the three sets.

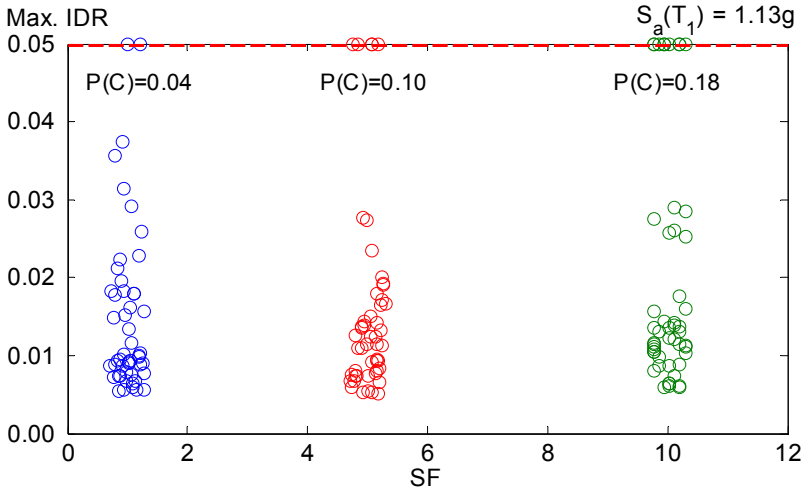

Figure 11. Inelastic displacement demands and collapse probabilities of the T=0.63s two-story MDOF when subjected to the MCE intensity (blue: SF between 0.5 and 1.5; red: scale factors between 4.5 and 5.5; and green: SF between 9.5 and 10.5). The collapse IDR is represented with a horizontal red dashed line.

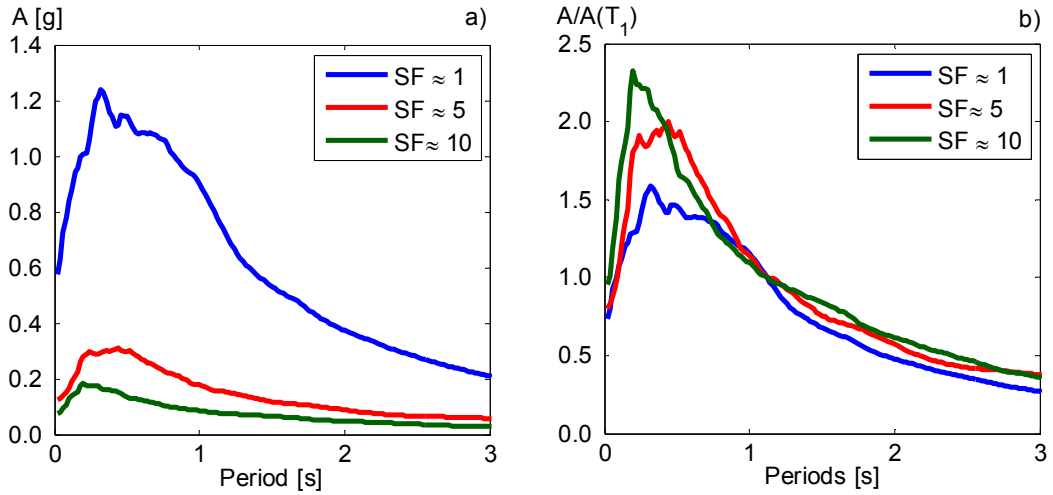

Figure 12. (a) Median spectra of the three sets used for the T_n = 1.12s MDOF without scaling; and (b) Normalized median spectra of the three sets.

The results of the maximum IDR computed with the three sets scaled to the MCE intensity are presented in figure 13. Again, results suggest that the use of scale factors introduce a bias in the collapse risk estimation. For example, using the records with scale factors of approximately 5, the probability of collapse of this structure would be 26% which corresponds to an overestimation by a factor of 2.25. In this case, this ratio is the same if the records from Set C are used.

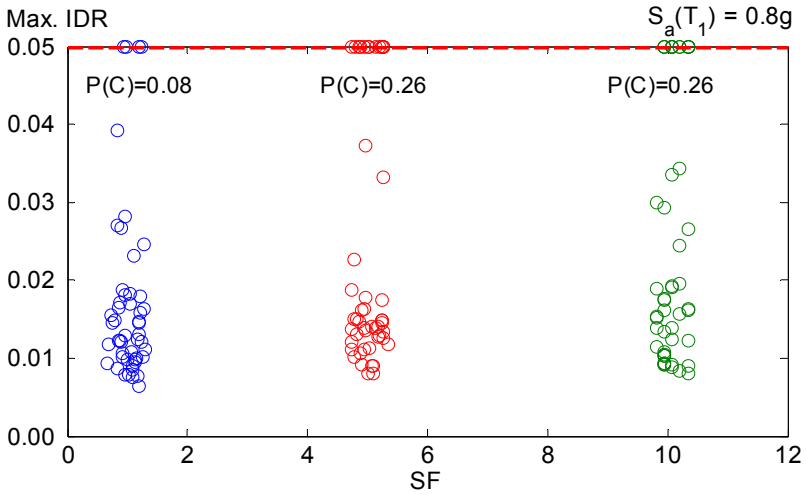

Figure 13. Inelastic displacement demands and collapse probabilities of a T=1.12s four-story MDOF when subjected to the MCE intensity (blue: SF between 0.5 and 1.5; red: scale factors between 4.5 and 5.5; and green: SF between 9.5 and 10.5). The collapse interstory drift ratio is represented with a horizontal red dashed line.

Conclusions and recommendations

Efficiency

This study presented an evaluation of the efficiency of two intensity measures that are commonly used: *Sa(T1)* and *Sa(T1)* adjusted using the spectral shape proxy ε, and two other alternate scalar IM candidates: Sa_{avg} and *FIV*.

A four story special moment frame steel structure was subjected to a set of 265 ground motions to evaluate the dispersion in the collapse capacities obtained with each of the IM candidates. From the results, the following conclusions can be drawn:

1) $Sa(T_1)$ is the IM that leads to the largest dispersion in the collapse capacities estimated, indicating that of the parameters evaluated is also the least correlated with collapse intensities.
2) Even when the bias that is introduced by ignoring the spectral shape of the records when $Sa(T_1)$ is used as the IM is partially reduced by taking into account ε, this correction does very little in reducing the dispersion in the collapse capacities. Furthermore, it is concluded that ε is not a good measure of spectral shape.
3) The scalar intensity measure Sa_{avg} proved to be a much better option than $Sa(T_1)$ and also when this parameter is combined with the spectral shape proxy ε. By considering the spectral ordinates of a wide range of periods, Sa_{avg} indirectly accounts for the underlying pulses in the ground motion record that produce the response spectrum and therefore practically eliminates the bias induced when the spectral shape is ignored. The reduction in the logarithmic standard deviation when Sa_{avg} is 45% and 41% when compared to the one computed using $Sa(T_1)$ alone or with the adjustment using ε, respectively. This reduction mean that, to obtain the desired structural response parameter with the same confidence, if Sa_{avg} is chosen as the IM, one needs to use only one third of the number of records that are required if $Sa(T_1)$ is used, hence leading to a substantial reduction in the computational effort to estimate the probability of collapse of a structure.
4) A new intensity measure termed *FIV* was proposed and it was seen that its efficiency is slightly higher than the one using Sa_{avg}. This new IM is based on a period-dependent incremental velocity computed from a low-pass filtered ground motion and considers the three pulse segments that added together have the largest area.
5) The use of either Sa_{avg} or *FIV* is strongly recommended for seismic collapse estimation as those two IM candidates gave collapse capacities with the least dispersion.

Scaling factor bias

The scaling factor bias evaluation was conducted using both, SDOF and MDOF structures with positive post elastic stiffnesses as well as degrading systems. Following common practice, the intensity measure used in this evaluation was $Sa(T_1)$. Results suggest that:

1) The use of scale factors introduces a systematic bias in the peak inelastic displacement of SDOF systems with positive postelastic stiffness. This bias tend to increase as the lateral strength of the SDOF is decreased. More importantly, the bias is clearly seen and much larger in the short period spectral region (e.g., in an SDOF with T_1 = 0.25s) than structures with long periods of vibration (e.g., SDOFs with T_1 = 1.50s).
2) In the case of the degrading SDOFs, the bias seems to appear on all SDOFs regardless of their period of vibration, but the bias is larger in SDOFs in the short period region.
3) Both MDOF studied presented a clear bias in both, inelastic displacement estimates and collapse probabilities. In general, the bias increases as the scale factor used increases. After analyzing the responses of two MDOF structures with periods of vibration of 0.63s and 1.12s at two high intensity levels, using scale factors of approximately 10 led, on average, to an overestimation of the probability of collapse of a factor of 3.65. Even when

the scale factors required to reach the target intensity are approximately 5, an overestimation of a factor of 2.8 was also be computed.

4) The bias is also higher as the structure is subjected to larger intensity levels. This means that the overestimation caused by the use of large scale factors is higher on the probability of collapse than on the estimation of inelastic displacement demands, especially in mildly inelastic systems.
5) As noted previously by some researchers, ignoring the spectral shape of the records has a major influence in the overestimation of the structural responses.
6) Based on these results, we recommend limiting scale factors to a maximum value of 2.0, recognizing that even those scale factors can introduce a small overestimation of inelastic displacements and collapse probabilities.

Acknowledgements

Several aspects of the research being conducted in this study are based on research conducted by Dr. Laura Eads while she was a doctoral student working under the guidance of the first author. Her work provides the basis of one of the spectral-based intensity measure being evaluated in this study and have also provided some guidance for the exploration of new improved intensity measures based on time domain features of the acceleration time histories.

This study was supported by the California Strong Motion Instrumentation Program of the California Geological Survey. Their financial support is gratefully acknowledged. Special thanks are given to Anthony Shakal, Moh Huang as well as members of the Strong Motion Instrumentation Advisory Committee for their comments and suggestions.

The second author acknowledges financial support from *Consejo Nacional de Ciencia y Tecnología* (CONACYT) in Mexico and the John A. Blume Fellowship to pursue his doctoral studies at Stanford University under supervision of the first author.

References

Anderson, J. C., & Bertero, V. V. (1987). Uncertainties in establishing design earthquakes. *Journal of Structural Engineering*, *113*(8), 1709-1724.

Ancheta, T. D., Darragh, R. B., Stewart, J. P., Seyhan, E., Silva, W. J., Chiou, B. S. J., & Kishida, T. (2014). NGA-West2 database. *Earthquake Spectra*, *30*(3), 989-1005.

Baker, J. W., & Allin Cornell, C. (2005). A vector-valued ground motion intensity measure consisting of spectral acceleration and epsilon. *Earthquake Engineering & Structural Dynamics*, *34*(10), 1193-1217.

Baker, J. W. (2007, December). Measuring bias in structural response caused by ground motion scaling. In *8th Pacific Conference on Earthquake Engineering, Singapore* (Vol. 8).

Baker, J. W., & Cornell, C. A. (2008). Vector-valued intensity measures for pulse-like near-fault ground motions. *Engineering structures*, *30*(4), 1048-1057.

Bazzurro, P., & Cornell, C. A. (1994). Seismic hazard analysis of nonlinear structures. II: Applications. *Journal of Structural Engineering*, *120*(11), 3345-3365.

Bazzurro, P., Cornell, C. A., Shome, N., & Carballo, J. E. (1998). Three proposals for characterizing MDOF nonlinear seismic response. *Journal of Structural Engineering*, *124*(11), 1281-1289.

Benioff, H. (1934). The physical evaluation of seismic destructiveness. *Bulletin of the Seismological Society of America*, *24*(4), 398-403.

Bianchini, M., Diotallevi, P. P., and Baker, J. W. (2009). "Prediction of inelastic structural response using an average of spectral accelerations." 10th International Conference on Structural Safety and Reliability (ICOSSAR09), Osaka, Japan.

Bojórquez, E., & Iervolino, I. (2011). Spectral shape proxies and nonlinear structural response. *Soil Dynamics and Earthquake Engineering*, *31*(7), 996-1008.

Center for Engineering Strong Motion Data (CESMD), 2015. Center for Engineering Strong Motion Data. Available online at: <http://www.strongmotioncenter.org/> [Accessed 14 March 2015].

De Biasio, M., Grange, S., Dufour, F., Allain, F., & Petre-Lazar, I. (2014). A simple and efficient intensity measure to account for nonlinear structural behavior. *Earthquake Spectra*, *30*(4), 1403-1426.

Eads L., Miranda E., & Lignos D. G. (2014). Seismic collapse risk assessment of buildings: effects of intensity measure selection and computational approach. Report No. 184, The John A. Blume Earthquake Engineering Center, Stanford University, Stanford, CA.

Eads, L., Miranda, E., & Lignos, D. G. (2015). Average spectral acceleration as an intensity measure for collapse risk assessment. *Earthquake Engineering & Structural Dynamics*, *44*(12), 2057-2073.

FEMA (2009). Quantification of Building Seismic Performance Factors (FEMA P695 Report), prepared by Applied Technology Council for the Federal Emergency Management Agency. Washington, D.C.: FEMA.

Ibarra, L. F., Medina, R. A., & Krawinkler, H. (2005). Hysteretic models that incorporate strength and stiffness deterioration. *Earthquake engineering & structural dynamics*, *34*(12), 1489-1511.

Haselton, C. B., & Deierlein, G. G. (2007a). Assessing seismic collapse safety of modern reinforced concrete moment frame buildings. PEER Report 2007-08, Pacific Earthquake Engineering Research Center, Berkeley, CA.

Haselton, C. B., Liel, A. B., Taylor Lange, S., & Deierlein, G. G. (2007b). Beam-column element model calibrated for predicting flexural response leading to global collapse of RC frame buildings. PEER Report 2007-03, Pacific Earthquake Engineering Research Center, Berkeley, CA.

Haselton, C. B., Baker, J. W., Liel, A. B., & Deierlein, G. G. (2009). Accounting for ground-motion spectral shape characteristics in structural collapse assessment through an adjustment for epsilon. *Journal of Structural Engineering*, *137*(3), 332-344.

Housner, G. W. (1952). Intensity of ground motion during strong earthquakes. 2nd Technical Report, under contract N6onr-244, Task order 25. Earthquake Research Laboratory, California Institute of Technology: Pasadena, California.

Iervolino, I., & Cornell, C. A. (2005). Record selection for nonlinear seismic analysis of structures. Earthquake Spectra, 21(3), 685-713.

Jalayer, F., & Cornell, C. A. (2003). A technical framework for probability-based demand and capacity factor (DCFD) seismic formats." RMS.

Kennedy, R. P., Short, S. A., Merz, K. L., Tokarz, F. J., Idriss, I. M., Power, M. S., & Sadigh, K. (1984). *Engineering characterization of ground motion. Task I. Effects of characteristics of free-field motion on structural response* (No. NUREG/CR-3805). Structural Mechanics Associates, Inc., Newport Beach, CA (USA); Woodward-Clyde Consultants, Walnut Creek, CA (USA).

Lignos, D. G., & Krawinkler, H. (2010). Deterioration modeling of steel components in support of collapse prediction of steel moment frames under earthquake loading. *Journal of Structural Engineering*, *137*(11), 1291-1302.

Lignos, D. G., and Krawinkler, H. (2012a). "Sidesway collapse of deteriorating structural systems under seismic excitations." Report No. 177, The John A. Blume Earthquake Engineering Center, Stanford University, Stanford, CA, <http://blume.stanford.edu/tech_reports> (14 Aug. 2013).

Luco, N., & Cornell, C. A. (2007). Structure-specific scalar intensity measures for near-source and ordinary earthquake ground motions. *Earthquake Spectra*,*23*(2), 357-392.

Luco, N., & Bazzurro, P. (2007). Does amplitude scaling of ground motion records result in biased nonlinear structural drift responses? *Earthquake Engineering & Structural Dynamics*, *36*(13), 1813-1835.

McKenna, F. T. (2009). Open System for Earthquake Engineering Simulation (OpenSees), Version 2.1.1, Pacific Earthquake Engineering Research Center (PEER), <http://opensees.berkeley.edu> (6 June 2010).

Miranda, E., & Akkar, S. D. (2003). Dynamic instability of simple structural systems. *Journal of Structural Engineering*, *129*(12), 1722-1726.

Shome, N., Cornell, C. A., Bazzurro, P., & Carballo, J. E. (1998). Earthquakes, records, and nonlinear responses. *Earthquake Spectra*, *14*(3), 469-500.

Shome, N., Cornell C. A. (1999) Probabilistic seismic demand analysis of nonlinear structures. Report RMS-35. RMS Program. Stanford University.

Watson-Lamprey, J., & Abrahamson, N. (2006). Selection of ground motion time series and limits on scaling. *Soil Dynamics and Earthquake Engineering*, *26*(5), 477-482.

Zacharenaki, A., Fragiadakis, M., Assimaki, D., & Papadrakakis, M. (2014). Bias assessment in Incremental Dynamic Analysis due to record scaling. *Soil Dynamics and Earthquake Engineering*, *67*, 158-168.